

INFORMATION TO USERS

This manuscript has been reproduced from the microfilm master. UMI films the text directly from the original or copy submitted. Thus, some thesis and dissertation copies are in typewriter face, while others may be from any type of computer printer.

The quality of this reproduction is dependent upon the quality of the copy submitted. Broken or indistinct print, colored or poor quality illustrations and photographs, print bleedthrough, substandard margins, and improper alignment can adversely affect reproduction.

In the unlikely event that the author did not send UMI a complete manuscript and there are missing pages, these will be noted. Also, if unauthorized copyright material had to be removed, a note will indicate the deletion.

Oversize materials (e.g., maps, drawings, charts) are reproduced by sectioning the original, beginning at the upper left-hand corner and continuing from left to right in equal sections with small overlaps. Each original is also photographed in one exposure and is included in reduced form at the back of the book.

Photographs included in the original manuscript have been reproduced xerographically in this copy. Higher quality 6" x 9" black and white photographic prints are available for any photographs or illustrations appearing in this copy for an additional charge. Contact UMI directly to order.

UMI

A Bell & Howell Information Company
300 North Zeeb Road, Ann Arbor MI 48106-1346 USA
313/761-4700 800/521-0600

Physical Properties of Mantle Silicates Under Upper Mantle Pressures

by

Mu Chai

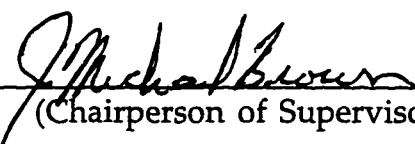
A dissertation submitted in partial fulfillment
of the requirements for the degree of

Doctor of Philosophy

University of Washington

1996

Approved by



(Chairperson of Supervisory Committee)

Program Authorized
to Offer Degree

Geophysics Program

Date

December 12, 1996


UMI Number: 9716822

**UMI Microform 9716822
Copyright 1997, by UMI Company. All rights reserved.**

**This microform edition is protected against unauthorized
copying under Title 17, United States Code.**

UMI
300 North Zeeb Road
Ann Arbor, MI 48103

In presenting this dissertation in partial fulfillment of the requirements for the Doctoral degree at the University of Washington, I agree that the Library shall make its copies freely available for inspection. I further agree that extensive copying of this dissertation is allowable only for scholarly purposes, consistent with "fair use" as prescribed in the U.S. Copyright Law. Requests for copying or reproduction of this dissertation may be referred to University Microfilms, 1490 Eisenhower Place, P.O. Box 975, Ann Arbor, MI 48106 to whom the author has granted "the right to reproduce and sell (a) copies of the manuscript in microfilm and/or (b) printed copies of the manuscript made from microfilm."

Signature 
Date Dec. 13, 1996

Abstract
Physical Properties of Mantle Silicates at Upper Mantle
Pressures

by Mu Chai

Chairperson of the Supervisory Committee: Professor J. Michael Brown
Geophysics Program

Impulsive stimulated scattering technique (ISS) has been applied to the determination of the elastic constants and equation of state at 25°C of a garnet of composition $\text{Py}_{51.6}\text{Al}_{31.7}\text{Gr}_{15.8}\text{Sp}_{0.9}$ to a pressure of 20 GPa, and of a natural Kilbourne Hole orthopyroxene of composition $\text{En}_{0.755}\text{Fs}_{0.085}\text{Ts}_{0.12}$ to 12.5 GPa. At 1 bar the isotropically-averaged longitudinal and shear velocities are 3 % higher than those found in non-aluminous orthopyroxenes. Above 4 GPa the averaged compressional wave velocities in the orthopyroxene exceed those in olivine. These results call into question the assumption commonly used in mineral physical models for the interpretation of mantle seismic data, that high velocities in garnet are balanced by low velocities in pyroxene.

Using the same techniques, the thermal diffusivity tensors at ambient pressure and temperature of a San Carlos olivine $[\text{Mg}_{0.89}\text{Fe}_{0.11}]_2\text{SiO}_4$, the orthopyroxene and the garnet were measured, with the components of the tensor along the *a*, *b*, and *c* crystallographic axes, in units of mm^2/sec , being [2.16 1.25 1.87] in the case of olivine and [1.26 1.05 1.66] in the case of the orthopyroxene. The isotropic thermal diffusivity in garnet is $1.06 \text{ mm}^2/\text{sec}$.

A new experiment was designed to study the R-line fluorescence spectroscopy of ruby ($\text{Cr:Al}_2\text{O}_3$) single crystals under controlled deviatoric stresses at high confining pressures in a diamond anvil cell. When ruby is loaded along the c -axis, the R_1 - R_2 splitting changes linearly with deviatoric stress at a rate of $-0.241 \pm 0.012 \text{ \AA/GPa}$ and does not depend on the confining pressure. The splitting increases non-linearly for ruby loaded along the a -axis. This technique has been applied to determine the yield strength and slip systems of the San Carlos olivine at transition zone pressures (14-20 GPa) and room temperature. Olivine is found to transform partially into β phase under those conditions.

Table of Contents

Chapter 1.....	1
1.1 Motivation and scope of the work.....	3
1.1.1 The elasticity of upper mantle minerals.....	3
1.1.2 Thermal transport.....	6
1.1.3 The rheological properties.....	7
1.2 Experimental techniques.....	9
1.2.1 ISS techniques.....	9
1.2.2 Sample preparation.....	10
1.2.3 Samples orientation.....	12
1.2.4 Cutting and cleaning sample disks	13
1.2.5 DAC techniques.....	14
1.2.6 Gaskets.....	16
1.2.7 Loading the cell	16
1.2.8 Pressure calibration	18
1.3 Illustrations.....	19
1.3.1 Figures.....	19
Chapter 2.....	25
2.1 Introduction.....	26
2.2 Experiments	28
2.2.1 Sample preparation and density and composition determination.....	28

2.2.2 Experiment techniques and the measurement of Rayleigh waves.....	29
2.3 Results and discussions.....	31
2.4 Illustrations.....	39
2.4.1 Tables.....	39
2.4.2 Figures.....	45
Chapter 3.....	59
3.1 Introduction.....	60
3.2 Experimental techniques.....	62
3.3 Results.....	65
3.4 Discussion.....	66
3.5 Illustrations.....	70
3.5.1 Tables.....	70
3.5.2 Figures.....	73
Chapter 4.....	90
4.1 Introduction.....	91
4.2 Experiment and results.....	92
4.2.1 Samples.....	92
4.2.2 Experimental techniques.....	92
4.2.3 Experimental errors, possible advantages and limitations of the technique.....	95
4.3 Relations between thermal and elastic anisotropy.....	97
4.4 Geological implications.....	101
4.5.1 Tables.....	105
4.5.2 Figures.....	108
Chapter 5.....	116

5.1 Introduction.....	117
5.2 Experimental technique	118
5.3 Results and discussion.....	120
5.4 Illustrations.....	128
5.4.1 Figures.....	128
Chapter 6.....	143
6.1 Introduction.....	144
6.2 Experimental technique	145
6.3 Results and discussions.....	146
6.3.1 Stress determination.....	146
6.3.2 Yield strength.....	148
6.3.3 Low temperature plastic deformation mechanisms.....	149
6.3.4 Deformation induced phase transformation.....	151
6.4 Geophysical implications.....	153
6.5 Illustrations.....	155
6.5.1 Tables.....	155
6.5.2 Figures.....	157
Chapter 7.....	165
Bibliography	170
Personal Vita.....	187

List of Figures

Figure 2.1 Time domain record of ISS signal of garnet	45
Figure 2.2 Fourier transformation of the ISS signal of garnet	46
Figure 2.1 Time domain record of the surface wave of garnet	47
Figure 2.4 Fourier transformation of the surface wave.....	48
Figure 2.5 Dispersion of surface wave on a layered surface.....	49
Figure 2.6 Longitudinal sound velocity of garnet as a function of direction.....	50
Figure 2.7 C11 of garnet.....	51
Figure 2.8 C12 and C44 of garnet.....	52
Figure 2.9 Bulk modulus of garnet	53
Figure 2.9 Shear modulus of garnet.....	54
Figure 2.11 Compression of garnet.....	55
Figure 2.12 Reduced bulk modulus of garnet.....	56
Figure 2.13 Reduced shear modulus of garnet	57
Figure 2.14 Temperature effect on the shear modulus of garnet	58
Figure 3.1 Time domain record of ISS signal of opx	73
Figure 3.2 Fourier transformation of ISS signal of opx	74
Figure 3.3 Sound velocities of opx at 0 GPa.....	75
Figure 3.4 Sound velocities of opx at 2.3 GPa.....	76
Figure 3.5 Sound velocities of opx at 4.3 GPa.....	77
Figure 3.6 Sound velocities of opx at 6.3 GPa.....	78
Figure 3.7 Sound velocities of opx at 8.5 GPa.....	79

Figure 3.8 Sound velocities of opx at 10.5 GPa.....	80
Figure 3.9 Sound velocities of opx at 12.5 GPa.....	81
Figure 3.10 Diagonal longitudinal elastic constants of opx.....	82
Figure 3.11 Diagonal shear elastic constants of opx.....	83
Figure 3.12 Off-diagonal longitudinal elastic constants of opx	84
Figure 3.13 Bulk modulus of opx	85
Figure 3.14 Shear modulus of opx.....	86
Figure 3.15 Cell-edge compression of opx.....	87
Figure 3.16 Compressional sound velocities of olivine, opx and garnet.....	88
Figure 3.17 Shear sound velocities of olivine, opx and garnet.....	89
Figure 4.1 Thermal decay signal of olivine.....	108
Figure 4.2 Log plot of Figure 6.1.....	109
Figure 4.3 Thermal decay rate as a function of grating spacing	110
Figure 4.4 Anisotropy of thermal diffusivities.....	111
Figure 4.5 Anisotropy of longitudinal sound velocities of silicates	112
Figure 4.6 Schematic diagram of mid-ocean ridge.....	113
Figure 4.7 Temperature profile of the oceanic lithosphere	114
Figure 4.8 Water depth of the ocean-floor as a function of time.....	115
Figure 5.1 Experimental arrangement.....	128
Figure 5.2 Ruby spectra of sandwiched samples.....	129
Figure 5.3 Apparent pressure profiles of sandwiched samples.....	130
Figure 5.4 Stress profiles S_r of a solid cylinder with no-slip B.C.....	131
Figure 5.5 Stress profiles S_θ of a solid cylinder with no-slip B.C.	132
Figure 5.6 Stress profiles S_z of a solid cylinder with no-slip B.C.	133
Figure 5.7 Stress profiles S_{rz} of a solid cylinder with no-slip B.C.....	134
Figure 5.8 Calculated vertically averaged stresses for a ruby cylinder.....	135

Figure 5.9 R-line splitting of uniaxially loaded c-normal ruby.....	136
Figure 5.10 R-line splitting as a function of (s1-s3).....	137
Figure 5.11 R-line splitting deviation along a-normal.....	138
Figure 5.12 A recovered ruby sample after deformation.....	139
Figure 5.13 Pressure profile of a ruby cylinder.....	140
Figure 5.14 Yield strength of ruby with friction B.C.....	141
Figure 5.15 Yield strength of ruby with free-slip B.C.....	142
Figure 6.1 Experimental arrangement.....	157
Figure 6.2 Top view of the sandwiched sample in the DAC.....	158
Figure 6.3 Pressure distribution across the olivine sample.....	159
Figure 6.4 Stress profile for a loaded cylindrical olivine sample.....	160
Figure 6.5 Yield strength of olivine.....	161
Figure 6.6 Electron image microstructure of deformed olivine.....	162
Figure 6.7 SAED pattern of structure disorders.....	163
Figure 6.8 Formation of β phase.....	164

List of Tables

Table 2.1 Chemistry of garnet.....	39
Table 2.2 Cell parameters and density of garnet.....	40
Table 2.3 Elastic and density data for garnet.....	41
Table 2.4 Pressure dependence of elastic constants of garnet	42
Table 2.5 Elastic constants of end-member garnet	43
Table 2.6 Derivatives of mean longitudinal and shear velocity.....	44
Table 3.1 Chemistry of Kh-opx.....	70
Table 3.2 Elastic constants of Kh-opx	71
Table 3.3 Pressure dependence of elastic constants of Kh-opx	72
Table 4.1 Data for olivine, opx and garnet.....	105
Table 4.2 Thermal diffusivity for olivine, opx and garnet.....	106
Table 4.3 Thermal anisotropy data and calculations.....	107
Table 6.1 Experimental conditions for San Carlos olivine single crystals.....	155
Table 6.2 Lattice mismatch.....	156

Acknowledgments

It is my greatest pleasure to thank my advisor, Professor J. Michael Brown, for all he has done for me during the course of my graduate education here. I owe this entire work to him, if not for him I would not have been in this field. I am equally grateful to Professor Leon J. Slutsky for his nearly infallible instruction and patience. I thank both of them for their guidance and support in many occasions extending beyond the scientific level.

I thank Professor Evan Abramson for his constant help with his resourceful experience in the optical experiments which are essential to this thesis. I thank Professor Ron Merrill for many useful suggestions in the rheology experiments.

To Professor Richard Stewart, thank you for your generosity in letting me using your microscopes to analyze my samples. To David McDougall, thank you for all the suggestions in preparing the samples which made the work much easier. To Bob Odom, thank you for helping to solve the puzzle of surface wave on garnet.

My thanks also go to Surya Wiryana, Mike Harrell and Andrew Newell. Surya has always been a great source of interesting conversations; Mike is one reason for my ever improving English; I thank Andrew for being such a tolerant officemate.

I am most in debt to my parents for their unselfish dedication. Finally my thanks go to my wife and best friend in life, Yang Liu, for giving me all the support and encouragement I need.

Dedication

To my wife Yang Liu and my parents.

Chapter 1

Introduction

This work covers three topics: elasticity, thermal transport, and low temperature plasticity of upper mantle minerals. The first two topics are interconnected not only by the underlying physics but also by the experimental technique, impulsive stimulated scattering (ISS), with which they have been investigated. The third topic is one the author found both geophysically important and experimentally challenging in trying to attack it with a new approach.

This chapter will give a brief account of the motivation of this work, the scope of the work and the experimental methods used in the investigations. Chapters 2 and 3 present experimental results of the elasticity of a garnet up to 20 GPa and a pyroxene up to a pressure of 12.5 GPa. Geophysical implications of these results are discussed. Chapter 4 reports thermal transport properties of the three most important upper mantle minerals: olivine, pyroxene and garnet. The effects of the anisotropy of the thermal transport on the development of the oceanic lithosphere is considered. A model which incorporates elastic anisotropy, anharmonicity as described by acoustic Grüneisen parameters, Brillouin zone structure, and the increased phase volume for the scattering of short wavelength phonons is developed to describe the anisotropy of thermal diffusivity. Chapter 5 deals with a problem encountered by all researchers using the diamond anvil cell, that is, how to calibrate pressures under non-hydrostatic conditions using ruby. The technique developed in this chapter is applied in Chapter 6 to investigate the yield strength and low temperature plasticity of olivine, and the effects of shear stress on pressure-induced phase transformations. In the

final chapter, Chapter 7, some important questions raised by the results from this work are discussed, and some future research which is needed for better understanding of these questions is suggested.

1.1 Motivation and scope of the work

1.1.1 The elasticity of upper mantle minerals

Because of the inaccessible nature of Earth's interior, our knowledge about the deep Earth, such as its chemical composition has to be deduced from indirect observations such as seismic measurements, magnetic field observations and field petrology. Laboratory measurements of the elasticity of mantle minerals provide an independent calibrations for seismic observations through the following relations:

$$V_{\phi} = \phi_2^{\frac{1}{2}} = \sqrt{V_p^2 - (4/3)V_s^2} = \sqrt{\frac{K_s}{\rho}} \quad (1.1)$$

$$V_p = \sqrt{\frac{K + 4/3\mu}{\rho}} \quad (1.2)$$

$$V_s = \sqrt{\frac{\mu}{\rho}} \quad (1.3)$$

where V_{ϕ} is the seismic parameter; V_p , the isotropic compressional velocity; and V_s , isotropic shear velocity. All are seismic observables. K , K_s and μ are the bulk and shear modulus; ρ , the density. All are determined experimentally as functions of pressure, temperature, and possibly frequency.

Seismic observations have shown that the upper mantle structure contains both radial discontinuities and lateral variations. The radial structure is dominated by two seismic discontinuities at 410 km, and 670 km [Niazi and Anderson 1965; Johnson 1967]. Waveform modeling of long-period refracted body waves indicates the velocity-depth gradient between 410

and 670 km is much higher than can be accounted for by simple compression of a single phase [e.g., *Wiggins and Helmberger 1973; Grand and Helberger 1984; Bowman and Kennett 1990*]. A minor discontinuity at 520 has been reported by *Shearer [1991]*; and *Revenaugh and Jordan [1991]*, but questioned in a subsequent study of *Bock et al. [1995]*. Strong lateral correlation between upper mantle tomography and surface tectonics have been demonstrated by regional travel-time residuals studies [*Cleary and Hales 1966, and Doyle and Hales 1967*], refraction surveys [*Wiggins and Helmberger 1973*], and regional and global tomography [*Nataf, Nakanishi and Anderson 1986; Grand 1994; Su et al 1994; Zielhuis and van der Hilst 1996*]. In general, the high velocities have been associated with old and cold continental roots; while the low velocities correspond to the hot mid-ocean ridges.

Mineral physics studies of phase equilibria of mantle minerals at high pressure and high temperature, on the other hand, have provided further constraints on possible petrological models. Based on the observed high seismic velocities between 200 and 900 km, *Birch (1952)* concluded in the early 1950s that the velocities were much too high to be explained by simple compression of the crustal oxides; therefore they must have been caused by pressure-induced phase transformations of the silicates. Based on the experimental data and thermal dynamic calculation on Ge-olivine, *Ringwood [1956]* further proposed that the 410 km seismic discontinuity was caused by the transformation of olivine to high pressure phases. Transformation of olivine to β phase and spinel phase at 1450°C and 14 GPa (410 km), was first confirmed experimentally in 1966 (*Akimoto and Fujisawa 1966; Ringwood and Major 1966*). Transformation of pyroxene and garnet to perovskite

structures at about 1600°C and 26 GPa (670 km) were demonstrated, subsequently, by *Liu* [1974, 1976] and *Liu and Ringwood* [1975].

In determining the chemical composition of the upper mantle, the following seismic observations have been commonly used: the absolute seismic velocities below 410 km, the two major seismic discontinuities at 410 and 670 km and the high velocity gradient in the transition zone (between 410 and 670 km). The absolute velocities below 410 km provide the general constraints on the elasticities and their pressure dependence of the candidate minerals. The 410 km discontinuity, which has been attributed to the α - β phase transition of olivine, serves to constrain the olivine content of the upper mantle. The high velocity gradient in the transition zone, which has been attributed to the continuous transformation of pyroxene to garnet, is sensitive to the details of this transformation.

The prevailing views of the upper mantle composition are consistent with the petrological model, pyrolite, proposed first by *Ringwood* [*Ringwood* 1962; *Weidner* 1984; and *Ito and Stixrude* 1992], which consists of 60% olivine, 30% orthopyroxene and clinopyroxene and 10% garnet. However, these model employed equations of state with parameters extrapolated well beyond their experimental range [e.g., *Weidner* 1984; *Ito and Stixrude* 1992]. It has been demonstrated in the case of olivine and orthopyroxene by *Chai et al* [1993] and *Zaug et al* [1993], that the discrepancies between the extrapolation and experimental measurement cannot be ignored.

It is one of the primary goals of this work to provide better experimental data for the constraints for the upper mantle composition. The elasticity of two major mantle silicates, orthopyroxene and garnet, have been measured for the first time throughout their stability fields.

1.1.2 Thermal transport

The evolution of Earth and other planetary bodies is to a considerable degree controlled by internal heat production and transport. Although advection of heat through the process of convection is the large-scale mechanism of planetary heat transport, within boundary layers (at Earth's surface, at the core-mantle boundary, and at any other barrier to mass transport) thermal conduction must become locally predominant. Thermal conductivity within Earth is usually assumed scalar and nearly constant (i.e.. [Kieffer, 1976; Spohn and Schubert, 1982]). However, the experimental and theoretical basis for such assumptions is not compelling. The predominate minerals of the upper mantle are anisotropic, preferred orientation has been observed [Babuska and Cara, 1991], and pressure and temperature dependencies clearly exist [Ross *et al.*, 1984].

Thermal conductivity data at near ambient conditions have been obtained for many minerals. However, several important dependencies have received scant attention. [Ross *et al.*, 1984] noted that relatively little data constrain high pressure behavior. The difficulty of the measurements has led to only isolated reports of high pressure data (i.e. [Fujisawa *et al.*, 1968; Scharmeli, 1982]). In the deeper mantle, thermal diffusivity is one of the largely uncertain parameters that enters into the determination of the Rayleigh number defining the nature of convective motion. Uncertainties in the extrapolation of thermal conductivity to lower mantle conditions have been noted [Brown, 1986].

Although some studies of the anisotropy of thermal transport in minerals were undertaken early in this century [Wooster, 1936] most recent

investigations have involved polycrystalline aggregates (e.g. [Horai, 1971]) or have been confined to a single crystallographic direction (e.g. [Schatz and Simmons, 1972]). The observation of seismic anisotropy in the oceanic lithosphere indicates that the crystals of the dominant mineral phases, olivine and orthopyroxene, are in fact strongly oriented. Such preferred orientation of lithospheric minerals due to flow-induced recrystallization is expected. The effects of such preferred orientation on the mechanical properties of the lithosphere are discussed by [Hearn *et al.*, 1996].

1.1.3 *The rheological properties*

Crystalline solids, when subject to non-hydrostatic stresses, will deform either elastically or plastically, or fracture, depending upon the size of the stress, the temperature and time scale. Plastic deformation (flow) is caused by shear or the deviatoric part of the stresses, and is described by the rate-equations which prescribe the relation between the strain rate and the shear stresses. Plastic deformations can be divided into three different types by their rate-equations [Frost and Ashby 1982]:

Low temperature plasticity: Plastic deformation through gliding motion of dislocations or twinings, which operates normally at high stresses more than a few percent of the shear modulus and low temperatures a fraction of the crystal's melting temperature.

Diffusion flow: Deformation by the diffusion of single ions at very high temperature and low stresses, leading to Newtonian flow in which the strain rate is proportional to the stress.

Power-law creep: A non-linear flow involving both the climb and glide motion of dislocations at temperature and stress between diffusion flow

and low-temperature plasticity. The viscosity of the flow is a power function of the stress.

Low-temperature plasticity of mantle minerals at high confining pressure is the primary interest of the study, because it may concern the physical state of part of Earth's interior, such as the subducted slabs. At ambient temperature and pressure, minerals usually fracture by cleavage before they yield. If confining pressure is provided, low-temperature plasticity will be exhibited. A subducted slab may lie at a depth of 700 km, at which depth the temperature of its interior can be as low as 600°C (e.g., Kirby [1995]). Under such conditions, both theory and experiments suggest that rapid seismic failure, such as occurs at shallow depths should be replaced by ductile deformation [Griggs, 1972; Kirby, 1987; Kirby *et al.*, 1991; Burnley *et al.*, 1991]. However, the largest magnitude deep earthquake (deeper than 350 km) ever recorded was imaged at a depth of 635 km in a subducted slab beneath Bolivia [Silver *et al.*, 1995]. The origin of the stresses giving rise to the ruptures and the nature of the physical process of the failure are not understood in terms of low-temperature plasticity.

Because of the high pressure and temperature, long time scale, and small displacements involved, many rheological properties have to be inferred through indirect methods. For example, the viscosity of silicates under lower mantle condition has been estimated through seismic anelasticity (Q^{-1}) (e.g., Sato [1992]), or through glacial rebound (e.g., Turcotte and Schubert [1982]).

Some efforts have been made to experimentally determine the pressure dependence of the yield strength of silicates in the diamond anvil cell (DAC). In the late 1970s, Kinsland and Bassett [1977] conducted a set of

experiments in which the samples were pinched between the diamonds. The shear stress was inferred by the shape of the x-ray diffraction spots. A more recent examples are demonstrated by the work of *Meade and Jeanloz* [1988a, 1988b, and 1990]. The shear stress was deduced by the slope of the pressure profiles. One disadvantage common to both approaches is that the samples were not gasketed, under which conditions the confining pressure is not clearly defined.

In this work, a new experiment has been designed for the diamond anvil cell to impose a confining pressure equivalent to that of lower mantle. The stress state is accurately measured. The yield strength, the deformation mechanisms (dislocations and twinings), and the effects of shear stress on the phase transformation have been investigated.

1.2 Experimental techniques

1.2.1 ISS techniques

The optical technique is discussed in general in *Fayer*, [1986] and *Yan et al.*, [1987] and specifically in the context of the diamond-anvil cell in *Brown et al.* [1989] and *Zaug et al.* [1992; 1993]. The block diagram of the ISS experiment arrangement is shown in Figure 1.1. Briefly, two successive 1064nm excitation pulses, ≈ 80 ps in duration, are selected from the output train of a Q-switched, mode-locked, Nd-YAG laser and recombined in the sample at an angle 2θ , but otherwise coincident in space and time. Their interference establishes a periodic distribution of intensity and, in a medium that absorbs in the near infrared, a spatially periodic variation in the temperature ensues. In an anisotropic crystal, the associated thermal pressure launches a set of three counterpropagating acoustic waves, one quasilongitudinal and two

quasi- transverse, of acoustic wavelength λ_A , which in terms of λ , the wavelength of the laser light and θ being

$$\lambda_A = (\lambda/2\sin\theta) \quad (1.1)$$

The impulsively excited acoustic waves induce a temporally and spatially periodic variation in the index of refraction of the sample. A third pulse selected from the same Q-switched envelope as the excitation pulses is doubled to 532 nm and delayed by time of flight to generate the probe. Observation of the intensity of the Bragg scattering of the probe by the acoustic grating as a function of probe delay serves to determine the frequency (f_A), and hence the velocity ($c = \lambda_A f_A$), of the acoustic waves. In a diamond anvil cell, the orientation of the acoustic grating with respect to the crystal axes may be varied by rotating the cell about an axis normal to the diamond faces. The velocity of sound measured as a function of crystallographic direction serves to determine the independent elastic constants. The exponential decay of the periodic distribution of temperature created by the excitation process can be used to determine the thermal conduction.

1.2.2 *Sample preparation*

The impulsive stimulated scattering experiments require an optically clean sample, meaning it should be free of inclusions, cracks or any type of impurities. The samples need first to be examined for visible impurities under a microscope of at least 60x under crossed polarizer.

Samples of more than one crystallographic orientation are sometimes necessary if the crystal is anisotropic in terms of certain physical properties such as the elastic constants. These anisotropic physical properties can be only constrained adequately with observations measured along certain crystallographic directions. Once the orientation has been established

through optical and x-ray diffraction methods, the sample can be sliced into thin plates with diamond saw along the desired direction. The preferred thickness is usually about 200 μm .

Both sides of the thin plates are then polished. The samples are usually polished with diamond powder of 6 μm and 1 μm and fine-finished with 1/4 μm . The final thicknesses of the sample plates are usually about 20~40 μm thick depending upon the highest pressure at which the sample is studied. Optical quality of the sample surface is required to reduced unwanted scattering in ISS experiments. There should no visible scratches on the sample surface under microscopic examination at 60x.

Large high quality single-crystal samples are sometimes rare, as in the case of pyroxene. It is difficult to obtain more than one orientation from small grains (millimeters in diameter) using the procedures described above. If small crystals can be found in large numbers, it is helpful to pot many crystals in an epoxy plug. There are several advantages of potting small samples. First one can hope to get many different orientation; second it increases the rigidity of the epoxy and reduces the rounding of the samples which is a serious problem when small samples are polished. The following procedures are recommended for potting the samples:

A cylindrical aluminum mold and a piece of glass plate are sprayed with Buehler Release Agent (Buehler Ltd., Evanston, Illinois) and are placed on top of a hot plate set at about 70°C. Small crystals are distributed into the aluminum mold until the glass surface is almost covered by them. The mold is then filled with epoxy to about 10 mm, supposing the crystals are smaller than a few millimeters in diameter. The epoxy is cured for at least 6 hours to form a rigid plug. After the plug is properly cured, with the help of a screw

driver, it is easy to remove it from the mold. The plug is ready for slicing and polishing.

The side of the plug away from the crystals, which usually has a concave surface, is ground first with a thin section grinder to a flat surface parallel to the crystal side. This side then is used as a reference for grinding the crystal side. The crystal side is ground until a sizable flat surface is produced in most of the crystals. The crystal side is polished as described above. The polished surface is glued to a clean slide with superglue this time. The plug is sliced, ground and polished as described above. In order to produce a flat surface on these small samples, a nylon polishing cloth (Buehler Ltd., Evanston, Illinois) is recommended. The polished sample can be removed from the slide after being soaked in acetone for about an hour.

1.2.3 Samples orientation

The orientation of the sample needs to be determined precisely after it is polished. This step is important in determining the anisotropic tensor quantities of the sample. The polished sample is glued to a piece of optical fiber and placed on the goniometer of a precession x-ray machine. The angles on the goniometer are recorded as 'zero' when the surface of the sample is normal to the x-ray beam. This can be achieved by introducing a He-Ne laser beam through the collimator of the x-ray machine and adjusting the sample so that the reflection returns through the collimator. The crystallographic axes can be found and rotated using the goniometer so that one is parallel to the x-ray beam. The angles now are recorded and the difference between them and the 'zero' can be easily converted into direction cosines of the normal of the sample surface in terms of its crystallographic axes. The

precision of this procedure is quite high, but due to the small curvature produced on the sample surfaces during the polishing, the uncertainty is estimated at about 1 degree.

Much time can be saved if one can select samples of different orientation among the many small polished, randomly oriented crystals before putting them onto the x-ray machine for precise determination of the orientations. This is done by an optical method, employing a petrographic microscope. With the help of an optical mineralogy handbook [e.g., *Deer et al.*, 1976; *Phillips*, 1971], samples with crystallographic axes normal to their surfaces can be recognized. The orientation of the samples chosen this way were verified later through x-ray-diffraction.

1.2.4 *Cutting and cleaning sample disks*

Small disks of samples for the DAC are produced using a coring drill made of small gauge hypodermic needles. The thin polished crystal plate is glued to a microscope slide with low viscosity superglue. The slide is held onto a platform which is attached to a vertically positioned linear track. The hypodermic needle is held by a precision drill press, and the platform is pushed upward by weights acting on a lever arm to ensure a gentle touch between the sample and the coring drill (see Figure 1.2). A slurry of 1 μm diamond powder mixed with a TAPMATIC cutting fluid is used as the cutting agent. To avoid breaking or detaching the sample from the slide before it is cut, the drill speed and the amount of weight on the lever arm are critical, and need to be adjusted by trial and error. Drilled olivine disks are shown in Figure 1.3.

The sample disks were removed from the slide and cleaned with methanol and acetone. The cleaning procedure needs to be carefully executed and is very tedious. This step can never be emphasized too much, since any trace of dirt can cause the burning of the diamond of the DAC. The following methods have been proven effective. The sample is immersed in a beaker filled with methanol and/or acetone and cleaned in an ultrasonic-cleaner. It can also be cleaned using an aspirator by sucking it up and then dropping it into the solution repeatedly. Finally, the sample is dried by dragging it on a very clean microscope slide with a clean fine needle point.

1.2.5 DAC techniques

Historically, the drive for achieving higher pressure has been fueled by the desire to produce man-made diamonds. But it was not until Jamieson at University of Chicago and Van Valkenburg and Weir at the National Bureau of Standards came up with the ideas in the late 1950s to use diamond, the hardest material on Earth, to generate high pressures, that the high pressure research had come to the modern era. Since then, diamond anvil cell has gone through many modifications and new designs. Now hundreds of GPa pressure have become routinely attainable in many labs worldwide.

Among all the designs of DAC, one of the most widely used types is the Merrill-Bassett DAC. The Merrill-Bassett DAC was used in all the experiments presented in this work except the thermal experiments. In the rheology experiments, some runs were carried out in a DAC designed by Boehler of the Max Planck Institute at Mainz, Germany. Figure 1.4 is the schematic diagram of the Merrill-Bassett DAC. The DAC consists of a few major parts: the triangular frames, the diamond seats and the diamonds

themselves. The diamonds used in the experiments are standard brilliant-cut with the tapered point ground to a small flat surface, known as a culet, which is parallel to the table surface of the diamonds. Usually the diamonds are glued to the seats with cement and the seats are set into the countersink of the triangular frames. The two triangular frames are bolted together using three bolts, and pressure is generated by apposing the two diamonds against each other with the sample in between them. It is very important to maintain alignment of the two diamonds. The alignment can be made by adjusting the seats using set screws which hold them in place in the countersink of the frames.

In the ISS experiments, the diamond cannot be held onto the seat by any cement or glue, since any slightest contamination of the sample area by organic substances, like oil, can cause burning of the diamonds during the experiments. A mechanical hold-down is necessary. It is also important to keep the gasket in place while the sample is loaded, because one common way to lose a carefully prepared sample is by the movement of the gasket. To overcome those shortcomings, some modifications have been made to the DAC. Figure 1.5 shows parts of the new design of the DAC. In this design, the diamonds are mounted using the elasticity of a 125 μ m thick hard stainless steel shim stock washer. The washers are clamped by a tapped ring which is bolted to the seat. This change also makes mounting and dismounting of the diamonds onto and from the seat much easier. A gasket holder has also been added, which is a cap with a countersink in it. A circular gasket is placed into this countersink and sandwiched with a snugly-fit shim stock washer. The gasket holder is then bolted to the same tapped ring which hold the diamond until the gasket is firmly against the diamond.

1.2.6 Gaskets

The DAC was initially used with the sample directly compressed between the two apposing diamonds. Later Van Valkenburg found by putting the sample in a small hole drilled in a piece of metal shim, sandwiched between the diamonds, not only was the volume of the sample increased, but also higher and more hydrostatic pressure permitted. This gasket forms a chamber for both the sample and the pressure medium. Materials used for gaskets in this work include prehardened stainless steel, Inconel 750 and Inconel 718, air cooled steel, and rhenium. Among all the materials, rhenium is found to be ideal, as it is both strong and ductile. In most experiments, thicker samples and higher pressure are generally desired. But the final thickness of the gasket for a given pressure is determined by the strength of the material. It can be shown easily that the ratio of the thickness of the gasket to the diameter of the culet is proportional to the yield strength and inversely proportional to the pressure. For a given sample, the smaller the hole in the gasket the higher the pressure which can be achieved. For example, if the sample is 200 μm in diameter and 20 μm thick, and the culet of the DAC is 550 μm , the rhenium gasket is usually preindented to 70–80 μm , and a hole of less than 250 μm is drilled, under which conditions a pressure of more than 20 GPa can be easily obtained. In this work, an electrode discharge machine is used to drill the hole. A drilled gasket with an olivine sample loaded in it is shown in Figure 1.6.

1.2.7 Loading the cell

The purpose of using a pressure medium is to create an environment which is as hydrostatic as possible. Many substances can be used as pressure

medium depending upon the application and the pressure desired. These include: NaCl, mineral oils, methanol, methanol-ethanol mixture (4:1 by volume), methanol-ethanol-water mixture (16:3:1 by volume), Ar, Ne, I, N, etc. In this work only Ar and a methanol-ethanol-water mixture are used.

Liquid Ar is used as a pressure medium in most of the experiments in this work. Loading liquid Ar cryogenically can be frustrating. It is not uncommon that the sample is washed off by the vigorous boiling of the Ar, and more than half of the time one cannot tell whether the cell is loaded before the cell is removed from the Ar bath. To load the cell efficiently, the following procedure has been used.

The DAC is tightened within the elastic limit of the gasket after a sample is loaded and before the cell is immersed into liquid Ar. There are two reasons for this step. First, the sample can be flushed out if the cell is not tight. Second, if the cell is compressed before loaded with pressure medium, the sample is likely to be crushed. With the cell tightened, one can watch the cell being filled as one untightens the cell. Springs are used on the guiding pins of the cell which serve to push the cell apart as the cell is untightened.

Only the bottom half of the DAC is attached to the cell-rack, which is a metal frame for holding the DAC inside the Ar bath. A piece of fiber optic connected to a light source is placed next to the bottom diamond to illuminate the sample chamber. A microscope is set above the bath.

The liquid Ar in the bath should be maintained to a level just below the surface of the top diamond, because a unsettled liquid surface will disturb the view of the sample chamber in the microscope. A test tube of liquid nitrogen, inserted as cold finger, will help to put the boiling to rest very efficiently.

The cell is untightened by unscrewing the bolts very slowly. The sample chamber starts to wet slowly as one sees a bubble forming. The bubble eventually disappears at the center of the chamber in a minute or so, at which point one knows the cell is loaded with Ar.

The cell is tightened slowly and evenly by screwing each bolt 5-10 degrees at a time. One mistake one is likely to make is to take the cell out too soon. Even though the cell is loaded in the bath, the Ar can still escape out of the cell because the cell relaxes due to thermal expansion. Therefore the DAC should not be taken out until one sees Ar starts to solidify (at about 1.6 GPa), which is indicated clearly by phase boundaries between the liquid and the solid.

Although the methanol-ethanol-water solution is much easier to load, care needs to be taken to make sure the sample not be washed off by the solution. A way of avoiding this is to place a droplet of solution on the gasket beside the sample chamber, and drag the solution into the chamber, then position the upper half of the cell on the load.

1.2.8 Pressure calibration

Once the cell is loaded, the pressure must be measured. Ruby fluorescence is used as the pressure gauge [*Piermarini et al.*, 1975]. In most experiments, hydrostatic pressure is desired. Unfortunately, no pressure medium can stay perfectly hydrostatic at very high pressure. Correct pressure calibration under non-hydrostatic conditions are discussed in detail in Chapter 5.

1.3 Illustrations

1.3.1 Figures

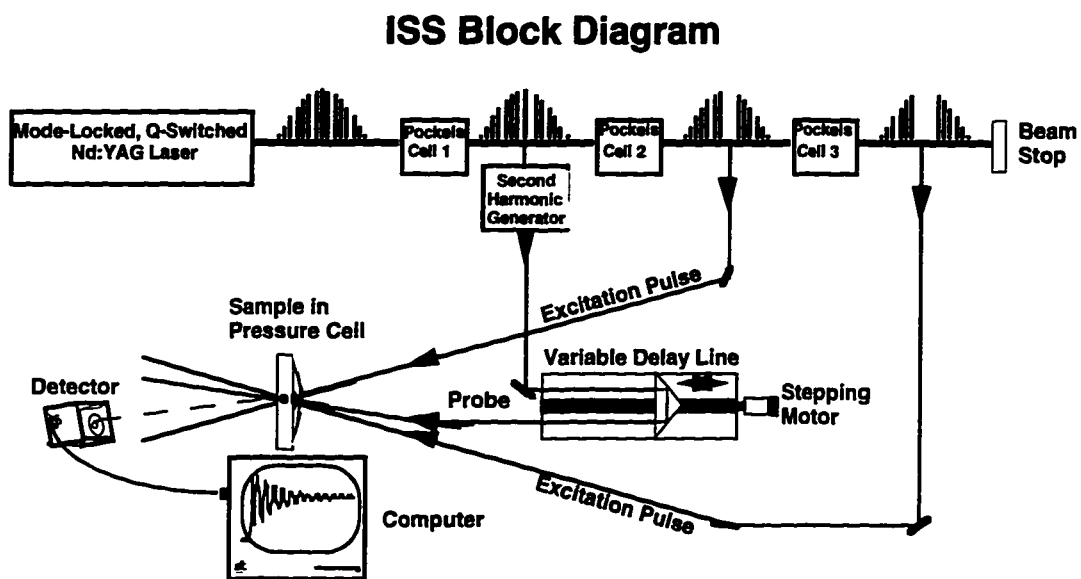


Figure 1.1 Block diagram for impulsive stimulated scattering experiment

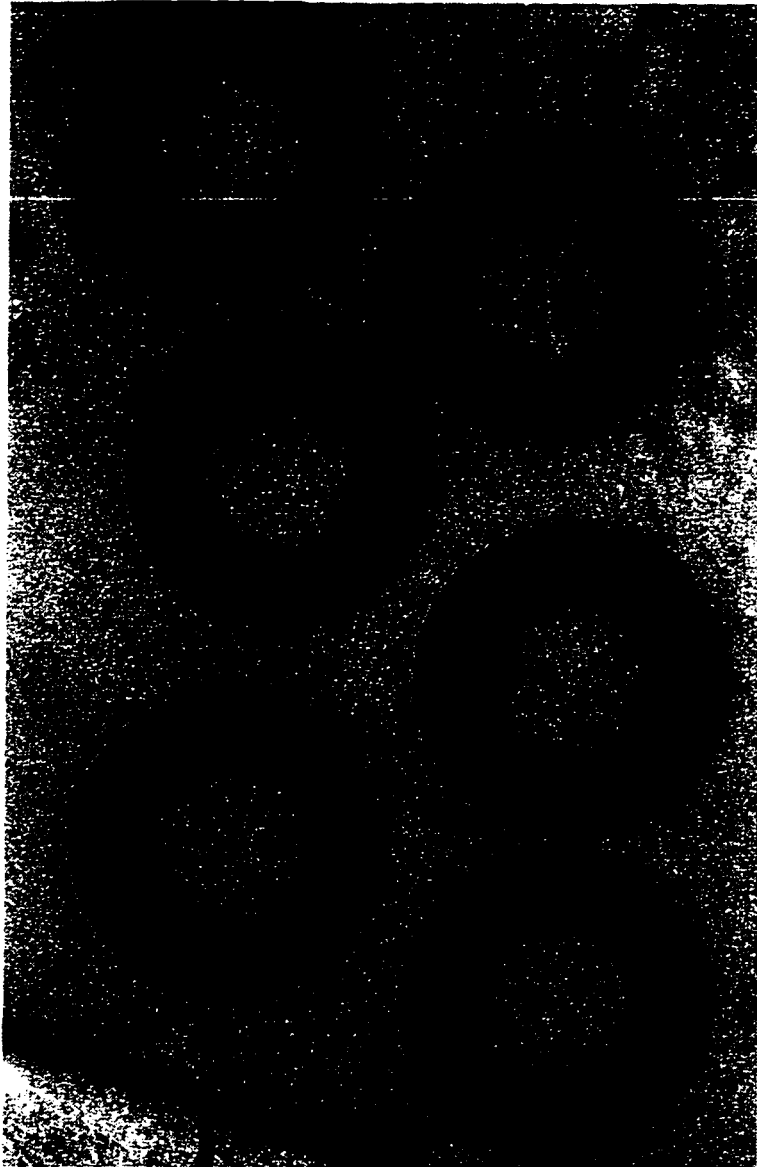


Figure 1.2 Coring drilled olivine samples

The disks were core-drilled on a polished olivine plate using hypodermic needle with a slurry of 1 μm diamond. The dark circles are the removed areas. The diameter of the disks is 200 μm .

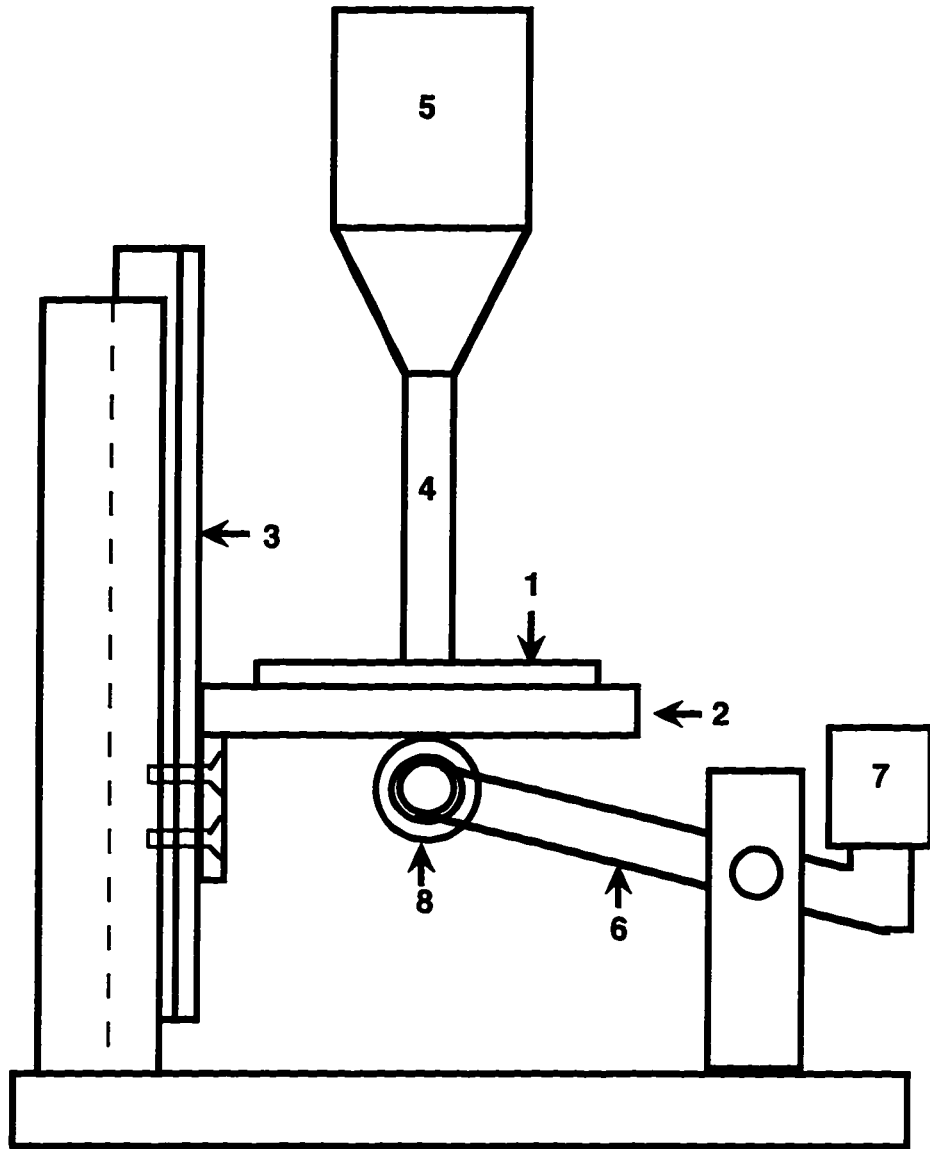


Figure 1.3 Schematic diagram of the coring drill and platform

1) Sample; 2) platform; 3) linear track; 4) hypodermic needle; 5) drill press; 6) lever arm; 7) weight; 8) ball bearing.

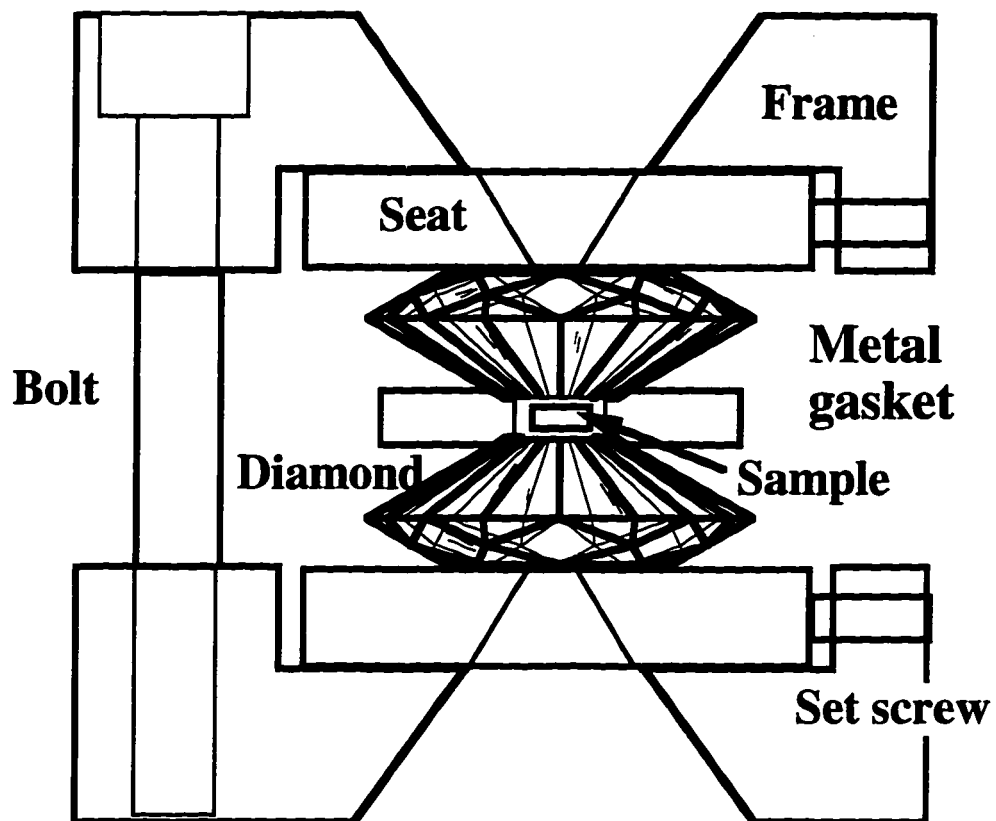


Figure 1.4 Schematic diagram for diamond anvil cell

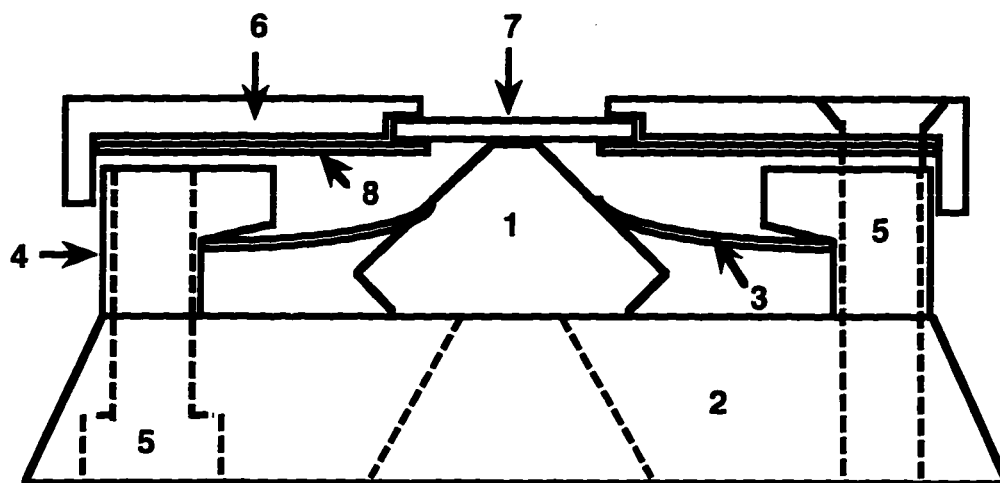


Figure 1.5 Assemble diagram for the new design of diamond anvil cell
1) Diamond; 2) seat; 3) spring washer; 4) tapped ring; 5) bolts; 6) gasket holder; 7) gasket; 8) shim stock washer.

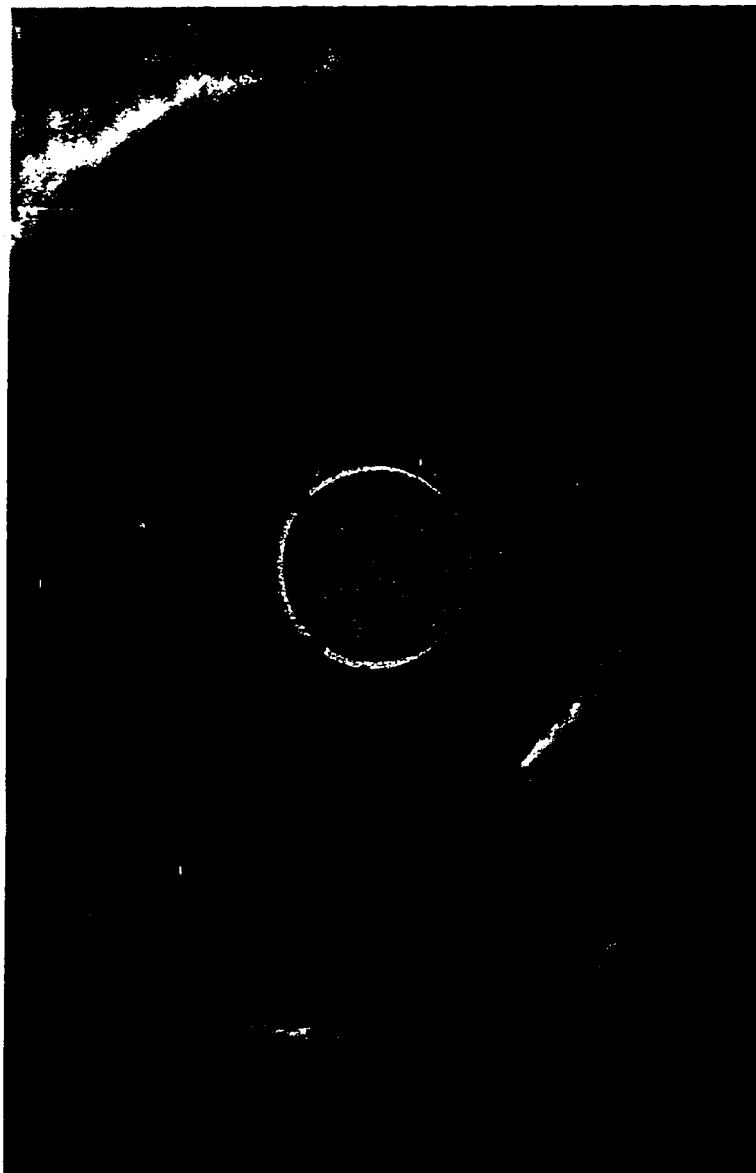


Figure 1.6 Top view of a sample olivine in an indented and drilled gasket
The circle inside the gasket chamber (the circular hole) is an olivine sample disk.
The small dots on each quadrant are ruby chips for pressure calibration.

Chapter 2

Elasticity of a Pyrope-Grossular-Almandine Garnet up to a Pressure of 20 GPa

2.1 Introduction

Natural garnets possess a body-centered cubic unit cell with a general formula $X^{VIII}_3Y^{VI}_2Z^{IV}_3O_{12}$, where X, Y and Z are cations at special polyhedral sites [Meagher, 1982]. The superscripted Roman numerals indicate the coordination number of the cations, for example, each X cation is coordinated to 8 oxygens of a slightly distorted dodecahedron. There are eight formula units per unit cell. The most common cations found in natural garnets are the abundant di-, tri-, and tetravalent cations such as: Al, Mg, Si, Ca, Ti, Mn, and Fe. The SiO_4 tetrahedra and SiO_6 octahedra in garnet share corners with each other alternatively. Each octahedron shares six of its twelve edges with adjacent dodecahedra. These corners and edges shared between the polyhedras make garnets one of the most incompressible mineral. A wide range of sizes and valence states of cations can be accommodated the garnet structure. Natural garnets display a wide range of variations both in chemical composition and in physical appearance. The common garnet end members were divided by *Winchell* (1933) into two groups within which complete solid solution exists:

	Ugrandite group		Pyralspite group
Uvarovite	$Ca_3Cr_2Si_3O_{12}$	Pyrope	$Mg_3Al_2Si_3O_{12}$
Grossular	$Ca_3Al_2Si_3O_{12}$	Almandine	$Fe_3Al_2Si_3O_{12}$
Andradite	$Ca_3Fe_2Si_3O_{12}$	Spessartine	$Mn_3Al_2Si_3O_{12}$

The name of the two groups are acronyms of the end members. The most abundant natural garnets are the pyrope-almandine series. The pressure induced phase transitions of variety of garnets have been widely studied. Most natural garnets are stable up to a pressure of 24 GPa (into the transition zone of the Earth's mantle) and then transform into a high pressure phase of the ilmenite structure before turning into post-spinel structures [Akaogi and Akimoto, 1979].

Elasticity of almandine and garnets were first measured by *Bridgman* [1928, 1949] and *Adams and Gibson* [1929] using a volumetric method in which samples were compressed in a piston cylinder type of device. *Ramachandra Rao* [1945] studied the elasticity of a number of pyrope-almandine garnets using a wedge technique. *Babuska et al.* [1978] used a parallelepiped resonance method, in which the resonance frequencies in a particular shaped sample were measured for a variety of garnets. They inferred from their measurement the individual elastic constants for five of the six rock-forming garnets. Ultrasonic interferometry, in which the travel time of the ultrasound generated by a transducer is measured, have been widely used to study the elastic constants of gem quality samples. Using this technique, almandine-pyrope garnets were measured by *Verma* [1960] and *Soga* [1976], spessartine-almandine by *Simmons* [1964] and grossular by *Halleck* [1973]. *Isaak and Graham* [1976] measured the elasticity of an almandine-spessartine garnet and *Bonczar et al.* [1977] measured the pressure and temperature derivative of a pyrope garnet. *Webb et al.* [1989] measured pyrope garnet to a pressure of 3 GPa, and *Rigden et al.* [1994] measured the wave velocities of pyrope-majorite garnet also to a pressure of 3 GPa. Brillouin scattering has been used to study the elasticities of various garnets:

majorite-pyrope solid solution by *Bass and Kanzaki [1990]*; pyrope by *Leitner et al. [1980]* and *O'Neill et al. [1989]*; grossular and spessartine by *Bass [1989]*; a grossular-pyrope-almandine garnet by *O'Neill et al. [1989]*; uvarovite and andradite by *Bass [1986]*. Static measurements of cell parameter as a function of pressure using X-ray analysis include pyrope [*Hazen and Finger, 1978; Hazen and Finger, 1989; Leger et al., 1990; Takahashi and Liu, 1970*], almandine [*Takahashi and Liu, 1970*] grossular [*Weaver et al., 1976*], spessartine [*Leger et al., 1990*], and andradite [*Hazen and Finger, 1989*] up to a pressure of 25 GPa. Since the bulk moduli at pressures depends upon the second pressure derivative of density, the uncertainties involved in the X-ray data lead to poor constraints and to large covariance with the ambient pressure bulk moduli. Thus, the elasticity of garnets at pressures in excess of 3 GPa have not been available in general.

2.2 Experiments

2.2.1 Sample preparation and density and composition determination.

A natural gem quality sample which was dark red in color was used in this study. The cell parameters at room pressure were determined from X-ray analysis and the composition was determined using microprobe analysis. The composition is tabulated in second column of Table 2.1. However, Fe^{2+} and Fe^{3+} could not be distinguished in the analysis, and was simply assumed to be in form of FeO . The fact that the total cations in the final analysis was 3.056 instead of 3 indicates some Fe^{3+} might have been incorrectly assigned as Fe^{2+} , leading to an unbalanced charge. This can be somewhat overcome by reassigning some Fe^{+2} as Fe^{+3} such that the total charge is balanced. The corrected composition is listed in the third column of Table 2.1. This

correction can be only justified by further fine structure analysis in which the site of each cation can be determined. The density calculated with the corrected value agree with that of Archimede's method within the uncertainties of the experiments.

The cell parameters were also calculated from its major end-member components [Skinner, 1956] using linear interpolation (no excess volume). The cell parameters so obtained are smaller than those measured. The densities obtained in various ways are listed in Table 2.2.

Two sample plates were sliced and polished to 20 μm and 500 μm thick, respectively. The thick sample was used for one bar pressure measurements. The thin sample was core-drilled into disks of 20 μm thick and 200 μm in diameter and then loaded in the diamond anvil cell. A portion of the thick sample was broken off and coated with a gold layer about 650 \AA for surface wave studies.

2.2.2 *Experiment techniques and the measurement of Rayleigh waves*

The optical technique has been discussed in Chapter 1. Figure 2.1 and Figure 2.2 show the time domain and frequency domain record of the ISS signal of the garnet at 2.3 GPa, respectively, in which two of the three acoustic branches were observed.

Most silicates are elastically anisotropic, even for cubic symmetry. Three frequencies, one quasilongitudinal and two quasishear, in general, can be excited in a bulk sample. However, thermoacoustic excitation of all three modes depends on the partial longitudinal character of each acoustic wave in a general direction in an anisotropic medium. In the case of elastic isotropy, or along special directions where pure longitudinal and pure transverse

modes are possible, only the longitudinal mode is excited. So the efficiency of generating shear waves in a bulk material depends, besides upon its absorption, thermal expansivity, and strain optical constants, also upon how anisotropic the sample is, and upon the direction of the wave vector of the thermal grating with respect to the crystal axis of the sample. Garnet comes close to meeting the condition for elastic isotropy of a cubic crystal, *i.e.* $(c_{11} - c_{12})/2 = c_{44}$. Therefore, for most of the experiments, quasitransverse modes are not observable, thus causing difficulties to constrain the shear elastic constants.

To overcome this difficulty, experiments have been constructed to measure surface waves which are dominated by the shear modulus. The gold coated garnet sample was used in these experiments. The excitation beams were absorbed by the gold layer, causing rapid thermal expansion, therefore a surface undulation. This rapid thermal expansion launches two counter-propagating surface waves, the Rayleigh waves. This acoustically modulated surface undulation serves as a surface grating, giving rise to the time-varying intensity of the diffracted signal of the probe beam. The experimental arrangement was the same as described Chapter 1 except that the back-diffracted signal was monitored instead of the transmitted signal. A surface wave signal and its Fourier transformation are shown in Figure 2.3 and Figure 2.4.

Rayleigh waves propagate along a free surface with both P and S motions, and strictly speaking only exist in a vacuum. The wave decays very fast with depth, so normally only extends into the medium for no more than a few wavelengths. For an isotropic half-space, Rayleigh wave is non-dispersive. However, since the thickness of the gold layer is not infinitely

small compared with the wavelength of the excited Rayleigh wave, and the difference of rigidity between the gold layer and the underlying garnet substrate is large, the dispersion of the Rayleigh wave is a function of the ratio of the thickness of the coated layer to the wavelength. This dispersion can be calculated as a Rayleigh wave propagating in a multiple-layered medium [Ewing *et al.*, 1957]. The dispersion is plotted in Figure 2.5. The speed asymptotically approaches to that of the garnet as the ratio approaches zero. Experimentally, the ratio can be changed easily by varying the convergence angle of the two excitation beams. Figure 2.5 shows two velocities (solid circles) of the Rayleigh waves as a function of the ratio. The solid curve is calculated using a perturbation approximation for a layered surface [Barnett *et al.*, 1985].

At room pressure a set of low velocities were observed in a non-coated thick sample. The average value of those velocities was 4.60 km/s about 10% smaller than the expected body shear velocities with about 1.5 % variation. The calculated Rayleigh wave velocity on a half space garnet yields a value of 4.61 km/s which agreed excellently with average low velocity observed in the sample. Those velocities were converted into body shear velocities with a perturbation approach, in which the garnet was treated as being isotropic in each propagation direction.

2.3 Results and discussions

The velocity of an acoustic wave with direction cosines y_1 , y_2 , and y_3 with respect to the cubic axes is expressed, in terms of the elastic constants, by

$$|A - \rho V^2 I| = 0 \quad (2.1)$$

where I is the 3x3 identity matrix, ρ is the density and the elements of A in terms of the elastic constants c_{ij} are

$$\begin{aligned}
 A_{11} &= y_1^2 c_{11} + y_2^2 c_{44} + y_3^2 c_{44} \\
 A_{22} &= y_1^2 c_{44} + y_2^2 c_{11} + y_3^2 c_{44} \\
 A_{33} &= y_1^2 c_{44} + y_2^2 c_{44} + y_3^2 c_{11} \\
 A_{12} &= y_1 y_2 (c_{12} + c_{44}) \\
 A_{23} &= y_2 y_3 (c_{12} + c_{44}) \\
 A_{13} &= y_1 y_3 (c_{12} + c_{44}).
 \end{aligned}
 \tag{2.2}$$

The elastic constants are determined by a least squares adjustment of the parameters of Equation (2.1) so as to optimally describe the velocity as a function of crystallographic orientation.

As the pressure is increased, preliminary values of the elastic moduli and hence an approximate adiabatic bulk modulus

$$K_S = \frac{c_{11} + 2c_{12}}{3}
 \tag{2.3}$$

can be derived from Equation (2.3) and the densities at lower pressure.

Three independent acoustic velocities are sufficient to determine the three elastic constants, provided that the density of the sample and the propagation directions are precisely determined. Data were taken at a 10° rotational increment around a full rotation at each pressure (Figure 2.6). The longitudinal velocities were generally of good quality. The shear velocities were only observed at 6 GPa, 12 GPa and ambient pressure. The elastic constant C_{11} is entirely constrained by the quasilongitudinal velocities; some

data were collected along [100] direction in which pure longitudinal wave is generated. The anisotropy in the quasilongitudinal velocities dictates the size of the difference between the two shear elastic constants C_{44} and $(C_{11}-C_{12})/2$. At the pressure where shear velocities were measured, the limited number of shear velocities give good constrains on all three elastic constants. Regardless of the initial values, the elastic constants obtained at 6 and 12 GPa and room pressure always converged to the same results with uncertainties of less than few tenths of a percent, and very small covariance between the two shear elastic constants. The initial values for the shear elastic constants at other pressures were either interpolated between or extrapolated from those at 0, 6, and 12 GPa, then added with 10% noise. The resultant shear elastic constants eventually converge to values within 1~2% of the interpolated or extrapolated values, but have large covariance. In Figure 2.6 the best fitting set of constants gives a curve with a root-mean-square misfit of 0.16%.

The elastic constants of the sample are plotted as a function of pressure in Figures 2.7 and 2.8. The 2σ uncertainties for individual constants are 1% or less and the root-mean-square misfits of constants to linear pressure dependencies are 0.7% for the shear constants and 0.5% for C_{11} . Thus, within experimental uncertainties, all constants are linear functions of pressure to 20 GPa. The elastic constants and their pressure derivatives are tabulated in Table 2.3.

The Hashin-Strickman (HS) [Watt and Peselnick, 1980] average was used in the calculation of the bulk and shear moduli. The HS average assumes minimum strain energy. It usually gives much tighter bounds than other average schemes such as Voigt and Reuss [Watt and Peselnick, 1980].

The difference between the upper and lower bounds is smaller than few tenth of a percent.

Bulk moduli and shear moduli at 1 bar as well as the pressure derivatives necessary to calculate these quantities at higher pressures are given in Table 2.4, as are the measurements of [Webb, 1989] on a pyrope-rich garnet measured up to 3.0 GPa. Both the bulk modulus and shear modulus along with those of Webb [1989] are shown in Figure 2.9 and Figure 2.10. A substantial negative second derivative is required to describe the data in Webb [1989]. An extrapolation from 3.0 to 20 GPa on the basis of Webb's first and second pressure derivatives gives constants over 10% less than those directly measured here. Measurements at mantle pressures would then appear to be a valuable adjunct in the interpretation of seismic profiles.

The small correction from the adiabatic to the isothermal modulus is calculated from

$$K_S = K_T(1 + \gamma\alpha T). \quad (2.4)$$

Where K_S is the Reuss average. For garnets of composition similar to this sample, γ the Grüneisen parameter, is equal to 1.0 [Sumino and Anderson, 1984], and at 1 bar α the coefficient of thermal expansion determined from the data of Suzuki and Anderson [1983], is $2.55 \times 10^{-5} \text{ K}^{-1}$. At 298 K and ambient pressure, $K_S / K_T = 1.0076$. From the isothermal modulus more accurate densities and elastic moduli are recursively computed.

The pressure dependence of the density is adequately described by a Murnaghan equation with $\rho^0 = 3.810 \text{ g/cm}^3$, $K = 169.4 \text{ GPa}$, $K' = 4.11$, i.e. $\rho = 3.810 (1 + 0.0241 P)^{0.244}$. The result can be compared with X-ray compression of

garnets with similar composition. Shown in Figure 2.11 are the single crystal pyrope data of *Hazen and Finger* [1989] to 6 GPa, the powdered pyrope data of *Leger et al.* [1990] to 25 GPa, and the powdered grossular data of *Weaver et al.* [1976] to 24 GPa. These data are chosen, because they are the end members of the garnet in this study and their scattering is relatively small. The compressions at high pressure, determined by x-ray diffraction, of the garnets differ little as a function of composition and are in good agreement with the elastic equation of state determined in this study. It can be seen that the density determined in this study has much smaller scattering.

The reduced moduli, μ/μ° and K/K° (where the modulus in the denominator is the value at 1 bar and 298 K) derived from these measurements are plotted versus reduced density (ρ/ρ°) in Figure 12 and Figure 13 as are μ/μ° and K/K° determined up to 993 K, at a constant pressure of 1 bar by [*Suzuki and Anderson, 1983*].

The volume dependence, both slope and curvature, of the bulk moduli determined in isothermal compression closely matches those measured in isobaric thermal expansion. The explicit temperature dependence of the bulk modulus would appear to be small. The change in reduced shear modulus in the 695 degree interval between 298 K and 993 K is 1.9% greater than that predicted by extrapolation of the high pressure data to the appropriate volume. A constant explicit temperature derivative $(\partial \ln \mu / \partial T)_\rho = -2.43 \times 10^{-5} \text{ K}^{-1}$ gives an excellent account of the deviation of the extrapolated isothermal from observed isobaric results (Figure 2.14).

The logarithmic derivatives of the average longitudinal and transverse acoustic velocity with respect to density and the covariance derivative $(\partial \ln V_s / \partial \ln V_p)$ can be determined at constant temperature from the current

elasticity data. It is however the isobaric covariance rather than the isothermal derivative that is of primary interest for interpreting the seismic data:

$$\left(\frac{\partial \ln V_s}{\partial \ln \rho}\right)_P = \left(\frac{\partial \ln V_s}{\partial \ln \rho}\right)_T - \frac{1}{2} \left(\frac{\partial \ln \mu}{\partial T}\right)_P \alpha^{-1} \quad (2.9)$$

where α is the coefficient of thermal expansion. If the bulk modulus is a function only of the density it follows that

$$\left(\frac{\partial \ln \alpha}{\partial P}\right)_T = \frac{dK^{-1}}{d \ln \rho}. \quad (2.10)$$

The constant pressure derivatives listed in Table 2.6 are evaluated from the present results with the aid of Equations (2.9) and (2.10) and the coefficients of thermal expansion at 1 bar reported by [Webb and Jackson, 1993]. At 298 K, $\alpha = 2.55 \times 10^{-5} \text{ K}^{-1}$ and at 993 K, $\alpha = 3.31 \times 10^{-5} \text{ K}^{-1}$. At 20 GPa thermal expansion is reduced 32% from its 1 bar value. Perhaps the most striking feature of the data in Table 2.6 is the small variation of these properties with pressure and temperature for the pyrope-rich garnet.

Some efforts have been made to estimate elastic properties of a garnet with its end members. It has been suggested [O'Neill *et al.*, 1989] that aluminous garnet can be approximated as an ideal solid solution. Although there is no vigorous physical law to guide such a perform such a average, Takahashi and Liu [1970] have used the addition law of molar volume to derived an equation for calculating the elasticity from the end members. For a solid solution, it follows that

$$V_{SS} = \sum X_i V_i + \Delta V \quad (2.5)$$

where V_{SS} is the molar volume of the solid solution, V_i is the mole volume of the end member, X_i is the molar fraction of the end member, and ΔV is the deviation from ideal mixing. Differentiation of the equation at constant composition and temperature with respect to pressure yields

$$\begin{aligned} & \left(\frac{\partial V_{SS}}{\partial P} \right)_{x,T} \\ &= \sum X_i \left(\frac{\partial V_i}{\partial P} \right)_{x,T} + \left(\frac{\partial \Delta V}{\partial P} \right)_{x,T}. \end{aligned} \quad (2.6)$$

For an ideal solid solution the last term in the equation vanishes.

However, *Babuska et al.* [1978] calculated the elasticities of end member garnet from the elasticities of garnets of intermediate composition using simple linear interpolation, and showed that the difference from those calculated with the above equation was negligible, smaller than the experimental uncertainties. *O'Neill et al.* [1989] also showed that simple linear composition vs. modulus trends have been observed in the pyrope-almandine-spessartine system [*Leitner et al.*, 1980; *O'Neill et al.*, 1989]. The current measurement is compared with the calculation using the following linear addition equation:

$$M_{SS} = \sum X_i M_i \quad (2.7)$$

where M_i is the property of the end member and M_{SS} is the property of the solid solution. The calculated results are tabulated in Table 2.4. At 1 bar the

elastic constants and average bulk and shear moduli are systematically 1.1-1.8% less than those calculated. However, this linear trend does not generally apply to all garnets. Indeed, a pronounced nonlinear relationship between the Ca-bearing end member grossular and andradite is reported in earlier experiments [*Babuska et al.*, 1978; *Bass*, 1986]. *O'Neill et al.* [1989] suggested that the difference in the behavior of elasticity vs. composition lies in the valance state of the substituting ions and in their crystallographic site occupancy. In the andradite-grossular solution, Fe^{3+} substitute for Al on the octahedral site, while in the Al-carrying garnets, Mg, Fe^{2+} , and Mn can replace each other freely on the dodecahedral site.

2.4 Illustrations

2.4.1 Tables

Table 2.1 Chemistry of garnet

The chemical analysis are obtained using micorprobe analysis. They were corrected for Fe⁺³ (see text). The garnet is also expressed in terms of its end-members.

Cation	Based on 12 Oxygen	Corrected
Si	2.9735	2.9674
Ti	0.0206	0.0206
Al	1.9706	1.9666
Mg	1.5507	1.5475
Ca	0.4748	0.4738
Mn	0.0276	0.0275
Fe ²⁺	1.0029	0.9520
Fe ³⁺		0.0489
Total	8.0203	8.0040
Garnet Component	Mol %	Mol %
Pyrope	50.74	51.58
Almandine	32.82	31.74
Grossular	15.54	15.79
Spessartine	0.90	0.92

Table 2.2 Cell parameters and density of garnet

The uncertainties to the last digit are given in the parentheses as 2σ .

	Cell Parameter (cm^{-8})	Density (g/cm^3)
Measured	11.5543(15)	3.824(2)
Corrected		3.816
end-member	11.5471	3.820
Archimedes		3.810(5)

Table 2.3 Elastic and density data for garnet

Elastic constants were determined at each pressure, the uncertainties to the last digit are in the parentheses and were determined by rms.

P (GPa)	C ₁₁ (GPa)	C ₁₂ (GPa)	C ₄₄ (GPa)	ρ (g/cm ³)	V/V ₀
0	299.1(10)	106.7(10)	93.7(8)	3.810	1.000
3.15(2)	321.6(10)	113.1	99.9	3.879	0.982
5.99(2)	337.2(11)	123.6(8)	103.7(7)	3.938	0.968
9.10(2)	358.6(08)	132.01	109.8	3.999	0.953
12.28(10)	381.2(08)	140.7(22)	115.7(12)	4.059	0.939
15.14(10)	402.3(40)	149.9	120.2	4.110	0.927
18.50(20)	415.6(20)	158.5	125.9	4.168	0.914
∂/∂p	6.5(0.1)	2.9(0.1)	1.7(0.1)		

Table 2.4 Pressure dependence of elastic constants of garnet

The 2σ uncertainties to the last digit are given in the parentheses.

	Py _{51.6} Al _{31.7} Gr _{15.8} Sp _{0.9} ^a			Py ₆₃ Al ₃₇ ^b		
	(18.5 GPa)			(3.5 GPa)		
		d/dp	d ² /dp ²		d/dp	d ² /dp ²
C ₁₁	229.1(10)	6.54		301.4	7.0	-0.36
C ₁₂	106.7(10)	2.87		110.0	3.9	-0.24
C ₄₄	93.7(8)	1.72		94.3	1.5	-0.10
K	170.8(14)	4.09		173.6	4.9	-0.28
μ	94.7(6)	1.76		94.9	1.6	-0.08

^aThis work. ^bWebb (1989).

Table 2.5 Elastic constants of end-member garnet

The uncertainties to the last digit are in the parentheses .

	pyr ^a	alm ^b	gros ^b	spes ^b	this work	calc
K	172.8(2)	177(3)	168.4(7)	178.8(8)	170.7(3)	173.5
μ	92.0	97(1)	108.9(4)	96.3(5)	95.1(7)	96.3
C ₁₁	296.2(5)	309(3)	321.7(8)	309.5(10)	299.4(5)	304.4
C ₁₂	111.1(6)	111(3)	91.4(9)	113.5(11)	106.3(5)	108.0
C ₄₄	91.6(3)	96(1)	104.6(4)	95.2(6)	93.8(3)	95.1

^aO'Neill *et al.* (1989). ^bBass (1989).

Table 2.6 Derivatives of mean longitudinal and shear velocity

	1 bar	20 GPa	1 bar	20 GPa
	298 K	298 K	1000 K	1000 K
$\left(\frac{\partial \ln V_p}{\partial T}\right)_P \times 10^5 \text{ (K}^{-1}\text{)}$	-4.4	-2.9	-4.5	-3.6
$\left(\frac{\partial \ln V_s}{\partial T}\right)_P \times 10^5 \text{ (K}^{-1}\text{)}$	-3.8	-3.3	-4.7	-3.9
$\left(\frac{\partial \ln V_s}{\partial \ln \rho}\right)_P$	1.58	1.97	1.45	1.78
$\left(\frac{\partial \ln V_p}{\partial \ln \rho}\right)_P$	1.56	1.72	1.50	1.63
$\left(\frac{\partial \ln V_s}{\partial \ln V_p}\right)_P$	1.01	1.15	0.97	1.09

2.4.2 Figures

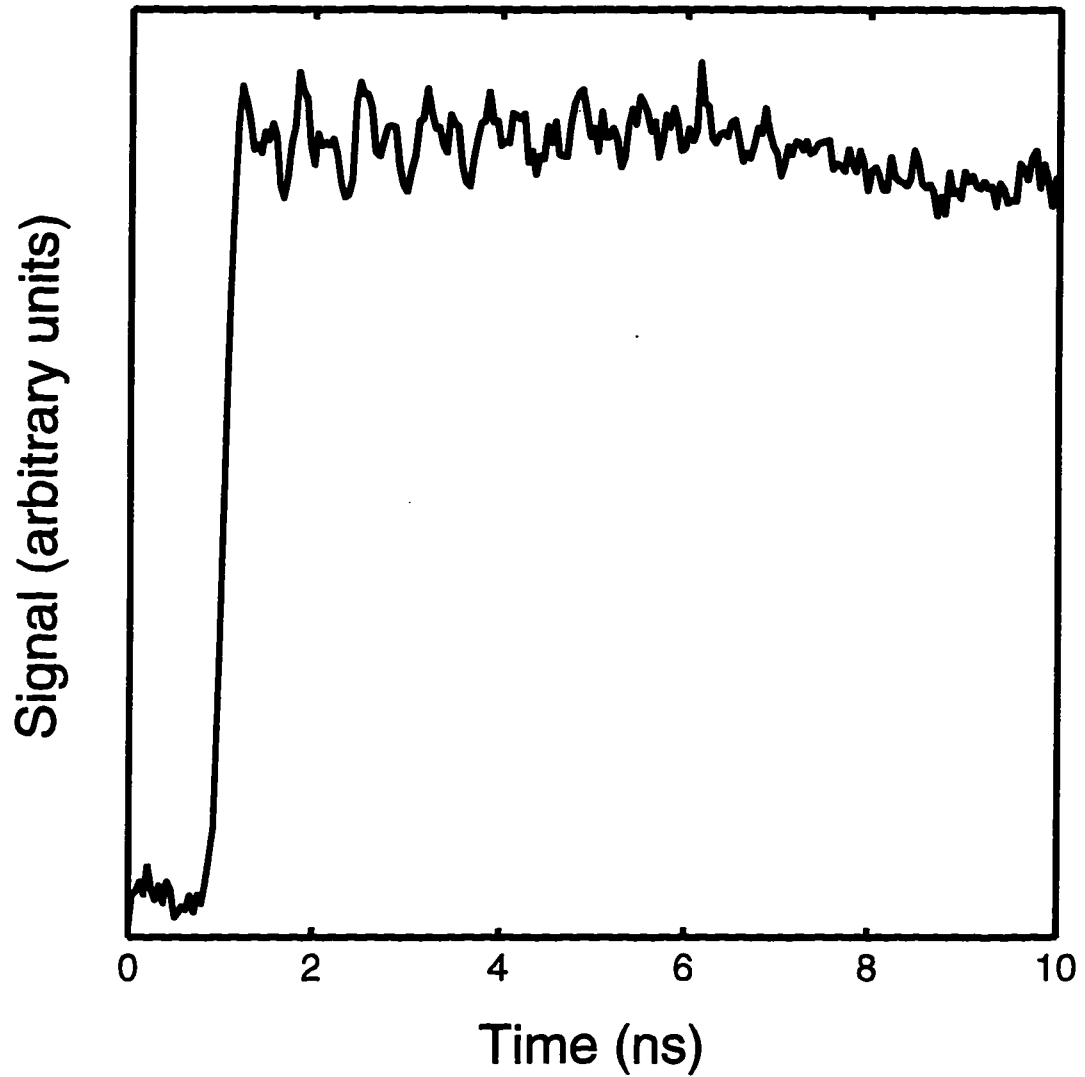


Figure 2.1 Time domain record of ISS signal of garnet

The first 10 ns of a time domain record of the ISS signal of garnet at 6.0 GPa.

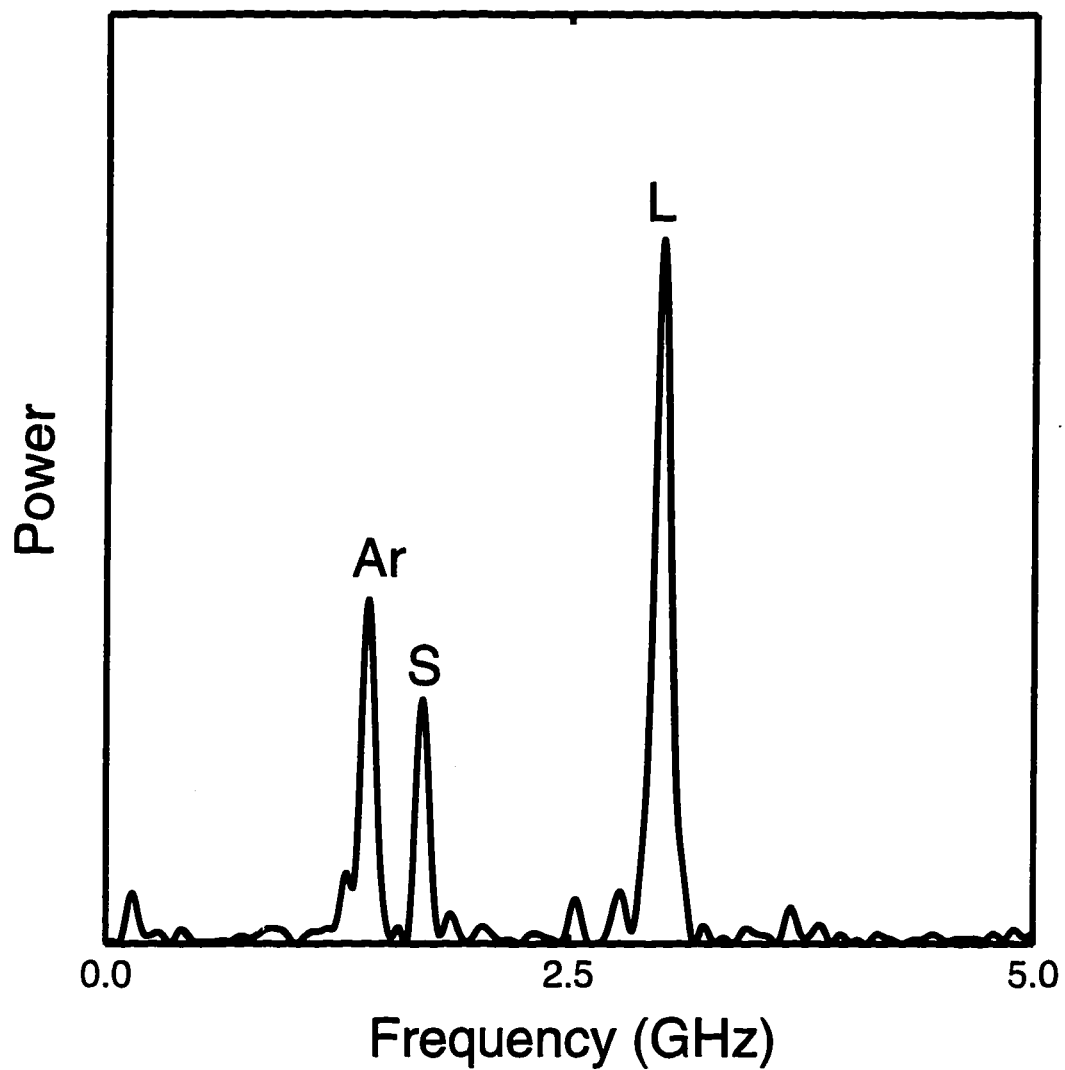


Figure 2.2 Fourier transformation of the ISS signal of garnet

Fourier transformation of the time domain record in Figure 2.1. Three peaks are present. The longitudinal velocity of garnet is indicated by L, one shear by S, and the longitudinal velocity of the argon pressure medium by Ar.

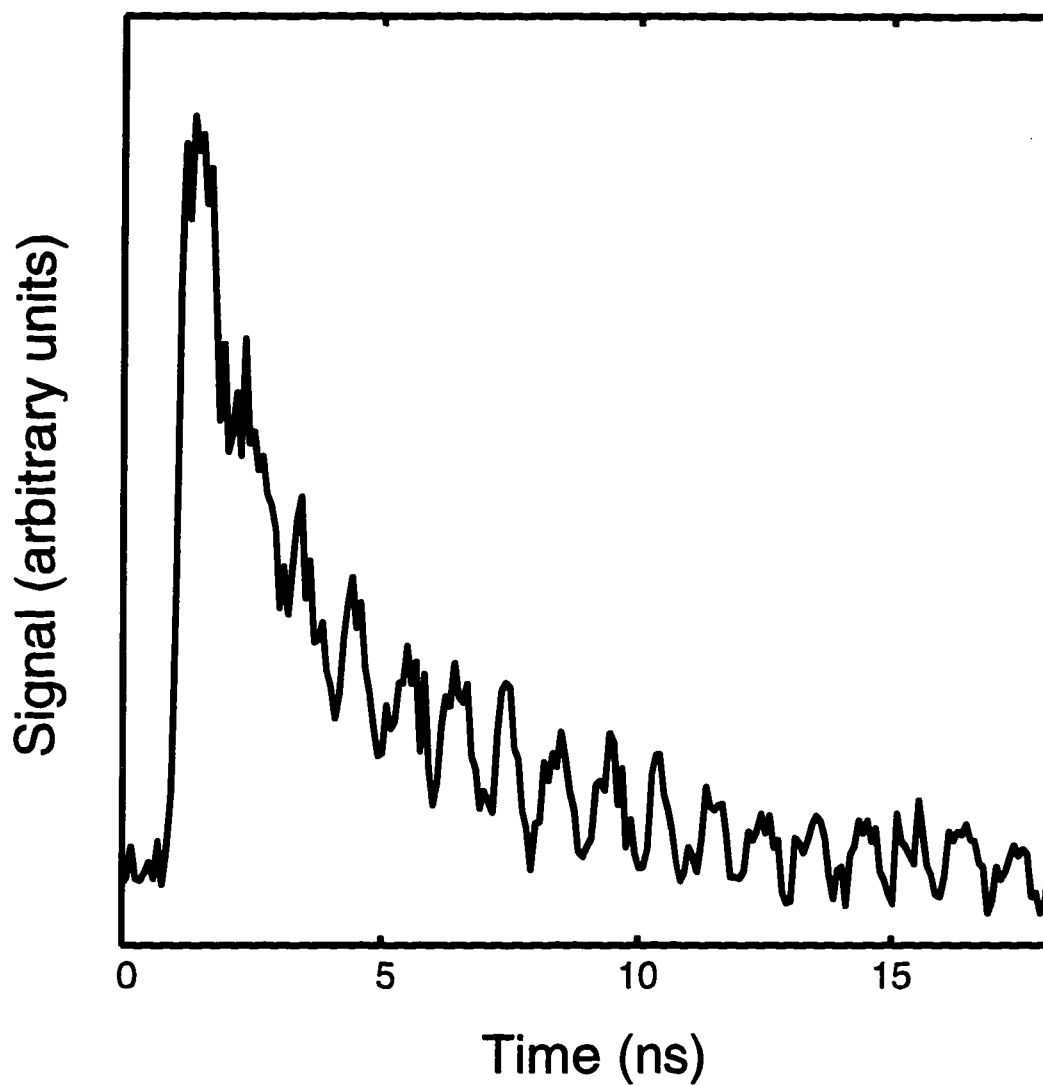


Figure 2.3 Time domain record of the surface wave of garnet

Time domain signal scattered off the surface of garnet coated with a 650 Å gold layer. A Rayleigh wave was excited on the sample surface.

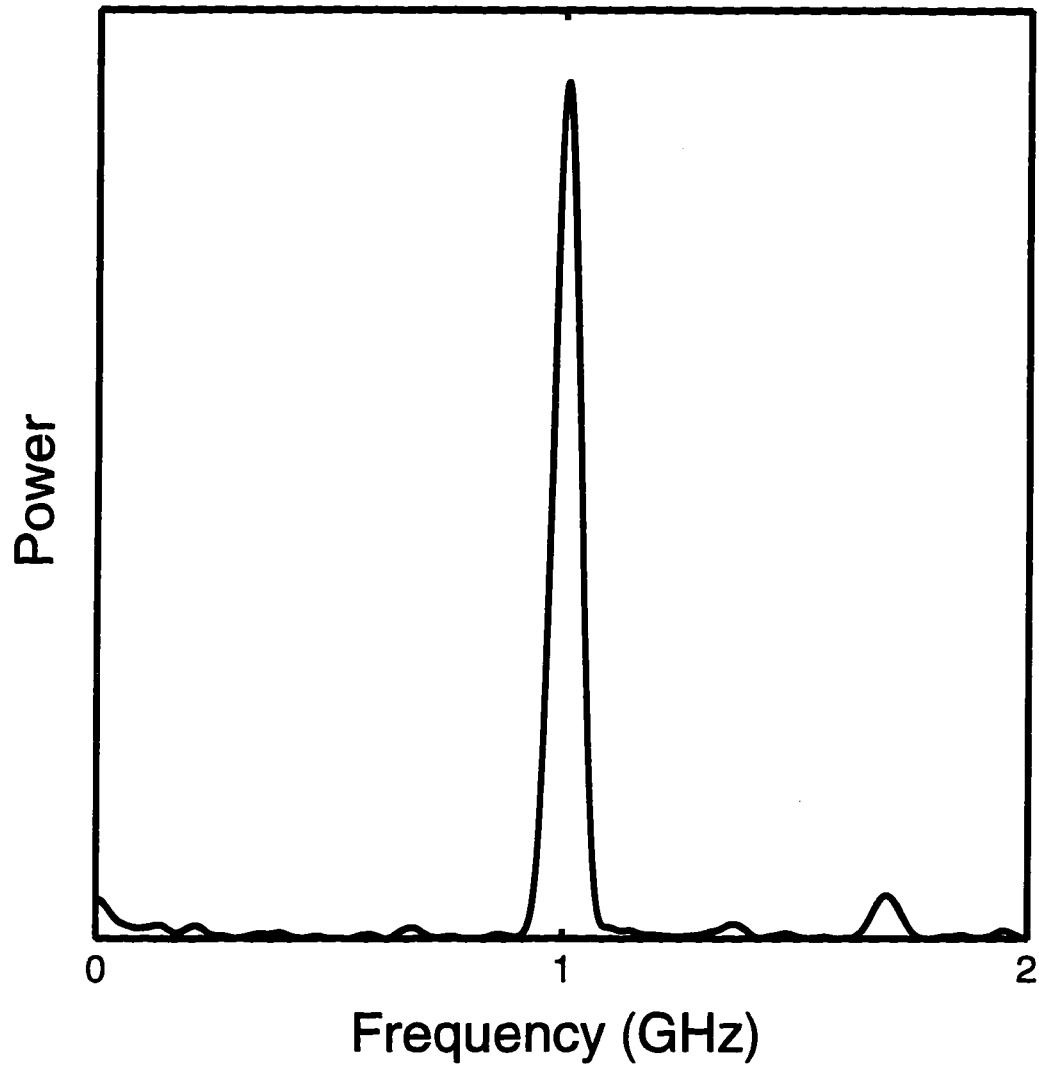


Figure 2.4 Fourier transformation of the surface wave

Fourier transformation of the signal scattered off the surface of garnet as shown in Figure 2.3. The peak corresponds to the Rayleigh wave excited on the sample surface.

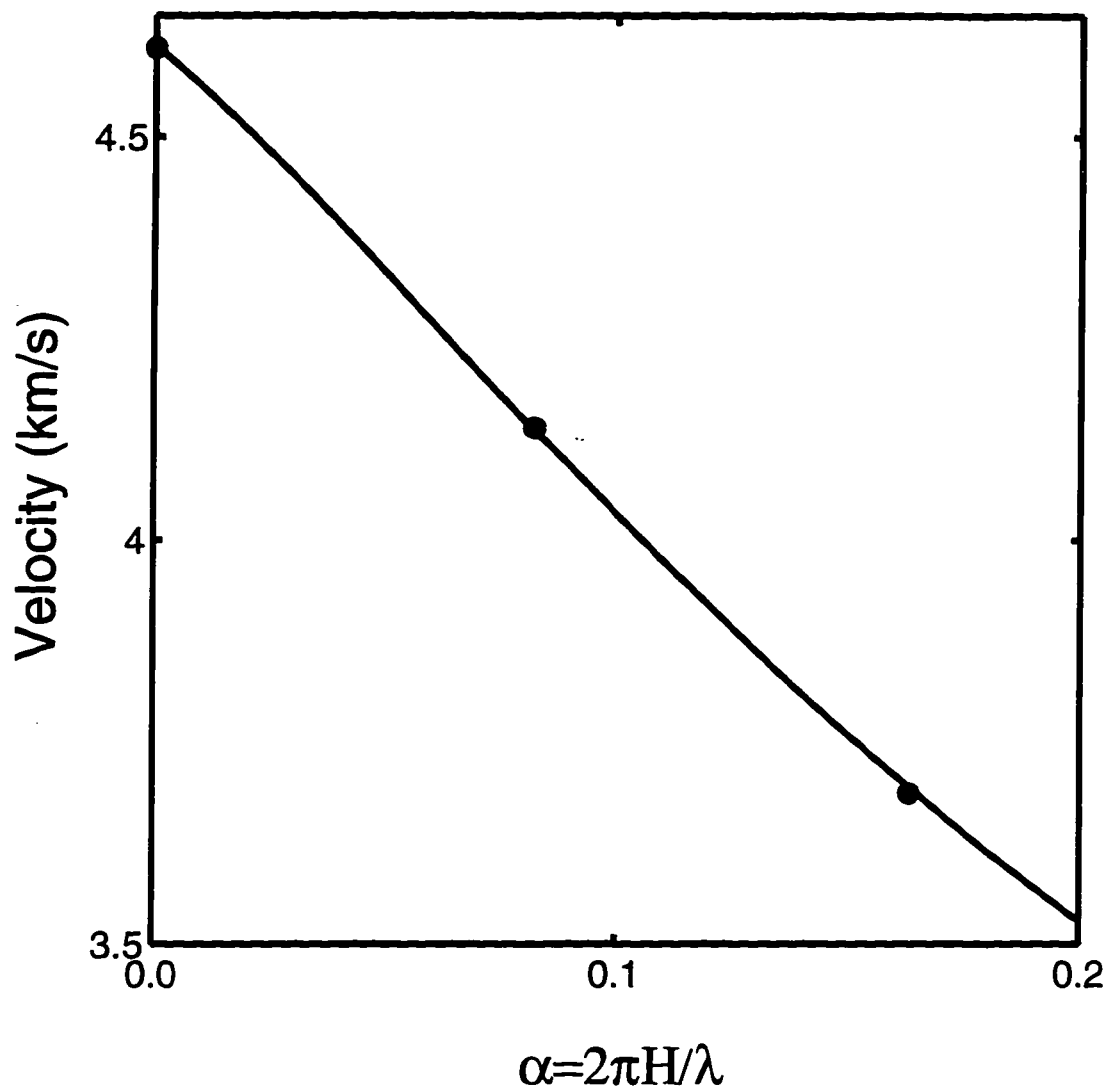


Figure 2.5 Dispersion of surface wave on a layered surface

Dispersion curve of Rayleigh wave on the pyrope-rich garnet coated with gold layer of 650 Å. The x-axis is the ratio of the thickness, H , of the gold layer to the wavelength, λ , of the Rayleigh wave. Solid circles represent the velocities of Rayleigh waves of different wavelength. The square is the Rayleigh wave observed on non-coated garnet sample. The solid curve is the calculated from a perturbation theory [Barnett *et al.*, 1985].

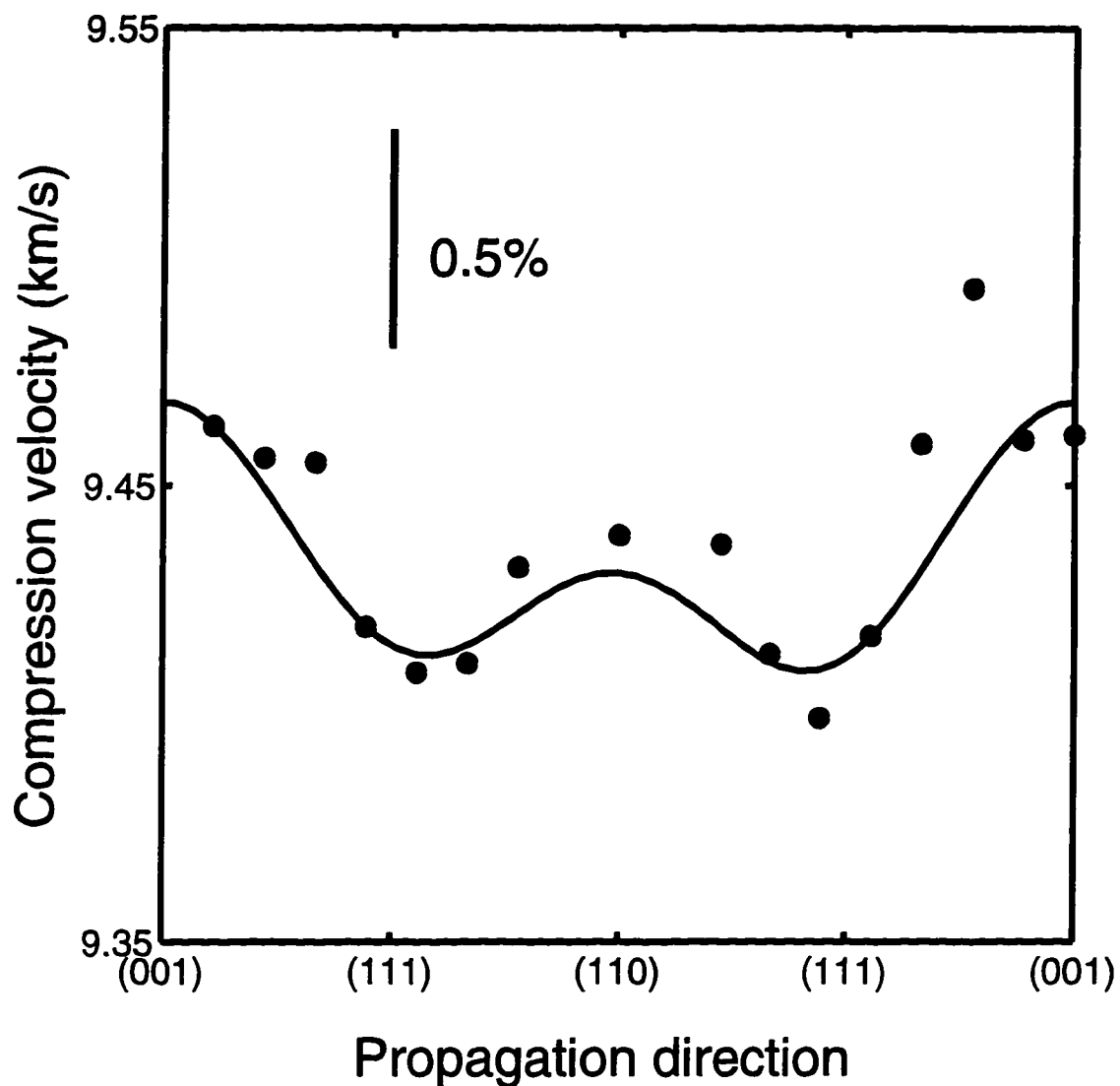


Figure 2.6 Longitudinal sound velocity of garnet as a function of direction

Compressional velocities in the pyrope-rich garnet as a function of crystallographic direction at 25°C and 9 GPa. The curve is calculated using an optimized set of elastic constants. The magnitude of elastic anisotropy is approximately 0.5% as shown by the vertical scale bar.

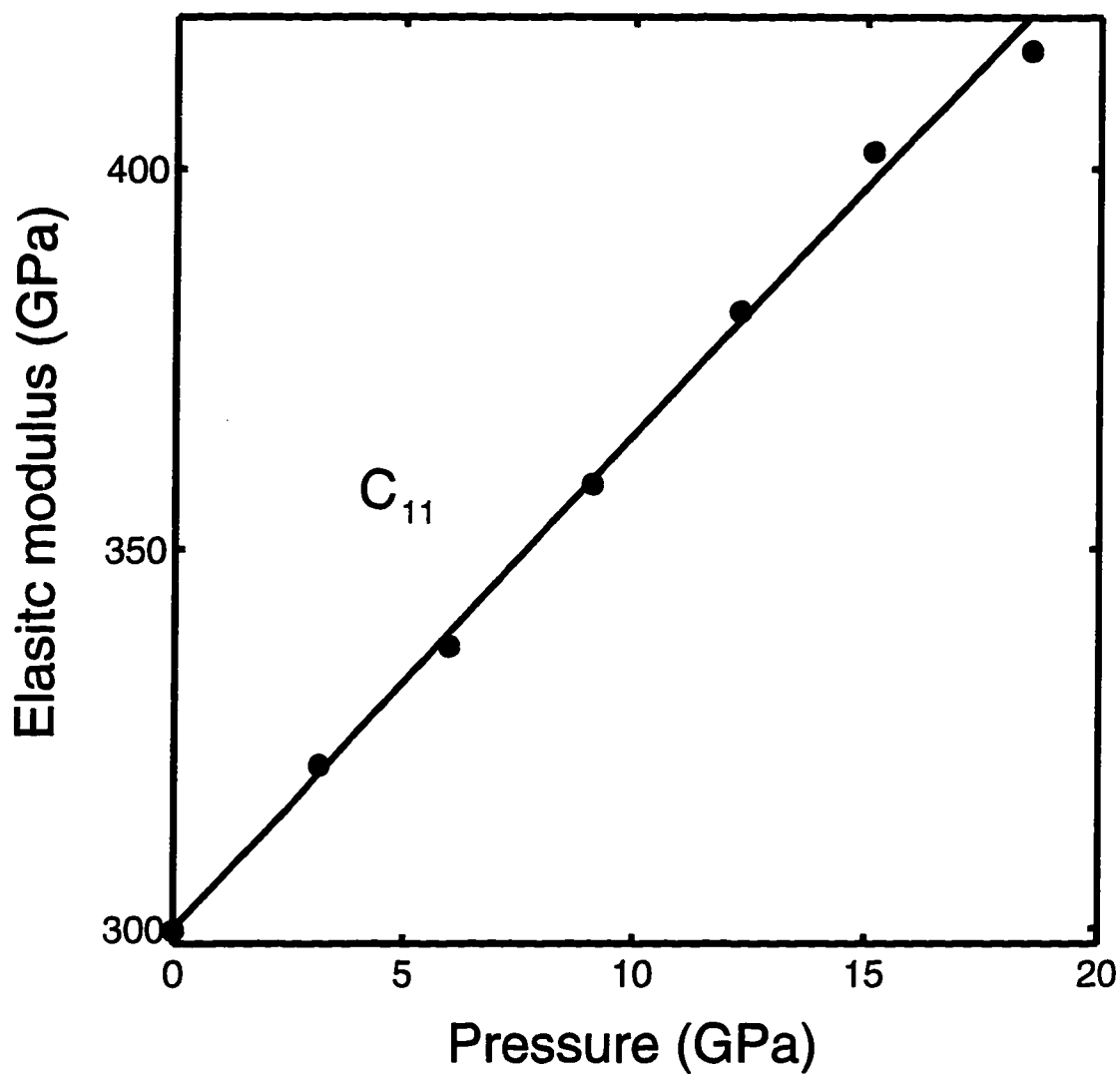


Figure 2.7 C_{11} of garnet

The elastic constant C_{11} of the garnet sample at 25°C as a function of pressure. The solid circles are the measured data, the solid line is the linear least-square fit to the data. Experimental uncertainties are within the symbol size.

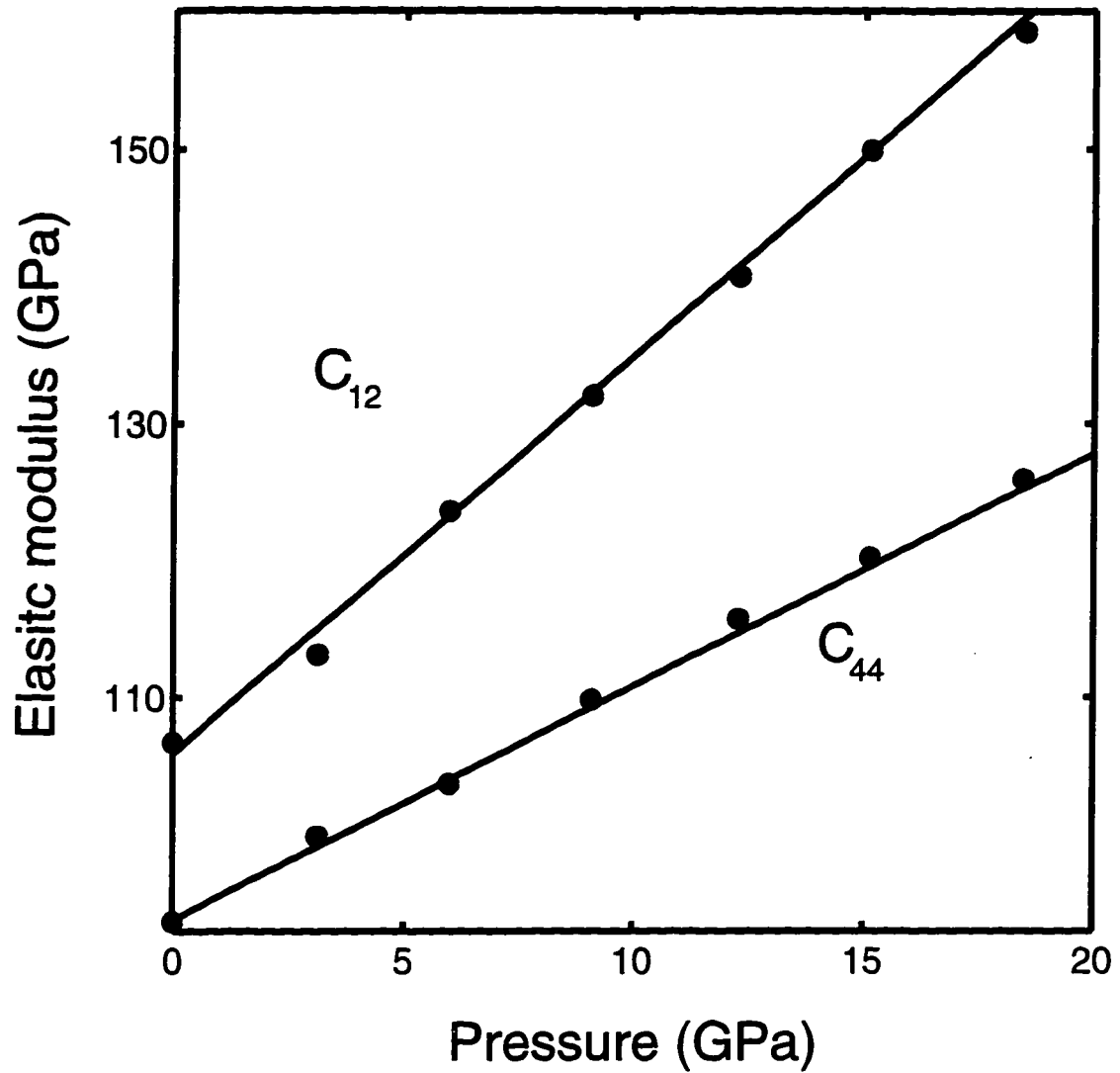


Figure 2.8 C_{12} and C_{44} of garnet

The shear elastic constants C_{12} and C_{44} of the garnet sample at 25°C as a function of pressure. The solid circles are the measured data, the solid line is the linear least-square fit to the data. Experimental uncertainties are within the symbol size.

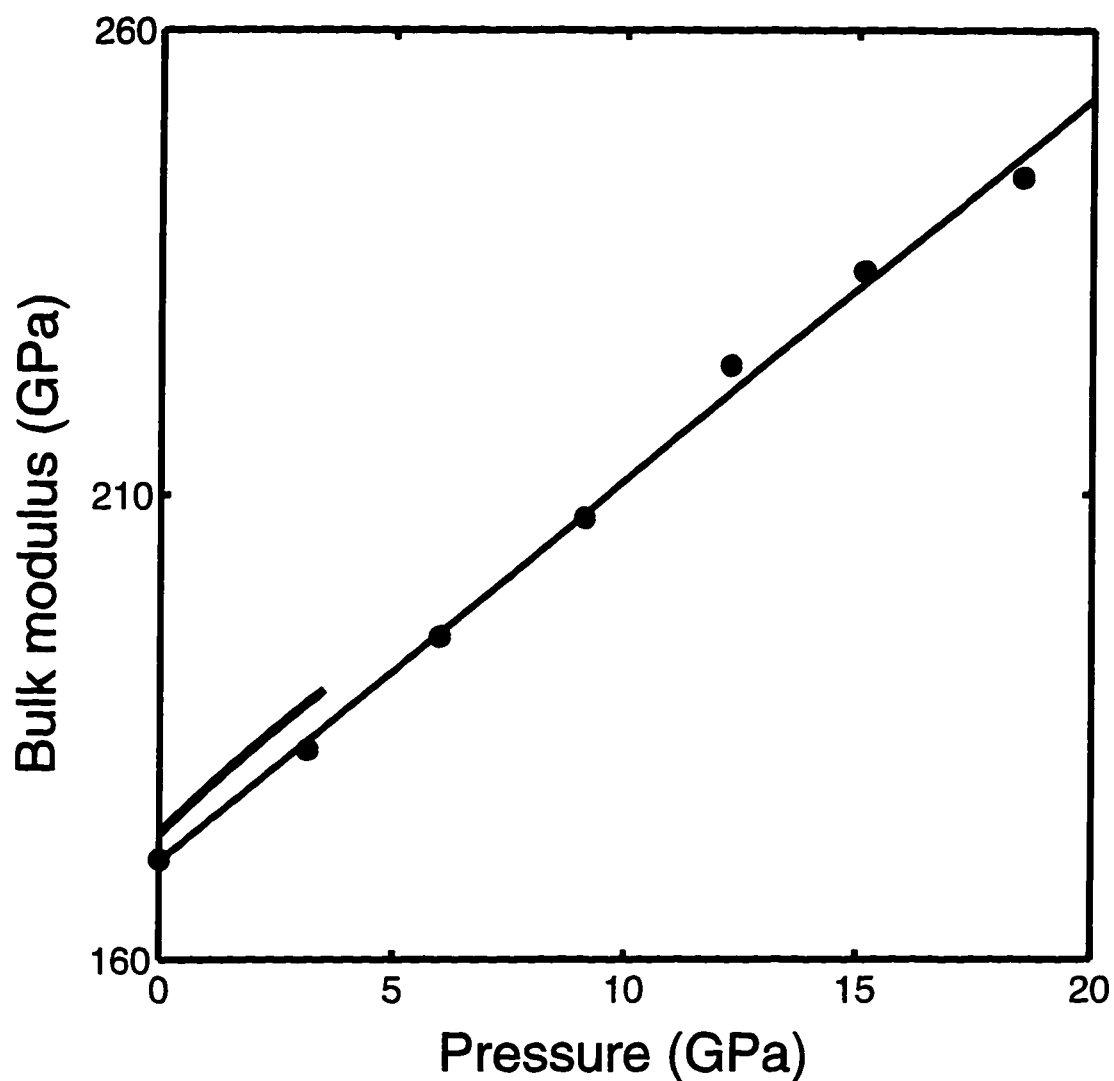


Figure 2.9 Bulk modulus of garnet

The bulk moduli of pyrope-rich garnets at 25°C as a function of pressure. The solid circles are the HS averaged values. The solid line is the linear least-square fit to the data. The thick line is from *Webb* [1989].

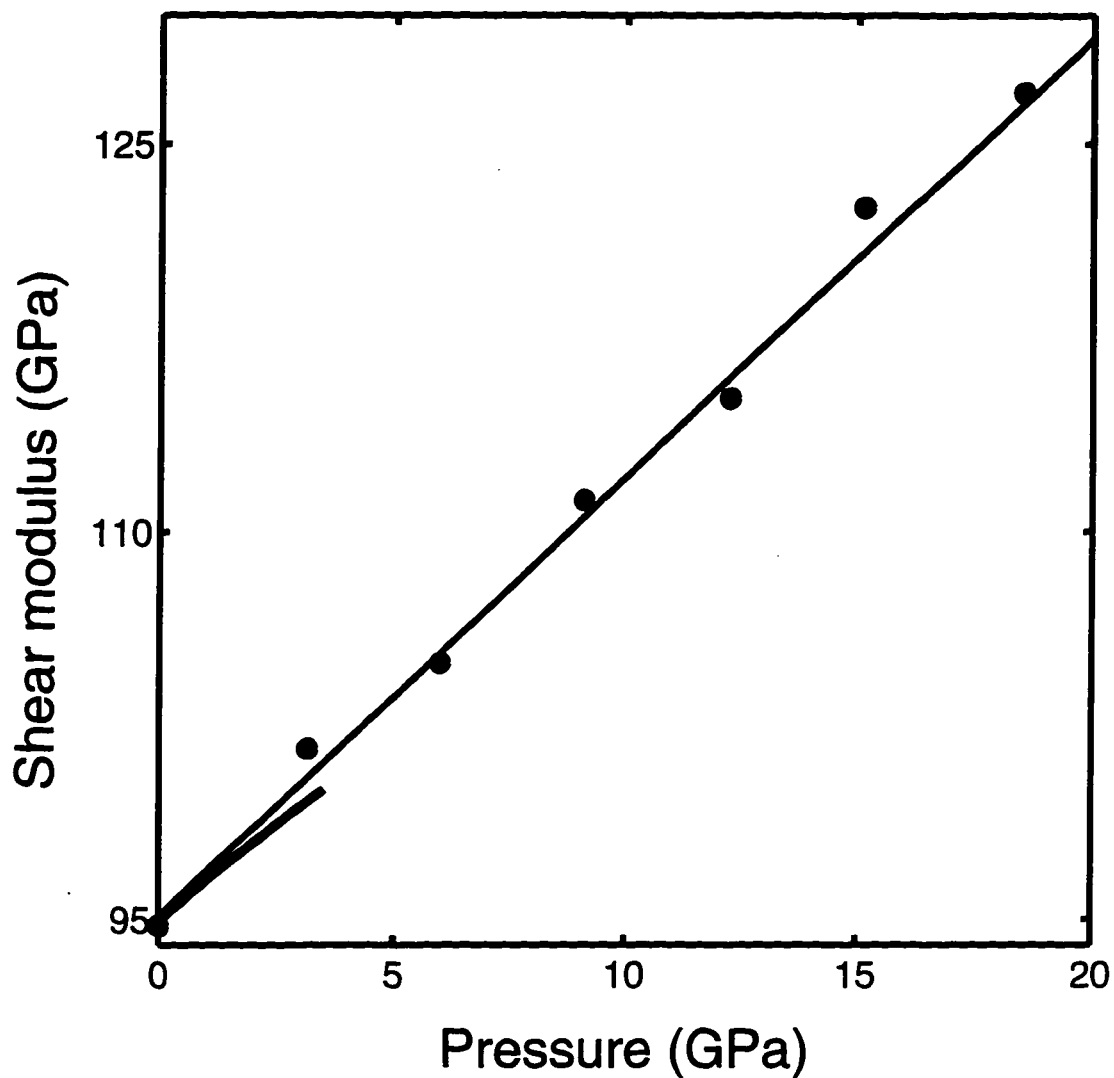


Figure 2.10 Shear modulus of garnet

The shear moduli of the pyrope-rich garnets at 25°C as a function of pressure. The solid circles are the HS averaged values. The solid line is the linear least-square fit to the data. The thick line is from *Webb* [1989].

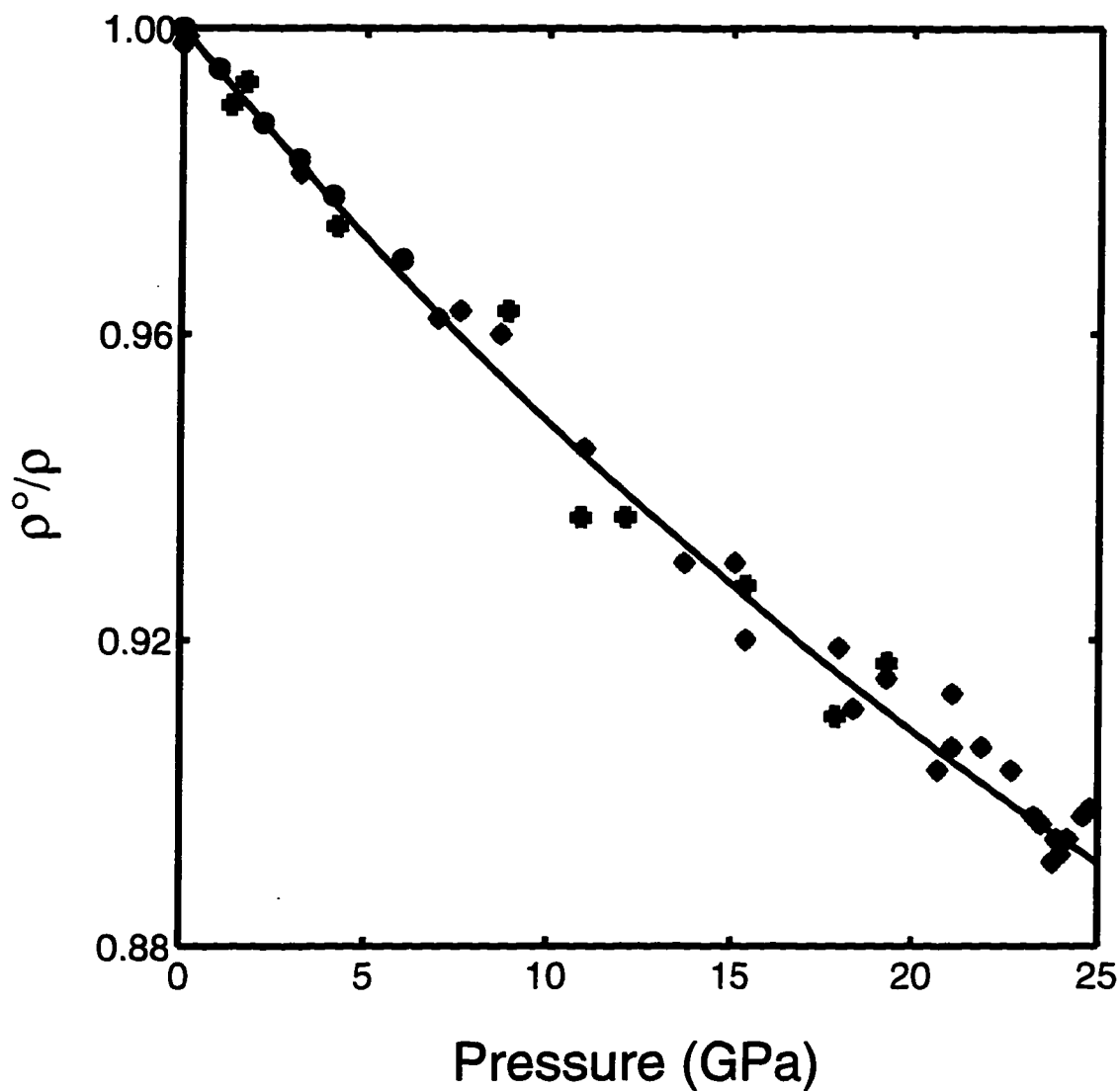


Figure 2.11 Compression of garnet

The compression of various garnets as a function of pressure at 25°C. The crosses represent the results for synthetic pyrope [Leger *et al.*, 1990], the solid circles are observations on $\text{Py}_{67}\text{Al}_{20}\text{Gr}_{10}\text{And}_3\text{Sp}_1$ [Hazen and Finger, 1989] and the diamonds are observations on $\text{Py}_1\text{Al}_2\text{Gr}_{90}\text{And}_6$ and $\text{Al}_1\text{Gr}_{97}\text{Sp}_2$ [Weaver *et al.*, 1976]. The continuous curve is the equation of state derived from the present work.

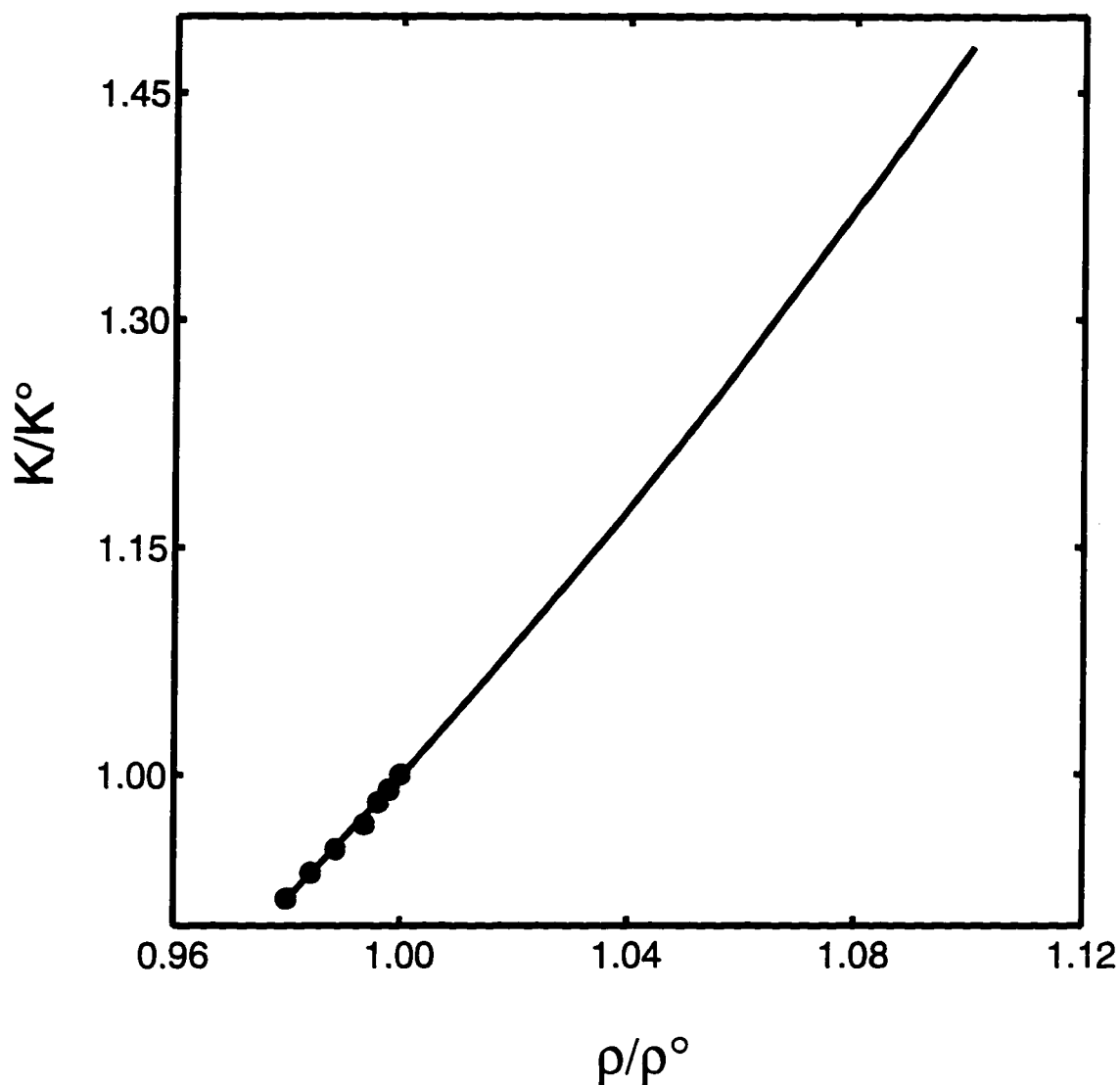


Figure 2.12 Reduced bulk modulus of garnet

The reduced bulk modulus (K/K°) of garnet versus the reduced density (ρ/ρ°). The isothermal compression data to 20 GPa at 298 K is extrapolated into the expanded state (The solid curve). The values (solid circles) below $\rho/\rho^\circ = 1$ are from isobaric heating to 993 K at 1 bar [Suzuki and Anderson, 1983; Webb and Jackson, 1993], and coincide with the extrapolation.

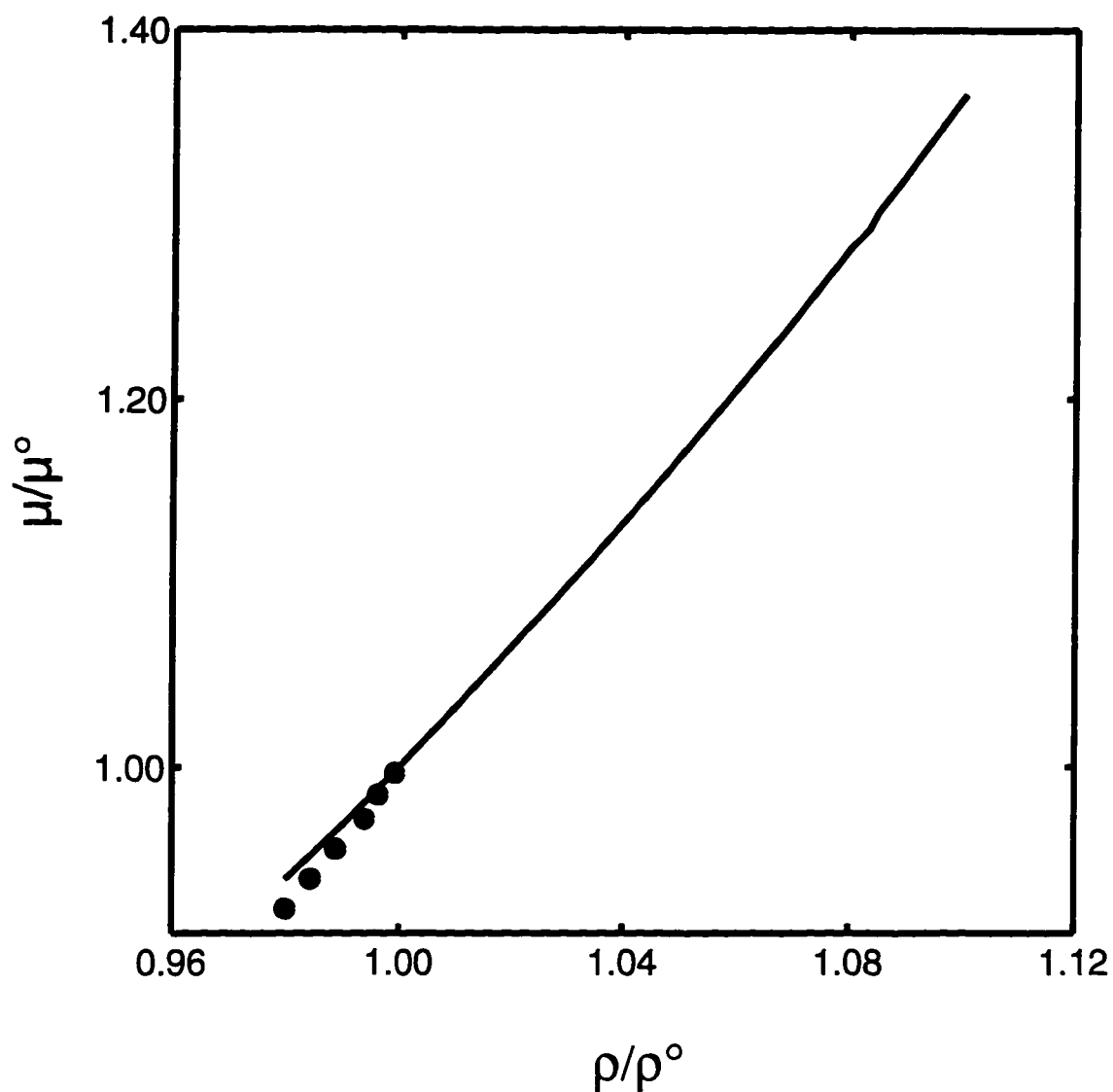


Figure 2.13 Reduced shear modulus of garnet

The reduced shear modulus (μ/μ°) of garnet versus the reduced density (ρ/ρ°). The isothermal compression data to 20 GPa at 298 K is extrapolated into the expanded state (The solid curve). The values (solid circles) below $\rho/\rho^\circ = 1$ are from isobaric heating to 993 K at 1 bar [Suzuki and Anderson, 1983], and deviate from the extrapolation.

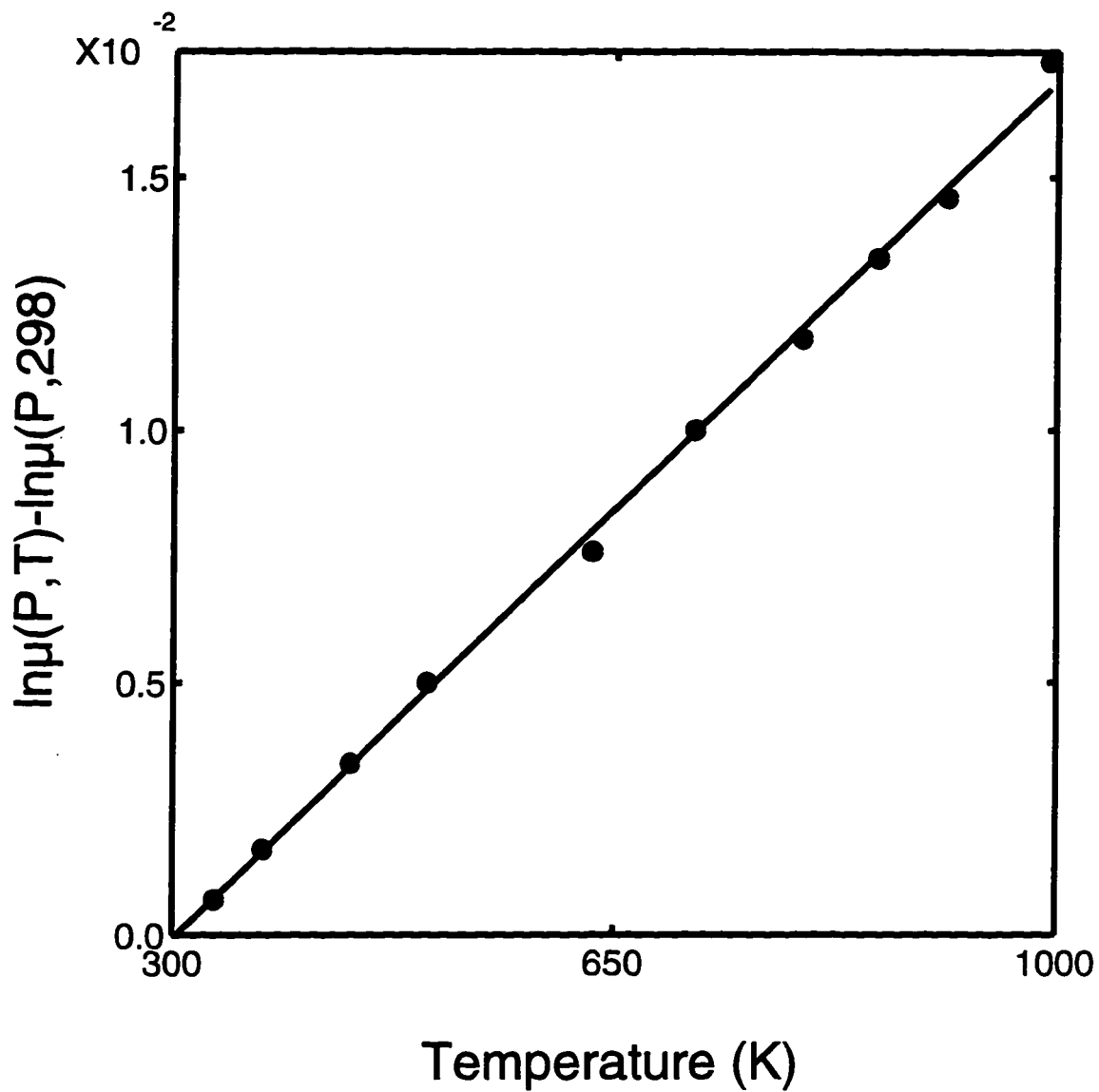


Figure 2.14 Temperature effect on the shear modulus of garnet

The constant-volume difference between the shear moduli of *Suzuki and Anderson* [1983] and the extrapolation of the current high pressure data plotted as a function of temperature.

Chapter 3

The Elastic Constants of Kilbourne Hole Orthopyroxene to 12.5 GPa

3.1 Introduction

Pyroxenes are abundant in xenoliths from deep seated volcanic processes [Menzies, 1990] with the typical modal distribution of phases in garnet lherzolites being approximately 60% olivine, 17% orthopyroxene, 13% clinopyroxene, and 10% garnet. Mantle pyroxenites and eclogites have even larger concentrations of the pyroxene minerals. In general, the magnesium number $Mg/(Mg+Fe)$ for mantle pyroxenes is between 0.8 and 0.95, with 0.9 being the most common value. Mantle orthopyroxenes (opx) typically contain about 1 wt% CaO and from 0.5 to 7 wt% Al_2O_3 . The monoclinic clinopyroxenes (cpx) are aluminous (approx. 5-10 wt% Al_2O_3) and sodic (several wt% Na_2O) diopsides. The variability of Fe, Al, Ca, and Na in pyroxenes may be described in terms of depletion (extraction of a basaltic melt) or enrichment (mantle metasomatism) processes relative to a reference bulk chemical state of the mantle (i.e. "pyrolite" [Ringwood, 1979] or "Bulk Silicate Earth" [Zindler and Hart, 1986]). In addition, the chemistry of coexisting phases is dependent on pressure and temperature.

Pacalo and Gasparik [1990] and *Kanzaki* [1991] have shown that pure enstatite transforms from the orthorhombic structure to the high clinoenstatite structure near 8 GPa and 1000°C. At still higher pressure pyroxenes become soluble in the majorite garnet phase. Thus, orthopyroxenes may not exist in the mantle below a depth of about 250 km.

Elastic properties at 1 bar of the orthorhombic pyroxenes ferrosilite ($FeSiO_3$) [Bass and Weidner, 1984], orthoenstatite ($MgSiO_3$) [Weidner et al., 1978], and several bronzites ($Mg_xFe_{1-x}SiO_3$) [Frisillo and Barsch, 1972;

Kumazawa and Anderson, 1969] have been reported. The monoclinic minerals diopside ($\text{CaMgSi}_2\text{O}_6$) [*Levien et al., 1979*], hedenbergite ($\text{CaFeSi}_2\text{O}_6$) [*Kandelin and Weidner, 1988a*] and jadeite (NaASi_2O_6) [*Kandelin and Weidner, 1988b*] have also been studied at one bar. Measurements by *Webb and Jackson [1993]* to 3 GPa support the conclusion by *Frisillo and Barsch [1972]*, based on data to 1 GPa, that the pressure derivatives of the elastic constants of orthopyroxenes are unusually large; $K' (\partial K/\partial P) = 9$ as reported by *Webb and Jackson* is twice the usual value of most silicates. Recent x-ray data to 8.5 GPa at room temperature for orthoenstatite by *Angel and Hugh-Jones [1994]* confirm that K' is large (14.9) below 4 GPa and decreases to 5.6 at higher pressures. They also reported $K'=6.6$ for low clinoenstatite to 8 GPa.

In the absence of better elastic data, efforts to interpret mantle seismic structure (e.g., [*Duffy and Anderson, 1989; Ita and Stixrude, 1992; Jordan, 1979*]) have commonly made the assumption that the elasticity of mantle pyroxenes can be modeled on the properties of pure (Mg,Fe) bronzites. Thus, clinoenstatites are assumed to have the same elastic properties as orthoenstatites. Furthermore, all enstatites have been assumed to have nominal ($K'=4-5$) pressure derivatives of elastic constants.

The elastic constants and equation of state of olivine has been measured up to 17.0 GPa [*Zaug et al., 1993*] and a pyrope rich garnet to 20.0 GPa [*Chai et al., 1996a*]. Densities and elastic constants of an orthopyroxene from Kilbourne Hole, NM, is here reported extending to 12.5 GPa, that is data for a pyroxene of typical mantle composition over the regime of pressure wherein orthopyroxene is postulated to be an important constituent of the mantle.

3.2 Experimental techniques

Approximately fifty, 2-3 mm, opx crystals (hereafter Kh-opx) were hand-picked from a single xenolith. On the basis of microprobe analysis, the chemistry was found to be identical within experimental uncertainty both within and among these crystals. The results of the chemical analysis are listed in Table 3.1. The formula of the samples, $(\text{Mg}_{1.63}\text{Fe}_{0.17}\text{Ca}_{0.04}\text{Mn}_{0.01})(\text{Al}_{0.12}\text{Cr}_{0.01})\text{-}(\text{Si}_{1.89}\text{Al}_{0.11})\text{O}_6$, corresponds to a composition in terms of the end-members enstatite, ferrosilite, and Mg-Tschermakite (MgAlSiAlO_6) of $\text{En}_{0.755}\text{Fs}_{0.085}\text{-Ts}_{0.12}$. The samples contain 5 wt% Al_2O_3 and 1 wt% CaO. The magnesium number $\text{Mg}/(\text{Mg}+\text{Fe})$ is 0.90. The density at one bar and 298 K (ρ°) based on the measured lattice constants ($a = 18.2457 \text{ \AA}$, $b = 8.7984 \text{ \AA}$, $c = 5.1959 \text{ \AA}$) and chemical analysis is 3.304 g/cm^3 . The samples, embedded in an epoxy, were double-side polished to a thickness of 20 μm . Crystals with polished faces nearly normal to either the a , b or c orthorhombic axes were optically selected. These samples were then oriented by x-ray precession analysis, core-drilled to form disks 200 μm in diameter, and loaded with argon in a Merrill-Basset diamond-anvil cell. Pressures, measured to 0.02 GPa by ruby fluorescence [Piermarini *et al.*, 1975], were adjusted as close as possible to seven nominal values from one bar to 12.5 GPa. Data at each pressure for samples of the three different cuts were obtained. The differences in pressure for the three cuts at each nominal pressure did not exceed 0.5 GPa. No data acquisition were attempted for the b -normal sample at 2.3 GPa.

Data were also obtained from the bronzite ($\text{Mg}_{0.80}\text{Fe}_{0.20}\text{SiO}_3$) studied by Webb and Jackson [1993]. This sample was less uniform in composition and phase than Kh-opx with a small volume percentage of amphibole in the form

of thin stringers, and was not suitable for study at all orientations and pressures with the optical techniques employed in this study. However, results for this sample both at ambient conditions and at 3 GPa were in excellent agreement with those of Webb and Jackson.

The optical technique is discussed in general in chapter 1. Figure 3.1 and Figure 3.2 show the time domain and frequency domain records of the ISS signal of Kh-opx at 2.3 GPa, respectively. The acoustic velocities of Kh-opx as a function of crystallographical directions, at all seven pressures are shown in Figures 3.3 to 3.9.

The velocity of an acoustic wave with direction cosines $y_1, y_2,$ and y_3 with respect to the $a, b,$ and c axes of an orthorhombic crystal is expressed in terms of the elastic constants by

$$|A - \rho V^2 I| = 0 \quad (3.1)$$

where I is the 3x3 identity matrix, ρ is the density, V the velocities and the elements of the symmetric matrix A in terms of the elastic constants c_{ij} are

$$\begin{aligned} A_{11} &= y_1^2 c_{11} + y_2^2 c_{66} + y_3^2 c_{55} \\ A_{22} &= y_1^2 c_{66} + y_2^2 c_{22} + y_3^2 c_{44} \\ A_{33} &= y_1^2 c_{55} + y_2^2 c_{44} + y_3^2 c_{33} \\ A_{12} &= y_1 y_2 (c_{12} + c_{66}) \\ A_{13} &= y_1 y_3 (c_{13} + c_{55}) \\ A_{23} &= y_2 y_3 (c_{23} + c_{44}) \\ A_{13} &= y_1 y_3 (c_{13} + c_{55}). \end{aligned} \quad (3.2)$$

At ambient conditions the elastic constants of Equation (3.1) were adjusted so as to optimally describe the velocity as a function of crystallographic orientation. As the pressure is increased, preliminary values of the elastic moduli c , the adiabatic compliance tensor, $s = c^{-1}$ and hence an approximate adiabatic compressibility can be derived from Equation (3.1) and densities at lower pressure. The small correction from the adiabatic to the isothermal modulus is calculated from

$$K_S = K_T(1 + \gamma\alpha T) \quad (3.3)$$

From the isothermal modulus more accurate densities, compliances and moduli are recursively computed using all data (three samples) at each pressure.

For samples of composition similar to the one studied here, the Grüneisen parameter is $\gamma=1.3$ [Sumino and Anderson, 1984] and, at 1 bar, the coefficient of thermal expansion is $\alpha=3.35 \times 10^{-5} \text{ K}^{-1}$ [Angel and Hugh-Jones, 1994; Yan *et al.*, 1987]. At 298 K and ambient pressure, $K_S / K_T = 1.008$. If, as would appear to be the case for olivine [Zaug *et al.*, 1993] and garnet [Chai *et al.*, 1996a], the bulk modulus is a function primarily of density, then

$$\left(\frac{\partial \ln \alpha}{\partial P} \right)_T = \frac{dK^{-1}}{d \ln \rho} \quad (3.3)$$

and the coefficient of thermal expansion, and thus K_S / K_T , at higher pressures can be estimated from the ambient pressure result and the present data.

3.3 Results

The elastic constants for Kh-opx and for the bronzite of *Webb and Jackson* [1993] are plotted as a function of pressure in Figures. 3.10 to 3.12 and listed in Table 3.2. The new bronzite points for c_{33} are also plotted. There is complete inter-laboratory agreement at one bar; c_{33} at 3 GPa agrees to within a 0.5 % uncertainty. The Kh-opx elastic constants are, within experimental accuracy, polynomial functions of the pressure to 12.5 GPa. Elastic constants, bulk moduli, and shear moduli at one bar as well as the pressure derivatives necessary to calculate these quantities at higher pressures are given in Table 3.2 as are the bronzite measurements of Webb and Jackson to 3.0 GPa. The pressure dependence of the density for Kh-opx is adequately described by a fourth order Eulerian finite strain equation with $\rho^0 = 3.304 \text{ g/cm}^3$ and the values of K , K' , and K'' are also given in Table 3.2. Cell edge strains are plotted in Figure 3 along with the orthoenstatite x-ray compression data of *Angel and Hugh-Jones* [1994].

The uncertainties specified in Table 3.2 and indicated as error bars in Figures. 3.10 to 3.12 are mostly formal 2σ errors determined by the covariance matrix weighted by the misfit to the data. However, thermoacoustic excitation of shear modes depends on the partial longitudinal character of quasitransverse waves in a general direction in an anisotropic medium. Along special directions, where pure longitudinal and pure transverse waves are possible, only the longitudinal mode is excited. Thus, in some cases, data were not collected in directions where a given shear constant is the sole or principal determinant of the velocity. In these circumstances the formal errors for the diagonal shear constants c_{44} , and c_{66} were found to underestimate the uncertainty; that is, the optimization process found

solutions which differed little in misfit but had constants differing by more than the formal uncertainty. For example, the constant c_{66} is most directly determined by the velocity of a shear wave propagating parallel to either the a axis or b axis (Figure 3.7 lower right panel). No data were obtained in the appropriate directions. Instead, c_{66} is constrained by the form of the shoulder in compressional velocities on either side of propagation parallel to a , but there is significant covariance between c_{66} and other constants. The scatter observed in Figure 3.12 of diagonal shear elastic constants at several pressures relative to the polynomial fits is consistent with this covariance. Errors of 4σ (rather than 2σ) were assigned to those elastic constants (c_{66} at 8.5, 10.5 12.5 GPa and c_{44} at 8.5 GPa) where shear wave data were particularly sparse.

Isotropically averaged (Hashin-Strikman bounds [*Watt and Peselnick, 1980*]) bulk and shear moduli are listed in Table 3.3 and are compared in Figure 3.13 and Figure 3.14 with the results of Webb and Jackson. Upper and lower Hashin-Strikman bounds are within the uncertainties.

3.4 Discussion

All elastic constants vary smoothly with pressure. A significant second derivative is required to fit the diagonal compressional constants c_{11} , c_{22} , and c_{33} and the off diagonal constants c_{12} , c_{13} , and c_{23} . The diagonal shear constants c_{44} , c_{55} , and c_{66} , However, are linear within experimental uncertainty. At 1 bar, the pressure derivatives of the diagonal compressional constants are greater than those of the off-diagonal elements, which in turn have larger pressure derivatives than the diagonal shears. The small difference between c_{11} and c_{33} is well constrained by the data and decreases at high pressure. At 12.5 GPa the two constants are identical within the uncertainties. The data

shown in Figure 3.7 suggest that the two are slightly different at 8.5 GPa. Both c_{11} and c_{33} lie above the polynomial fit at 2.3 GPa and slight below it at 6.3 GPa. Otherwise the data is well represented by the polynomial fit.

The Kh-opx is substantially less compressible, particularly along the c axis, than either orthoenstatite or bronzite. A simplistic argument is that tetrahedral Al in substitution for the smaller Si stiffens tetrahedral chains. In Figure 13, K' decreases from 7.8 at one bar to a more "normal" value of 4.3 at 10 GPa. The bronzite bulk modulus increases more rapidly at low pressure but has a larger negative second derivative.

The x-ray data for the orthoenstatite were interpreted by *Angel and Hugh-Jones* [1994] as having a discontinuity at 4 GPa. The data were fit using $K'=14.9$ below 4 GPa and $K'=5.6$ at high pressures. The current data, while supporting the decrease of K' at high pressure, do not validate the notion of a discontinuity at 4 GPa. However, a close examination of the pressure dependence of the diagonal constants c_{11} and c_{33} provides some support for a slight change in slope between 4 and 6 GPa. The bulk modulus determined in the x-ray measurements follows the current data closely between 4 and 8 GPa. The isotropic shear modulus in Figure 3.15 and Figure 3.16 is linear within experimental error. *Webb and Jackson* [1993] reported a larger derivative for G . Thus, Kh-opx and the bronzite have increasingly similar shear moduli at higher pressure.

In Figure 3.17 and Figure 3.18 isotropic compressional and shear wave velocities for San Carlos olivine [*Zaug et al.*, 1993], pyrope-rich garnet [*Chai et al.*, 1996a] and pyroxene (Kh-opx and bronzite) are compared as a function of pressure at room temperature. The short linear trend centered on the bronzite data represents the assumption frequently invoked by those who

prefer a nominal value for the pressure derivative of the bulk modulus in the absence of high pressure data (i.e. [Duffy and Anderson, 1989; Ita and Stixrude, 1992; Jordan, 1979]). However, the present data and the previous work ([Frisillo and Barsch, 1972; Webb and Jackson, 1993]) all argue for a rapid increase in V_p in opx at low pressure. This trend substantially reduces the difference in velocity between olivine and pyroxene. Both V_p and V_s in the Kh-opx are considerably higher than the non-aluminous pyroxenes. In fact, the Kh-opx compressional velocities exceed olivine beyond 4 GPa. The Kh-opx shear velocities are slightly higher than olivine over the entire range of pressure.

It has been argued that the seismic profiles for the upper mantle are close to that expected for olivine. By mixing a slower pyroxene component with a faster garnet component, a mineral physics model can be made consistent with seismology. This idea is further supported by the observation that the olivine to spinel transition has a velocity difference that is significantly larger than the observed seismic discontinuity at 410 km. Thus, a phase must be present other than olivine at 410 km to reduce the size of the discontinuity.

The present data can not address all of the assumptions associated with the standard model. In particular, temperature derivatives of the elastic constants are wholly unconstrained by data at high pressure. Furthermore, the elasticity of both high- and low-clinopyroxenes is relatively unknown either at one bar or at high pressure. However, the present data do indicate that the aluminum content of mantle orthopyroxenes is an important parameter in modeling the elastic response. High velocity garnets may not naturally be balanced against "low velocity" pyroxenes since a few wt% Al_2O_3 content in-

creases velocities by several percent. In addition, pyroxene velocities are more like olivine velocities at depths beyond about 100 km.

It would not appear that it is justified to assume *a priori* that clinopyroxene have velocities similar to orthopyroxenes. Since the cpx phase preferentially collects the large cations (principally Na, Ca, Al, and K), it might equally be expected, on the basis of jadeite, hedenbergite, and diopside elasticity, that velocities will be higher in coexisting clinopyroxenes. Increased solubility of pyroxene into garnet at high pressure introduces yet another uncertainty in modeling efforts.

The current data highlight a need to better define the problem of mineral elasticity as a function of composition as well as pressure, and temperature. Consideration of pyroxene elasticity solely in terms of $Mg/(Mg+Fe)$ is inadequate. Thus, efforts to interpret lateral variation in upper mantle velocities in terms of the degree of chemical fractionation (e.g. [Humphreys and Dueker, 1994]) should be modified.

3.5 Illustrations

3.5.1 Tables

Table 3.1 Chemistry of Kh-opx

The chemical analysis was obtained by microprobe analysis. The numbers in the parentheses represent the uncertainties to the last digit based on more than 50 samples.

Cations	Based on six Oxygen
Si	1.8877(4)
Mg	1.6428(6)
Ca	0.0362(15)
Fe	0.1717(20)
Ti	0.0035(02)
Al	0.2229(48)
Mn	0.0039(04)
Cr	0.0145(05)
Na	0.0090(05)
Ni	0.0035(04)
Mg/(Mg+Fe)	0.90
End-member	Mole fraction
Enstatite	75.5
Mg-Tschermakite	12.0
Ferrosilite	8.5

Table 3.2 Elastic constants of Kh-opx

Elastic constants of Kh-opx at 298 K. The elastic constants are in GPa, the pressure derivatives per GPa. Uncertainties in the last digit are indicated in parentheses.

	0	2.3	4.3	6.3	8.5	10.5	12.5
C ₁₁	236.9(10)	263.4(16)	276.5(10)	288.0(10)	308.5(12)	321.3(12)	327.6(12)
C ₁₂	79.6(16)	94.0(10)	103.8(18)	112.5(20)	119.4(20)	126.6(20)	132.2(20)
C ₁₃	63.2(18)		88.6(16)	104.2(24)	106.9(24)	117.6(24)	126.6(24)
C ₂₂	180.5(8)	202.1(8)	216.0(8)	228.7(10)	234.0(10)	252.1(10)	262.4(10)
C ₂₃	56.8(24)	75.5(28)	83.8(16)	93.1(22)	109.4(22)	118.4(22)	121.7(22)
C ₃₃	230.4(10)	258.2(30)	274.0(10)	286.4(10)	305.4(12)	318.7(12)	327.6(12)
C ₄₄	84.3(12)	86.8(30)	89.2(6)	92.1(12)	95.2(12)	97.6(12)	99.1(12)
C ₅₅	79.4(8)		83.2(12)	83.7(12)	86.2(12)	85.9(12)	90.0(16)
C ₆₆	80.1(12)	85.6(8)	90.7(14)	95.8(14)	103.7(16)	112.6(16)	114.1(16)
K	115.5(5)	134.4(9)	145.6(9)	157.0(8)	168.5(8)	178.7(10)	185.5(8)
μ	78.1(4)	81.9(8)	84.7(6)	86.7(5)	90.8(5)	93.6(7)	95.7(6)
ρ	3.306(2)	3.369(2)	3.419(3)	3.465(4)	3.512(4)	3.553(5)	3.593(5)
ρ_0/ρ	1.0000	0.981	0.967	0.954	0.941	0.930	0.921

Table 3.3 Pressure dependence of elastic constants of Kh-opx

Pressure dependence of the elastic properties orthopyroxenes at 298 K. The elastic constants, average bulk modulus (K), average shear modulus (M) are in GPa, the pressure derivatives are per GPa.

	$\text{En}_{0.815}\text{Fs}_{0.085}\text{Ts}_{0.100}^{\text{a}}$			$\text{Mg}_{0.80}\text{Fe}_{0.20}\text{SiO}_3^{\text{b}}$		
	M at 1 bar (GPa)	$\frac{dM}{dP}$	$\frac{d^2M}{dP^2}$ (GPa) ⁻¹	M at 1 bar (Gpa)	$\frac{dM}{dP}$	$\frac{d^2M}{dP^2}$ (GPa) ⁻¹
C11	236.9(10)	10.27	-0.47	231.0	11.0	-0.96
C12	79.9(16)	6.22	-0.33	78.9	7.8	-1.01
C13	63.2(18)	6.63	-0.26	61.4	14.0	-3.8
C22	180.5(8)	8.87	-0.38	169.8	10.7	-1.11
C23	56.8(24)	7.26	-0.31	49.1	8.5	-0.7
C33	230.4(10)	11.07	-0.53	215.7	16.1	-2.3
C44	84.3(12)	1.23	0.00	82.8	2.26	-0.27
C55	79.4(8)	0.75	0.00	76.5	2.65	-0.42
C66	80.1(12)	2.78	0.00	78.1	2.76	-0.23
K	115.5(5)	7.82	-0.35	109.4	10.8	-1.6
μ	78.1(4)	1.45	0.00	75.2	2.06	-0.12

a) Present work

b) [Webb and Jackson, 1993]

3.5.2 Figures

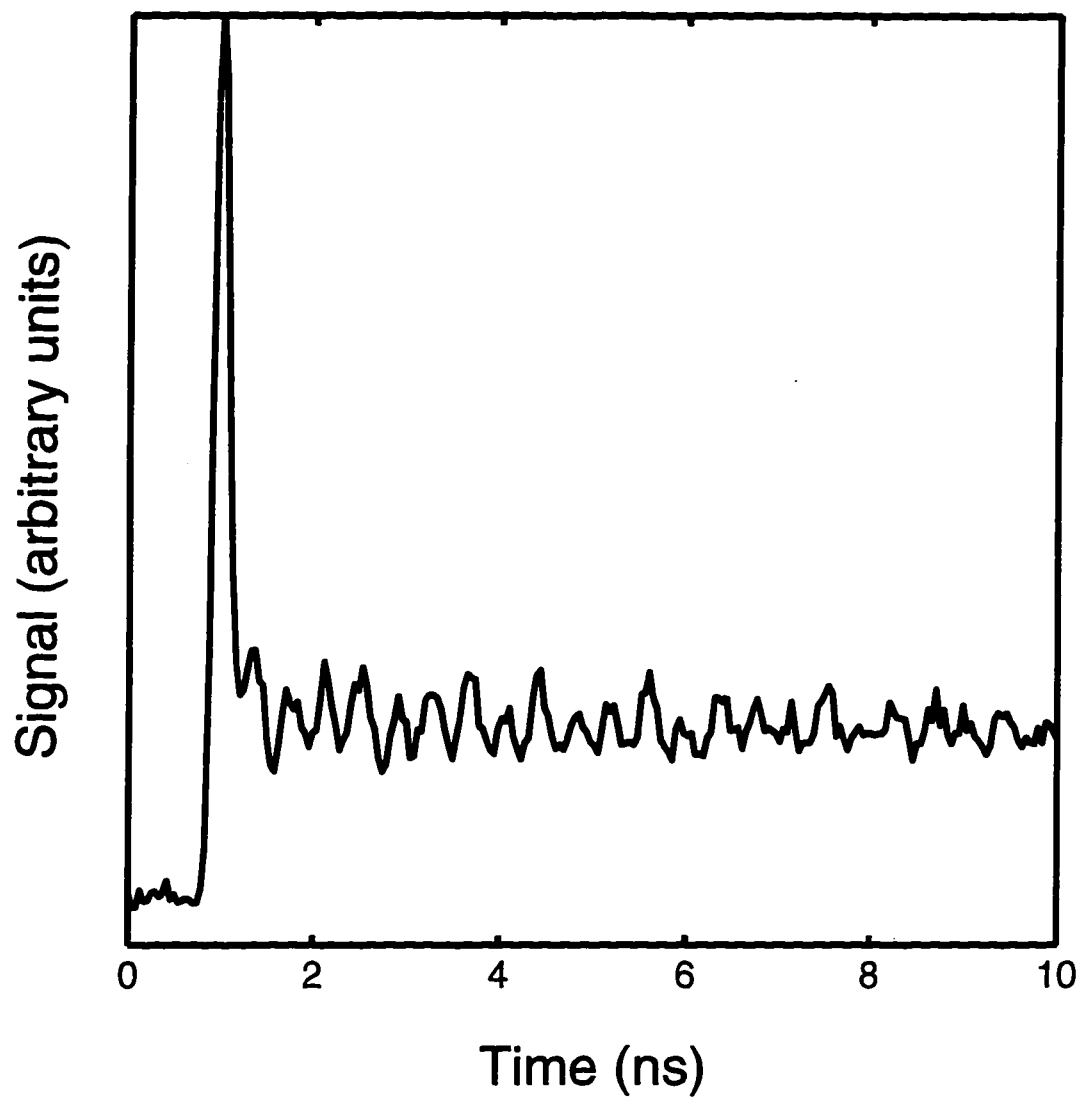


Figure 3.1 Time domain record of ISS signal of opx
The first 10 ns of a time domain record of the ISS signal of opx at 2.3 GPa.

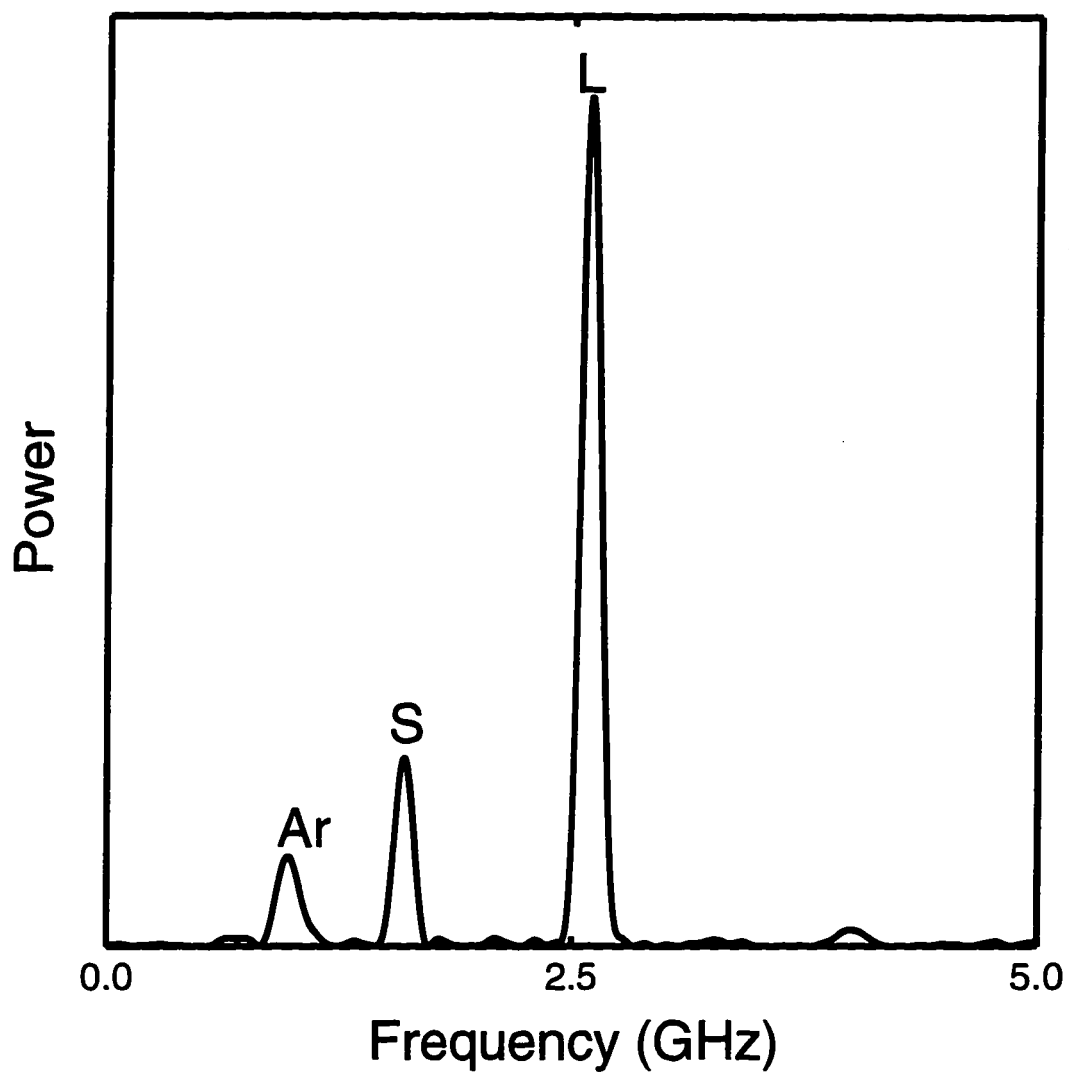


Figure 3.2 Fourier transformation of ISS signal of opx

Fourier transformation of the time domain record in Figure 2.1. Three peaks are present. Longitudinal velocity of opx is indicated by L, one shear by S, and the longitudinal velocity of the argon pressure medium by Ar.

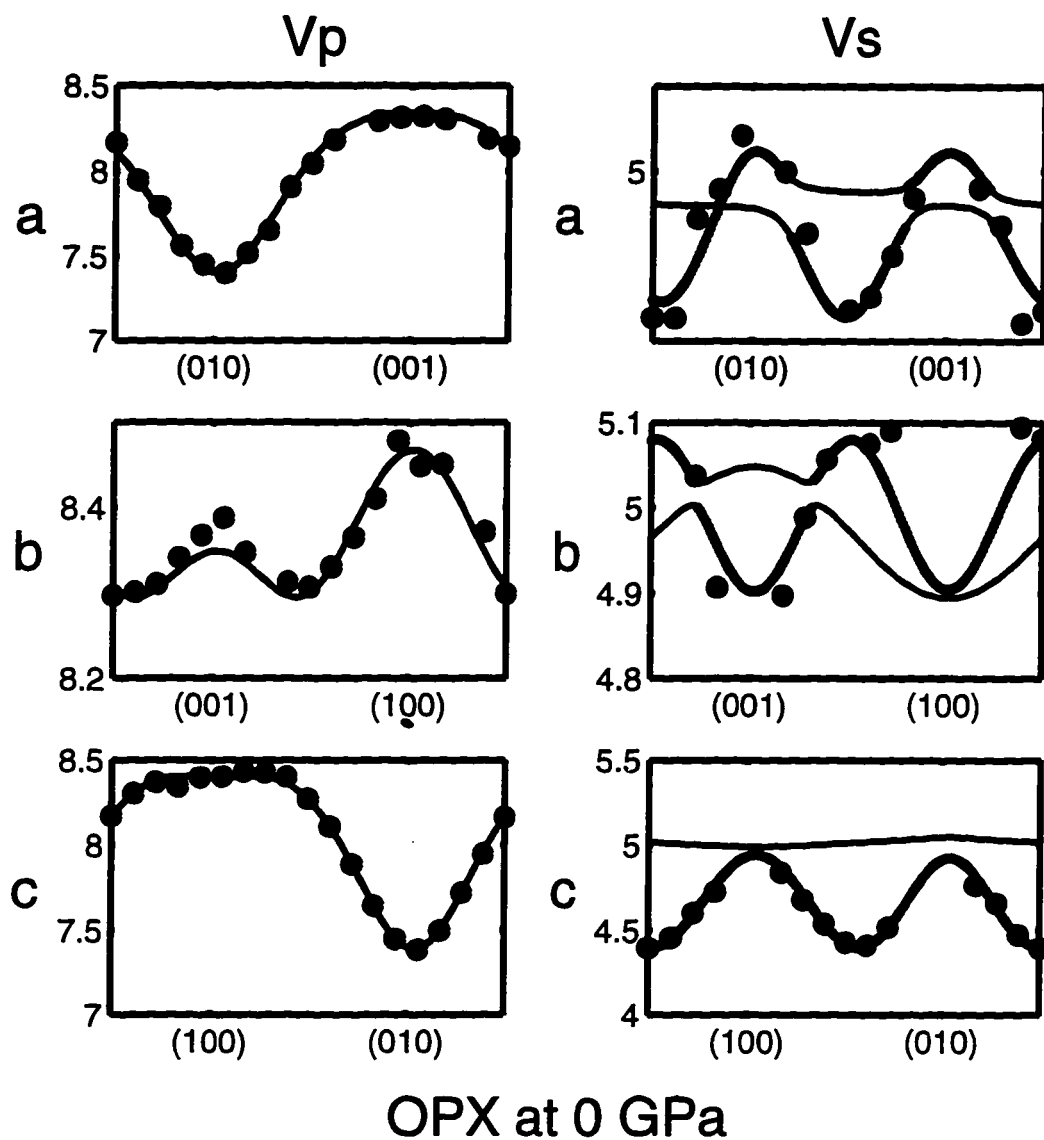


Figure 3.3 Sound velocities of opx at 0 GPa

The velocity of quasilongitudinal and quasitransverse acoustic waves in Kh-opx ($\text{En}_{0.755}\text{Fs}_{0.085}\text{Ts}_{0.12}$) at 298 K and 0 GPa as a function of crystallographic direction. Data from samples with principal faces perpendicular to the *a*, *b* and *c* axes are shown. The vertical axes are in km/s. The thick curves for shear velocities are in-plane polarization; the thin ones are out plane polarization.

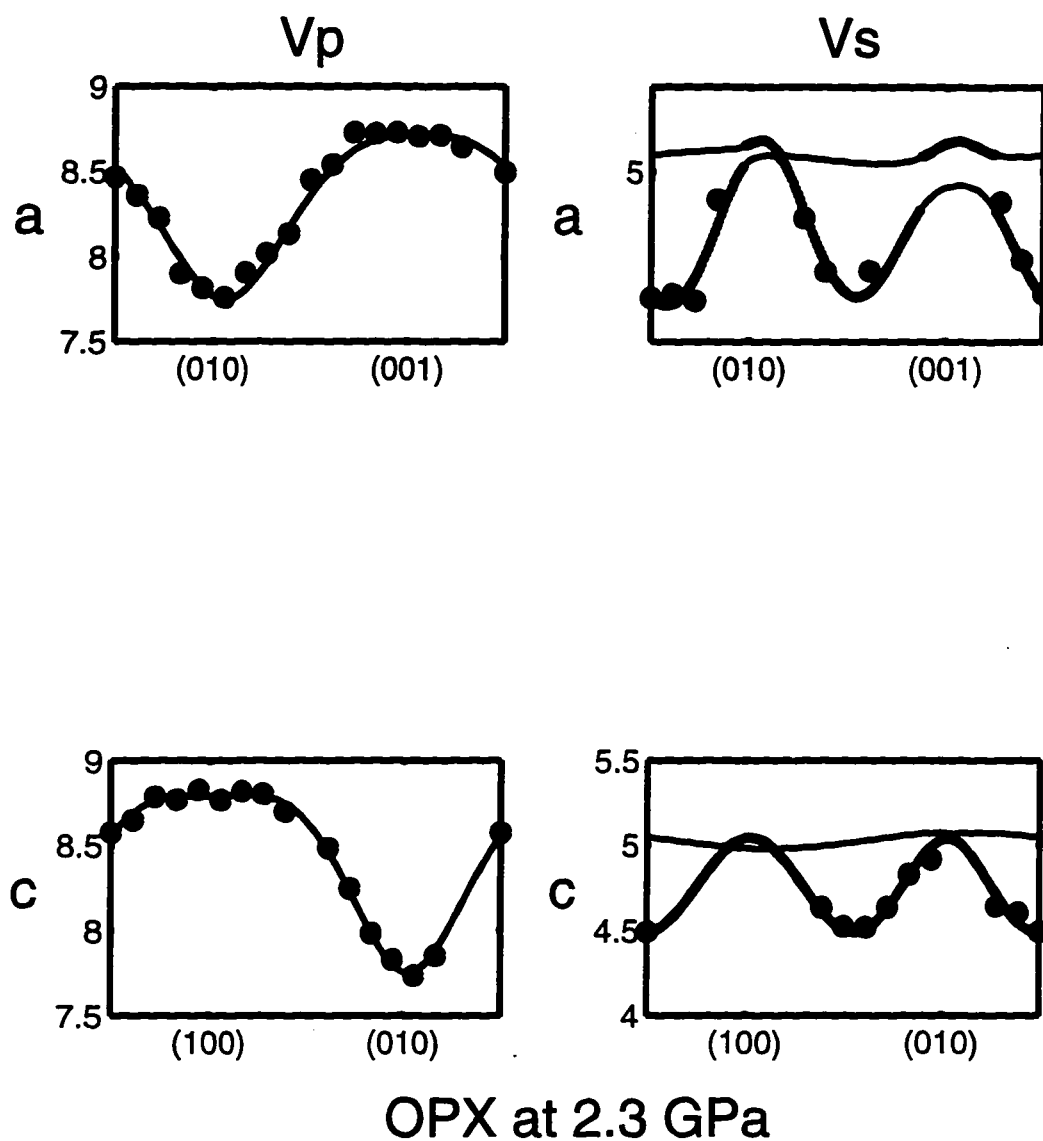


Figure 3.4 Sound velocities of opx at 2.3 GPa

The velocity of quasilongitudinal and quasitransverse acoustic waves in Kh-opx ($\text{En}_{0.755}\text{Fs}_{0.085}\text{Ts}_{0.12}$) at 298 K and 2.3 GPa as a function of crystallographic direction. Data from samples with principal faces perpendicular to the *a*, *b* and *c* axes are shown. A 1% variation is illustrated by a heavy bar adjacent to the vertical axis. The vertical axes are in km/s. The thick curves for shear velocities are in-plane polarization; the thin ones are out plane polarization.

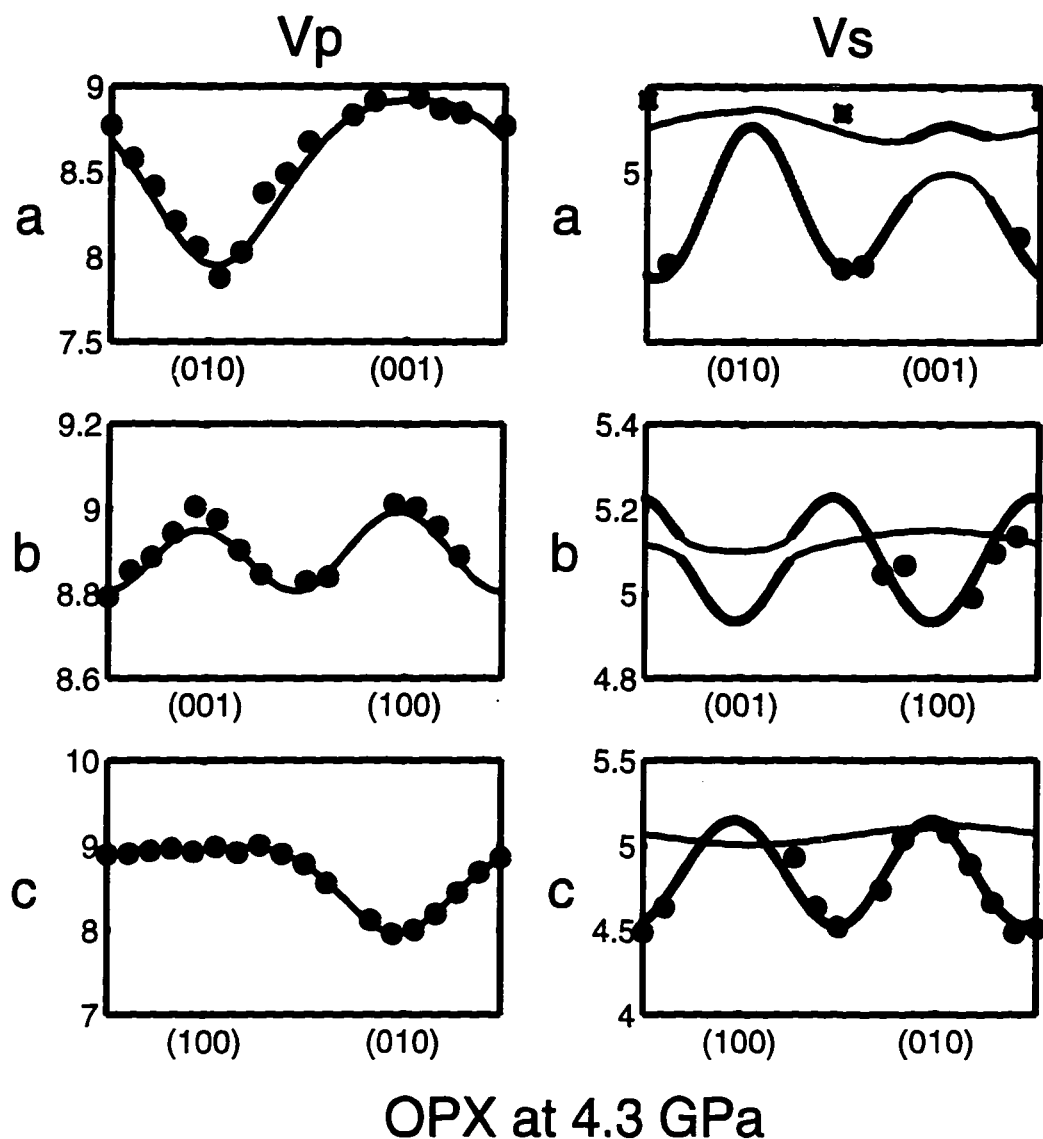


Figure 3.5 Sound velocities of opx at 4.3 GPa

The velocity of quasilongitudinal and quasitransverse acoustic waves in Kh-opx ($\text{En}_{0.755}\text{Fs}_{0.085}\text{Ts}_{0.12}$) at 298 K and 4.3 GPa as a function of crystallographic direction. Data from samples with principal faces perpendicular to the *a*, *b* and *c* axes are shown. The vertical axes are in km/s. The thick curves for shear velocities are in-plane polarization; the thin ones are out plane polarization.

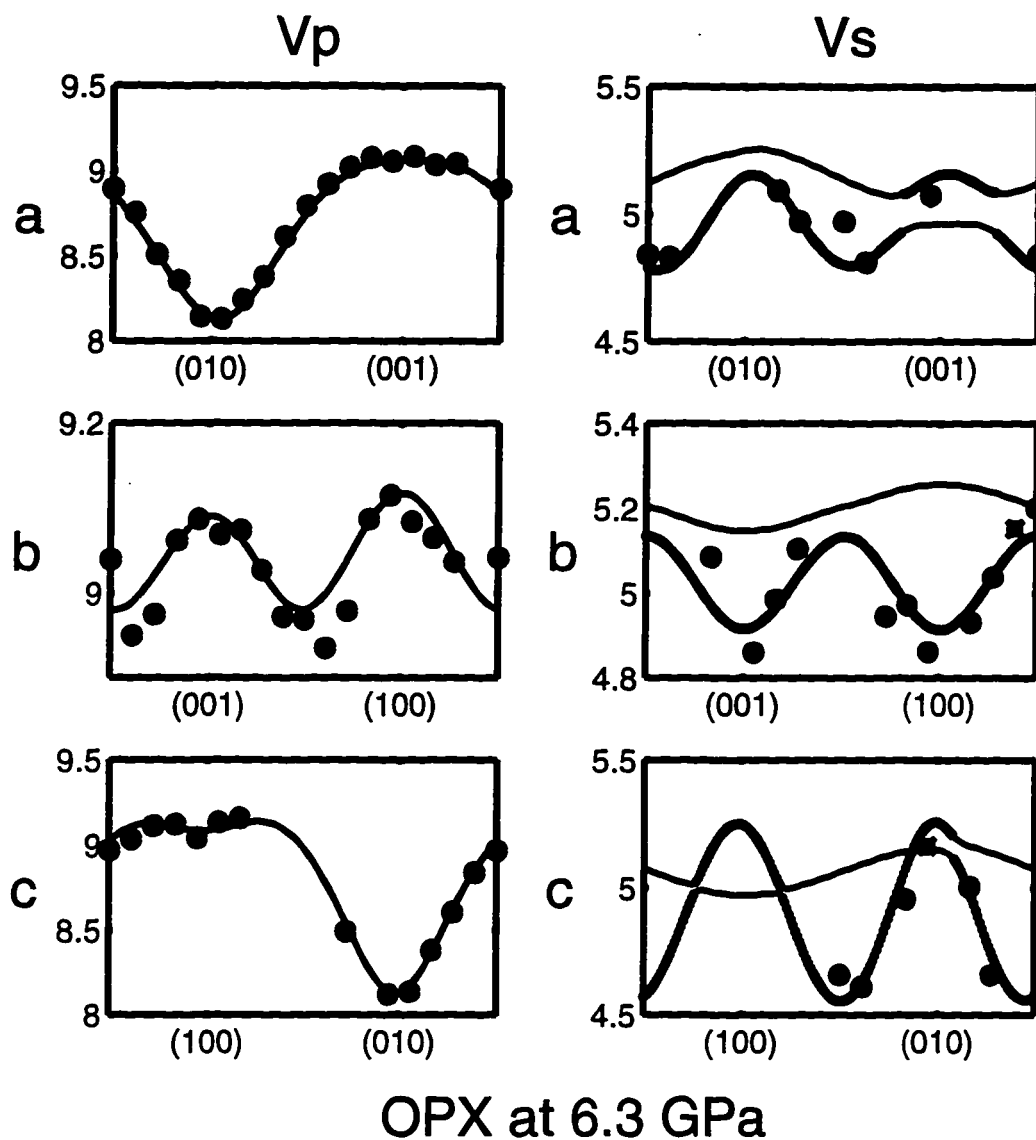


Figure 3.6 Sound velocities of opx at 6.3 GPa

The velocity of quasilongitudinal and quasitransverse acoustic waves in Kh-opx ($\text{En}_{0.755}\text{Fs}_{0.085}\text{Ts}_{0.12}$) at 298 K and 6.3 GPa as a function of crystallographic direction. Data from samples with principal faces perpendicular to the *a*, *b* and *c* axes are shown. The vertical axes are in km/s. The thick curves for shear velocities are in-plane polarization; the thin ones are out plane polarization.

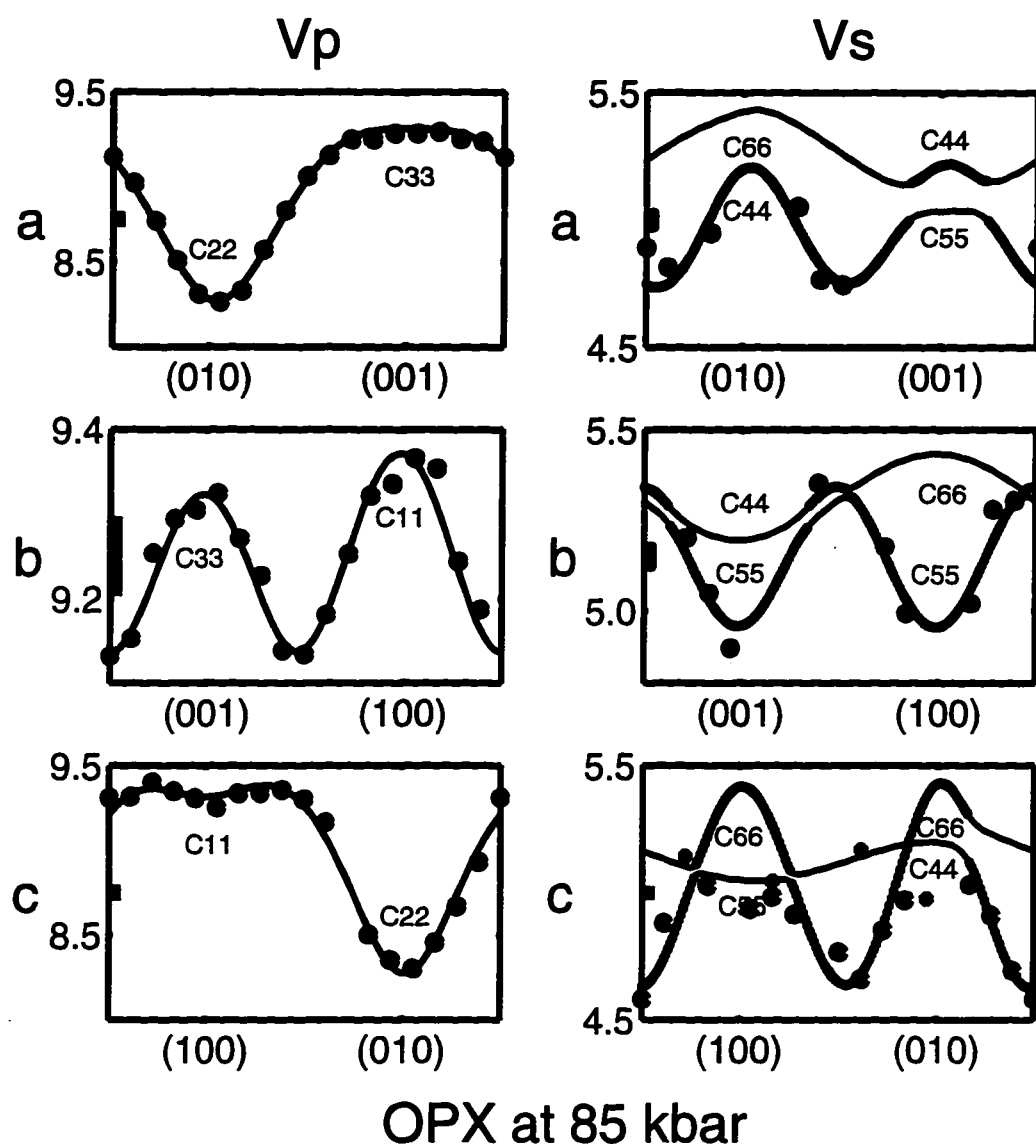


Figure 3.7 Sound velocities of opx at 8.5 GPa

The velocity of quasilongitudinal and quasitransverse acoustic waves in Kh-opx ($\text{En}_{0.755}\text{Fs}_{0.085}\text{Ts}_{0.12}$) at 298 K and 8.5 GP as a function of crystallographic direction. Data from samples with principal faces perpendicular to the *a*, *b* and *c* axes are shown. Simple crystallographic directions and points where the velocity is determined by a single elastic constant are indicated. A 1% variation is illustrated by a heavy bar adjacent to the vertical axis. The vertical axes are in km/s.

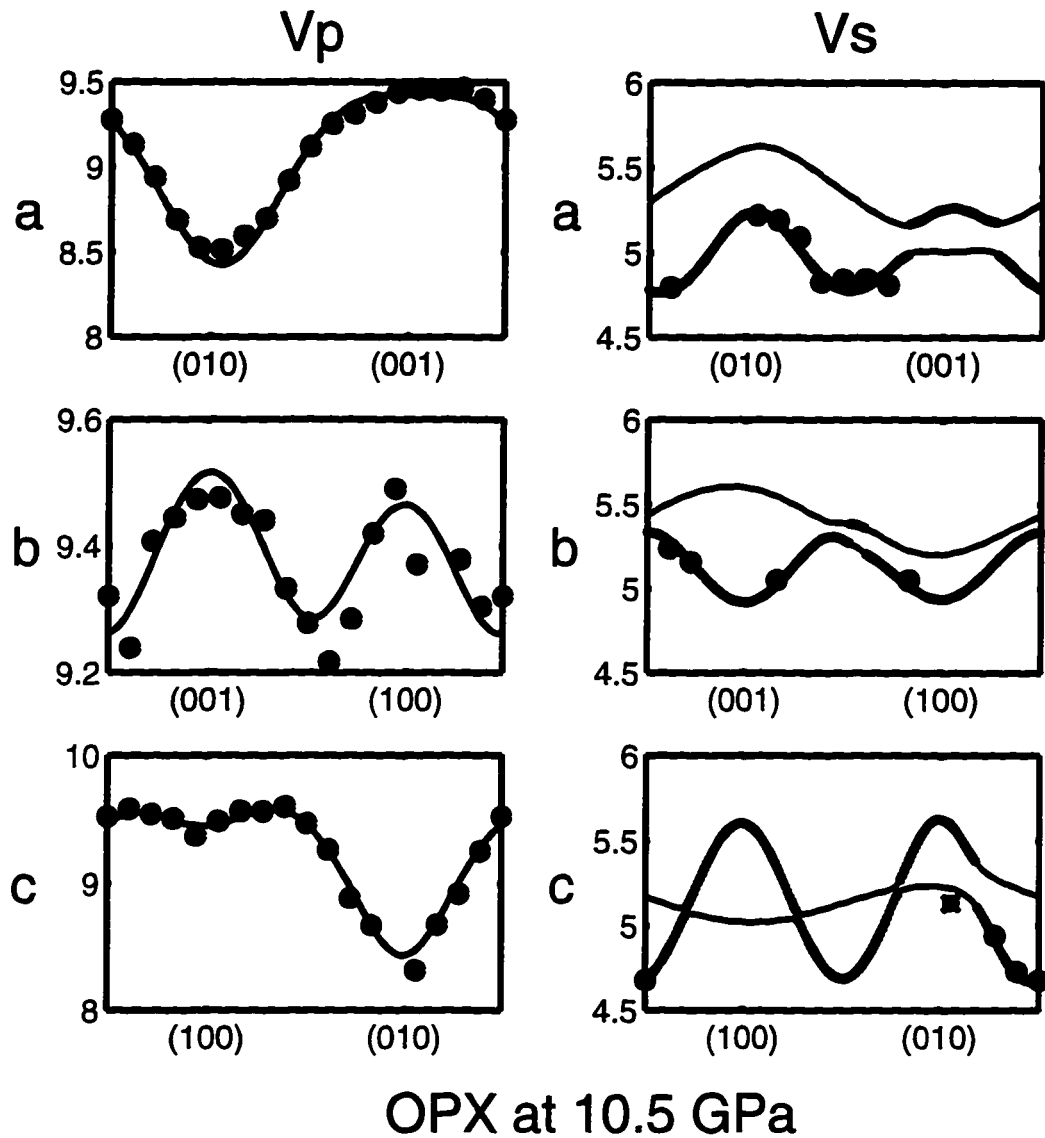


Figure 3.8 Sound velocities of opx at 10.5 GPa

The velocity of quasilongitudinal and quasitransverse acoustic waves in Kh-opx ($\text{En}_{0.755}\text{Fs}_{0.085}\text{Ts}_{0.12}$) at 298 K and 10.5 GPa as a function of crystallographic direction. Data from samples with principal faces perpendicular to the *a*, *b* and *c* axes are shown. The vertical axes are in km/s. The thick curves for shear velocities are in-plane polarization; the thin ones are out plane polarization.

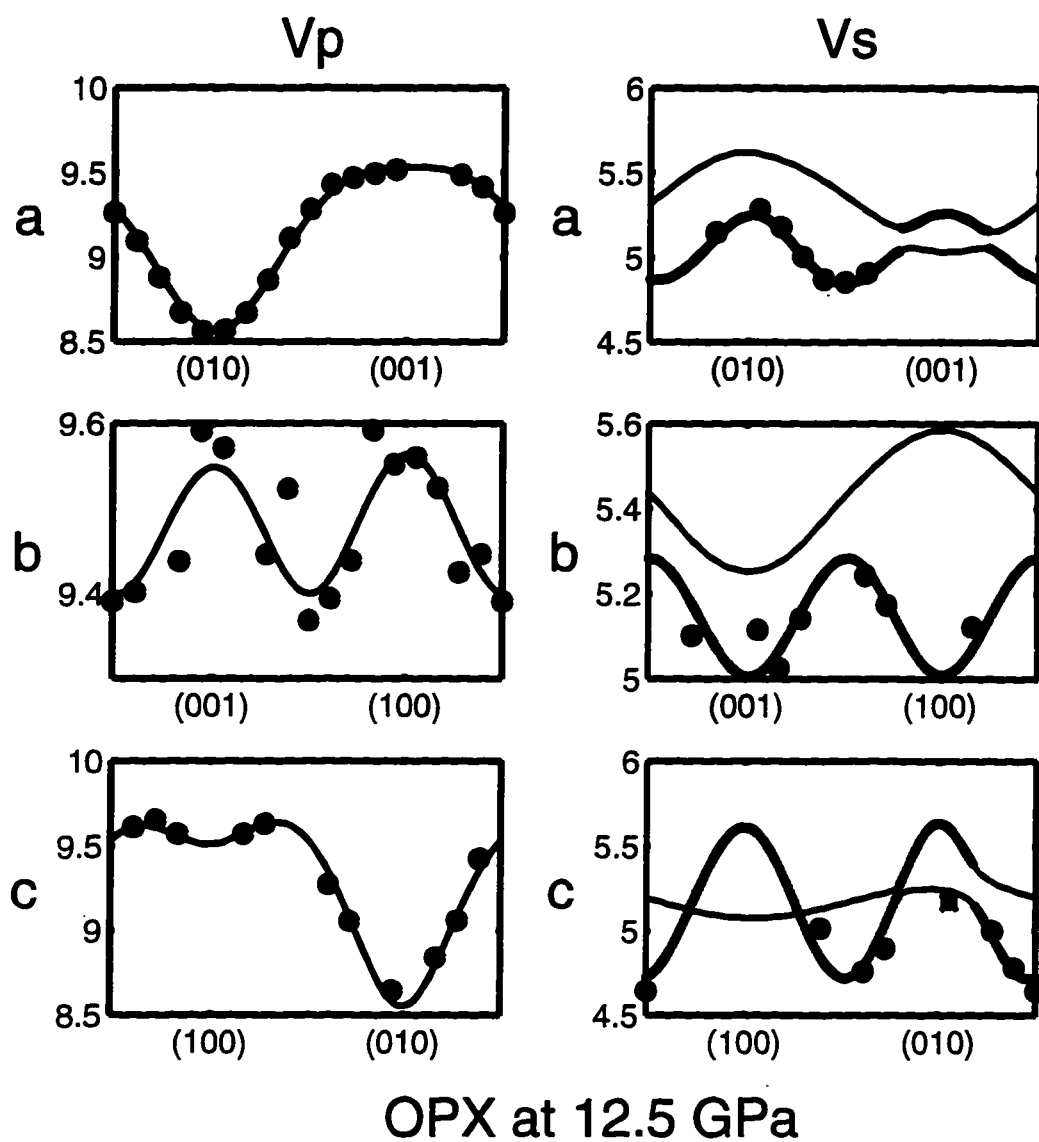


Figure 3.9 Sound velocities of opx at 12.5 GPa

The velocity of quasilongitudinal and quasitransverse acoustic waves in Kh-opx ($\text{En}_{0.755}\text{Fs}_{0.085}\text{Ts}_{0.12}$) at 298 K and 12.5 GPa as a function of crystallographic direction. Data from samples with principal faces perpendicular to the a , b and c axes are shown. The vertical axes are in km/s. The thick curves for shear velocities has in plane polarization; the thin ones are out plane polarization.

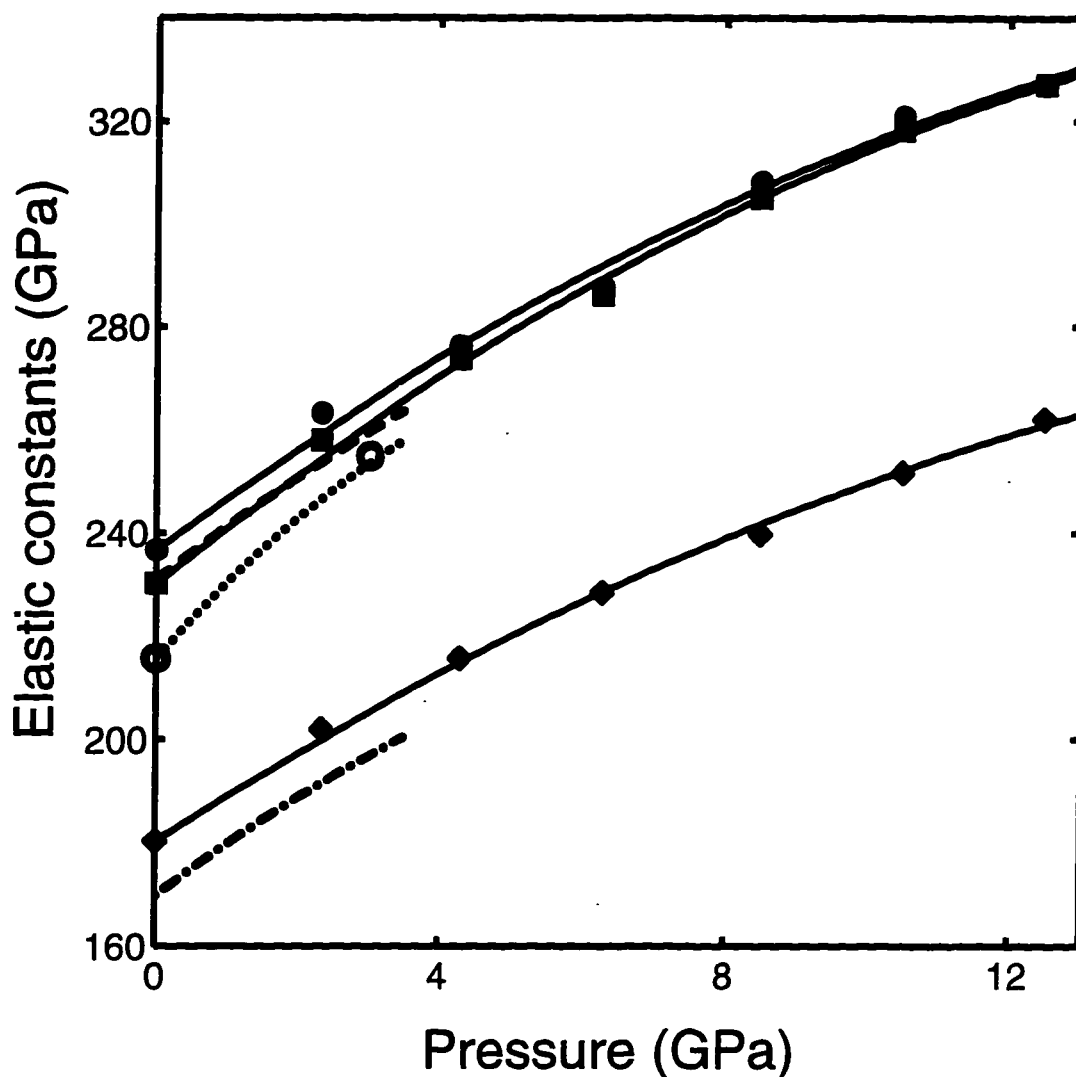


Figure 3.10 Diagonal longitudinal elastic constants of opx

Experimental points and polynomial fits (solid curves) for C_{11} (upper curve), C_{33} (middle curve) and C_{22} (lower curve) of Kh-opx at 298 K as a function of pressure. The results of *Webb and Jackson* [1993] for C_{11} , C_{33} and C_{22} for bronzite at 25°C are plotted as dashed, broken, and dotted curves. The open circles represent the current measurement of C_{33} for the Webb and Jackson sample.

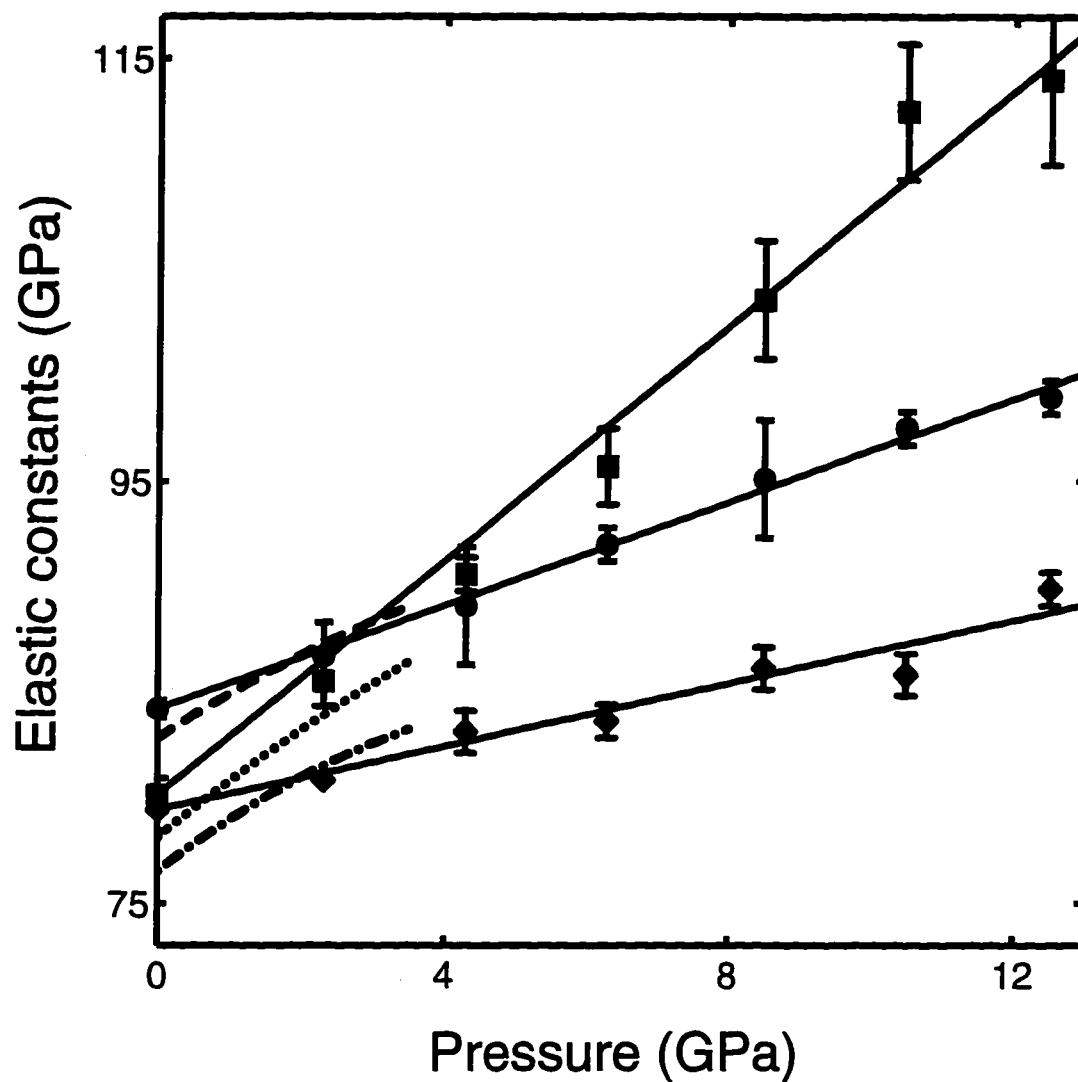


Figure 3.11 Diagonal shear elastic constants of opx

The shear constants C_{66} (squares) C_{44} (circles) and C_{55} (diamonds) of Kh-opx as a function of pressure. The results of *Webb and Jackson* [1993] for C_{66} , C_{44} and C_{55} for bronzite at 298 K are plotted respectively as dashed, dotted, and broken curves.

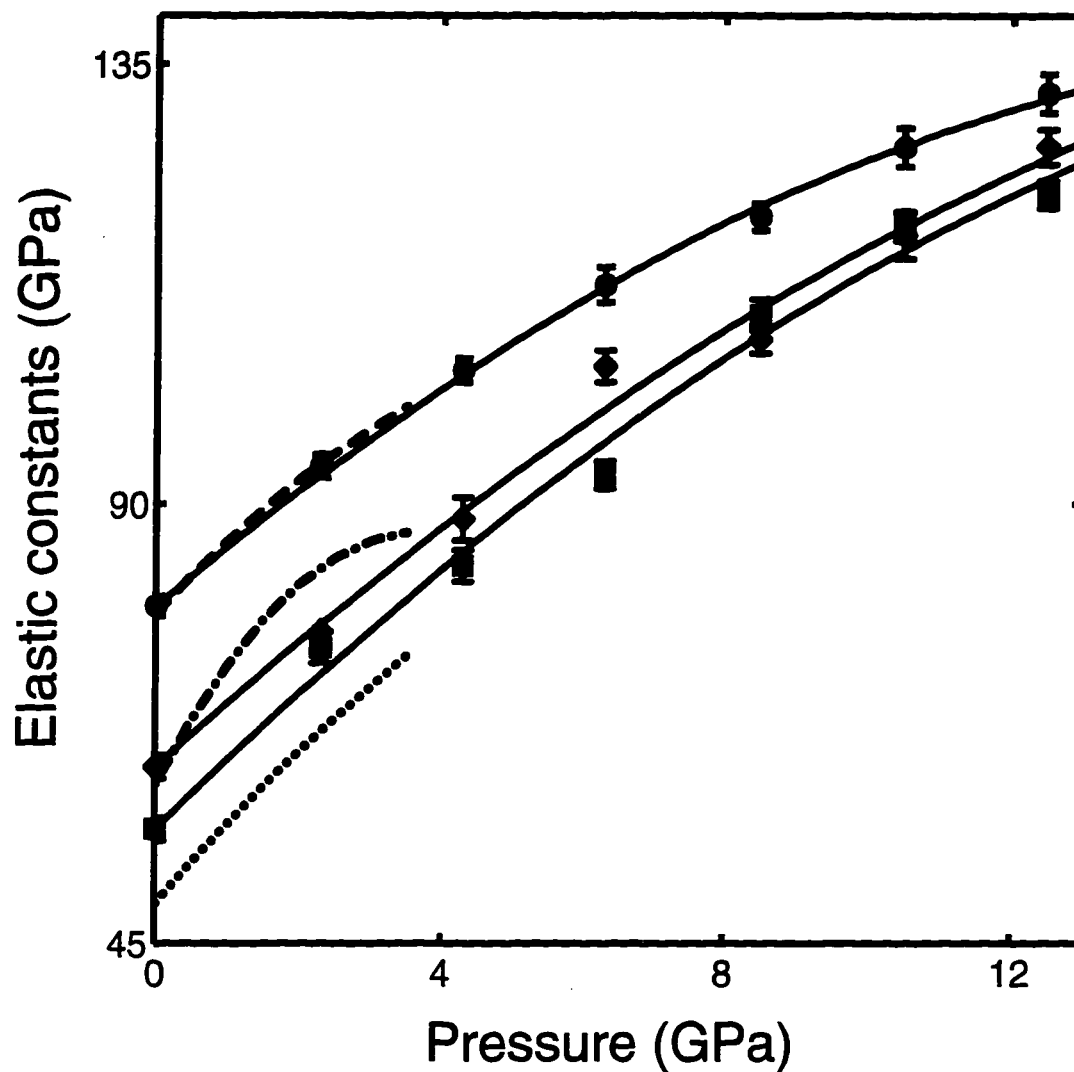


Figure 3.12 Off-diagonal longitudinal elastic constants of opx

The off-diagonal elastic constants C_{23} (squares) C_{12} (circles) and C_{13} (diamonds) of Kh-opx as a function of pressure. The results of *Webb and Jackson* [1993] for C_{23} , C_{12} and C_{13} for bronzite at 25°C are plotted respectively as dashed, broken, and dotted curves.

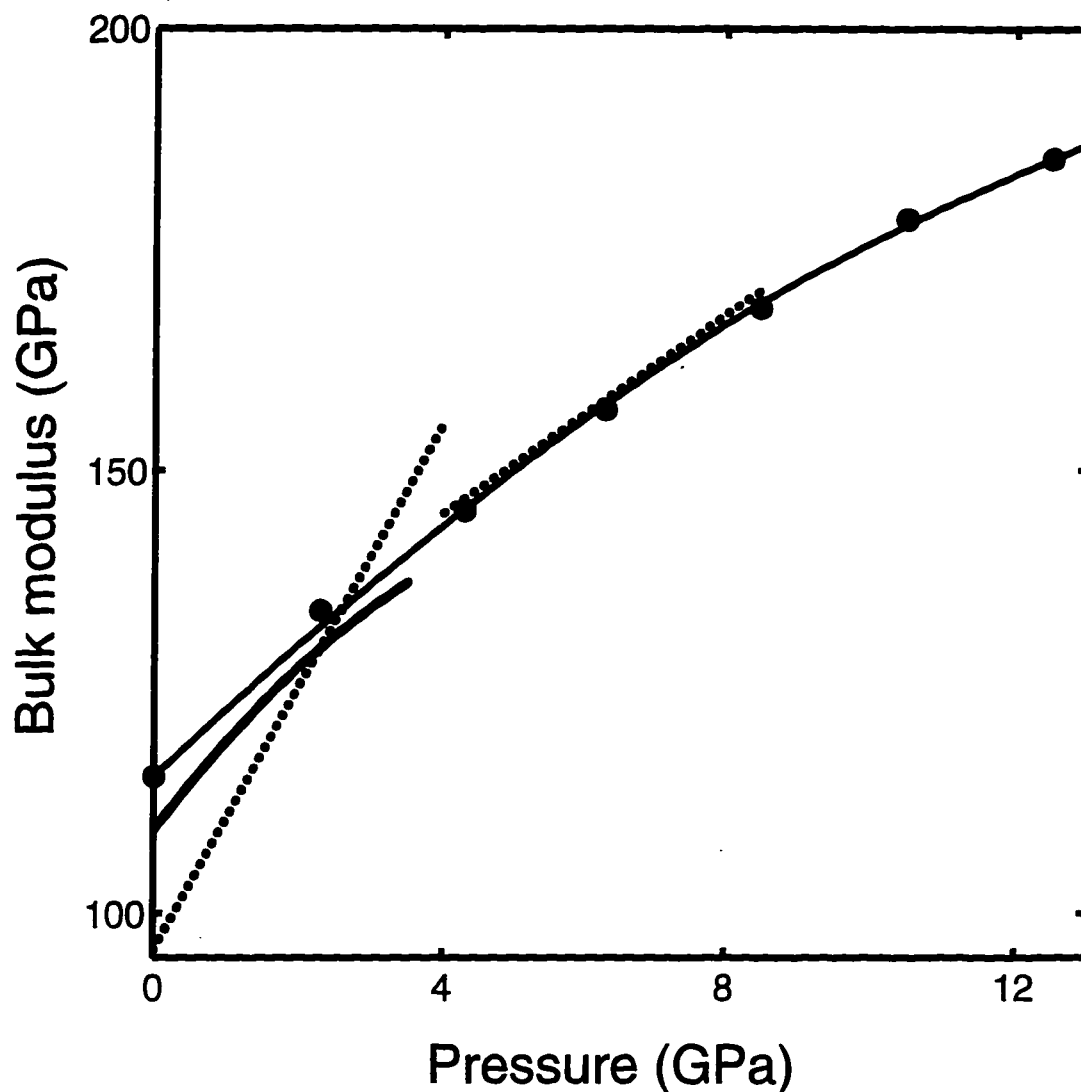


Figure 3.13 Bulk modulus of opx

Experimental points and a quadratic representation of the pressure-dependence of the adiabatic bulk modulus of Kh-opx at 298 K. The lower solid curve is calculated from studies of $\text{Mg}_{0.80}\text{Fe}_{0.20}\text{SiO}_3$ up to 3.0 GPa reported by *Webb and Jackson* [1993]. The dotted lines represent the interpretation, given in *Angel and Hugh-Jones* [1994], of crystallographic studies of synthetic enstatite in terms of a discontinuity in K' at 4 GPa.

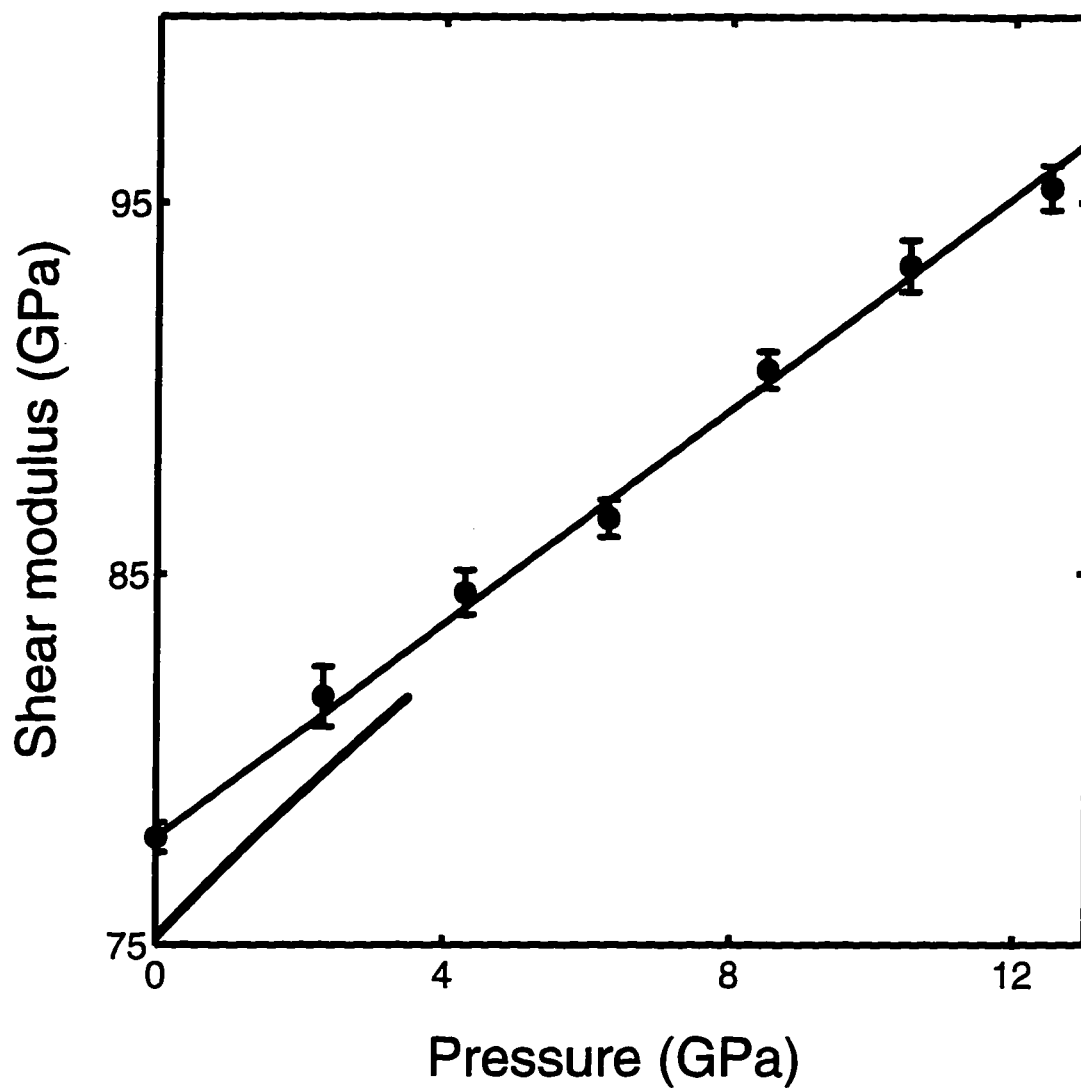


Figure 3.14 Shear modulus of opx

The shear modulus of Kh-opx as a function of pressure. The lower solid curve is calculated from studies of $\text{Mg}_{0.80}\text{Fe}_{0.20}\text{SiO}_3$ up to 3.0 GPa reported in *Webb and Jackson* [1993].

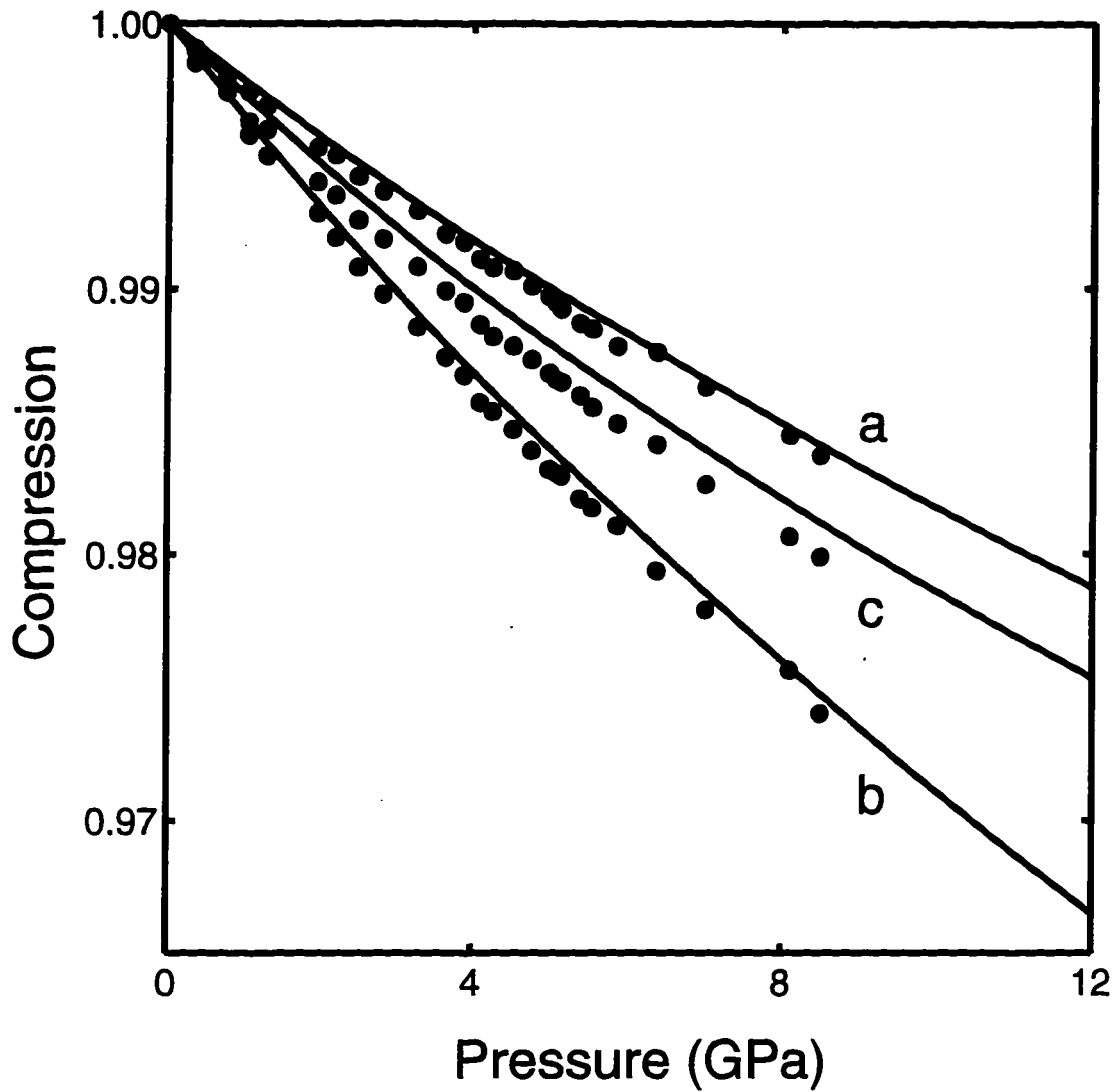


Figure 3.15 Cell-edge compression of opx

The calculated lattice constants of Kh-opx as a function of pressure at 298 K. The circles represent the results of crystallographic studies of synthetic enstatite *Angel and Hugh-Jones* [1994]. The continuous curves are derived from the present work.

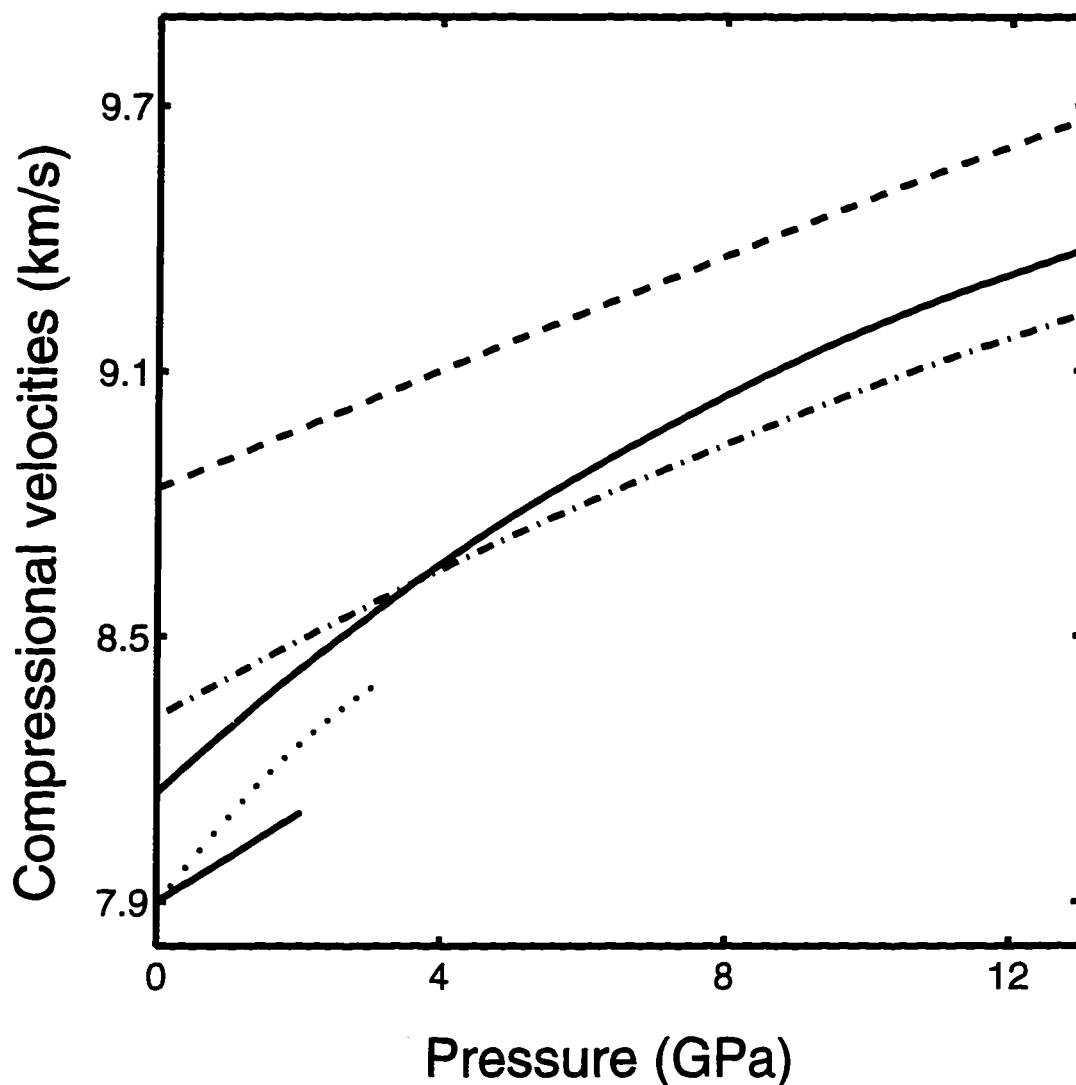


Figure 3.16 Compressional sound velocities of olivine, opx and garnet
 Aggregate-averaged compressional wave velocities in a pyrope-rich garnet [*Chai et al.*, 1996a] (dashed curve), San Carlos olivine [*Zaug et al.*, 1993] (upper broken curve), Kh-opx (solid curve) and bronzite [*Webb and Jackson*, 1993] (lower dotted curve) as a function of pressure. The straight line is the consequence of assuming that $K' = 4.5$.

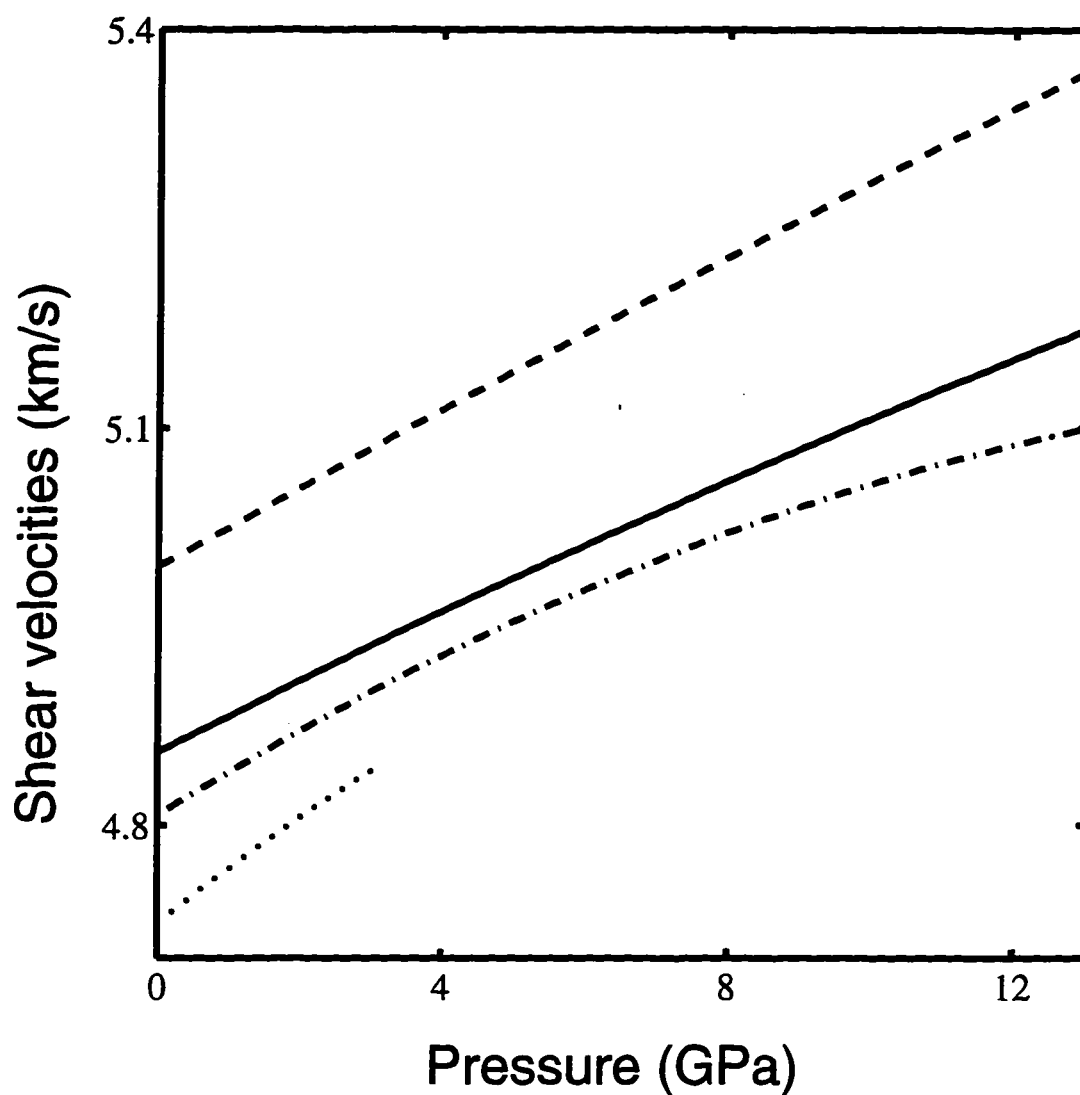


Figure 3.17 Shear sound velocities of olivine, opx and garnet

Aggregate-averaged shear wave velocities in a pyrope-rich garnet [Chai et al., 1996a] (dashed curve), Kh-opx (solid curve), San Carlos olivine [Zaug et al., 1993] (upper broken curve), and bronzite [Webb and Jackson, 1993] (lower dotted curve) as a function of pressure.

Chapter 4

Thermal Diffusivity of Mantle Minerals

4.1 Introduction

The thermal diffusivity tensors at ambient pressure and temperature of three silicate mineral phases abundant in the upper mantle (San Carlos olivine $[\text{Mg}_{0.89}\text{Fe}_{0.11}]_2\text{SiO}_4$, Kilbourne Hole orthopyroxene $[\text{Mg}_{1.67}\text{Fe}_{0.17}\text{Al}_{0.10}](\text{Si}_{1.87}\text{Al}_{0.13})\text{O}_6$ and a garnet of intermediate composition $\text{Py}_{51}\text{Al}_{33}\text{Gr}_{16}$) are reported. The extension to high pressure and temperature of the experimental technique employed here is discussed and, for olivine, data at high pressure are also reported. The diffusivity in the two orthorhombic minerals is highly anisotropic, the components of the tensor along the a, b, and c crystallographic axes, in units of mm^2/sec , being [2.16 1.25 1.87] in the case of olivine and [1.26 1.05 1.66] in the case of the orthopyroxene. The isotropic thermal diffusivity in garnet is $1.06 \text{ mm}^2/\text{sec}$. The experimental uncertainty is approximately 2%. The pressure dependence of thermal diffusivity is approximately 4% per GPa. The relation of thermal to elastic anisotropy is briefly considered. A model incorporating elastic anisotropy, anharmonicity described by acoustic Grüneisen parameters, Brillouin zone structure, and the increased phase volume for the scattering of short wavelength phonons provides a qualitatively reasonable description of the thermal diffusivity anisotropy. Since both olivine and orthopyroxene are aligned by flow deformation processes, the upper mantle is expected to be thermally anisotropic.

4.2 Experiment and results

4.2.1 Samples

The same garnet and opx used for experiments in Chapters 2 and 3, and a San Carlos olivine are used in this experiment. Measured lattice parameters and densities of these samples are reported in Table 4.1 as are the specific heats, determined by *Sumino and Anderson* [1984]. Elastic data at high pressure for these samples are reported elsewhere ([*Chai et al.*, 1996a; *Chai et al.*, 1996b; *Zaug et al.*, 1993]). Three slabs were cut nominally normal to the crystallographic axes for the olivine and pyroxene samples. An off-axis slice through the garnet crystal had a surface normal orientation of approximately [1 2 3]. Sample orientations were determined to 0.2° by x-ray precession camera analysis. The samples were polished to a thickness of 0.5 mm with plane, parallel faces.

4.2.2 Experimental techniques

The experimental technique, ISS, has been discussed in general in Chapter 1. The samples studied here are optically thin in the sense that, if μ is the optical absorption coefficient and L the thickness of the sample, then $\mu^{-1} \gg L$. However, the samples are all thermally thick, that is $L \gg d$. For the ambient pressure experiments $L/d \geq 150$, at high pressure $L/d \approx 20$. In these cases, the periodic distribution of temperature created by the excitation process relaxes to uniformity by one-dimensional thermal conduction. The rate constant, r , and relaxation time, τ , for the exponential decay of the thermal grating are

$$r = \frac{1}{\tau} = \frac{4\pi^2 D}{d^2} + A \quad (4.1)$$

where thermal diffusivity D is equal to thermal conductivity divided by the heat capacity per unit volume and the radiative contribution, A , is discussed below. Since the scattered intensity is proportional to the square of the amplitude of the temperature grating, the directly observed decay rate is $2r$. The variation of r with the angle of intersection, specified by Equations. (1.1) and (4.1), serves to distinguish one-dimensional thermal diffusion from other relaxation processes (i.e. the diffusional relaxation rate must be proportional to the square of the inverse of the grating spacing).

In a uniform sample that is optically thin at wavelengths near the peak of the emission curve at the temperature of the experiment, the surroundings serve as an effectively infinite heat bath initially in a steady state with respect to the exchange of energy with the sample. The effect of radiative transport (for small laser-induced perturbations in T) is then to add to the diffusion equation a local relaxation rate proportional to the temperature excursion at each point in the sample. In such circumstances, the constant A (in Equation (4.1)) depends both on the geometry and material parameters governing the rate of radiative transfer. When the inverse optical absorption coefficient is small compared to the grating spacing, and radiative emission is sufficiently intense to make a significant contribution to D , Equation (4.1) will remain an adequate description. In any case a plot of r versus d^{-2} serves to determine when thermal diffusion is an appropriate description of thermal transport. Since the optical absorption coefficient is small for the samples studied here, the diffusive process observed in these experiments is associated with lattice

contributions to thermal transport and the radiative transport, A , is negligible.

The orientation of the thermal grating with respect to the crystallographic axes may be varied by rotating the sample or, for work at high pressure and temperature, the entire cell or furnace about an axis normal to the sample face. Time domain records for scattering from thermal gratings directed along the a , b , and c axes of a crystal of San Carlos olivine are given in Figure 4.1. Thermally induced elastic strain also excites counterpropagating elastic waves. The acoustic response is responsible for the weak and undersampled oscillatory behavior seen at short delay times in Figure 4.1. The corresponding logarithmic plot (Figure 4.2) indicates that, at times longer than 30 ns when the acoustic waves have spread beyond the area illuminated by the probe, a single relaxation time satisfactorily describes the data. The relaxation rates derived from data such as those in Figure 4.2 are plotted as a function of d^{-2} in Figure 4.3. Equation (4.1) is shown to give a good account of the results.

The symmetry of olivine and orthopyroxene requires that the thermal conductivity and diffusivity tensors referred to a coordinate system with the Cartesian x , y , and z axes along the crystallographic a , b , and c axes be diagonal:

$$\mathbf{D} = \begin{vmatrix} D_{xx} & 0 & 0 \\ 0 & D_{yy} & 0 \\ 0 & 0 & D_{zz} \end{vmatrix} \quad (4.2)$$

Garnet is thermally isotropic. Measured diffusivities in olivine are plotted as a function of crystallographic direction in Figure 4.4 and the principal components of \mathbf{D} , determined through least-square fits of the data,

are given in Table 4.2. The elements of the thermal conductivity tensor can be calculated with the aid of the data in Table 4.1. Data of *Kanamori et al.* [1968] reported for the *c*-axis of olivine, agree with the current *c*-axis value within 0.8 % and an extrapolation of the high temperature *b*-axis data of *Schatz and Simmons* [1972] is also in agreement with the current olivine *b*-axis result.

The anisotropy observed here for olivine, $D_b/D_a = 0.578$ and $D_c/D_a = 0.871$) is comparable with that seen in α -quartz where $D_b = D_a$ and $D_a/D_c = 0.53$ and in rutile where $D_a/D_c = 0.57$ and is considerably larger than that of sapphire where again $D_b = D_a$ and $D_a/D_c = 0.93$). The value of D_c/D_a for olivine determined here is very close to that of 0.869 found by *Schärmeli* [1982], *Schärmeli* has However reported a larger value of D_b and consequently less anisotropy for San Carlos olivine at ambient temperature and 2.5 GPa.

4.2.3 Experimental errors, possible advantages and limitations of the technique

The time-domain data of Figures 4.1 and 4.2 give relaxation times that are reproducible to better than 2%. Deviations from linearity in plots of r versus d^{-2} in Figure 4.4 are consistent with this error. Data were taken over more than two order of magnitude of scattered intensity, therefore non-linearity in the detector and associated electronics is potentially a problem. However, the photomultiplier voltage and the intensity of the excitation and probe pulses were varied without evidence of error from this source

At very large grating spacings, where d is no longer small with respect to the thickness of the sample, positive deviations from a linear variation of r with d^{-2} are to be expected and have been observed. Unless one is prepared to correct numerically for surface effects, such data do not usefully contribute to the determination of D . At small grating spacings thermal decay times and

acoustic damping may not be completely separated. In such cases a fit of the time domain record to the form

$$I = \left(A_{th}e^{-rt} - A_{ac}C(t)e^{-\gamma t} \cos \omega t \right)^2 \quad (4.3)$$

where A_{th} is the amplitude of the thermal grating, A_{ac} the amplitude of the acoustic grating, ω the circular acoustic frequency ($\omega=2\pi f$) and γ the temporal acoustic absorption coefficient, will in many circumstances permit the calculation of r .

The apparent decay of the acoustic modulation stems in part from true absorption and in part from purely geometric attenuation as the acoustic disturbance propagates beyond the volume illuminated by the probe. In crystals, γ is small and the acoustic attenuation, $C(t)$, due to runout is determined by the distance traveled by a wave in time t . At fixed angle of intersection the wavelength is the same in all samples (Equation (4.3) in *Zaug et al.* [1992]). Therefore, at constant geometry, the apparent damping per acoustic cycle associated with runout is also the same in all samples. The decrement per cycle in the amplitude of the acoustic oscillation in a material with negligible absorption (glass) then serves to determine $C(t)$ in an absorbing medium [*Zaug et al.*, 1994].

The parameters that are to be deduced from the record are then the time dependent amplitude and frequency of the acoustic oscillation and the thermal decay time r . The separation of the oscillatory and exponential components is not difficult; moreover the frequency derived from a long record in a material where the velocity is well known also provides an accurate measure of the angle of intersection of the excitation pulses. Separation of

multiple exponentials is less straightforward. Long-lived excited electronic states that produce gratings in the imaginary part of the index of refraction comparable in lifetime to the thermal gratings may set serious limitations to these techniques in some samples.

This experimental approach requires suitable optical absorption at some conveniently accessible excitation wavelength where electronic and vibrational relaxation times do not overlap with thermal relaxation throughout the geometrically practical range of angles. Given that diamond remains transparent from the near infrared to the tripled Nd:YAG wavelength (355 nm) a large variety of materials, among them, for example, the silicate and oxide minerals, are amenable to study by these techniques. The scattered probe is both monochromatic and well collimated. At high temperature a pinhole, a notch filter, or if necessary a Fabry Perot, will efficiently discriminate against the thermal radiation from the sample. The capacity to vary the length scale of the grating will permit separation of lattice and radiative contributions to transport. The absence of any requirement for physical contact with the sample is also in many circumstances an advantage.

4.3 Relations between thermal and elastic anisotropy

Even an approximate microscopic description of lattice thermal transport in crystals rests on knowledge not only of the acoustic dispersion relations but also on the anharmonic contributions to the internuclear interaction potential *Ziman* [1962]. The cubic and quartic terms in the potential are constrained, but not fully characterized by the measured density dependence of the elastic constants. It is therefore an experimental approach to the determination of quantities not yet accessible to *a priori* prediction that is of

primary interest here. However in circumstances where measurement is also difficult, empirical relations with some basis in approximate theory are also of interest.

Ideally a microscopic theory of thermal transport would account for the value of all three independent elements of the diffusivity tensor. If C_i is the heat capacity (per unit volume) associated with the i th mode, the contribution, K_i , of a single phonon to the lattice thermal conductivity, K , is approximately expressed as

$$K_i = \frac{1}{3} C_i u_i \lambda_i = \frac{1}{3} C_i u_i^2 \tau_i \quad (4.4a)$$

where u_i , λ_i , and τ_i are respectively the group velocity, the mean free path and the mean lifetime of the phonon in question. The anisotropy of longitudinal velocities of olivine and opx are plotted in Figure 4.5 in comparison with Figure 4.4. The j th diagonal element of thermal diffusivity in an anisotropic crystal can then be written as a sum over all wavevectors and branches

$$D_{jj} = \frac{1}{c_p} \sum C_i u_i \lambda_i \cos^2 \theta_{ij} = \frac{1}{c_p} \sum C_i u_i^2 \tau_i \cos^2 \theta_{ij} \quad (4.4b)$$

where θ_{ij} is the angle between the group velocity of the i th phonon and the j th Cartesian axis and c_p is the heat capacity per unit volume.

At low temperature, at which only the long waves of the acoustic branches are excited, the velocity of elastic waves is an adequate approximation for velocities of the phonons which make the largest contributions to D

and K . At higher temperature, knowledge of the dispersion relations of all branches as well as of the anharmonic potential is required. The structures of the mantle minerals are too complex for an explicit discussion in terms of Equation (4.4b) to be practical. However, since velocities of long acoustic waves are directly measurable in a geophysical context and the pressure dependence of the velocity is a qualitative measure of anharmonicity, an empirical or approximate theoretical correlation between velocities, the pressure derivatives of velocities, and the elements of D is of some utility.

The elastic constants of these samples have been measured as a function of pressure. The equation of state and the velocity of sound in any crystallographic direction are implicit in these measurements. Although there is no *a priori* reason why mean-free times τ should be isotropic, the simplest procedure based on Equation (4.4b) is to estimate the anisotropy in D as the anisotropy in sound velocity, c , where the average $\langle c_i^2 \cos^2 \theta_{ij} \rangle$ is over the three acoustic branches and all directions of propagation. In Table 4.3 the result of such an approximation (second row) is compared with experiment (first row). The relative magnitudes of the diagonal components in olivine are correctly accounted for (i.e., $D_a > D_c > D_b$). However, the predicted relative values of the transport coefficients along the a and c axes of orthopyroxene are the reverse of what is observed.

A number of approximate forms have been offered for the mean free path or mean relaxation time in isotropic crystals under conditions where Umklapp processes dominate the thermal resistivity. *Leibfried and Schlomann* [1954] suggested

$$D \approx \frac{r \langle c^3 \rangle \sqrt[3]{V^0}}{c_p g^2 T} \quad (4.5a).$$

where the Grüneisen parameter, γ , of a mode of frequency ν is defined by $\gamma = -d \ln \nu / d \ln V$ and V^0 is the volume per atom. *Roufosse and Klemens* [1973] also argued that the mean free path and hence the high-temperature thermal conductivity, varies as γ^2 , their explicit expression for the mean free path in the case of an isotropic crystal being

$$\lambda = \frac{\sqrt{2} M c^4}{3 kT 4\pi^3 \nu^2 \gamma^2 \sqrt[3]{V^0}} \quad (4.5b)$$

where M is the mass per atom. In the absence of dispersion, 4.5b becomes

$$\lambda = \frac{\sqrt{2} M c^2}{3 kT 4\pi^3 y^2 \gamma^2 \sqrt[3]{V^0}} \quad (4.5b)$$

where y is the phonon wave vector. The Grüneisen parameters of long wave acoustic modes can be deduced from the pressure-dependence of the elastic constants. The result of approximating the anisotropy in τ or λ by the anisotropy in γ^2 for long waves is given in the third row of Table 4.3. The agreement with experiment is significantly improved when the anisotropy in the relaxation time is thus approximately taken into account.

A literal interpretation of Equation (4.5b) suggests that the anisotropy D_{ii}/D_{jj} is given by the ratio S_{ii}/S_{jj} of sums in the form:

$$S_{jj} = \sum_{y_1 y_2 y_3} \cos^2 \theta_i \frac{c^3}{y^2 \gamma^2} C(\nu) \quad (4.6)$$

where y_i represents the m th component of the wavevector, y is the magnitude of the wavevector, $C(\nu)$ is the heat capacity of a harmonic oscillator of frequency ν at the temperature in question and θ_i is the angle between the wavevector specified by y_1, y_2 and y_3 and the i th Cartesian axis. The sum extends over the Brillouin zone and the Grüneisen parameter as a function of y_1, y_2 and y_3 is again calculated from the pressure dependence of the elastic constants. The result of such a calculation, for orthopyroxene and olivine, is given in the fourth row of Table 4.3. In this case, where the zone structure and the increased phase volume for the scattering of short wavelength phonons is approximately taken into account, the predicted order of the sizes of the three elements of the diffusivity tensor is correct for both olivine and orthopyroxene.

4.4 Geological implications

In the oceanic lithosphere lattice preferred orientation (LPO) develops in mantle peridotites undergoing progressive simple shear deformation via dislocation creep. As shown in Figure 4.6, olivine [100] axes and the [001] axes of orthopyroxenes, which are the directions of high thermal diffusivity for these two minerals, should align parallel to the major axis of the strain ellipsoid. In contrast, the axes of smallest thermal diffusivity for olivines and intermediate thermal diffusivity for orthopyroxenes are expected [Ribe and Yu, 1991], and observed [Nicolas and Christenson, 1987] to be oriented vertically. Thus, the oceanic lithosphere is likely to be both thermally as well

as seismically anisotropic. This thermal anisotropy can be caused by either the lattice component or the radiative component of the thermal diffusivity, or both, depending upon the grain size, the temperature and the pressure.

The radiative component is defined as:

$$K_r = \frac{\frac{16}{3} n^2 \sigma T^3}{\langle \varepsilon(P, T) \rangle} \quad (4.7)$$

where n is the index of refraction; σ , the Stefan-Boltzmann constant; T , temperature; and ε , the inverse of the mean free path of a photon, or the absorption coefficient. Anisotropy of the radiative component mostly comes from the anisotropy of the mean free path of photon. At 1000°C, the mean free path of a photon in olivine is about 1~2 mm [Schatz and Simmons, 1972].

For grains of the size of the mean free path of a photon, $L \sim \varepsilon^{-1}$, the mean free path is limited by the grain boundaries of the grains due to scattering. Therefore the anisotropy of heat transport due to radiation is strictly geometric. In this case, the ellipsoidal strain of the grains with preferred crystallographic orientation in the lithosphere may contribute to the anisotropy. The mean free path of photon is a function of both the temperature and the wavelength, but much less of the pressure.

For grains of size much larger than the mean free path of photon, the anisotropy of the mean free path can be experimental determined by the absorption. At ambient conditions, olivine has strong absorption peaks at 1 μ due to Fe²⁺ and at long wavelength above 3 μ m due to its vibrational bands Burns [1968]. For light of polarization parallel to a , the absorption is at least twice as strong as light with polarization parallel to b or c . However, the peak

at 1 μm corresponds to a black body radiation of 2700°C which is about 700°C higher than upper mantle temperature.

The peaks are broadened at high temperature (1300°C) [Fukao *et al.*, 1968]. The broadening causes absorption between 1 μm and 3 μm to increase by more than a factor of 100. This keeps K_r from going up with T^3 . The absorption in this region does not show much dependence on the polarization [Aronson *et al.*, 1970]. The effect of pressure, on the other and, is to shift the peak at 1 μm to the even shorter wavelengths [Shankland, 1970] At 15 GPa, the shift is about 0.1 μm , which is an order of magnitude smaller than the broadening caused by the temperature effect.

Temperature and pressure effects on the lattice component are not well understood. On one hand, the phonon velocities increase with pressure. On the other hand, pressure and temperature may increase the anharmonicity of the minerals, which leads to more scattering of phonons. The analysis of Sharmeli [1982] suggests that $K=1/(a+bT)$. Therefore the anisotropy might decrease with temperature, and the thermal effect due to preferred orientation will be reduced. But the experiment of Sharmeli may be in error. Their experiments could not completely separate the lattice component from radiative, since the sample thickness (2 mm) was comparable to the mean free path of a photon at the temperature of the experiments. Also the small aspect ratio (length to thickness, 4:1) of the sample may have introduced significant uncertainties.

The effects, due to the thermal anisotropy resulting from LPO, on the temperature profile and on the oceanic basin contraction has been investigated with a simplistic model. In this model, thermal diffusivity depends neither on pressure nor on temperature, except that the temperature

determines the thermal boundary of the oceanic lithosphere within which the LPO is frozen in. The 7~8% of seismic azimuthal anisotropy observed in the oceanic lithosphere [Farra and Vinnik, 1994; Hess, 1964; Kuo and Forsyth, 1992; Nishimura and Forsyth, 1989] can be explained by the reorientation of these minerals in the mantle, assuming a composition of 70% olivine and 30% orthopyroxene. Thus, the model mantle has a isotropic mantle overlain by a lithosphere with a smaller thermal diffusivity. This thermal boundary layer is taken at 800°C, which is progressively thickened away from spreading centers (Figure 4.6).

In the calculation, a half space cooling model was used. An averaged value of 5 kW/m was used for the mantle and a value for 70% olivine oriented along b and 30% opx oriented along a was used. The temperature profiles are plotted in Figure 4.7, the layered mantle (solid line) is slightly warmer than the isotropic mantle (dashed line). The thermal expansion of 2×10^{-5} was used with the thermal profiles to integrate to get the contraction of the oceanic basin. The results are plotted in Figure 4.8. At 150 million years, the contraction due to cooling for the layered mantle is about 0.5 km less contracted than the isotropic mantle (Figure 4.8), which is about the same size of the observed deviation of oceanic basin depth from the root t trend (square root of time) [Schroeder, 1984].

4.5 Illustrations

4.5.1 Tables

Table 4.1 Data for olivine, opx and garnet

Lattice parameters, densities, and specific heats under ambient conditions.

	Olivine	Orthopyroxene	Garnet
a in Å	4.76	18.25	11.55
b in Å	10.22	8.80	
c in Å	5.99	5.20	
r in g/cm ³	3.362	3.329	3.829
c_p in $\frac{j}{gK}$	0.809	0.792	0.812

Table 4.2 Thermal diffusivity for olivine, opx and garnet

Components of the thermal diffusivity tensor for olivine, orthopyroxene and garnet under ambient conditions. Numbers in parentheses are uncertainties based on least square fits to the data.

	Olivine	Orthopyroxene	Garnet
D_a (mm ² /s)	2.16 (4)	1.26 (2)	
D_b (mm ² /s)	1.25 (2)	1.06 (2)	1.02 (3)
D_c (mm ² /s)	1.87(4)	1.66 (2)	

Table 4.3 Thermal anisotropy data and calculations

Anisotropy of the thermal diffusivity in olivine and orthopyroxene (opx) related to elastic anisotropy by various approximate methods.

	$\frac{D_b}{D_a}$ olivine	$\frac{D_c}{D_a}$ olivine	$\frac{D_b}{D_a}$ opx	$\frac{D_c}{D_a}$ opx
Exp.	0.578	0.862	0.840	1.32
c^2	0.871	0.906	0.946	0.997
$\frac{c^3}{g^2}$	0.719	0.847	0.854	0.990
$C \frac{c^3}{g^2 k^2}$	0.421	0.661	0.918	1.165

4.5.2 Figures

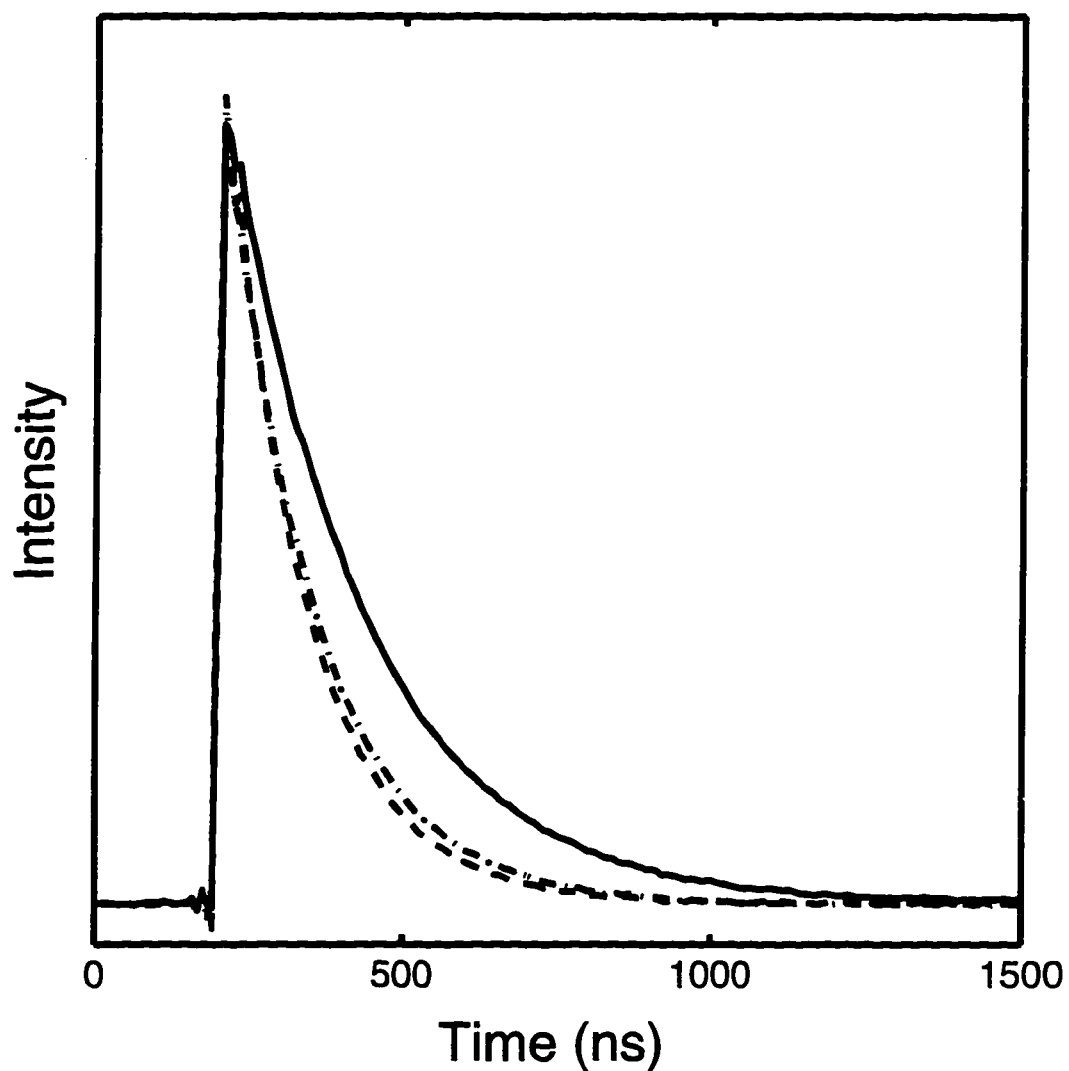


Figure 4.1 Thermal decay signal of olivine.

Time-domain records for scattering from thermal gratings directed along the *a* (dashed line), *b* (solid line) and *c* (broken) axes of a single crystal of olivine at 25°C and 1 bar.

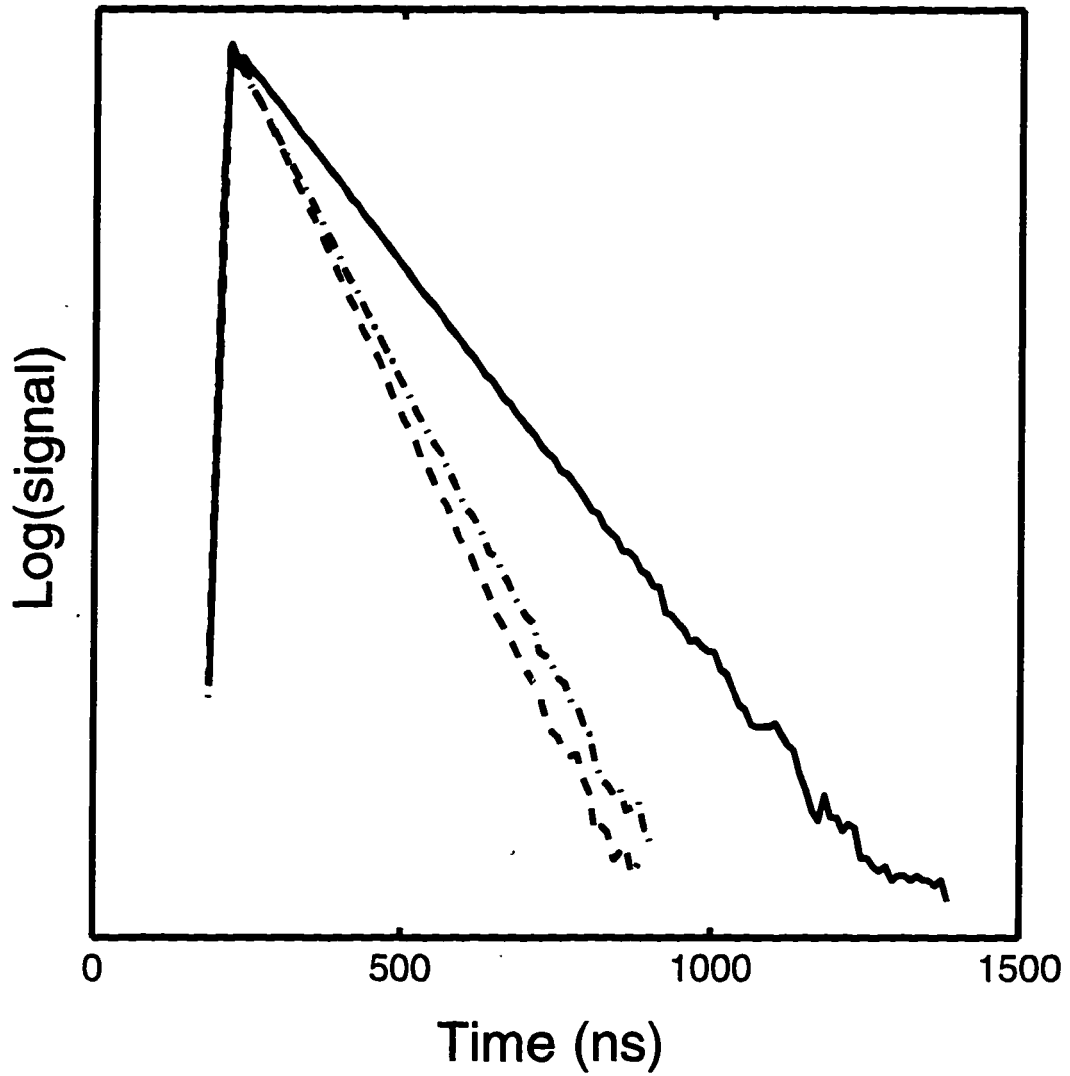


Figure 4.2 Log plot of Figure 6.1

Logarithm of signal strength vs . time for the data in Figure 6.1. The straight lines indicate the decay is exponential (dashed line, *a*; solid line, *b*; broken, *c*).

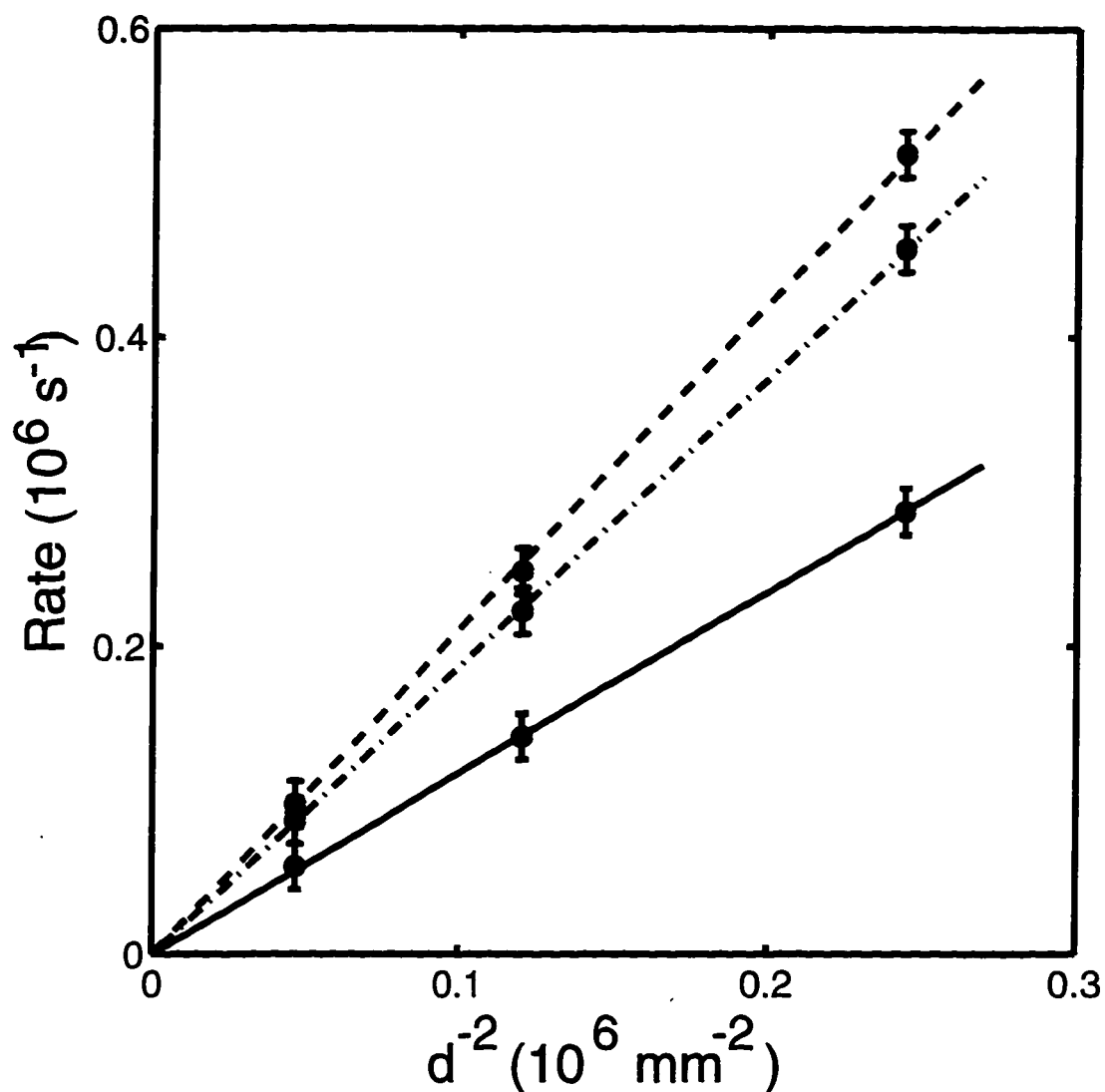


Figure 4.3 Thermal decay rate as a function of grating spacing

Relaxation rate versus the inverse square of the grating spacing for the decay of thermal gratings along the *a* (dashed line), *b* (solid line) and *c* (broken line) axes of a single crystal of olivine at 25°C and 1 bar. Linearity indicates that one-dimensional diffusion is the primary relaxation mechanism. Error bars give standard errors based on repeated measurements.

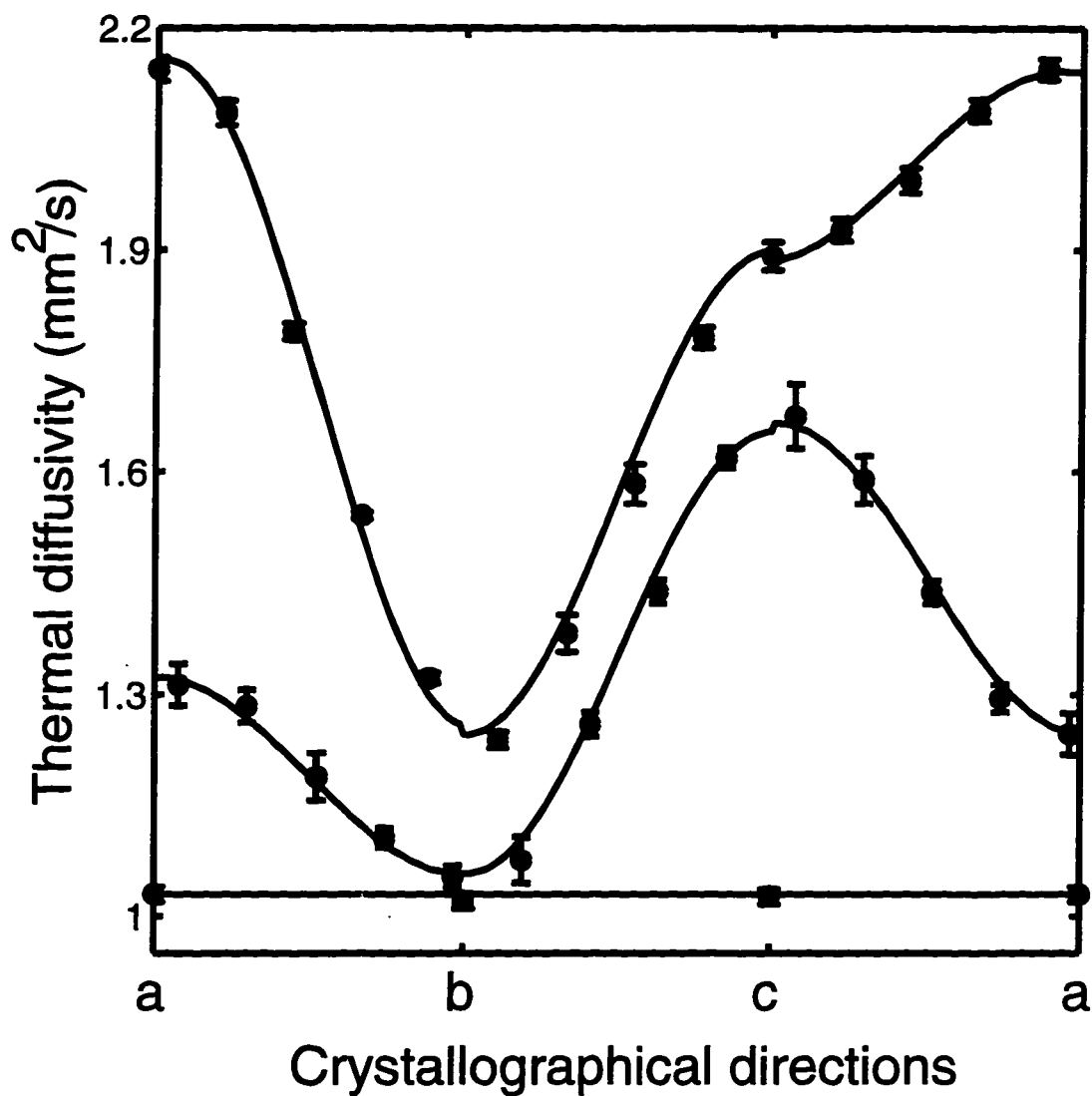


Figure 4.4 Anisotropy of thermal diffusivities

Thermal diffusivity as a function of crystallographic direction in olivine, orthopyroxene and garnet at 25°C and 1 bar. The *b-a* segment represents the result of a 90° rotation of the grating about the *c* axis from *b* to *a*, the *b-c* segment rotation about the *a* axis and the *a-c* segment rotation about the *b* axis. Error bars are the uncertainties in the fits to the data of Figure 4.

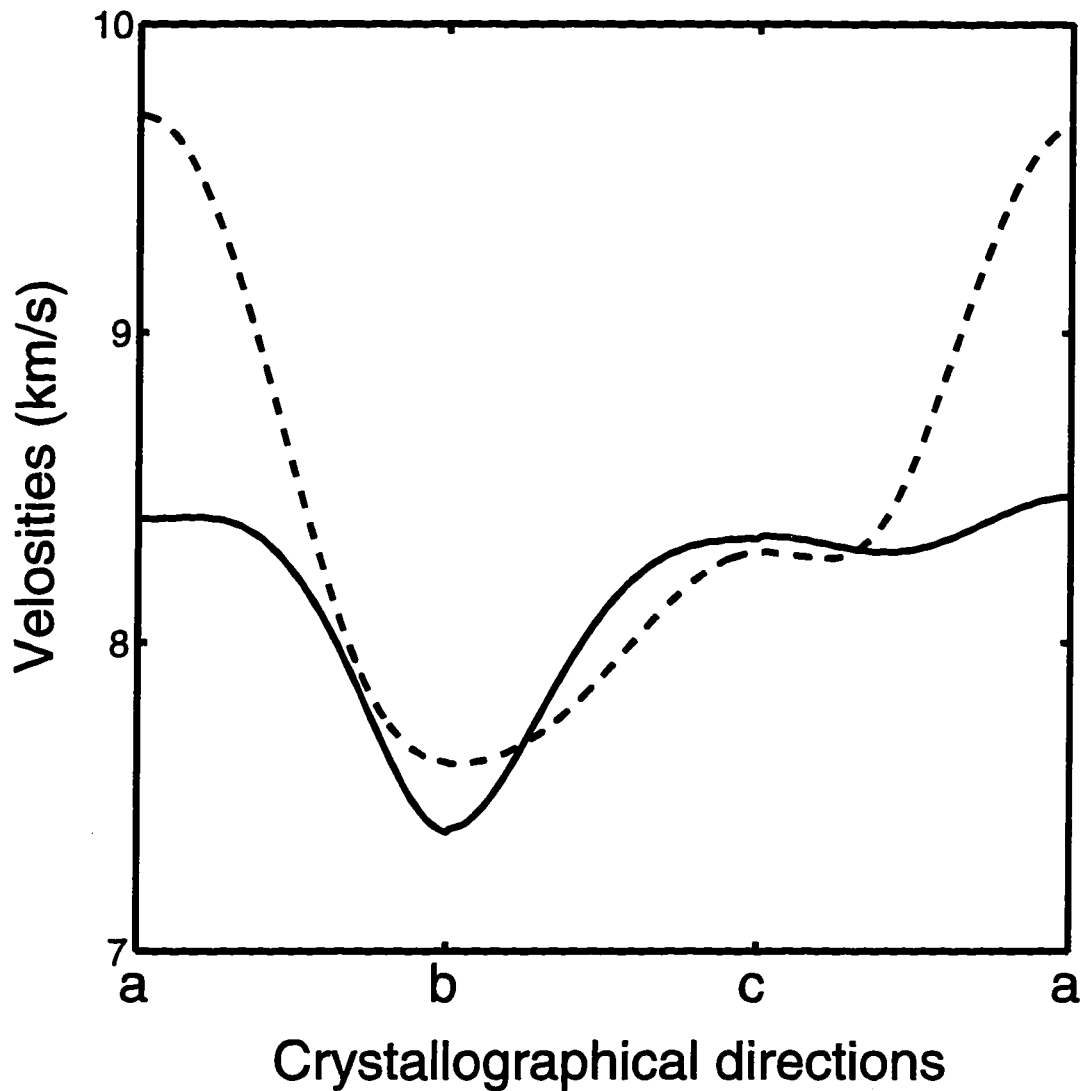


Figure 4.5 Anisotropy of longitudinal sound velocities of silicates

The anisotropy of longitudinal velocities of opx (solid line), and olivine (dashed line). The elastic constant of opx in Chapter 3 and those of olivine by *Zaug et al.* [1993] were used for the calculation. The correlation between the longitudinal velocities and the thermal diffusivities shown in Figure 4.5 and Figure 4.4 is apparent.

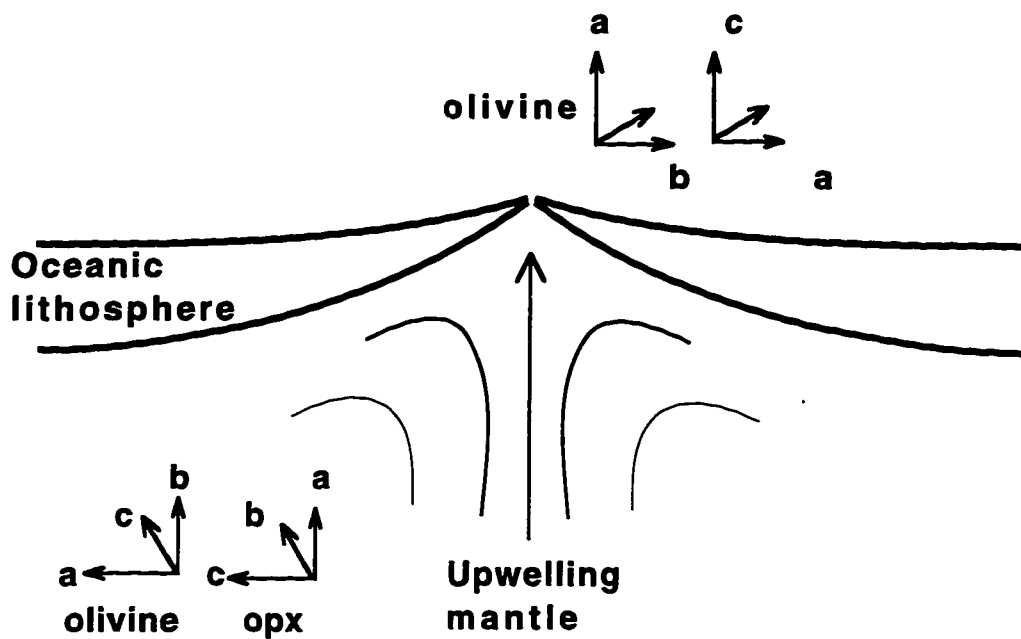


Figure 4.6 Schematic diagram of mid-ocean ridge

Schematic diagram of the recrystallization of the convecting mantle near mid-oceanic spread center. The LPO of olivine and opx with respect to the direction of flow is shown after *Ribe and Yu* [1991], and *Nicolas and Christenson* [1987].

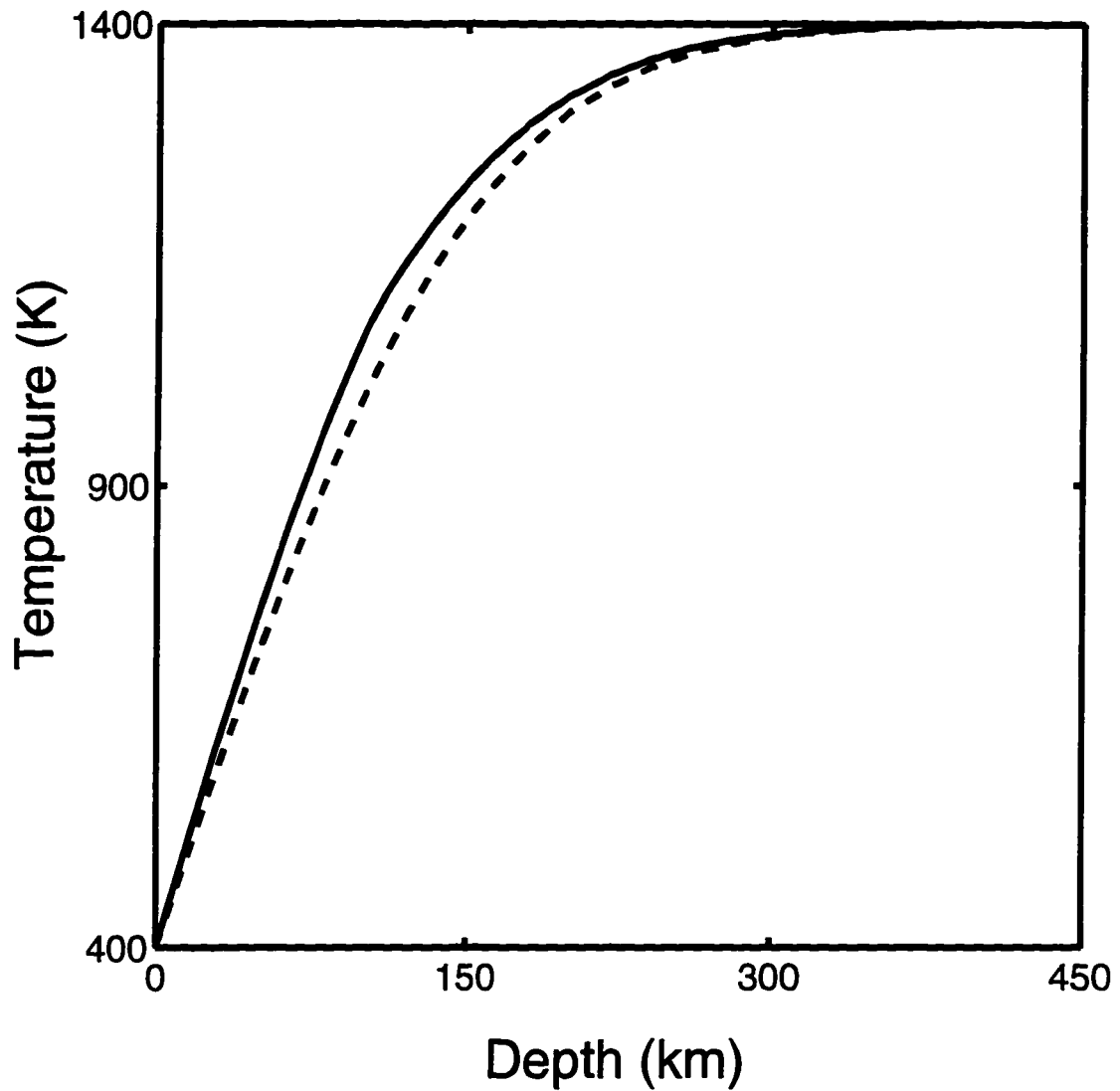


Figure 4.7 Temperature profile of the oceanic lithosphere

Temperature profile of the oceanic lithosphere as a function of depth at 140 million years. The solid line is calculated from a layered half space model. The dashed line is from an isotropic half space model.

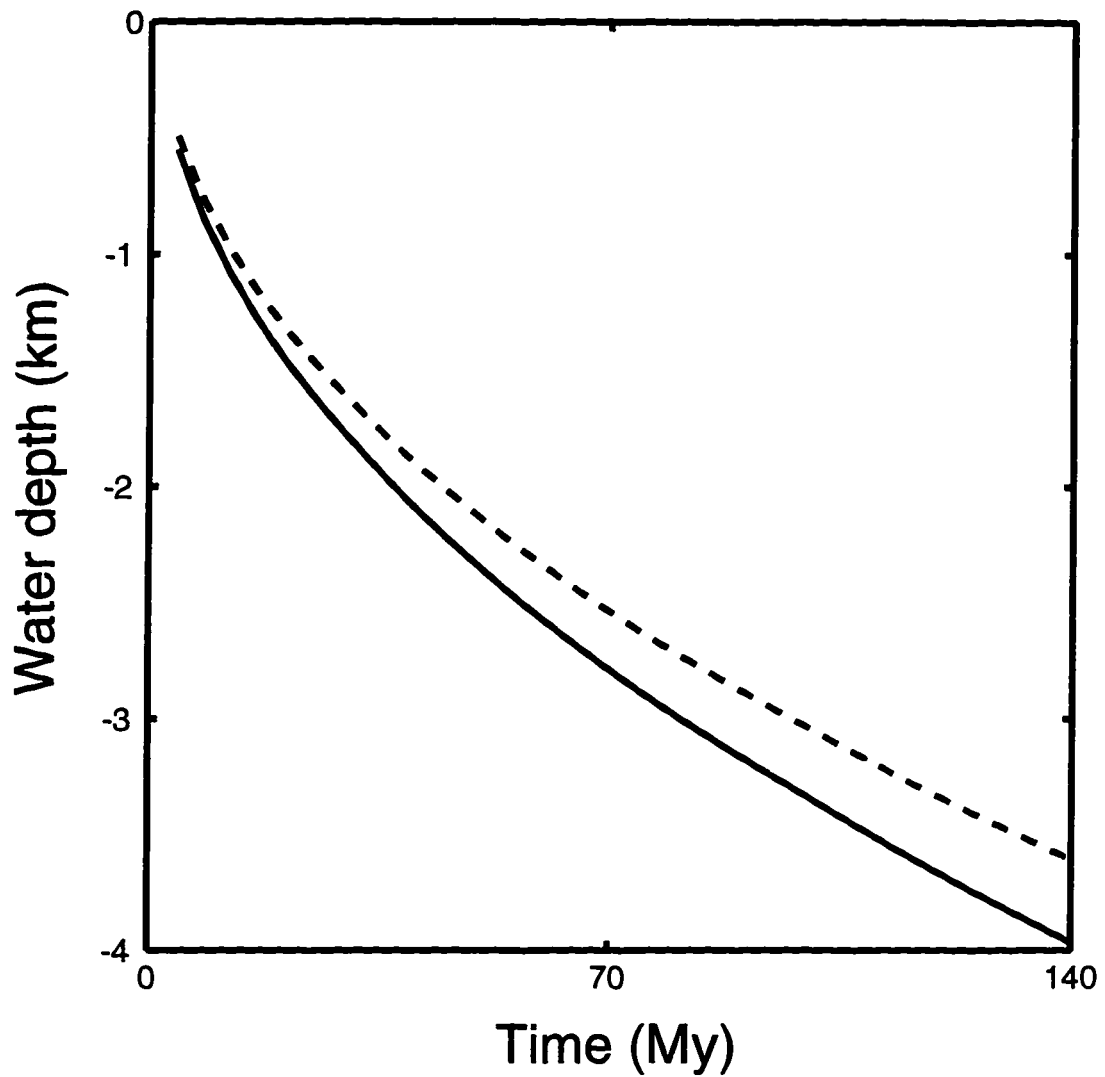


Figure 4.8 Water depth of the ocean-floor as a function of time.

The solid line is calculated from a layered half space model. The dashed line is from a isotropic half space model.

Chapter 5

Effects of Static Non-hydrostatic Stress on the R Lines of Ruby Single Crystals and Their Yield Strength

5.1 Introduction

Ruby is commonly used as a pressure calibrant in the diamond anvil cell (DAC) [Barnett *et al.*, 1973; Mao *et al.*, 1978]. Under hydrostatic conditions at room temperature, the ruby R-line fluorescence has a redshift with increasing pressure, while the R_1 - R_2 line separation (splitting) remains almost constant [Bi *et al.*, 1990]. However, in shock-wave (pure uniaxial strain) experiments [Sharma and Gupta, 1991; Shen and Gupta, 1993], the R_1 - R_2 splitting increased for ruby strained along the a -axis, and decreased when strained along the c -axis. Shen and Gupta [1993] argued that, in the reference frame of an octahedral Cr^{3+} site, trigonal and rhombic distortions change both the mean shift and splitting, tetragonal distortion causes splitting only. For the higher-energy R_2 line, distortion effects cancel, and the overall change in fluorescence wavelength is due to the volume change as in hydrostatic compression. Thus grounded on a crystal field analysis, they concluded that the R_2 line shift varies with pressure (i.e. the trace of the stress tensor) even in the presence of non-hydrostaticity. In contrast, the R_1 line shift is sensitive to inhomogeneous strain (i.e. deviatoric stress).

Since no pressure medium can remain completely hydrostatic at high pressures in DAC experiments [Mao *et al.*, 1986; Piermarini *et al.*, 1973] a better understanding of the ruby R line behavior under static conditions of deviatoric stresses is important. Okai *et al.* [1986] and Fujishiro *et al.* [1988] demonstrated that the shift of the R_1 of oriented ruby crystals depends on the direction of applied stress while the R_2 line shift has little dependence on the

stress direction. They parametrized R-line shifts as a function of principal stress along a -axis and c -axis.

R-line shifts and splittings of single ruby crystals under controlled deviatoric stress in the DAC is reported here. Stress tensors for the sample were calculated based on both a free-slip and a no-slip boundary approximation. The free-slip boundary condition gives a better account of the observed spectra. The line splittings versus stress state are compared with the theoretical [Shen and Gupta, 1993] and empirical [Fujishiro *et al.*, 1988] predictions.

5.2 Experimental technique

Single crystal ruby of the same source as in Sharma and Gupta [1991] were used. A 0.4 wt % of Cr^{3+} was estimated for the crystals. Thin oriented ruby plates were cut normal to either the a -axis or the c -axis. The plates were polished to a thickness of 50 μm with plane and parallel surfaces. Disks (200 μm in diameter) were cut using a coring drill.

The experimental arrangement is schematically shown in Figure 5.1. A single sample disk was placed in the chamber of a metal gasket between the diamonds. The diameter of the gasket chamber was about 250 μm and that of the diamond culets was 550 μm . The DAC was either cryogenically loaded with Ar or loaded with a methanol-ethanol-water solution (16:3:1 by volume) as a quasi-hydrostatic pressure medium. Micron-sized ruby chips were distributed in the pressure medium. The sample was first hydrostatically compressed until the surfaces of the diamonds came into direct contact with the sample. Deviatoric compression developed as the diamonds were further forced against the disk. The principle stresses in these experiments are an

axial load stress σ_1 and the stress σ_3 parallel to the diamond faces. At the interface between the sample and the pressure medium, σ_3 is equal to the confining pressure. Elastic anisotropy of ruby is small and is ignored. The mean stress (pressure) within the sample is taken to be $(\sigma_1+2\sigma_3)/3$ and deviatoric stress is $\sigma_1-\sigma_3$. Care was taken to elastically load the disks. Experiments were terminated on visual indication of yield or failure. Different confining pressures were achieved by varying the initial thickness of the pre-indented gasket. Clearance between the sample and the gasket chamber side wall insured that the sample was supported by the pressure-transmitting medium rather than the more rigid gasket material.

A 1 to 10 mW He-Cd laser (442 nm wavelength) beam was focused to a 10 μm spot on the ruby. Fluorescent light from the ruby was collected through a microscope, dispersed with a monochromator, and detected with a photomultiplier. Spectra were fit using a Gaussian-Lorentzian parameterization [Munro *et al.*, 1993] to determine positions and widths of both R_1 and R_2 fluorescence lines. The DAC was placed on a translation stage and profiles across the ruby disks were measured on a 20 by 20 μm grid. Results are interpreted as representing the vertically averaged properties of the ruby at each point.

In separate "sandwich" experiments, *a*-normal and *c*-normal disks were stacked together and loaded in the DAC. A thin Au foil sandwiched between the two ruby disks served to block the laser beam. The fluorescence spectra of each disk were separately measured from each side of the DAC.

Pressures are usually calibrated against the wavelength shift of the more intense R_1 line with respect to its ambient position [Barnett *et al.*, 1973; Mao *et al.*, 1978]. In the current study, apparent pressures were determined

from both R_1 and R_2 line shifts using the same formula with an appropriate substitution of wavelengths. Spectra from the small ruby chips in the pressure medium served to determine the confining conditions.

5.3 Results and discussion

R₁-R₂ splitting

Figure 5.2 shows a pair of spectra for *a*-normal and *c*-normal ruby disks taken at adjacent points on either side of the gold foil in the "sandwich" experiment. Pressure within the confining medium was 3.80 GPa. In Figure 5.3 apparent pressure (face value determined by the shifts with respect to the 1 bar pressure positions) profiles are shown based both on the R_1 and R_2 lines. One vertical axis shows the change in wavelength from 1 bar while the other gives the apparent pressure. Stress conditions appeared approximately uniform across the entire sample. Since the geometry of the experiment should lead to nearly identical stresses within the two ruby disks, the observed differences in the spectra must result from an anisotropic response of the R-line fluorescence to stress. The lower intensity R_2 lines for both the *a*-normal and *c*-normal disks lie at the same wavelength in Figure 5.2, in support of the [Shen and Gupta, 1993] conclusion that the R_2 line is little affected by non-hydrostatic strain. The R_2 pressure profiles in Figure 5.3 are nearly coincident across the entire disk, at an average pressure of 6.6 GPa. In contrast, the R_1 lines for the sandwiched *a*-normal and *c*-normal samples lie at different wavelengths. At a pressure of 1 bar the splitting of the R_1 - R_2 lines is 14.5 Å. In Figure 5.3 the *a*-normal splitting is about 20 Å while the *c*-normal splitting is about 12 Å. If incorrectly used to determine pressure, the

R_1 lines in Figure 5.3 systematically differ by almost 3 GPa, with c -normal spectra underestimating pressure and a -normal overestimating it.

Equation (9) of [Shen and Gupta, 1993] provides the means to calculate R_1 - R_2 splitting under a specified state of stress with known elastic constants. The original paper contains several typographical errors. The corrected form of equation (9) in Shen and Gupta [1993] and equation (2) in TABLE II of Sharma and Gupta are (1991):

$$\Delta = (\varepsilon_+ - \varepsilon_-)$$

$$= \left[\left(\frac{4K\zeta}{A} \right)^2 + 2 \left(\frac{4K_1\zeta}{A} \right)^2 \left| e_{x-}^* \right| + 4 \left| qe_{u-} - \frac{(12K_1Ke_{x-} + 6K^2)}{A} \right| \right]^{\frac{1}{2}}$$

and

$$e_{u+}(E) = -e_{u-}^*(E) = -\frac{1}{\sqrt{6}} \left[e_{xx} - e_{yy} - 2ie_{xy} + 22(e_{zx} + ie_{zy}) \right]$$

respectively.

The tensor stress state within a non-hydrostatically compressed sample depends on the external loads and boundary conditions. With free slip between the sample and the diamonds, stresses are uniform within the sample (the lateral stress σ_3 is everywhere equal to the confining pressure). Friction between the sample and the diamond surfaces leads to nonuniform stress states. No-slip is the limiting case.

Stresses for the no-slip boundary condition were calculated for a elastically loaded isotropic cylinder using an analytical model [Balla, 1960]. In this model, a cylinder is compressed between two infinitely rigid end plates. A friction factor between the sample and the end plates (varied from 0 to 1) corresponds respectively to free-slip and no-slip boundaries. The parameters

needed in the calculation are aspect ratio (height to diameter), Poisson's ratio, the average load stress, and the lateral stress on the sides of the cylinder. The parameters of the model can be directly measured in the experiments, with the exception of the average load stress. In the calculations, an isotropically average Poisson's ratio of 0.25 was used for ruby. The aspect ratio was 1:4 and the lateral stress at the cylinder surface was set equal to the confining pressure.

Except for free-slip boundary condition, the stress profiles across the cylinder are different with depth. In a sample calculation shown in Figure 5.4 to 5.7, the stresses are calculated, in a cylindrical coordinates, at a interval height of $\Delta H = 0.2$ (the total height of the cylinder is $H = 2$). In those figures, the vertically averaged values are also plotted. It is clear that only the shear stress S_{rz} changes significantly, the other stresses do not deviate significantly from their vertically averaged values. In the current experiments, only vertically averaged pressures are measured, so stresses in Figure 5.8 were integrated vertically over the top half of the cylinder. The average load stress was determined by trial and error such that the calculated pressures best match the observed pressures. For free-slip, the average load stress was 18 GPa, and for no-slip, the average load stress was 13 GPa.

Experimental data for both pressure (shift of the R_2 line) and deviatoric stress (R_1 - R_2 splitting) were obtained in a *c*-normal disk at a confining pressure of 7.35 GPa. The data are compared with predictions based on free-slip and no-slip. In Figure 5.8 an R_2 pressure profile is plotted (solid circles). As in Figure 5.3 radial symmetry was again observed. However, in this sample pressures dropped by almost 1 GPa from a central nearly constant pressure zone (11.5 GPa) in a 40 μm rim. Two possible reasons to account for the

deviation of pressure at the edge are: (1) sample preparation may have led to slight rounding of the surfaces near the edges and (2) plastic yielding may have occurred since local shear stresses are highest at the edges. In Figure 5.9, measured R_1 - R_2 splittings are shown at the same points given in Figure 5.8.

In Figure 5.8, the calculated stresses for no-slip (heavy lines) and free-slip (thin lines) boundary conditions are both in partial accord with the data. The no-slip profile, although similar to the measured profile, does show a systematic difference: the model profile has smooth curvature while the observed profile has a discontinuous edge gradient. The free-slip approximation matches the constant pressures within the central region but diverges from observation near the edges. One cannot clearly differentiate the stress models on the basis of pressure profiles alone. However, in Figure 5.9 a clear distinction is apparent. The smaller deviatoric stress implied by the no-slip model does not correctly predict the observed splitting, while the larger deviatoric stress associated with the free-slip approximation is in accord with the splitting data. (In calculating the splitting, the stresses derived in cylindrical coordinates need to be transformed to Cartesian coordinates.) If the additional assumption is made that the variation of pressure data shown in the Figure 5.9 is a result of the variation in the local load stress σ_1 , the third curve in Figure 5.9 nearly matches the entire splitting profile. It is speculated that a thin layer of the pressure medium may have been trapped between the ruby and diamond, thus facilitating the unexpectedly low interfacial friction.

Based on the idea that stresses in the loaded ruby disks are best approximated by free-slip boundaries, a number of experiments were undertaken on c -normal and a -normal samples to document the deviatoric stress versus R -line splitting behavior. The confining pressures in these experiments ranged

from 2 to 12 GPa. Observed and predicted splittings as a function of deviatoric stress are plotted in Figure 5.10. The agreement between the prediction and the observation is excellent for *c*-normal samples throughout the elastic range (12.5 GPa). The agreement for *a*-normal is excellent up to a deviatoric stress of 6 GPa. Above 6 GPa for *a*-normal samples, a sharp change in the splitting and an increase in scatter in the data were observed (Figure 5.11) A discontinuity in splitting was also noted by Fujishiro *et al.* [1988] at about the same deviatoric stress. Further investigation is needed to understand this phenomena.

The experimental results of Figure 5.10 and supporting calculations show that confining pressure has little effect on the splitting of *c*-normal samples. The best fit to *c*-normal data gives a splitting dependence on deviatoric stress of $0.241 \pm 0.012 \text{ \AA/GPa}$. *Feher and Sturge* [1968] reported that the splitting in unconfined ruby to a maximum uniaxial load of 0.2 GPa is $0.273 \pm 0.015 \text{ \AA/GPa}$.

Stress component σ_1 and σ_3 can also be calculated using the pressures determined from R_1 and R_2 and the empirical equations of *Fujishiro et al.* [1988]. However, the results are far less satisfactory. Assigning $\sigma_1 = \sigma_3$, Equation (1) of *Fujishiro et al.* [1988] gives 3 \AA/GPa for the pressure dependence of R_2 which does not compare well with the measured 3.65 \AA/GPa under hydrostatic conditions [*Piermarini et al.*, 1975].

The R lines of ruby are optical emissions associated with electronic transitions of Cr^{+3} atoms in the crystal field. At ambient temperature, the R line width is mostly a result of strains in the crystal since energy levels of Cr^{+3} are altered by the local crystal field [*Kiel*, 1962]. The line broadening has in general been attributed to non-hydrostaticity in the pressure medium

[Piermarini *et al.*, 1973]. The current experiments, indicate that line broadening results predominately from pressure gradients since the spectra in Figure 5.2, obtained in samples where stresses were uniform but non-hydrostatic, have line widths unchanged from those at 1 bar. The spatial averaging of spectra from several randomly oriented ruby chips may also contribute to line broadening.

5.3.2 Yield strength of single-crystal ruby

The stresses measured when the plastic lamellae first appeared can also be used to determine the yield strength of ruby. Ruby disks of a unknown orientation were tested for strength. For this sample there seemed to have a easy slip system aligned at a small angle with maximum shear stress (45° with respect to the normal to the surface of the disks). As the lamellae grew, the sample disc elongated perpendicularly to the lamellae. Upon further compression, the sample continued to elongate while shearing slightly along them. Figure 5.12 shows a recovered ruby disk deformed at high pressure. Only one slip system was observed upon microscopic examination of the recovered samples.

Figure 5.13 shows the pressure profile of a plastically deformed ruby disk. The yield strength can be derived by applying the free-slip boundary condition. The shear stress at each point is given by $\sigma_s = (\sigma_1 - \sigma_3)/2$. Shear stress σ_{13} as a function of confining pressure is plotted in Figure 5.13. There is a wide range of σ_s at each confining pressure, the top envelope of them is defined here as the yields strength. However, the slope of the pressure profile in Figure 5.13 suggests significant friction may exist between the sample and the diamonds. The friction can be estimated by trial and error using the

following approach, using full tensor notation such as σ_{xx} , instead of the truncated counterpart σ_1 .

Assuming that the simple friction law is still valid under the experimental conditions, the end friction should be balanced by the gradient in the radial stresses:

$$\mu\sigma_{xx} = \frac{h}{2} \frac{\partial\sigma_{xx}}{\partial x} \quad (5.1)$$

and

$$\mu\sigma_{xx} = \frac{h}{2} \frac{\partial\sigma_{yy}}{\partial y} \quad (5.2)$$

At the cylindrical surface all shear stresses vanish. The principal stresses are equal to confining pressure:

$$\sigma_{xx} = \sigma_{yy} = P_c \quad (5.3)$$

In the above equations, P is the pressure measured by R_2 line, h is thickness of the sample disc, μ the coefficient of friction, and P_c the confining pressure.

To first order, there was little shear strain in the xy plane, so that $\sigma_{xy}=0$ ($\sigma_{23}=0$). The shear stress at the end surface, where it is the largest, can be estimated by:

$$\sigma_{xz} = \frac{h}{2} \frac{\partial\sigma_{xx}}{\partial x} \quad (5.4)$$

In deriving equation (5.4), $\frac{\partial \sigma_{xx}}{\partial x}$ was taken as a vertically averaged value, as measured in the current experiment.

$$\frac{1}{3}(\sigma_{xx} + \sigma_{yy} + \sigma_{zz}) = P \quad (5.5)$$

In general, σ_3 (σ_{xx}) is very close to σ_2 (σ_{yy}), so that $\sigma_{xx} \sim \sigma_{yy}$ ($\sigma_3 \sim \sigma_2$) was assumed. This effectively reduces the two dimensional problem into a one dimensional one, and may affect the accuracy of the solution. Stresses σ_3 and σ_1 can be then solved using (5.1) to (5.5), and a trial value for μ , the coefficient of friction. Reasonable solutions can be found for $\mu=0 \sim 0.02$ at all pressures.

The yield strength obtained with $\mu=0.02$ is plotted in Figure 5.14 as a function of confining pressure. It is about a factor of two smaller than that obtained with free-slip assumption. The results agree well with that of [Meade and Jeanloz, 1990b]. However, there are fundamental differences both in the experimental arrangements and the interpretation of the results. This experiment differs from the previous ones in that single crystals and a quasihydrostatic pressure medium were used. The yield strength in the current analysis is determined by the difference between the principle stresses $(\sigma_1 - \sigma_3)/2$, instead of the shear stress σ_{31} at the interface.

5.4 Illustrations

5.4.1 Figures

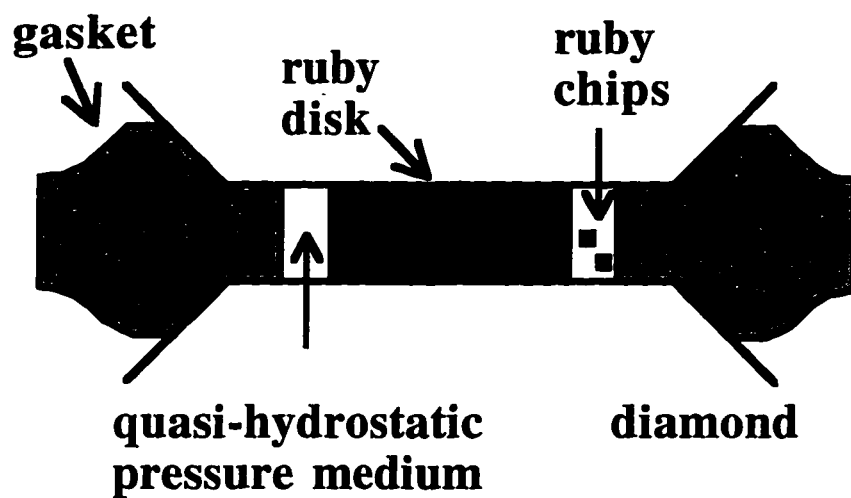


Figure 5.1 Experimental arrangement

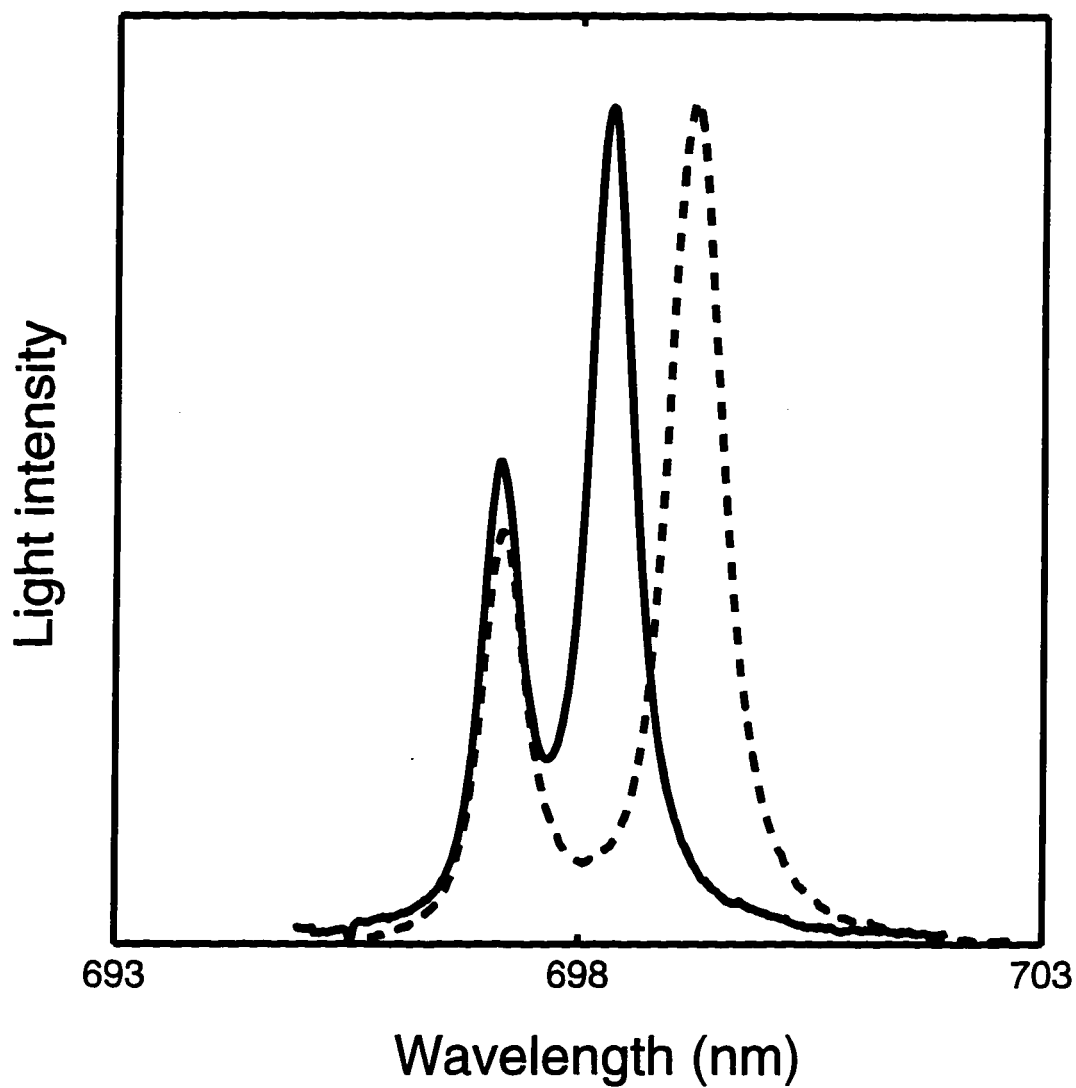


Figure 5.2 Ruby spectra of sandwiched samples

Ruby spectra of the sandwiched samples taken at two adjacent points. The splitting for *a*-normal (dashed line) is about 20 Å and that of the *c*-normal (solid line) is about 12 Å. The R_2 lines are coincident.

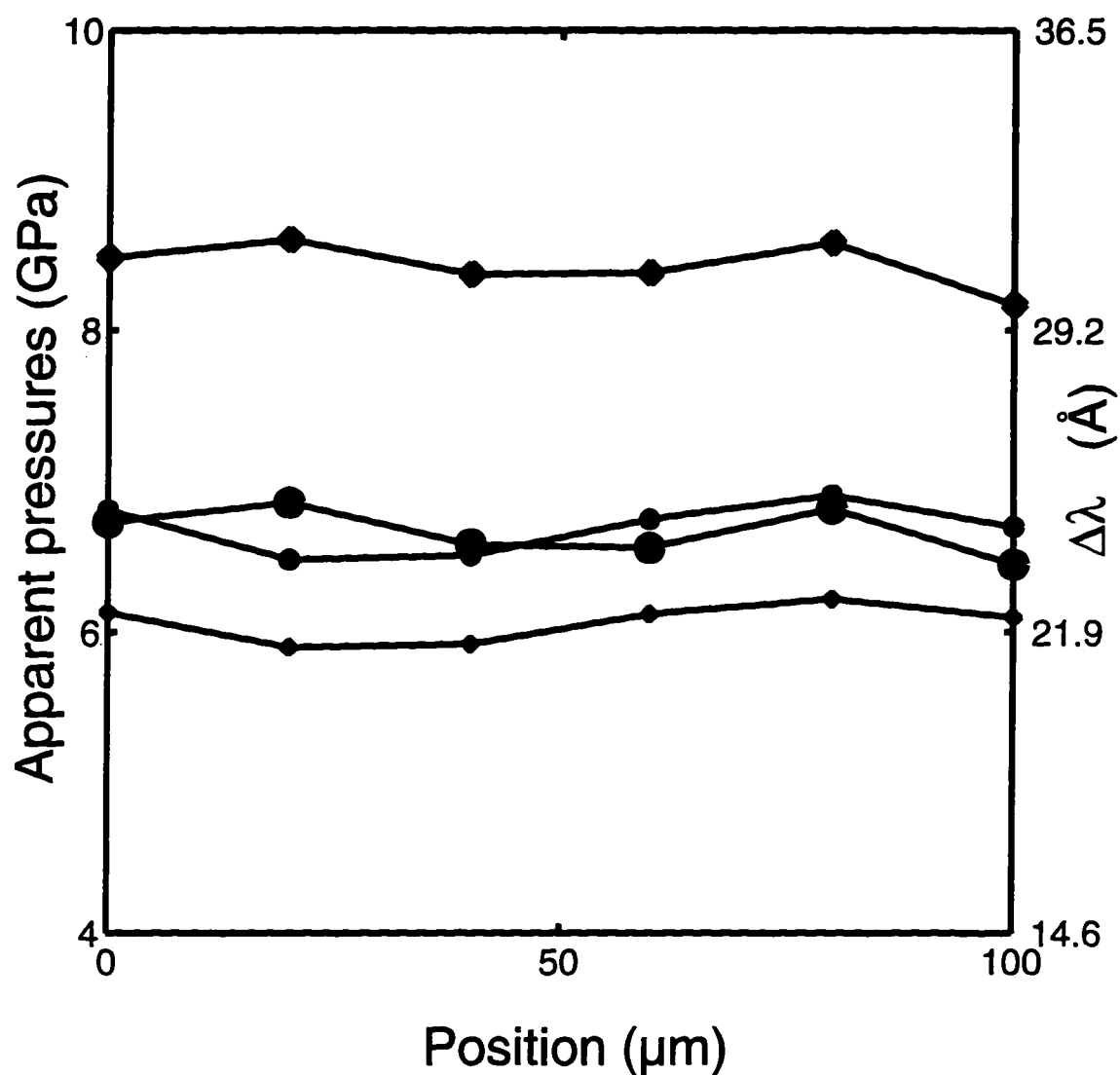


Figure 5.3 Apparent pressure profiles of sandwiched samples

Profiles of apparent pressure for the sandwich the *a*-normal and the *c*-normal samples. The small diamonds are determined from R_1 of the *a*-normal ruby and the heavy diamonds from R_1 of *c*-normal. The small closed circles are determined from R_2 of *a*-normal ruby and the heavy closed circles from the R_2 of *c*-normal.

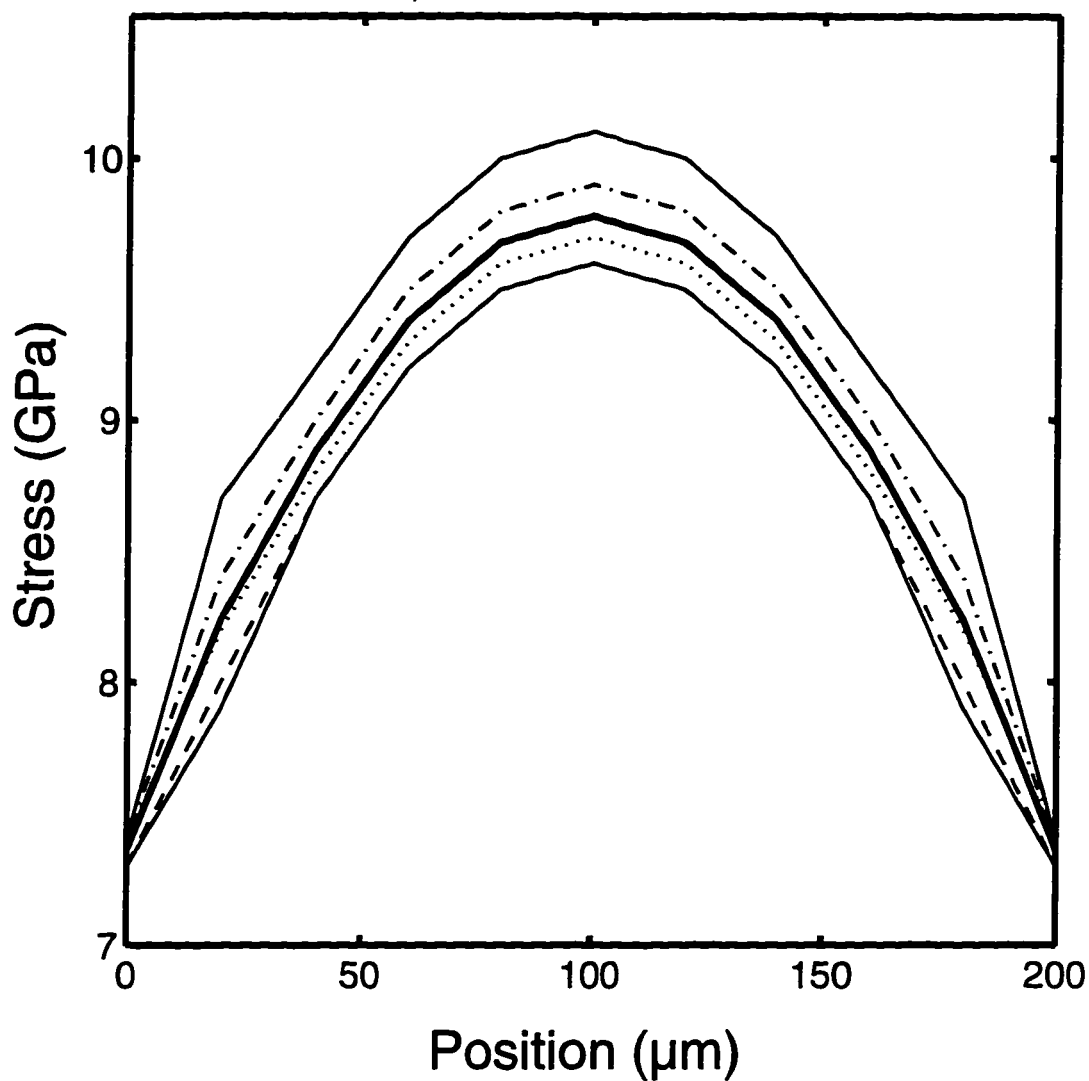


Figure 5.4 Stress profiles S_r of a solid cylinder with no-slip B.C.

Radial component of the stresses for upper-half of a solid cylinder with no-slip boundary condition. The curves from the bottom to the top represent the stress at $H=0$ (lower solid curve), $H=0.25$ (dashed curve), $H=0.5$ (dotted curve), $H=0.75$ (broken curve), $H=1$ (upper solid curve). The thick solid curve in the middle is the vertically averaged stress.

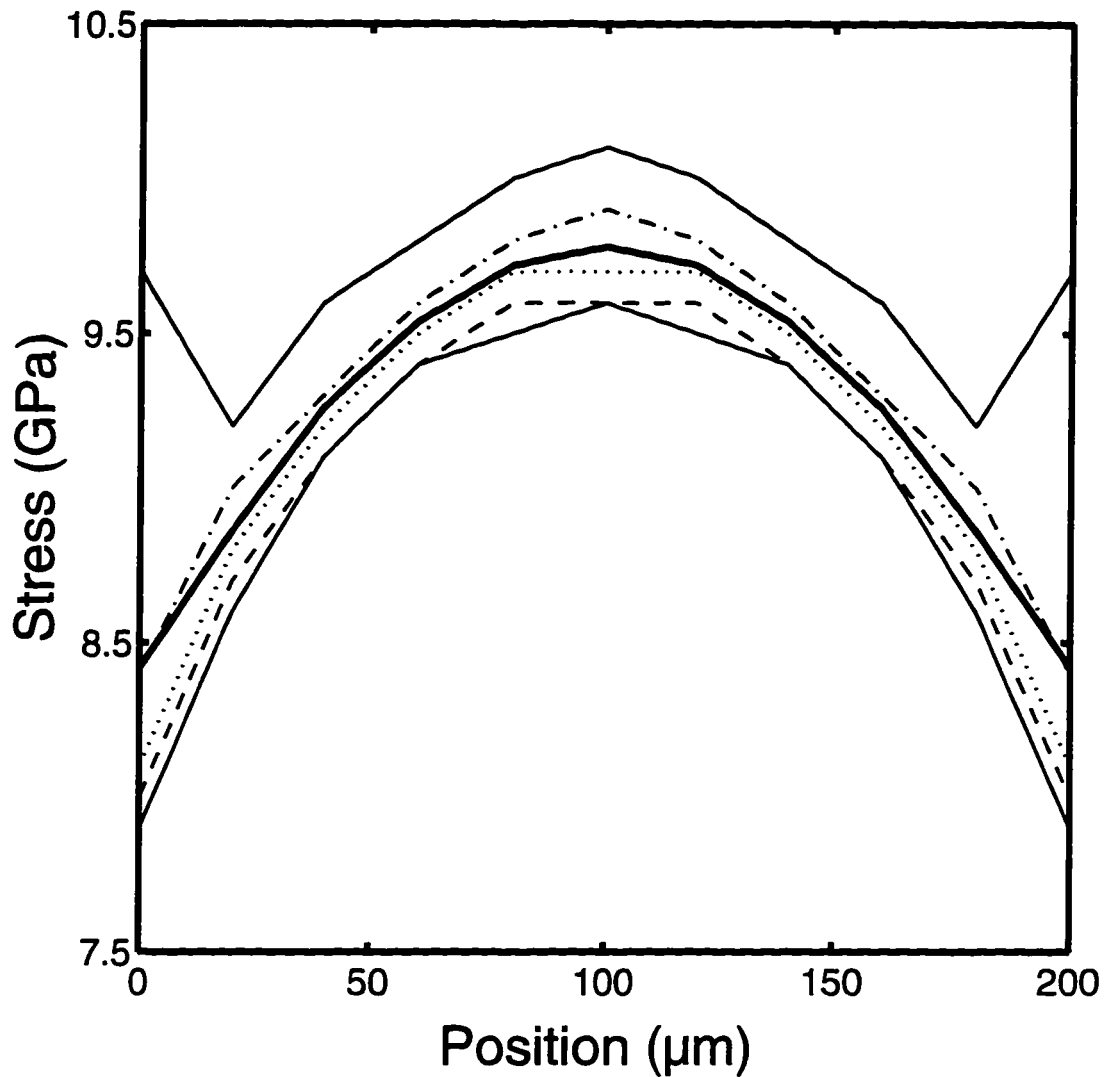


Figure 5.5 Stress profiles S_θ of a solid cylinder with no-slip B.C.

Azimuthal component of the stresses for upper-half of a solid cylinder with on-slip boundary condition. The curves from the bottom to the top represent the stress at $H=0$ (lower solid curve), $H=0.25$ (dashed curve), $H=0.5$ (dotted curve), $H=0.75$ (broken curve), $H=1$ (upper solid curve). The thick solid curve in the middle is the vertically averaged stress.

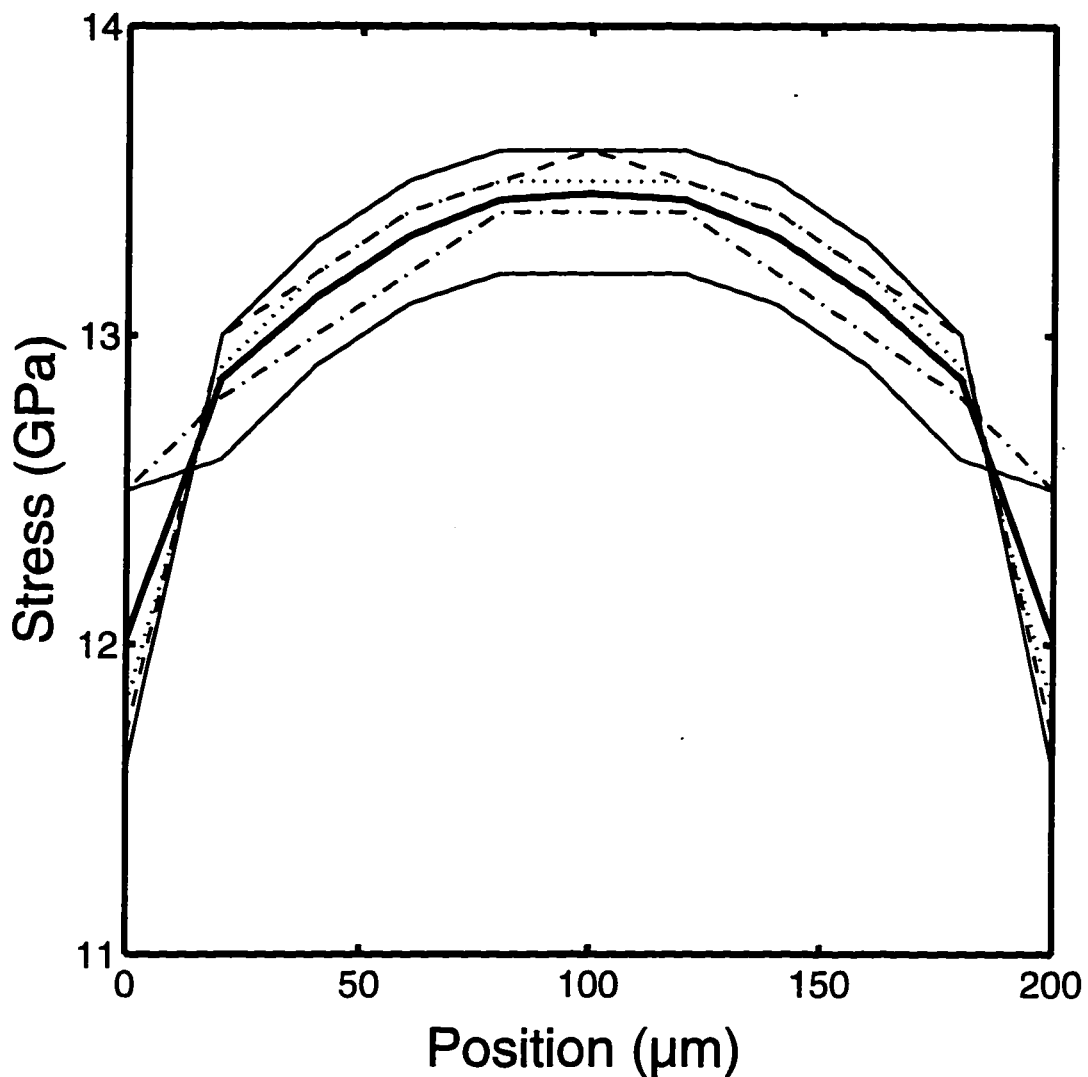


Figure 5.6 Stress profiles S_z of a solid cylinder with no-slip B.C.

Uniaxial component of the stresses for upper-half of a solid cylinder with on-slip boundary condition. The curves from the bottom to the top represent the stress at $H=0$ (lower solid curve), $H=0.25$ (dashed curve), $H=0.5$ (dotted curve), $H=0.75$ (broken curve), $H=1$ (upper solid curve). The thick solid curve in the middle is the vertically averaged stress.

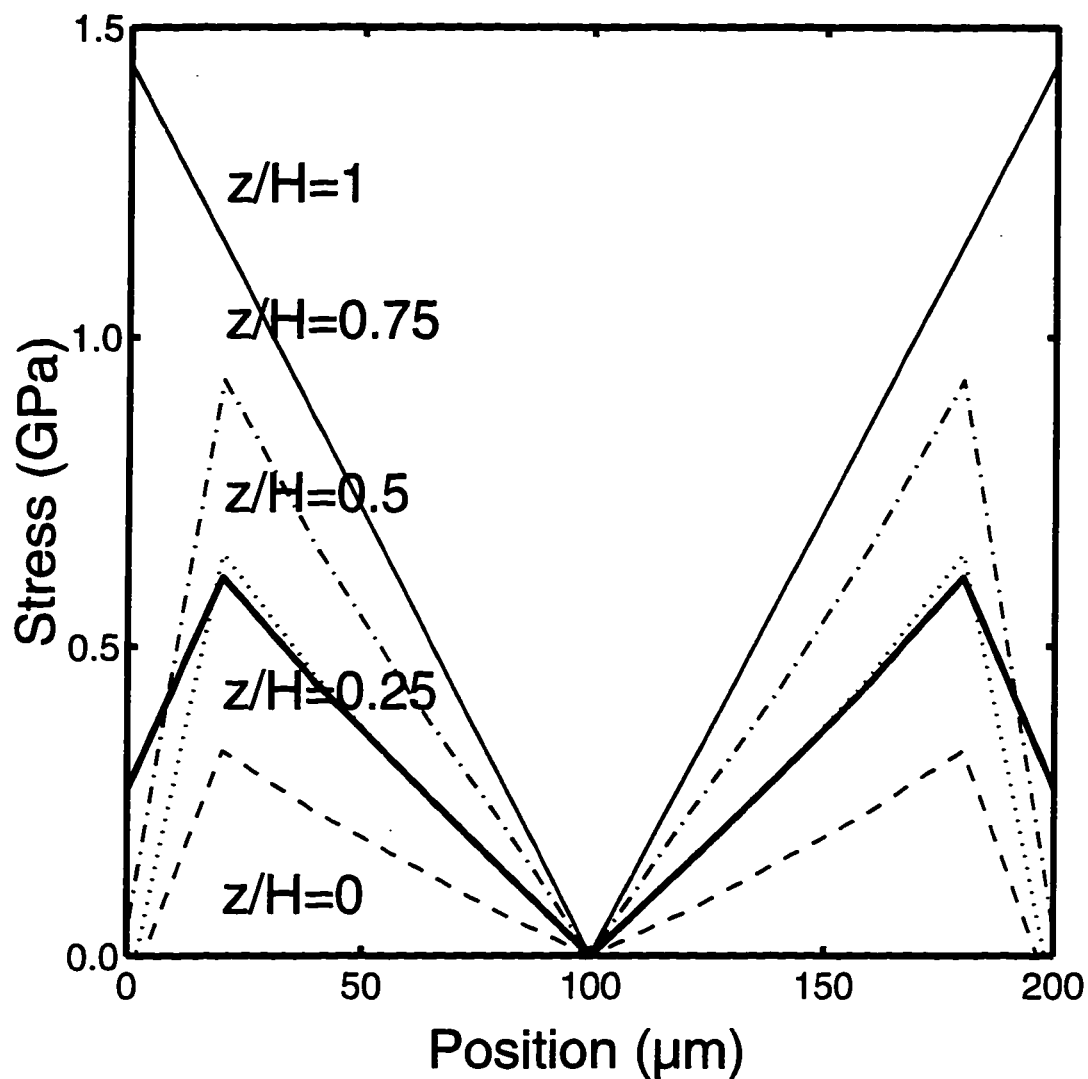


Figure 5.7 Stress profiles S_{rz} of a solid cylinder with no-slip B.C.

Shear stress for the upper-half of a solid cylinder with on-slip boundary condition. The lines from the bottom to the top represent the stress at $H=0$ (lower solid line), $H=0.25$ (dashed line), $H=0.5$ (dotted line), $H=0.75$ (broken line), $H=1$ (upper solid line). The solid line in the middle is the vertically averaged stress. In the case of free slip, this component vanishes.

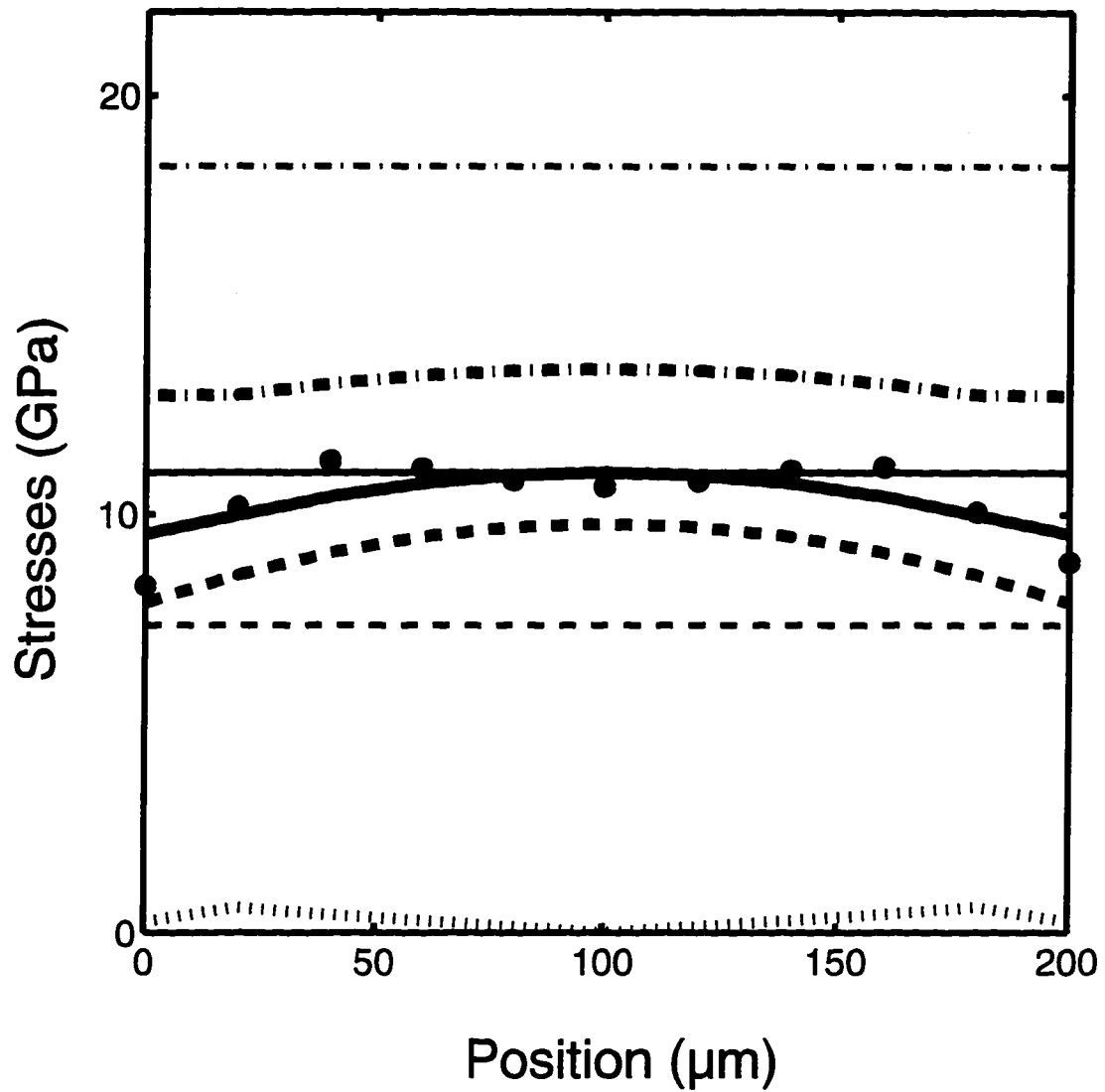


Figure 5.8 Calculated vertically averaged stresses for a ruby cylinder

Calculated vertically averaged stress profiles for a cylindrical plate with both no-slip boundary condition (heavy lines) and free-slip boundary condition (thin lines). The solid line is P , dashed line σ_3 , broken line σ_1 , and dotted line σ_{13} .

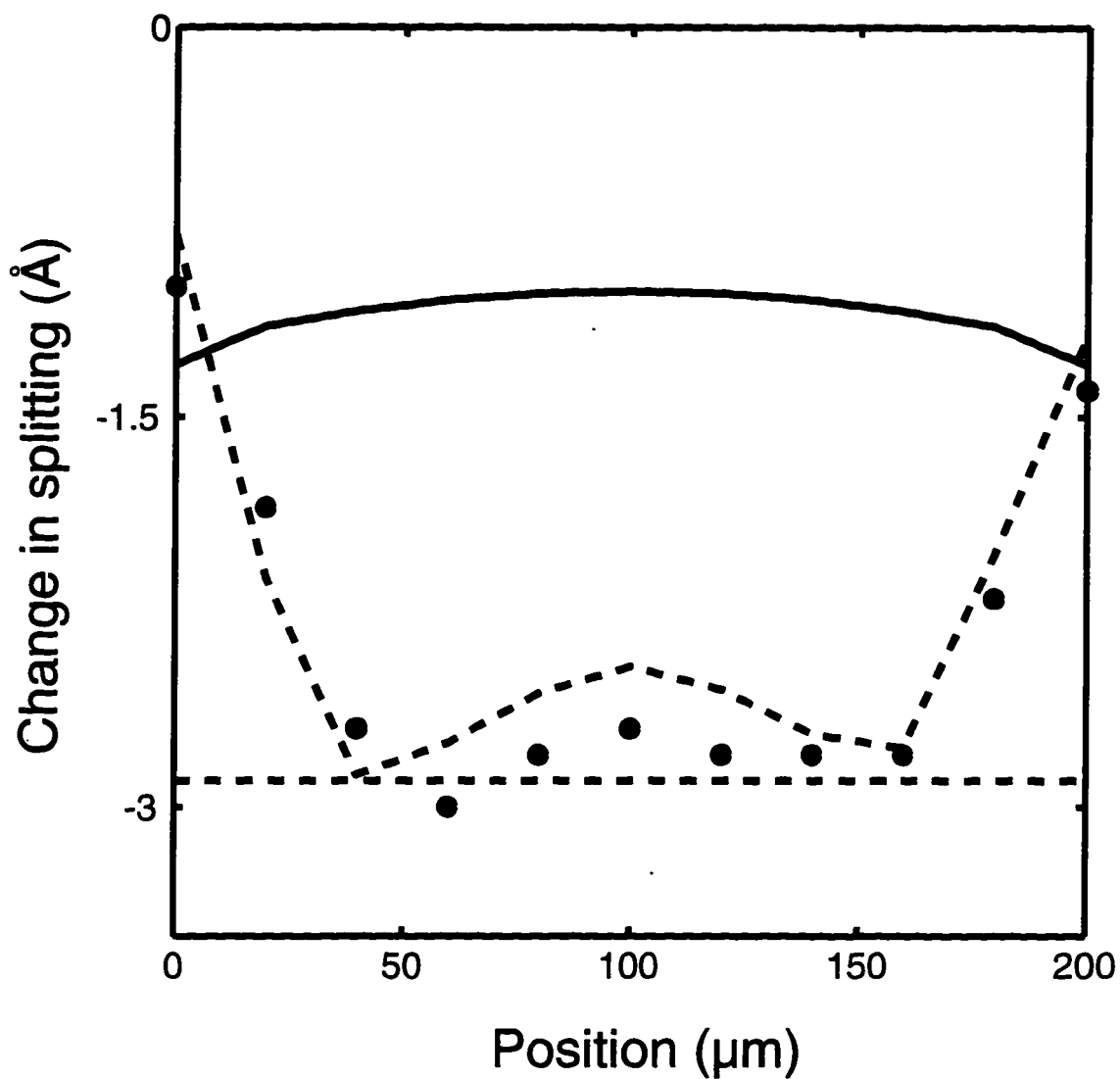


Figure 5.9 R-line splitting of uniaxially loaded *c*-normal ruby

The solid circles are the *c*-normal ruby data. The dashed lines are the calculated splitting using stresses determined from the free-slip boundary condition. The solid line is the calculated splitting using stresses determined from the no-slip condition.

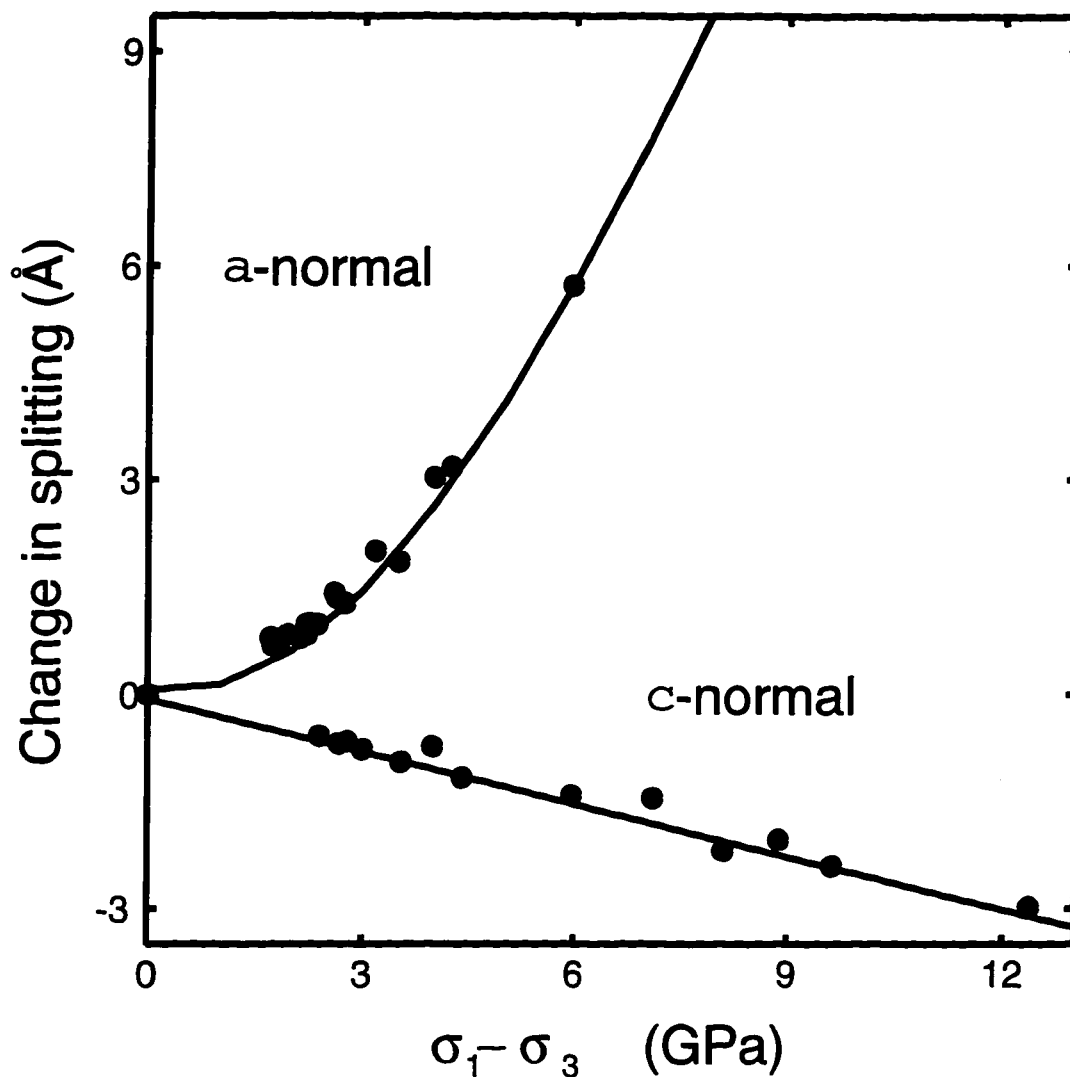


Figure 5.10 R-line splitting as a function of $(\sigma_1 - \sigma_3)$

The change of the $R_1 - R_2$ splitting as a function of deviatoric stress. The open circles are the current data interpreted using the free-slip boundary condition. The solid lines are calculated using eq. 9 of *Shen and Gupta* [1988].

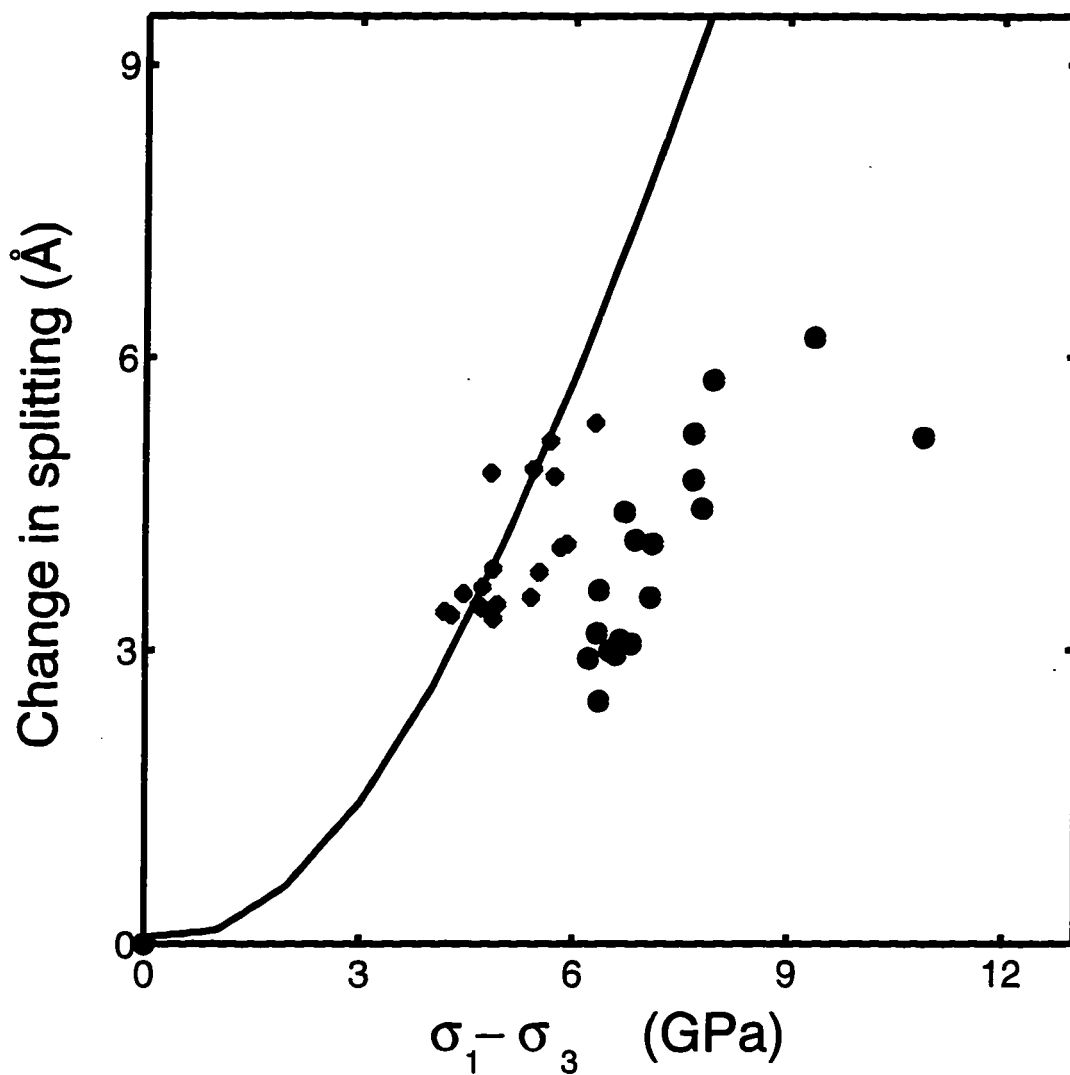


Figure 5.11 R-line splitting deviation along *a*-normal

As $(\sigma_1 - \sigma_3)$ exceeds 6 GPa, observed splitting for *a*-normal ruby deviates (solid circles) from the calculated values. Upon decompression, the splitting tends to come back (diamonds) to the predicted values.

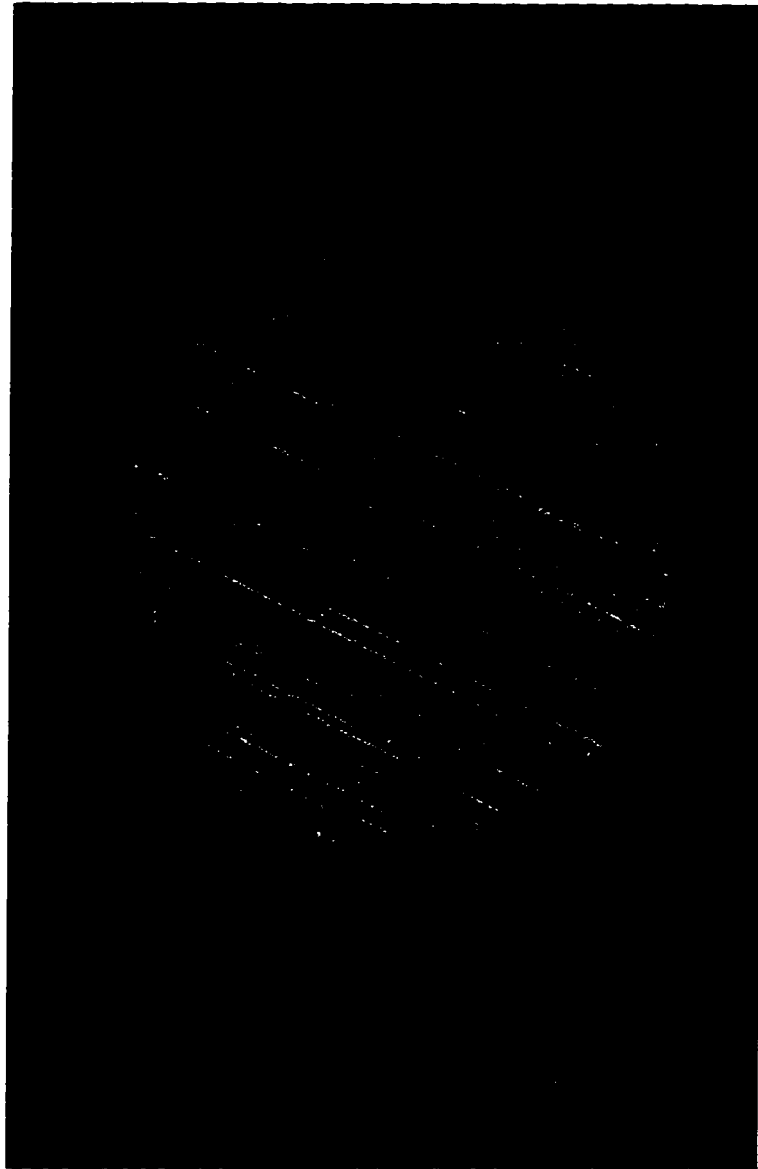


Figure 5.12 A recovered ruby sample after deformation

The sample was a perfect disk before the experiments. It elongated laterally by about 20%. The linear features on the sample are plastic deformation lamellae.

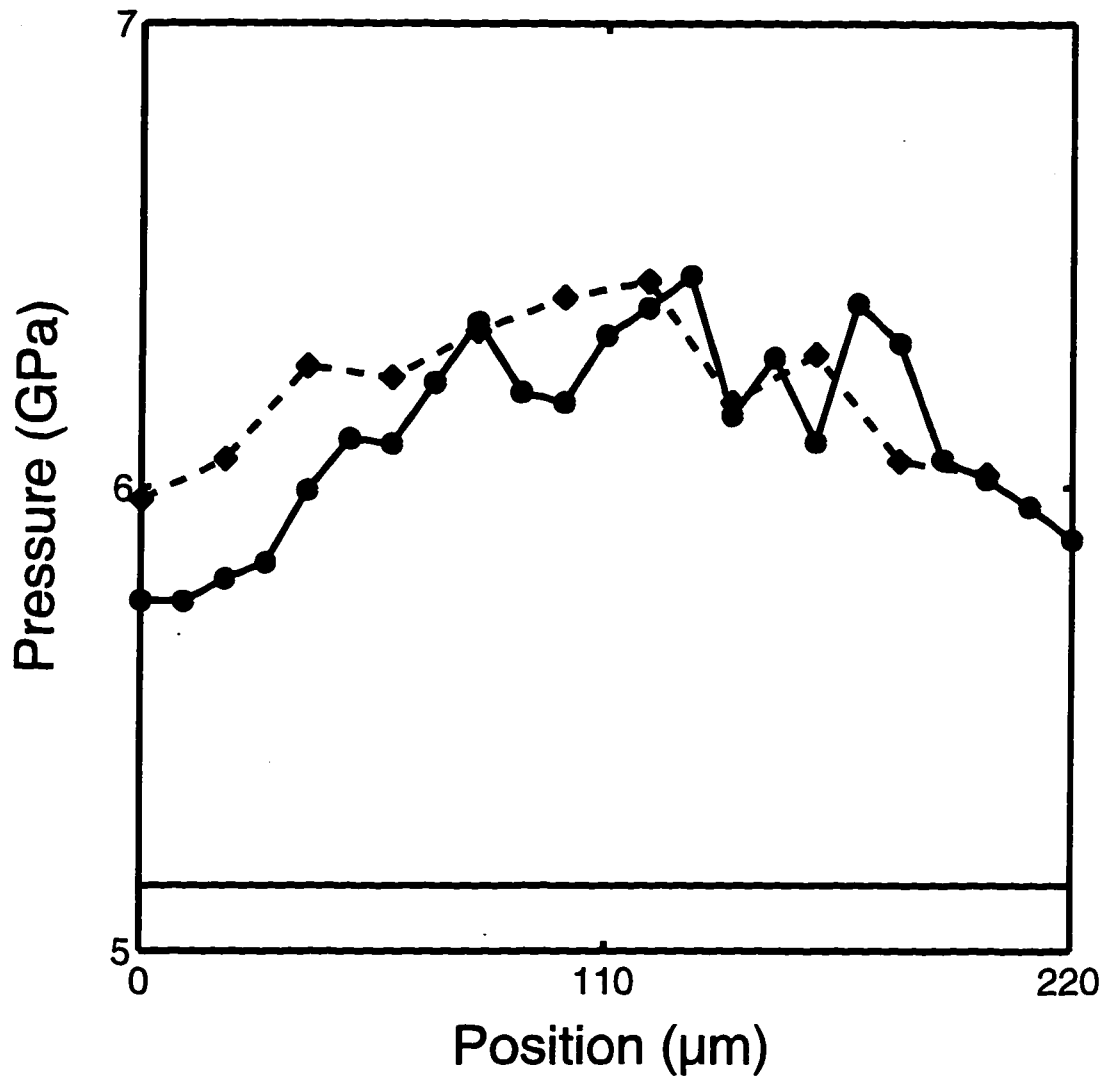


Figure 5.13 Pressure profile of a ruby cylinder

The pressures were taken after the deformation lamellae formed. The traces are perpendicular to one another.

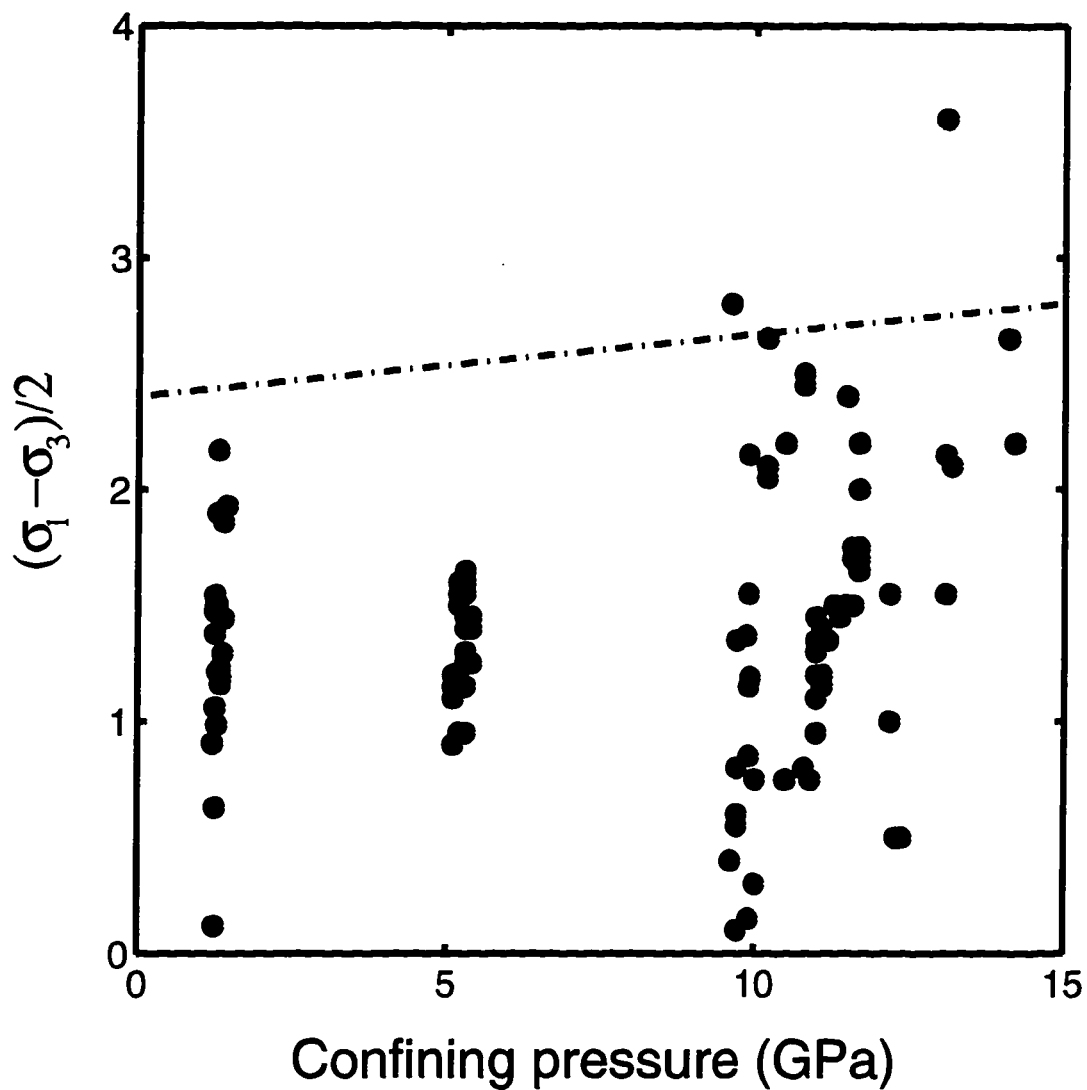


Figure 5.14 Yield strength of ruby with friction B.C.

Stresses $(s_1 - s_3)/2$ were determined with an assumed coefficient of friction $\mu = 0.02$. The yield strength is taken as the top envelope. The broken line is 3% of the shear modulus of ruby.

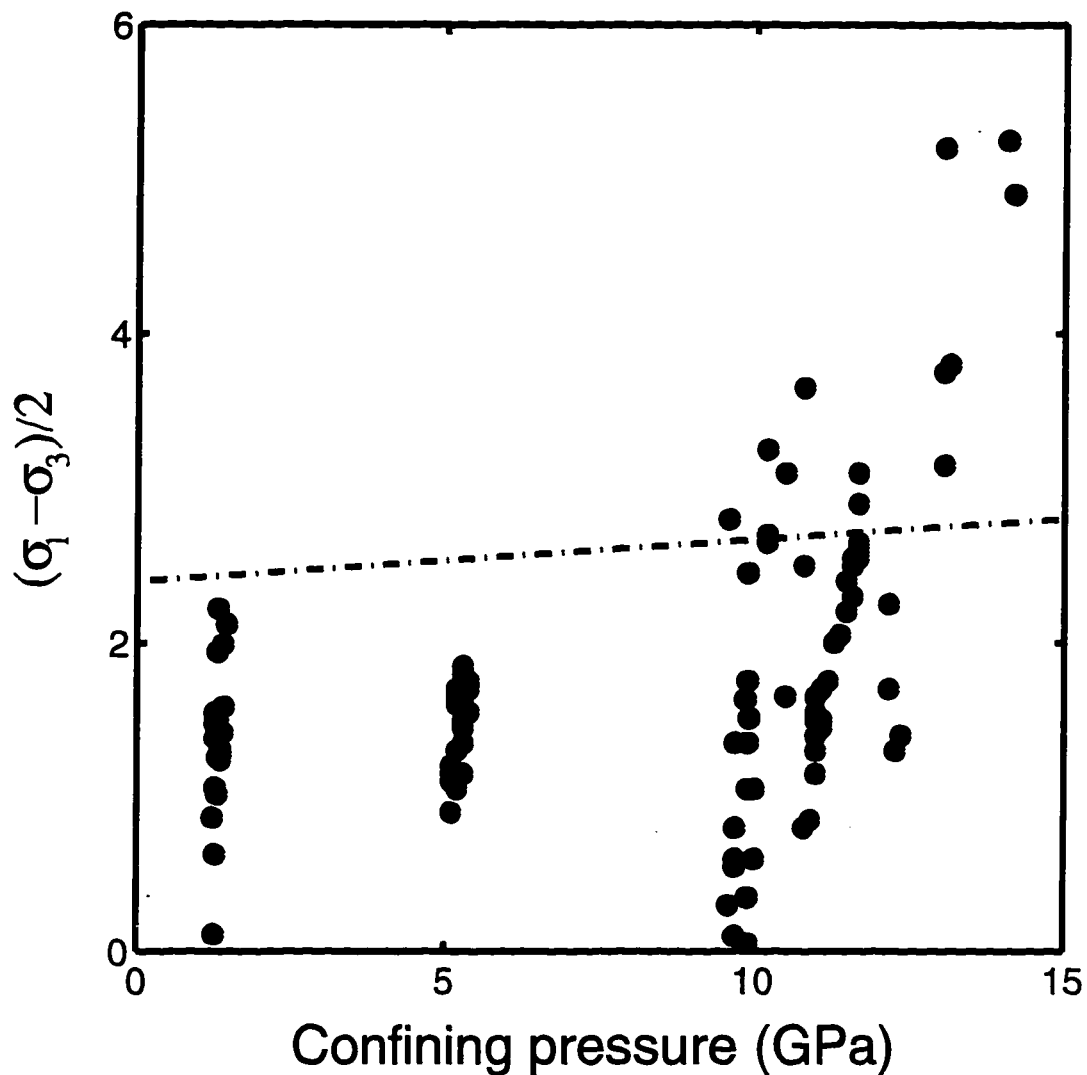


Figure 5.15 Yield strength of ruby with free-slip B.C.

Stresses $(s_1 - s_3)/2$ were determined with a free-slip boundary assumption. The yield strength is taken as the top envelope. The broken line is 3% of the shear modulus of ruby.

Chapter 6

**Yield Strength, Slip Systems and Deformation Induced
Phase Transition of San Carlos Olivine up to Transition
Zone Pressure at Room Temperature**

6.1 Introduction

Rheological investigations of mantle minerals at high pressures include studies of (1) yield strength, (2) the deformation mechanism, and (3) the effect of the deviatoric stress on phase transformations. Most deformation experiments have been carried out in a piston cylinder type apparatus where pressures are generally below 5 GPa. Recently, progress has been reported in using multianvil presses for rheological studies [Weidner *et al.*, 1995] and some effort has been directed at conducting deformation experiments in the diamond anvil cell (DAC) [Kinsland and Bassett, 1977; Meade and Jeanloz, 1988]. In general, accurate stress calibrations remain problematic in the high pressure regime.

The technique introduced in last chapter has been used to deform San Carlos olivine single crystals at room temperature under confining pressures of up to 16 GPa, with measured differential stresses of up to 15 GPa. The yield strength has been measured under those conditions. Transmission electron microscopy (TEM) analysis on the recovered samples indicates (1) that the deformation is completely plastic and (2) that deformation has induced phase transformation even at room temperature

Olivine is believed to be the most abundant mineral within the lithosphere [Ringwood, 1970]. As the thermal boundary layer of a convecting mantle, subducting slabs are expected to be much colder and stronger than the surrounding mantle. For a slab subducting at a rate of 10 cm per year, the interior could be as cold as 600 °C at a depth of 650 km [Wiens *et al.*, 1993]. At such pressures and temperatures, deformation through low temperature plas-

ticity is expected [Frost and Ashby, 1982] The study of low temperature plasticity of olivine is therefore directly relevant in the understanding of physical processes associated with the dynamics of the mantle.

6.2 Experimental technique

The experimental arrangement in the current study, schematically shown in Figure 6.1, is the same to that in last chapter except that an oriented single crystal disk of San Carlos olivine, 200 μm in diameter and 35 to 75 μm thick was sandwiched between the ruby disk and one of the diamonds. Similar to the approach used in last chapter, the areal distribution of pressures and R_1 - R_2 splittings of the ruby fluorescence in the olivine-ruby stack were used to characterize the state of stress in the olivine. The load stress (σ_1) was inferred on the basis of the pressure measurements. Further details are given below.

Plastic deformation was optically monitored through a microscope as shown in Figure 6.2, Fig 6.2A shows the top views of the sandwiched sample in the DAC. Deformation of the sample is associated with the occurrence of linear plastic lamellae (Figure 6.2B and 3B). The stress state of the sample was measured at the onset of plastic deformation. This provided an estimate of the yield strength of the sample. Figure 6.2D shows a recovered sample. Radial strain was measured optically to a precision of a few microns. Recovered samples were transferred onto copper grids, Ar-ion thinned, and carbon coated for TEM studies.

6.3 Results and discussions

6.3.1 Stress determination

Figure 6.3 shows one profile of the mean stress $((\sigma_1 + 2\sigma_3)/3)$ distribution across a axially loaded sandwiched sample. The confining pressure is indicated by the horizontal straight line. All profiles were characterized by a nearly discontinuous jump from the confining medium pressure (10.5 GPa in Figure 6.3) to a nearly constant mean stress across the sample stack (14 GPa in Figure 6.3). The kinks in the mean stress profile appeared to be associated with the deformation lamellae of the sample.

The tensor stress state within an elastically compressed sample depends on the external loads and boundary conditions. With free slip between the sample and the diamonds, stresses would be uniform within the stack (the lateral stress σ_3 everywhere equal to the confining pressure and the axial stress σ_1 equal to the load stress).

Stresses were calculated for a elastically loaded isotropic cylinder using an analytical model [Balla, 1960]. In this model, a cylinder is compressed between two infinitely rigid end plates (in reality the rigidity of a diamond is finite). A friction factor between the sample and the end plates varied from 0 to 1, corresponding to free-slip and no-slip boundaries, respectively. The parameters needed in the calculation are aspect ratio (height to diameter), Poisson's ratio, the average load stress, and the lateral stress on the sides of the cylinder. The parameters of the model can be directly measured in the experiments, with the exception of the average load stress. In the calculations shown in Figure 6.4, an isotropically average Poisson's ratio of 0.25 was used for olivine. The aspect ratio was 1:4 and the lateral stress at the cylinder

surface was set equal to the confining pressure. Calculated stresses were integrated vertically over the top half of the cylinder. The average load stress was determined by trial and error such that the calculated mean stress best matches the observed mean stress.

In Figure 6.4 stress profiles are plotted including (1) the vertically averaged stresses across the cylinder with a no-slip boundary condition, (2) the stresses expected for free-slip boundaries, and (3) the mean stress profile from Figure 3. In contrast to the free-slip situation and the experimental data, the axial (σ_1) and lateral stresses (σ_3) in the no-slip situation vary from the center to the edge by almost 30%. Although friction between the diamonds and sample would be expected to inhibit slip, it is evident that the mean stress distribution of the sample is more consistent with free slip condition (uniform stress distribution). The free-slip boundary condition gives the highest estimated differential stress.

The free-slip approximation was further validated by *Chai and Brown* [1996] through measurements of the R_1 - R_2 splitting in ruby as a function of differential stress. The R-line separation increases when loaded along the a -axis and decreases when loaded along the c -axis. Using the free-slip approximation, observed R_1 - R_2 splittings are in excellent agreement with the calculation from equation (9) of *Shen and Gupta*, [1993], based on shock wave data.

Finally, as discussed below, the lack of a dependence of $(\sigma_1 - \sigma_3)$ at yield on sample thickness is an additional test of the free-slip approximation in the current experiments. The no-slip analysis of *Meade and Jeanloz* [1990] was based on the idea that the radial stress gradient in an axially loaded sample is balanced by the shear traction σ_{13} . Yield strength is proportional to $h(\partial p / \partial r)$,

where h is the thickness of the sample and $\partial p/\partial r$ is the radial pressure gradient in the sample. The absence of a radial stress gradient and no thickness dependence for differential stress at the yield point in the current study argues against this stress balance.

6.3.2 Yield strength

Yield strength plotted in Figure 6.5 is taken to be equal to the maximum resolved shear stress $(\sigma_1 - \sigma_3)/2$ at visual onset of deformation. Three different crystallographic orientations (with crystal axes parallel to load axes) and two different thicknesses (35 and 70 μm) were investigated. Based on the current data, strength measurements on olivine at high pressure and room temperature are plotted in Figure 6.5. An approximate uncertainty of about 1 GPa is estimated on the basis of fits to the primary data as shown in Figure 4. Also plotted in Figure 6.5 are the ambient pressure data of *Evans and Goetze* [1979], the shock wave results of *Furnish et al.* [1986], and a line giving the results of *Meade and Jeanloz* [1990].

The yield strengths of some samples were recorded again after further deformation. These points (denoted with numerical subscript 2 in the figure) may have higher strength as a result of strain hardening [*Nicolas and Poirier*, 1976]. Sample thickness had no discernible effect on the determination of the yield strength and no strong orientational dependence is apparent. *Evans and Goetze* [1979] also reported no orientation dependence. *Furnish et al.* [1986] measured the single crystal yield strength of olivine (the Hugoniot elastic limit) at 18.5 GPa. The strength of olivine shocked along (100) was 6.5 GPa and for a direction midway between (100) and (013) the strength was 7.8 GPa.

A dashed line, drawn by visual inspection, through the zero-pressure point of *Evans and Goetze* [1979] and the current data is shown in Figure 6.5. The *Meade and Jeanloz* [1990] result, plotted in the figure as the solid line, has a similar slope with the current data being offset upward by a little more than 1 GPa. The yield strength in a single crystal normally represents that of a particular slip system. As discussed in the next section, the orientations of the samples did not favor the easy slip systems. A lower strength may be expected in polycrystals with randomly oriented grains. Thus, the results are considered to be in generally good agreement.

6.3.3 Low temperature plastic deformation mechanisms

Recovered samples from the deformation experiment (Table 1 gives the experimental conditions) were analyzed with TEM. All of the examined samples show high dislocation densities throughout the crystals. An accurate determination of the dislocation density is difficult; a lower bound is estimated to be 10^{11} cm⁻². Each originally single crystal now contains numerous domains. In sample B1, the domains are generally rectangular and the domain boundaries are approximately parallel to the {100}, {010} and {001} planes, with the elongation direction parallel to 100°. The samples B2 and C1 contain extremely fine lamellar domains whose boundaries are again along the 100°. Selected-area electron diffraction (SAED) patterns taken from these areas show that the domains are related by twinning (Figure 6.6A). The most commonly observed twinning relation is rotation with respect to the [100] axis, with the (002) plane of one twin variant parallel to the (012) plane of the other. Other twinning relations are also observed, which all share the common (100) plane, with the perpendicular planes (011), (020), (021), (031),

and so forth, parallel to each other across the domains (see SAED pattern in Figure 6.6B). These complicated twinings contrast with the slip systems observed in experiments at low-pressure and low-temperature which are dominantly [001](100) [Carter and AveLallemant, 1970; Raleigh, 1968; Young, 1969]. The orientations of the samples do not favor these easy slip systems which are either parallel or perpendicular to loading axis, therefore extensive twinings are expected under such high shear stresses.

These twinning relations and the observed microstructures can be interpreted as a result of significant increase in stacking faults in directions perpendicular to the 100^* of the olivine crystals. In some areas, superlattice reflections are observed. In Figure 6.7A, taken from sample B1, the superlattice reflections indicate a twofold repeat in the $0\bar{1}2^*$ direction, with a corresponding d-spacing about 5.75 Å. Figure 6.7B shows another example where the superlattice reflections reveal a fourfold repeat in the 021^* direction, corresponding to a d-spacing as large as 15.5 Å. The superlattice reflections, forbidden in an ordinary olivine structure, indicate the loss of symmetry elements due to the presence of large number of stacking faults and may be an indication of onset of structural polymorphism. In Figure 6.6A, an additional set of diffraction spots are present (indicated by the white arrows), which cannot be explained by superlattice reflection in olivine. Additionally, nearly all of the electron diffraction patterns indicate a 4% shortening in the c -axis; the original 5.98 Å edge length now is about 5.7-5.75 Å. The other axes, on the other hand, do not show such large change in dimension. These observations indicate that the samples have undergone considerable structural modifications under the experimental conditions.

6.3.4 Deformation induced phase transformation

Upon close examination it was found that all three samples contain domains whose SAED patterns can be indexed on the basis of the β -phase, which has close toptaxial relationships with olivine. Unfortunately, the small domain sizes did not allow a complete structure identification. Figure 6.8 is a bright-field electron micrograph taken from a 0.5 μm wide zone in sample B1 which contains very thin layers of high-pressure phase. The (002) and (040) diffractions of olivine and (040) and (202) diffractions of β -phase are labeled in Figure 9 (A). Diffraction spots (040) of olivine and (202) of β -phase are well separated, while (002) of olivine and (040) of β -phase overlap due to the permanent shortening of olivine along c -axis. Diffraction (101) of β -phase (not labeled in the figure) is weak and connected with the (020) diffraction of olivine. Overall, three toptaxial relations between α and β have been observed:

$$\begin{aligned} &(100)_{\alpha} // (10\bar{1})_{\beta} \text{ and } (031)_{\alpha} // (040)_{\beta}, \\ &(100)_{\alpha} // (10\bar{1})_{\beta} \text{ and } (021)_{\alpha} // (040)_{\beta}, \\ &\text{and } (100)_{\alpha} // (020)_{\beta} \text{ and } (020)_{\alpha} // (101)_{\beta}. \end{aligned}$$

The subscripts α and β denote olivine and the β -phase, respectively. They are all different from those proposed by *Madon and Poirier* [1983], and *Poirier* [1981] for a martensitic-like transformation. These orientations have relatively small strain mismatch between the two crystal lattices. Table 2 summarizes d-spacings for the related directions, which exhibit strain mismatch of less than 4%, except for $(021)_{\alpha}$ and $(040)_{\beta}$ for which the strain mismatch is as large as 18%.

It is unlikely that the phase transformation observed in the samples occurs via the so-called martensitic-like mechanism for the following reasons: (1) samples were deformed with various orientations relative to the maximum compressive principal stress (σ_1), and yet there is no unique topotaxy that relates the two structures; (2) microstructurally, the majority of the areas do not show clearly defined interfaces between the two phases; and (3) no macroscopic faulting was observed at strains as large as 30%.

Based on the microstructure, the twinning relations, the superlattice reflections in olivine, as well as the various orientational relations between olivine and the β -phase, it is proposed that a mechanism of structural polymorphism via the generation of high density of stacking faults. An intermediate highly disordered phase provides a low activation energy path for the reaction, thereby enhancing the rate of transformation. The intermediate disordered step is "frozen in" at laboratory time scales by low temperature; a moderate increase in temperature would likely lead to rapid transformation. Indeed, *Guyot et al.* [1991] proposed a two-step mechanism for the α - β transformation in forsterite.

Since the stresses involved in these experiments are tremendous, it is important to know the temperature rise during these experiments. The temperature can be estimated by dimensional analysis. A conservative estimate is to convert the total work done to the sample during the deformation completely to heat. The averaged stress is taken as $\sigma=20$ GPa; the total volume deformation is on the order of $\Delta V=3 \cdot 10^{-13}$ m³, corresponding to a linear strain of 10%. The total work done to the sample is $Q=\sigma \cdot \Delta V=10^{-3}$ J. The strain rate was observed to be on the order of 1~5 seconds. The volume of the heat diffused during the time can be estimated by $V=d \cdot S=\sqrt{KT}=10^{-3}$ m, where $K=10^{-6}$

m^2s^{-1} is the thermal diffusivity; T the time; S , the surface area. The temperature rise is then calculated by

$$\Delta T = \frac{Q}{V \cdot C_p \cdot \rho} = 50 \text{ K.} \quad (6.1)$$

This temperature rise is far below the 600°C threshold temperature for the phase transformation under hydrostatic conditions [Kirby, 1995].

6.4 Geophysical implications

While shallow earthquakes, caused by friction sliding, are restricted to a depth of 30-60 km (1-2 GPa), deep earthquakes occur at depths as great as 690 km where the pressure is about 24 GPa and temperature is estimated to be as high as $500\text{-}700^\circ\text{C}$. Experiments suggest that under the latter conditions, rapid seismic failure such as occurs at shallow depths should be replaced by ductile deformation [Burnley *et al.*, 1991; Griggs, 1972; *et al.*, 1991]. Obviously this is not the case; the origin of the stresses giving rise to these ruptures and the nature of the failure are not understood.

Several source mechanisms have been proposed for deep earthquakes. [Green and Burnley, 1989; Green *et al.*, 1992; Kirby, 1987; Kirby *et al.*, 1991] propose that the shear instability caused by the phase transformation in the subducting slabs may be responsible for the deep earthquakes. In this transformational faulting mechanism, it is hypothesized that in subducting slabs, where temperatures are considerably cooler than in the surrounding mantle, olivine may remain metastable to depths well below 410 km. The α - β and α - γ phase transformation in the metastable olivine matrix is envisioned to nucleate so as to form lens-shaped, fine-grained pockets, or "anticracks", forming narrow bands of the high pressure phase, eventually

resulting in transformational faulting [Green *et al.*, 1992]. This mechanism requires a threshold temperature, 600°C, below which olivine remains untransformed under high pressures [Kirby, 1995]. Although knowledge of the kinetics of such transformations is crucial in this hypothesis, virtually no experimental kinetic data exist for the (Mg,Fe)₂SiO₄ system. In particular, effects of non-hydrostatic stress on the kinetics are largely unknown. So far most of the experimental evidence pertinent to this mechanism is based on experiments on analogous materials such as Mg₂GeO₄ or ice [Burnley *et al.*, 1991; Green and Burnley, 1989; Green *et al.*, 1990; Kirby, 1987]. Despite the attractiveness of this mechanism, it cannot explain the many features displayed by some deep earthquakes. For example, the size of the imaged faults are much larger than the width of the cold wedge of subducting slabs [Silver *et al.*, 1995].

One of the critical assumptions in this proposal is that olivine to β -phase transformation is kinetically inhibited below certain temperature [Sung and Burns, 1976]. The current experiments produced the high-pressure β -phase of olivine at room temperature. The level of shear stress was high ($(\sigma_1 - \sigma_3)/\sigma_3 \approx 1$). However, the stress level required to introduce stacking disorder depends on the yield strength, which decreases with increasing temperature. Therefore, transformation by deformation may occur at a much low level of shear stress at temperatures more relevant to the interior of the subducting slab (e.g. 600 °C). The observed microstructure in the samples indicates that low-temperature plasticity is the dominant deformation mechanism in the laboratory. As long as the same yield mechanism operates under subduction zone conditions, the high-pressure phase may be quickly formed in locations of high stress within the downgoing slab.

6.5 Illustrations

6.5.1 Tables

Table 6.1 Experimental conditions for San Carlos olivine single crystals

An average value of the mean stress and differential stresses is listed. Stresses varied by less than 1 GPa across the sample disk. Total strain is based on the change in radius of the sample disks as measured before and after deformation. The mineralogical convention using the space group *Pbnm* for olivine, with edge lengths $b > c > a$, has been used. In this assignment, the "six-fold" axis of the pseudo-hexagonal close-packed oxygen sublattice is parallel to the [100] axis.

Sample	Orientation	Confining Pressure σ_3	Mean Stress $(\sigma_1 + 2\sigma_3)/3$	Differential Stress $\sigma_1 - \sigma_3$	Maximum Radial Strain
B1	[010]	14.0 GPa	19 GPa	15.0 GPa	15%
B2	[010]	16.5 GPa	21 GPa	13.5 GPa	30%
C1	[001]	15.5 GPa	20 GPa	13.5 GPa	10%

Table 6.2 Lattice mismatch

Zero-pressure lattice misfit between adjacent olivine and β -phase atomic planes.

Epitaxial Relation	Lattice Spacing, Å	Misfit (%)
$(100)_\alpha // (10\bar{1})_\beta$	$d_{100}^\alpha = 4.755, d_{10\bar{1}}^\beta = 4.67$	1.8
$(031)_\alpha // (040)_\beta$	$d_{100}^\alpha = 2.955, d_{101}^\beta = 2.85$	3.6
$(100)_\alpha // (10\bar{1})_\beta$	$d_{100}^\alpha = 4.755, d_{10\bar{1}}^\beta = 4.67$	1.8
$(021)_\alpha // (040)_\beta$	$d_{021}^\alpha = 3.477, d_{040}^\beta = 2.85$	18
$(001)_\alpha // (020)_\beta$	$d_{001}^\alpha = 5.982, d_{020}^\beta = 5.79$	3.2
$(020)_\alpha // (101)_\beta$	$d_{020}^\alpha = 5.102, d_{101}^\beta = 4.67$	8.5

*The *Imma* space group for the β -phase ($a=8.248$ Å, $b=11.444$ Å, and $c=5.696$ Å) has been adapted .

6.5.2 Figures

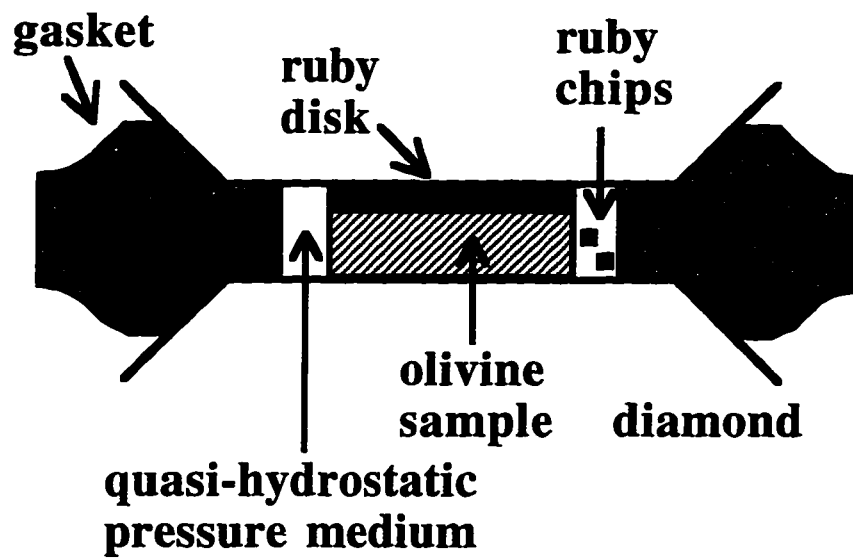


Figure 6.1 Experimental arrangement

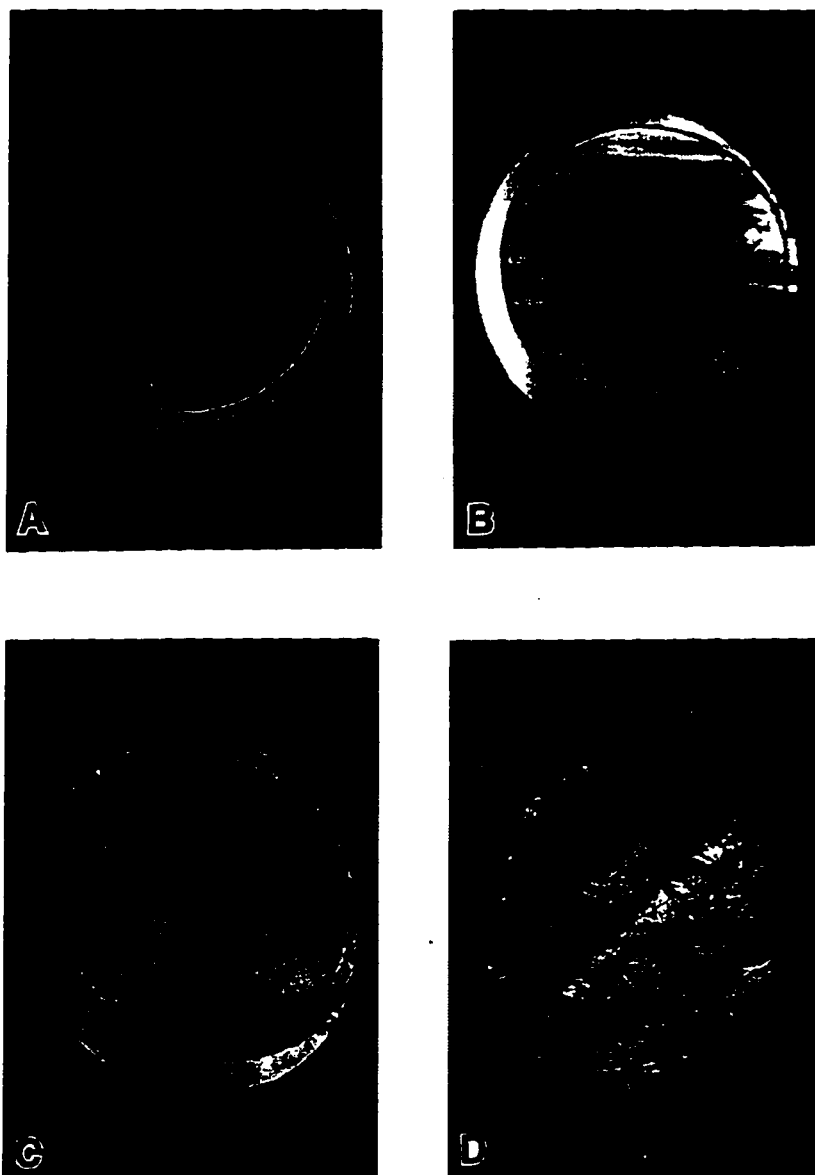


Figure 6.2 Top view of the sandwiched sample in the DAC

Top view of the sandwiched sample in the DAC. (a) The sample sandwich has not yet been touched by the diamonds. The small ruby chips on the side in the pressure medium are used to measure the confining pressure. Two ruby chips drifted onto the top of the sandwiched sample. The pressure in the cell was at 9 GPa. (b) Plastic lamellae first occurred as the diamond squeezed the sample. The crack was probably caused by local high stress due to the ruby chips on the top. (c) As the sample further squeezed, more slip system were activated as indicated by the lineations. (d) A recovered sample.

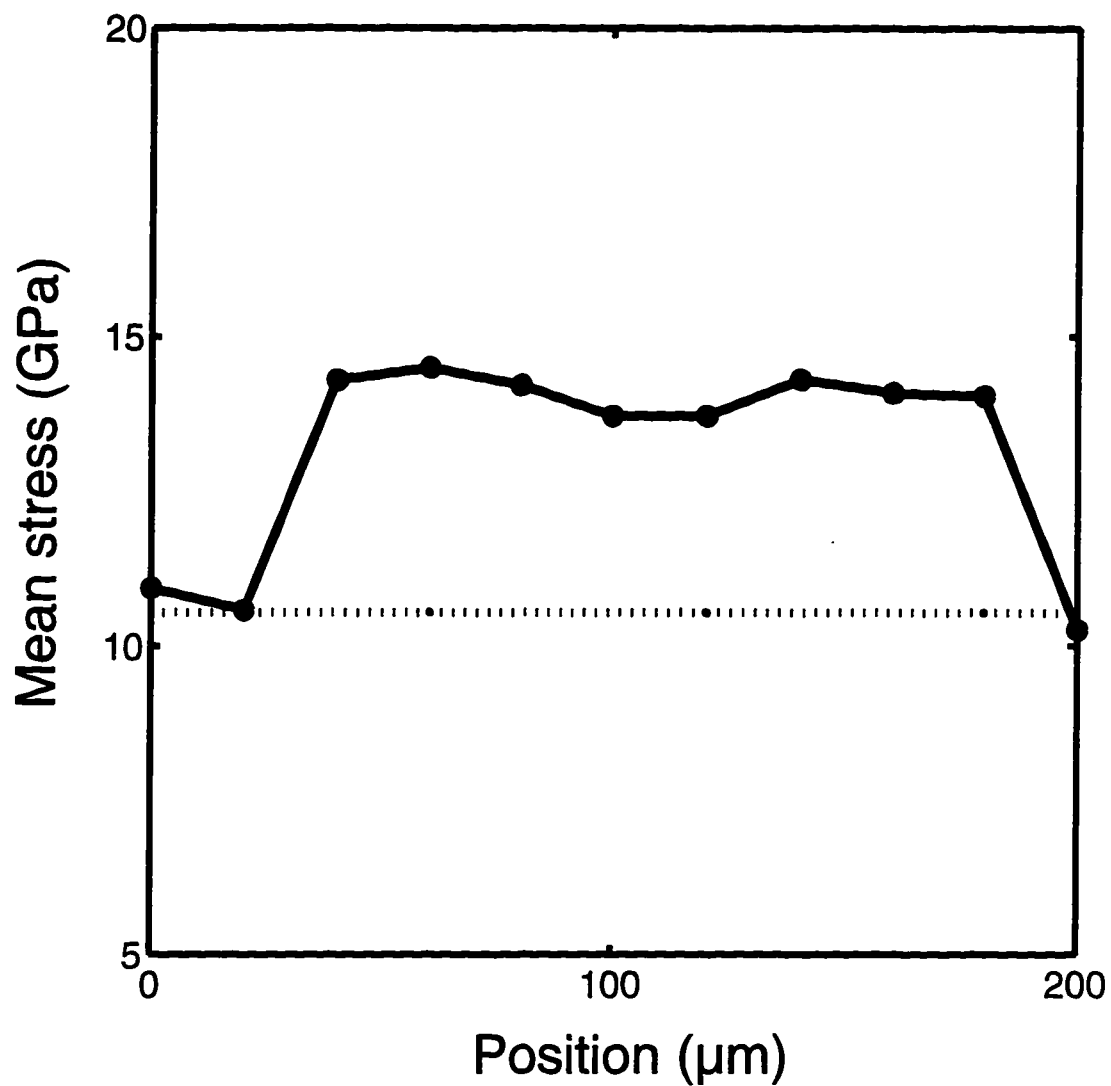


Figure 6.3 Pressure distribution across the olivine sample
One profile of the mean stress distribution across the sandwiched sample.

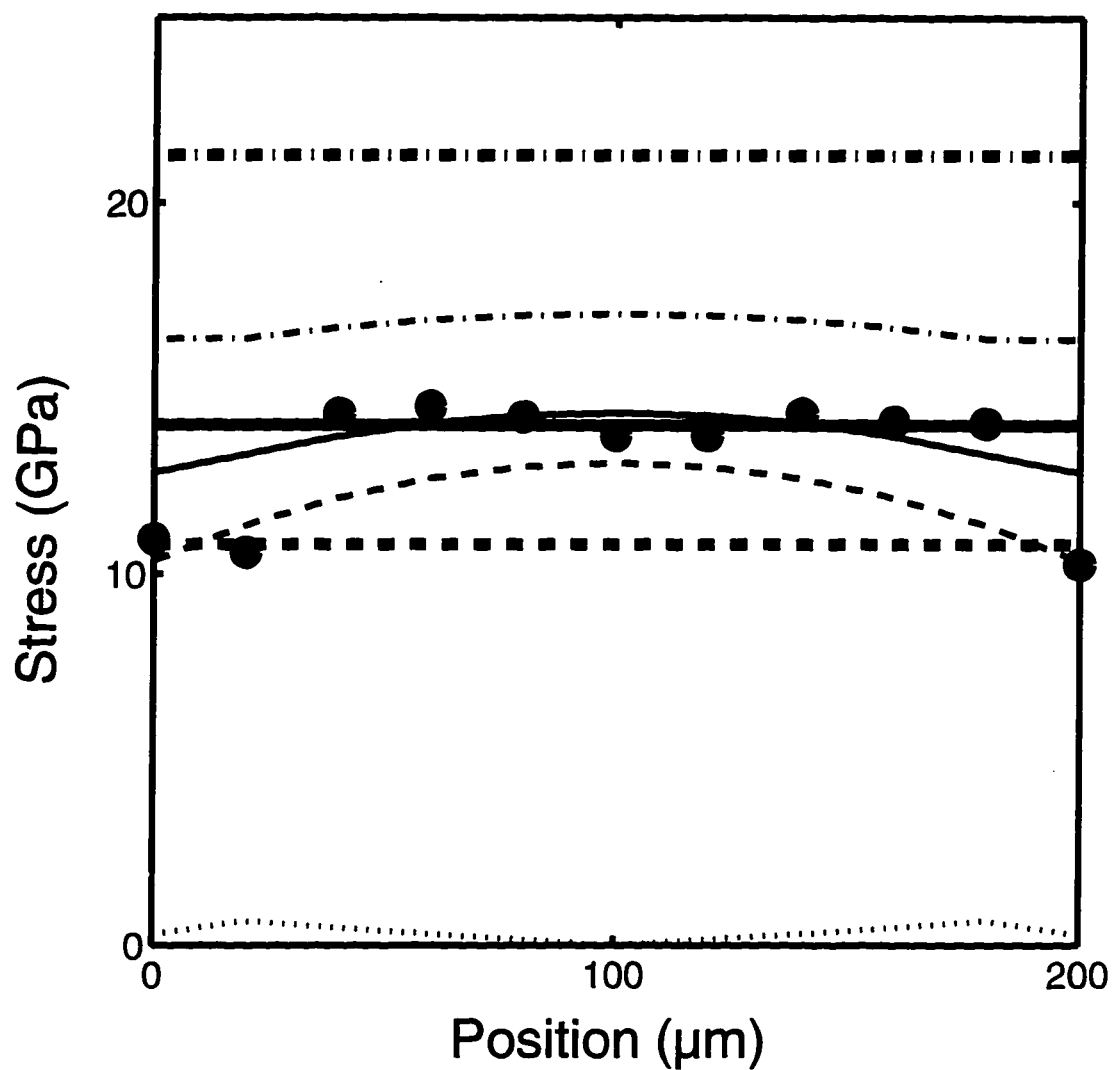


Figure 6.4 Stress profile for a loaded cylindrical olivine sample

Calculated stress profiles for a loaded cylindrical plate. The thick lines are for the free-slip condition and the thin lines for the no-slip condition, respectively. Solid lines are mean stresses; dot-dashed lines, σ_1 ; dashed lines, σ_3 ; and the dotted line is σ_{13} . Distribution of mean stress from Figure 3 is plotted as the filled circles.

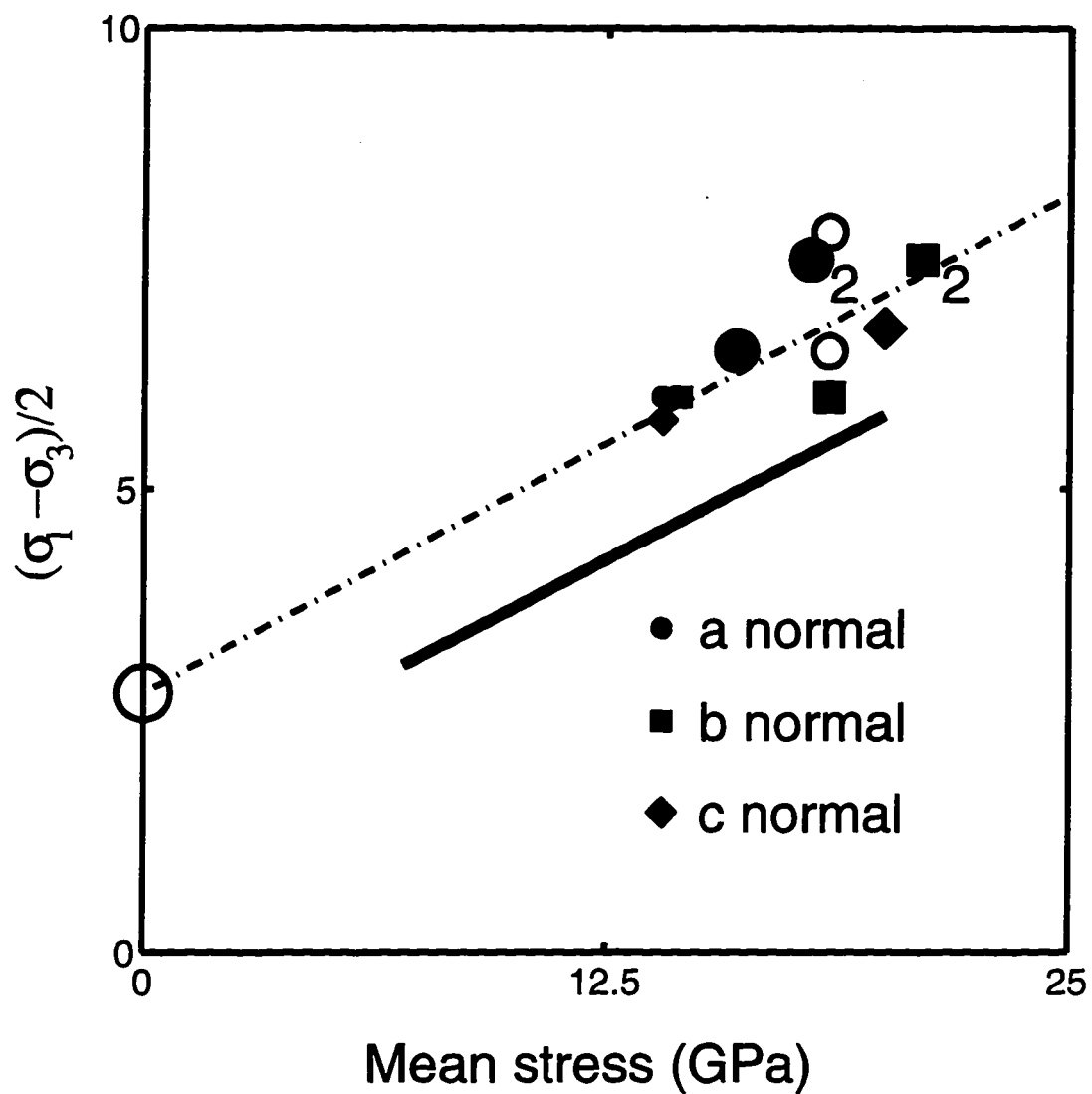


Figure 6.5 Yield strength of olivine

The yield strength of olivine as a function of mean stress. Different symbols represent different orientations of the olivine. Larger and small solid symbols represent 75 micron and 35 micron olivine samples, respectively. The large circle is the ambient pressure yield strength of *Evans and Goetze* [1979]; the heavy line is from *Meade and Jeanloz* [1990].; the small circles are from *Furnish et al.* [1986].

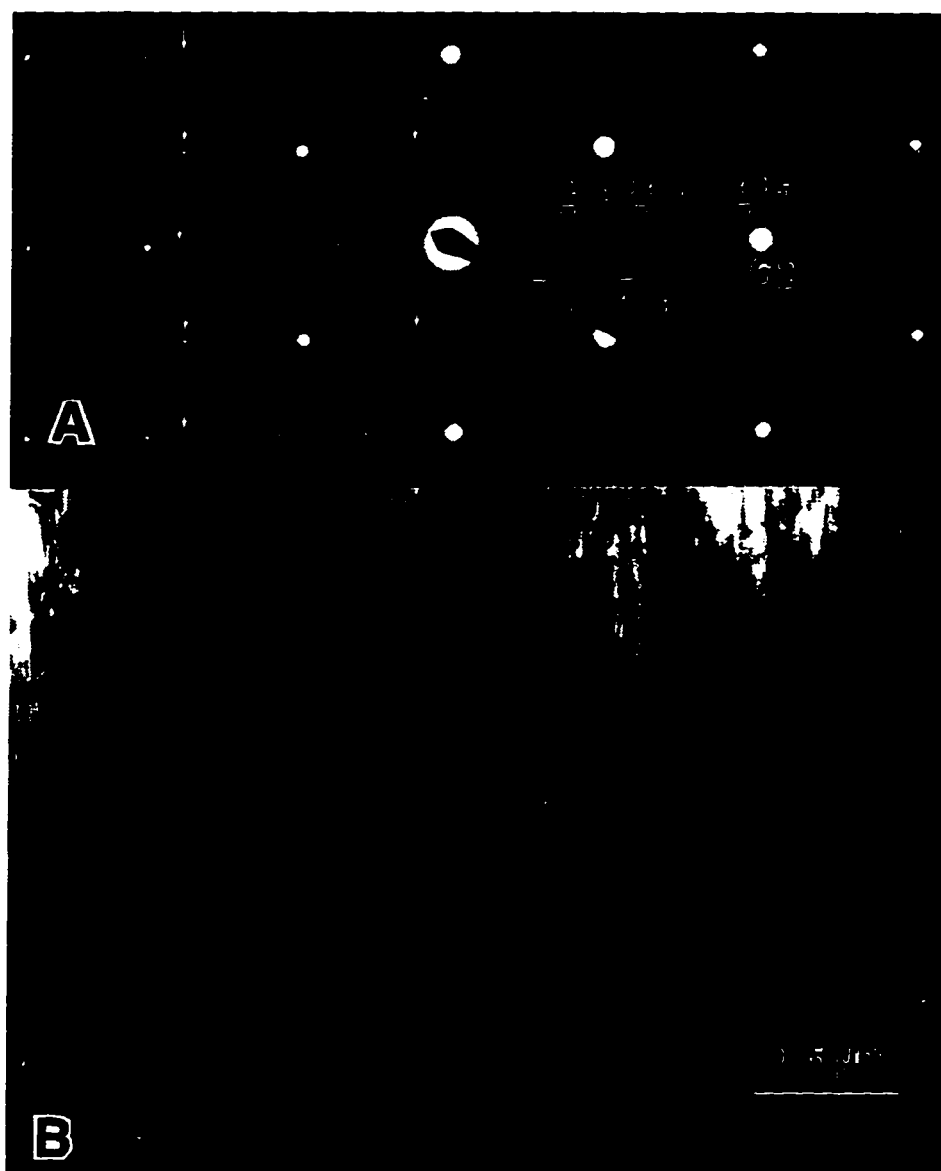


Figure 6.6 Electron image microstructure of deformed olivine

Typical deformation microstructure (sample C1). Selected-area electron diffraction (SAED) pattern (A) from a homogeneous microstructure (B) with lineations whose traces are parallel to the 100^* direction. The SAED pattern indicates complex twinning relations. Spots 200 and 062 are from the olivine matrix. Spots due to five different twinning orientation relations are labeled by numerical subscripts. Additional superlattice spots are also present (e.g., vertical white arrows), which cannot be indexed as from the Pbnm olivine structure.

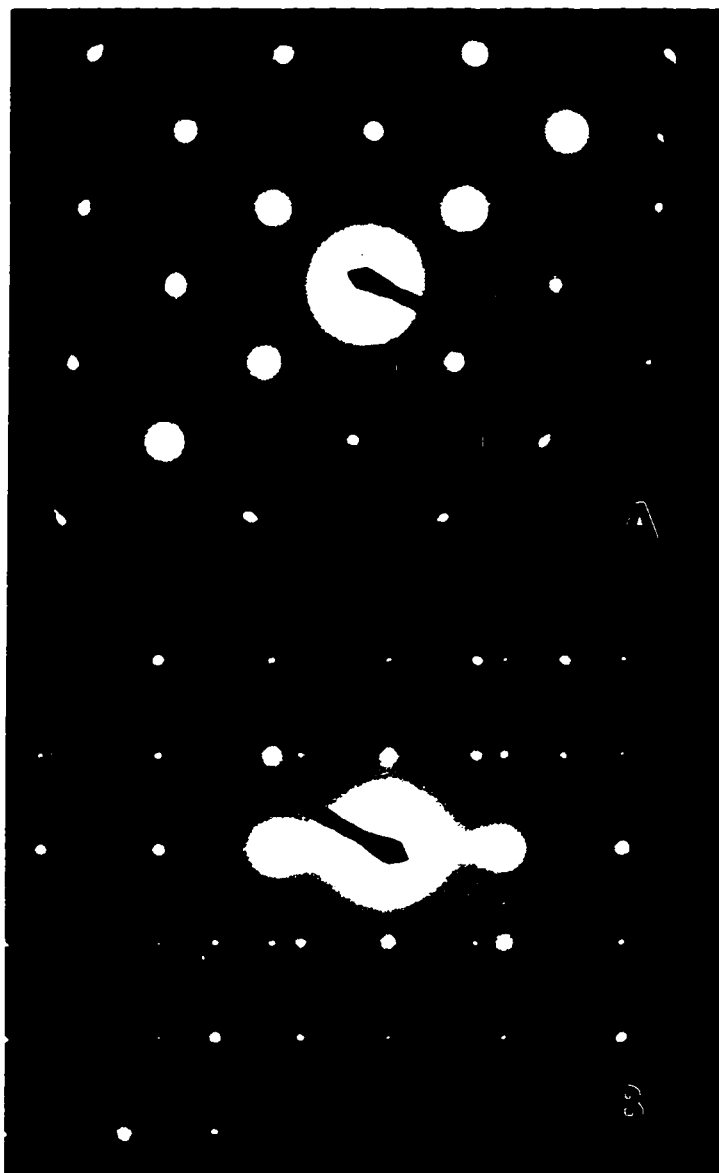


Figure 6.7 SAED pattern of structure disorders

SAED patterns showing structure disorder in the deformed samples. A: SAED pattern, taken from sample B1, arrowheads indicate twofold repeat along the $0\bar{1}2^*$ and 120^* directions. B: A pattern from sample C1 showing a fourfold repeat along the 021^* direction, resulting in a superstructure with a d-spacing of 15.5 Å.



Figure 6.8 Formation of β phase

Formation of β in the deformed olivine (sample B1). The SAED pattern (A), taken from a linear, highly deformed band (Vertical band in the middle of B), can be indexed as a combination of olivine (denoted by subscript a) and β -phase (denoted by subscript b).

Chapter 7

Summary and Future Research

It has been demonstrated in this thesis that the diamond anvil cell , combined with laser spectroscopic techniques, provides a powerful tool in studying physical properties of minerals at very high pressures from elasticity and heat transport to mechanical strength. With new high pressure apparatus capable of megabar and with the assistance of other techniques such as electron microscopy, X-ray diffraction, synchrotron diffraction etc., more measurements can be made and the discovery of novel properties and new phases of minerals at pressures equal to those at the center of the Earth is promised. However, the author makes no attempt to enumerate all the possibilities, but instead will only discuss briefly some experiments which have immediate relevancy to the experiments presented in this thesis and of great importance in addressing some fundamental questions in geophysics.

In Chapter 3, the results showed that the natural Kh-opx is more incompressible than the non-aluminous pyroxenes. The measured average longitudinal and shear velocities of the Kh-pyroxene is about 3% higher. The compressional velocities exceed olivine beyond 4 GPa. The shear velocities are slightly higher than olivine over the entire range of pressure. These results have posed a new challenge to the conventional assumption, which is based on the elastic measurements of non-aluminous pyroxenes, that the high velocity phase garnets need to be balanced by the low velocity phase orthopyroxenes and clinopyroxenes to give a seismic profile which mimics that of olivine. As discussed in Chapter 3, orthopyroxene transforms into clinopyroxene at about 10 GPa, and the elasticity of both high- and low-clinopyroxenes is relatively unknown either at one bar or at high pressure.

Furthermore, the clinopyroxene phase preferentially collects the large cations, principally Na, Ca, Al, and K. To address this apparent difference, immediate efforts are required to study the elasticity of aluminum bearing clinopyroxenes at both one bar and high pressures. It is equally important to study the temperature derivatives of the elasticity of the pyroxenes both at one bar and at high pressures.

Based on the thermal anisotropy results presented in Chapter 4, *Hearn et al.* [1996] proposed a model which evaluates the effects of the recrystallization in the oceanic lithosphere with lattice preferred orientation (LPO) on the thermal state of the lithosphere, the depth of oceanic basins, and the shear strength of the asthenosphere. They concluded, based on their model calculation, that with a well developed LPO in the oceanic lithosphere consistent with the seismic observations, the oceanic lithosphere was hotter, the oceanic basin contraction was less, and the strength of the asthenosphere was weaker than those predicted by a thermally isotropic model. Another issue for which thermal anisotropy may have consequences is the temperature structure of the subducted slab: the size of the faults of the 1994 deep Bolivian earthquake imaged seismically [*Silver et al.*, 1995] at 636 km depth is about 35 km. In order to explain deep earthquakes with a transformational faulting mechanism [*Green and Burnley*, 1989; *Green et al.*, 1992; *Kirby*, 1987; *Kirby et al.*, 1991], a metastable olivine Wedge of similar size, within which the temperature cannot exceed 600 °C (e.g. [*Rubie and Ross*, 1994]), needs to be invoked. However, the thermal calculation using an isotropic thermal model showed that the 600 °C Wedge could not be more than 10 km thick at a depth of 600 km (e.g. [*Kirby et al.*, 1991]). In both cases illustrated above, the knowledge of thermal anisotropy as a function of

temperature is essential. Using the techniques employed in Chapter 4, the temperature dependence of thermal anisotropy due to lattice transport can be easily measured up to a moderate temperature.

Reliable pressure calibration under high non-hydrostatic pressure has been one of the biggest obstacles to the rheological study of minerals under such conditions. The experimental method presented in Chapters 5 and 6 provides both a solution to this problem and a new approach which may lead to a new breed of experiments. The results reported in Chapter 6 are quite significant. First, the observation of partial transformation of olivine to β -phase at room temperature call into question the assumption of metastability of cold olivine within subducted slabs. The importance of this assumption in the transformational faulting mechanism for deep-focal earthquakes has been discussed in Chapter 6. In order to investigate the metastability of olivine under conditions appropriate to subducting slabs, it is necessary to study olivine's plastic behavior and the effect of non-hydrostatic stress on the kinetics of the olivine α - β phase transformation at higher temperatures (600°C) and lower deviatoric stresses.

The author would like to delve a little into another proposed mechanism for the deep-focal earthquake, dehydration embrittlement, which also receives wide attention. *Raleigh and Paterson* [1965] showed that dehydration of serpentine makes it brittle at pressures where the non-hydrous minerals alone are ductile and strong. This embrittlement is caused by water released from serpentine during dehydration because it increases the pore pressure and reduces the effective stress, leading to failures. While dehydration embrittlement of various hydrous minerals is believed to be responsible for the intermediate earthquakes (70-350 km) [*Kirby, 1995*], dehydration

of serpentine as a source mechanism for deep earthquakes remains doubtful since serpentine is likely to be dehydrated at a depth of about 300 km (*Ulmer et al.*, 1995). However, recent studies show that K-amphibole is stable to a depth of about 500 km before dehydration (*Inoue and Irifune*, 1995). The released water then reacts with β phase olivine to form hydrous β phase. So it is still possible that dehydration of high pressure hydrous phases of Mg-silicates may reactivate preexisting faults, causing deep earthquakes.

The technique employed in Chapter 6 can be used to study of the effect of non-hydrostatic stress on the dehydration of high pressure hydrous phases such as β phase olivine, to examination of the strength and embrittlement of these minerals as possible sources for the deep earthquakes.

Another interesting result revealed by TEM analyses of the recovered samples is that the transformation mechanism in the experiments is different from the martinsitic-like transformation predicted by *Madon and Poirier* [1983]. In fact, it is proposed that the transformation of olivine to β phase under current experimental conditions is initiated through stacking disorder [*Wang et al.* 1995]. It is important to determine what mechanisms can operate under conditions within the subducting slab.

Bibliography

- Adams, L. H., and R. E. Gibson, The elastic properties of certain basic rocks and of their constituent minerals, *Proc. Nati. Acad. Sci.*, **15**, 713-724, 1929.
- Akaogi, M., and S. Akimoto, High-pressure phase equilibria in a garnet lherzolite, with special reference to Mg^{2+} - Fe^{2+} partitioning among constituent minerals, *Phys. Earth Planet. Int.*, **19**, 31-51, 1979.
- Akimoto, S. and Fujisawa, H., Olivine-spinel transition in system Mg_2SiO_4 - Fe_2SiO_4 at 800°C, *Earth Planet. Sci. Lett.*, **1**, 237-240, 1966.
- Anderson, D. L., and J. Bass, Mineralogy and composition of the upper mantle, *Geophys. Res. Lett.*, **11**, 637-640, 1984.
- Angel, R. J., and D. A. Hugh-Jones, Equation of state and thermodynamic properties of enstatite pyroxene, *J. Geophys. Res.*, **99**, 19777-19783, 1994.
- Aronson, J. R., L. H. Bellotti, S. W. Eckroad, A. G. Emslie, R. K. McConnell, and P. C. V. Thuna, Infrared spectra and radiative thermal conductivity of minerals at high temperatures, *J. Geophys. Res.*, **Vol. 75**, 3443-3456, 1970.
- Babuska, V., and Cara, M. Seismic Anisotropy in the Earth. 217 p. Kluwer Academic Publ., Dordrecht, 1991.
- Babuska, V., J. Fiala, M. Kumazawa, and I. Ohno, Elastic properties of garnet solid-solution series, *Phys. Earth Planet. Int.*, **16**, 157-176, 1978.
- Balla, A., Stress conditions in triaxial compression, *Journal of the Soil Mechanics and Foundations Division*, **SM 6**, 57-84, 1960.

- Barnett, D.M., J. Lothe, S.D. Gavazza, and M.J.P. Musgrave, Considerations of the existence of interfacial (Stoneley) waves in bonded anisotropic elastic half-space, *Proc. R. Soc. Lond., A* **402**, 153-166, 1985.
- Barnett, J. D., S. Block, and G. J. Piermarini, An optical fluorescence system for quantitative pressure measurement in the diamond-anvil cell, *Rev. Sci. Instr.*, **44**, 1-9, 1973.
- Bass, J. D., Elasticity of uvarovite and andradite garnets, *J. Geophys. Res.*, **91**, 7505-7516, 1986.
- Bass, J. D., Elasticity of grossular and spessartine garnets by Brillouin spectroscopy, *J. Geophys. Res.*, **94**, 7621-7628, 1989.
- Bass, J. D., and D. L. Anderson, Composition of the upper mantle: Geophysical tests of two petrological models, *Geophys. Res. Lett.*, **11**, 237-240, 1984.
- Bass, J. D., and M. Kanzaki, Elasticity of a majorite-pyrope solid solution, *Geophys. Res. Lett.*, **17**, 1989-1992, 1990.
- Bass, J. D., and D. J. Weidner, Elasticity of single-crystal orthoferrosilite, *J. Geophys. Res.*, **89**, 4359-4371, 1984.
- Bi, Q., J. M. Brown, and Y. S. Sorensen, Calibration of Sm:YAG as an alternate high-pressure scale, *J. Appl. Phys.*, **68**, 5357-5359, 1990.
- Bina, C. R., and B. J. Wood, The eclogite to garnetite transition - experimental and thermodynamic constraints, *Geophys. Res. Lett.*, **11**, 955-958, 1984.
- Bina, C. R., and B. J. Wood, Olivine-spinel transition: Experimental and thermodynamic constraints and implications for the nature of the 400-km discontinuity, *J. Geophys. Res.*, **92**, 4853-4866, 1987.
- Birch, F., Elasticity and constitution of earth's interior, *J. Geophys. Res.*, **57**, 227-286, 1952.

- Bock, G., J. Gossler, W. Hanka, R. Kind, G. Kosarev, N. Petersen, K. Stammer and L. Vinnik, On the seismic discontinuities in the upper mantle, *Phys. Earth Planet. Int.*, **92**, 39-43, 1995.
- Bonczar, L. J., and E. K. Graham, The pressure and temperature dependence of the elastic constants of pyrope garnet, *J. Geophys. Res.*, **82**, 2529-2534, 1977.
- Bowman, J.R. and B.L.N. Kennett, An investigation of the upper mantle beneath northwestern Australia using a hybrid seismograph array, *Geophys. J. Int.*, **101**, 411-424, 1990.
- Bridgman, P. W., The linear compression waves in rocks to 10 Kbar, *Am. J. Sci.*, **15**, 287-296, 1928.
- Bridgman, P. W., Linear compression to 30,000 kg/cm², *Am. Acad. Arts Sci.*, **77**, 218-219, 1949.
- Brown, J. M., Interpretation of the D" zone at the base of the mantle: Dependence on assumed values of thermal conductivity, *Geophys. Res. Lett.*, **13**, 1509-1512, 1986.
- Brown, J. M., L. J. Slutsky, K. A. Nelson, and L.-T. Cheng, Single-crystal elastic constants of San Carlos Peridot: An application of impulsive stimulated scattering, *J. Geophys. Res.*, **94**, 9485-9492, 1989.
- Burnley, P.C., H.W. Green, and D.J. Prior, Faulting associated with the olivine to spinel transformation in Mg₂GeO₄ and its implications for deep-focus earthquakes, *J. Geophys. Res.*, **96**, 425-443, 1991.
- Burnley, P. C., & Green, H. W, Stress dependence of the mechanism of the olivine-spinel transformation, *Nature*, **338**, 753-756, 1989.
- Burns, R. G., *Optical Absorption in Silicates*, J. Wiley and Sons, New York, 1968.

- Carter, N. L., and H.G. AveLallemant, High temperature flow of dunite and peridotite, *Geol. Soc. Amer. Bull*, **81**, 2181-2202, 1970.
- Chai, M., J. M. Brown, and L. J. Slutsky, The elastic constants of pyrope-grossular-almandine garnet to 20 GPa, *Geophys. Res. Lett.*, 1996a.
- Chai, M., J. M. Brown, and L. J. Slutsky, Elasticity of a Kilbourne Hole enstatite to 12.5 GPa, *J. Geophys. Res.*, Submitted, 1996b.
- Chai, M., and J.M. Brown, Effects of static non-hydrostatic stress on the R lines of ruby single crystals, *Geophys. Res. Lett.*, 1996, in press.
- Chai, M., J. M. Brown and Y. Wang, Yield strength, slip systems and deformation induced phase transition of San Carlos olivine up to transition zone pressure at room temperature, US-Japan Research at High Pressure, submitted
- Cleary, J.R. and A.L. Hales, An analysis of the travel times of P waves to North America stations in the distance range 32 - 100°, *Bull. Seis. Soc. Am.*, **56**, 467-489, 1966.
- Deer, W. A., R. A. Howie, J. Zussman, An Introduction to the Rock-Forming Minerals, pp. 528, Longman, London, 1976.
- Doyle, H.A. and D.A.L. Hales, AN analysis of the travel times of S waves to North America stations, in the distance range 28° to 82°, *Bull. Seis. Soc. Am.*, **57**, 7610771, 1967.
- Duffy, T. S., and M. T. Vaughan, Elasticity of enstatite and its relationship to crystal structure, *J. Geophys. Res.*, **93**, 383-391, 1988.
- Duffy, T. S., and D. L. Anderson, Seismic velocities in mantle minerals and the mineralogy of the upper mantle, *J. Geophys. Res.*, **94**, 1895-1912, 1989.

- Evans, B., and C. Goetze, The temperature variation of the hardness of olivine and its implication for polycrystalline yield stress, *J. Geophys. Res.*, **84**, 5505, 1979.
- Ewing, W.M., W.S. Jardetzky and F. Press, *Elastic Waves in Layered Media*, Edited by R.R. Shrock, McGraw-Hill, New York, 1957.
- Farra, V., and L. Vinnik, Shear wave splitting in the upper mantle of the Pacific, *Geophys. J. Int.*, **119**, 1994.
- Fayer, M. D., Holographic grating generation of ultrasonic waves, *IEEE J. Quantum Electronics*, **22**, 1444, 1986.
- Feher, E., and M. D. Sturge, Effect of stress on the trigonal splittings of d^3 ions in sapphire ($\alpha\text{-Al}_2\text{O}_3$), 244-249, 1968.
- Frisillo, A. L., and G. R. Barsch, Measurement of single crystal elastic constants of bronzite as a function of pressure and temperature, *J. Geophys. Res.*, **77**, 6360-6384, 1972.
- Frost, H.J., and M.F. Ashby, *Deformation-Mechanism Maps-the Plasticity and Creep of Metal and Ceramics*, 166pp., Pergamon Press, 1982.
- Furnish, M.D., D. Grady, and J.M. Brown, Analysis of shock wave structure in single-crystal olivine using VISAR, in *Shock Waves in Condensed Matter*, edited by Y. Gupta, pp. 595-600, Plenum, New York, 1986.
- Fujisawa, H., N. Fuji, H. Mizutani, H. Kanamori, and S. Akimoto, Thermal diffusivity of Mg_2SiO_4 , Fe_2SiO_4 and NaCl at high pressure and temperature, *J. Geophys. Res.*, **75**, 4727-4733, 1968.
- Fujishiro, L., Y. Nakamura, T. Kawase, and B. Okai, The property of a ruby high pressure sensor under uniaxial compressive stress, *JSME International J.*, **31**, 136-141, 1988.

- Fukao, Y., H. Mizutani, and S. Uyeda, Optical absorption spectra at high temperatures and radiative thermal conductivity of olivine, *Phys. Earth Planet. Int.*, **1**, 57-62, 1968.
- Furnish, M. D., D. Grady, and J. M. Brown, Analysis of shock wave structure in single-crystal olivine using VISAR, in *Shock Waves in Condensed Matter*, Y. Gupta, Ed., Plenum, New York, 595-600, 1986.
- Grand, S.P., Mantle shear structure beneath the Americas and surrounding oceans, *J. Geophys. Res.*, **99**, 11591-11621, 1994.
- Grand, S.P. and D.V. Helmberger, Upper mantle shear structure beneath the Northwest Atlantic Ocean, *J. Geophys. Res.*, **89**, 11465-11475, 1984.
- Green, H.W., and P.C. Burnley, A new self-organizing mechanism for deep-focus earthquakes, *Nature*, **341**, 733-737, 1989.
- Green, H.W., T.E. Young, D. Walker, and C. H. Scholz, Anticrack-associated faulting at very high pressure in natural olivine, *Nature*, **348**, 720-722, 1990.
- Green, H.W., T.E. Young, D. Walker, and C.H. Scholz, Anticrack-associated faulting at very high pressure in nature olivine, *Nature*, **348**, 720-722, 1990.
- Green, H.W., T.E. Young, D. Walker, and C.H. Scholz, The effect of nonhydrostatic stress on the $\alpha - \beta$ and $\alpha - \gamma$ olivine phase transformations, in *High-Pressure Research Application to Earth and Planetary Sciences*, Geophys. Monog. Ser., edited by Y. Syono and M. H. Manghnani, pp. 229-235, Terra Scientific Publishing Company, Tokyo, AGU, Washington, D.C., 1992.
- Griggs, D. T., The sinking lithosphere and the focal mechanism of deep earthquakes, in *The Nature of the Solid Earth*, edited by E. C. Robertson, pp. 361-384, McGraw-Hill, New York, 361-384, 1972.

- Gupta, Y. M. and X. A. Shen, Potential use of the ruby R2 line shift for static high-pressure calibration, *Appl. Phys. Lett.* **58**, 583-585, 1991
- Guyot, F., G.D. Gwanmesia, and R.C. Liebermann, An olivine to beta phase transformation mechanism in Mg_2SiO_4 , *Geophys. Res. Lett.*, **18**, 89-92, 1991.
- Halleck, P.M., The compression and compressibility of grossular garnet-A comparison of X-ray and ultrasonic methods, Ph.D. thesis, University of Chicago, 1973.
- Hazen, R. M., and L. W. Finger, Crystal structure and compressibilities of pyrope and grossular to 60 kbar, *Am. Min.*, **63**, 297-303, 1978.
- Hazen, R. M., and L. W. Finger, High-pressure crystal chemistry of andradite and pyrope: Revised procedure for high-pressure diffraction experiments, *Am. Min.*, **74**, 353-359, 1989.
- Hearn, L., E.D. Humphreys, M. Chai, and J. M. Brown, Effect of anisotropy on development of oceanic asthenosphere, *J. Geophys. Res.*, submitted, 1996.
- Hess, H., Seismic anisotropy of the uppermost mantle under oceans, *Nature*, **203**, 629-631, 1964.
- Horai, K., Thermal conductivity of rock-forming minerals, *J. Geophys. Res.*, **76**, 1278-1308, 1971.
- Humphreys, E. D., and K. G. Dueker, Physical state of the western U.S. upper mantle, *J. Geophys. Res.*, **99**, 9635-9650, 1994.
- Inoue, T., and T. Irifune, Decomposition of K-amphibole at high pressure: implications for the origin of the third chain volcanism, *EOS, Trans. Am. Geophys. Union*, Vol. **76**, NO 46, F711, 1995.

- Isaak, D. G., and E. K. Graham, The elastic properties of an almandine-spessartine garnet and elasticity in the garnet solid solution series, *J. Geophys. Res.*, **81**, 2483-2489, 1976.
- Ita, J., and L. Stixrude, Petrology, elasticity, and composition of the mantle transition zone, *J. Geophys. Res.*, **97**, 6849-6866, 1992.
- Johnson, L.R., Array measurements of P velocities in the upper mantle, *J. Geophys. Res.*, **72**, 6309-6325, 1967.
- Jordan, T. H., Mineralogies, densities and seismic velocities of garnet lherzolites and the geophysical implications, in *The Mantle Sample: Inclusions in Kimberlite and Other Volcanics*, F. R. Boyd & H. O. A. Meyers, Ed., American Geophysical Union, Washington D. C., 1-14, 1979.
- Kanamori, H., N. Fujii, and H. Mizutani, Thermal diffusivity of rock-forming minerals from 300° to 1100° K, *J. Geophys. Res.*, **73**, 595-605, 1968.
- Kanzaki, M., Ortho/clinoenstatite transition, *Phys. Chem. Minerals*, **17**, 726-730, 1991.
- Kandelin, J., and D. J. Weidner, Elastic properties of hedenbergite, *J. Geophys. Res.*, **93**, 1063-1072, 1988a.
- Kandelin, J., and D. J. Weidner, The single-crystal properties of jadeite, *Phys. Earth Planet. Int.*, **50**, 251-260, 1988b.
- Kanzaki, M., Ortho/clinoenstatite transition, *Phys. Chem. Minerals*, **17**, 726-730, 1991.
- Kieffer, S. W., Lattice thermal conductivity within the earth and considerations of a relationship between the pressure dependence of the thermal diffusivity and the volume dependence of the Grüneisen parameter, *J. Geophys. Res.*, **81**, 3025-3030, 1976.

- Kiel, A., Temperature-dependent linewidth of excited states in crystals. I. Line broadening due to adiabatic variation of the local fields, *Phys. Rev*, **126**, 1292-1297, 1962.
- Kinsland, G. L., and W. A. Bassett, Strength of MgO and NaCl polycrystals to confining pressures of 250 kbar at 25°C, *J. Appl. Phys.*, **48**, 978-985, 1977.
- Kirby, S.H., Localized polymorphic phase transformation in high-pressure faults and applications to the physical mechanism of deep earthquakes, *J. Geophys. Res.*, **92**, 13789-13800, 1987.
- Kirby, S. and B. Hemingway and R. Lee, Anomalous fracture and thermal behavior of hydrous minerals, American Geophysical Union, *Geophys. Monograph*, **56**, 119-126, 1990
- Kirby, S.H., W.B. Durham, and L.A. Stern, Mantle phase changes and deep-earthquake faulting in subducting lithosphere, *Science*, **252**, 216-225, 1991.
- Kirby, S. H. Intraslab earthquakes and phase changes in subducting lithosphere, U.S. National Report to the I.U.G.G. 1990-1994, 1995
- Kumazawa, M., and O. L. Anderson, Elastic moduli, pressure derivatives and temperature derivatives of single-crystal olivine and single-crystal forsterite, *J. Geophys. Res.*, **74**, 5961-5972, 1969.
- Kuo, B. Y., and D. W. Forsyth, A search for split SKS waveforms in north Atlantic, *Geophys. J. Int.*, **108**, 557-574, 1992.
- Kudoh, Y., & Takeuchi, Y. (1985). The crystal structure of forsterite Mg_2SiO_4 under high pressure up to 149 kbar. *Z. Kristall.*, **171**, 291-302.
- Leger, J. M., A. M. Redon, and C. Chateu, Compression of synthetic pyrope, spessartine and uvarovite garnets up to 25 GPa, *Phys. Chem. Min.* **17**, 161-167, 1990.

- Leibfried, G., and Schlömann, E., Wärmeleitung in elektrische isolierende kristallen. *Nachr. Ges. Wiss. Goett., Math.-Phys., K1 (IIA)*, 71-93, 1954.
- Leitner, B. J., D. J. Weidner, and R. C. Liebermann, Elasticity of single crystal pyrope and implications for garnet solid solution series, *Phys. Earth Planet. Int.*, **22**, 111-121, 1980.
- Levien, L., D. J. Weidner, and C. T. Prewitt, Elasticity of diopside, *Phys. Chem. Min.* **4**, 105-113, 1979.
- Liu, L., The mineralogy of an eclogitic earth mantle, *Phys. Earth Planet. Int.*, **23**, 262-267, 1980.
- Liu, L., Silicate perovskite from phase transformations of pyrope-garnet at high pressure and temperatures, *Geophys. Res. Lett.*, **1**, 277-280, 1974.
- Liu, L., The high pressure phase of MgSiO_3 , *Earth Planet. Sci. Lett.*, **31**, 200-208, 1976.
- Liu, L. and A.E. Ringwood, Synthesis of a perovskite-type polymorph of CaSiO_3 , *Earth Planet. Sci. Lett.*, **28**, 209-211, 1975.
- Madon, M., and J. P. Poirier, Transmission electron microscope observation of α , β and γ $(\text{Mg,Fe})_2\text{SiO}_4$ in shocked meteorites: Planar defects and polymorphic transitions, *Phys. Earth Planet. Int.*, **33**, 31-44, 1983.
- Mao, H.K., P.M. Bell, J.W. Shaner, and D.J. Steinberg, Specific volume measurements of Cu, Mo, and Ag and calibration of ruby R_1 fluorescence pressure gauge from 0.06 to 1 Mbar, *J. Appl. Phys.*, **49**, 3276-3283, 1978.
- Mao, H. K., J. Xu, and P. M. Bell, Calibration of ruby pressure gauge to 800 kbar under quasi-hydrostatic conditions, *J. Geophys. Res.*, **91**, 4673-4676, 1986.
- Meade, C., and R. Jeanloz, Yield strength of B1 and B2 phases of NaCl, *J. Geophys. Res.*, **93**, 3270-3274, 1988.

- Meade, C., and R. Jeanloz, The strength of mantle silicates at high pressures and room temperature: implications for viscosity of the mantle, *Nature*, **348**, 533, 1990a.
- Meade, C., and R. Jeanloz, Yield strength of Al_2O_3 at high pressure, *Physical Review B*, **42**, 2532-2535, 1990b.
- Meagher, E.P., Silicate garnets, in *Reviews in Mineralogy Ortho-silicates*, Vol. 5, Edited by P. H. Ribbe, Min. Soc. Am., Bookcrafters, Inc., Chelsea, Michigan, 1982.
- Menzies, M. A., Petrology and geochemistry of the continental mantle: An historical perspective, in *Continental Mantle*, M. A. Menzies, Ed., Oxford University Press, p31-54, 1990
- Munro, R. G., G. J. Piermarini, and S. Block, Model line-shape analysis for the ruby lines used for pressure measurement, *J. Appl. Phys.*, **57**, 165-169, 1993.
- Nataf, H.C., I. Nakanishi, and D.L. Anderson, Measurements of mantle wave velocities and inversion for lateral heterogeneities and anisotropy 3. Inversion, *J. Geophys. Res.*, **91**, 7261-7307, 1986.
- Nicolas, A., and J. P. Poirier, *Crystalline Plasticity and Solid State Flow in Metamorphic Rocks*, John Wiley & Sons. Ltd, 1976.
- Nicolas, A., and N. Christenson, Formation of anisotropy in upper mantle peridotites-a review, in *Composition, Structure, and Dynamics of Lithosphere Systems*, K. Fuchs & C. Froidevaux, Eds., 1987.
- Nishimura, C., and D. Forsyth, The anisotropy structure of the upper mantle in the Pacific, *J. Geophys.*, **96**, 203-229, 1989.
- Niazi, M. D.L. Anderson, Upper mantle structure of western North America from apparent velocities of P waves, *J. Geophys. Res.*, **70**, 4633-4640, 1965.

- O'Neill, B., J. Bass, J. R. Smyth, and M. T. Vaughan, Elasticity of grossular-pyrope-almandine garnet, *J. Geophys. Res.*, **94**, 17819-17824, 1989.
- Okai, B., O. Shimomura, and I. Fujishiro, Measurement of anisotropic stress field in a gasketed diamond-anvil cell, *Physica*, **139 & 140 B**, 799-802, 1986.
- Pacalo, R. E. G., and T. Gasparik, Reversals of the orthoenstatite-clinoenstatite transition at high pressures and high temperatures, *J. Geophys. Res.*, **95**, 15853-15858, 1990.
- Paterson, M. S. Experimental Rock Deformation: The brittle field, Springer, Berlin, Springer-Verlag, 1978.
- Phillips, Wm. Revrill, Mineral Optics, Principles and Techniques, pp. 249, Freeman and Company, New York, 1971.
- Piermarini, G. J., S. Block, and J. D. Barnett, Hydrostatic limits in liquids and solids to 100 kbar, *J. Appl. Phys.*, **44**, 5377-5382, 1973.
- Piermarini, G. J., S. Block, J. D. Barnett, and R. A. Forman, Calibration of the pressure dependence of R₁ ruby fluorescence line to 195 kbar, *J. Appl. Phys.*, **46**, 2774-2780, 1975.
- Poirier, J. P., On the kinetics of olivine-spinel transition, *Phys. Earth Planet. Int.*, **26**, 179-187, 1981.
- Ramachandra Rao, B., Elastic constants of garnets, *Proc. Indian Acad. Sci., Sect A*, **22**, 194-198, 1945.
- Raleigh, C.B., Mechanisms of plastic deformation in olivine, *J. Geophys. Res.*, **73**, 5391-5406, 1968.
- Raleigh, C. B. and M. S. Paterson, Experimental; deformations of serpentine and its tectonic consequences, *J. Geol.*, **90**, 611-643, 1982
- Revenaugh, J. and T.H. Jordan, Mantle layering from ScS reverberations 2. The transition zone, *J. Geophys. Res.*, **96**, 19763-19780, 1991.

- Ribe, N. M., and Y. Yu, A theory for plastic deformation and textural evolution of olivine polycrystals, *J. Geophys. Res.*, **96**, 8325-8335, 1991.
- Rigden, S. M., G. D. Gwanmesia, and R. C. Liebermann, Elastic wave velocities of a pyrope-majorite garnet to 3 GPa, *Phys. Earth Planet. Int.*, **86**, 35-44, 1994.
- Ringwood, A.E., The olivine-spinel transition in the Earth's Mantle, *Nature*, **178**, 1303-1304, 1956.
- Ringwood, A.E. and A. Major, Synthesis of Mg_2SiO_4 - Fe_2SiO_4 spinel solid solutions, *Earth Planet. Sci. Lett.*, **1**, 241-245, 1966.
- Ringwood, A.E., Phase transformations and the constitution of the mantle, *Phys. Earth Planet. Int.*, **8**, 109-155, 1970.
- Ringwood, A. E., *Origin of the Earth and Moon*, Springer-Verlag, New York, 1979.
- Ringwood, A. E., Phase transformations and their bearing on the constitution and dynamics of the mantle, *Geochimica et Cosmochimica Acta.*, **55**, 2083-2110, 1991.
- Ross, R.G., P. Anderson, B. Sundqvist, and G. Backstrom, Thermal conductivity of solids and liquids under pressure, *Rep. Prog. Phys.*, **47**, 1347-1402, 1984.
- Roufousse, M., and P. G. Klemens, Thermal conductivity of complex dielectric crystals, *Phys. Rev. B*, **7**, 5379-5386., 1973.
- Rubie, D.C., and C.R. Ross, II, Kinetics of the olivine-spinel transformation in subducting lithosphere: experimental constraints and implications for deep slab processes, *Phys. Earth Planet. Int.*, **86**, 223-241, 1994.

- Ryzhova, T.V., K.S. Aleksandrov, and V.M. Korobkova, The elastic properties of rock-forming minerals, 5, Additional data on silicates, *Izv. Acad. Sci. USSR. Phys. Solid Earth*, Engl. Transl., 1966(2), 111-113, 1966.
- Sato, H., Viscosity of the upper mantle from laboratory creep and anelasticity measurements in peridotite at high pressure and temperature, *Geophys. J. Int.*, **105**, 587-599, 1991.
- Scharmeli, G.H., Anisotropy of olivine thermal conductivity at 2.5 GPa up to 1500 K measured on optically non-thick sample, In *High-Pressure Research in Geosciences*, W. Schreyer, Ed. p. 349-373. E. Schweizerbartsche Verlags., Stuttgart, 1982.
- Schatz, H. F., and G. Simmons, Thermal conductivity of Earth minerals at high temperatures, *J. Geophys. Res.*, **77**, 6966-6983, 1972.
- Schroeder, W., The empirical age-depth relation and depth anomalies in the Pacific Oceanic basin, *J. Geophys. Res.*, **89**, 9873-9884, 1984.
- Shankland, T. J., Pressure shift of infrared absorption bands in minerals and the effect on radiative heat transport, *J. Geophys. Res.*, **75**, 409-413, 1970.
- Sharma, S. M., and Y. M. Gupta, Theoretical analysis of R-line shifts of ruby subjected to deformation condition, *Phys. Rev. B*, **43**, 879-893, 1991.
- Shearer, P.M., Constraints on upper mantle discontinuities from observations of long-period reflected and converted phases, *J. Geophys. Res.*, **96**, 18147-18182, 1991.
- Shen, X. A., and Y. M. Gupta, Effect of crystal orientation on ruby line shifts under shock compression and tension, *Phys. Rev. B*, **48**, 2929-2940, 1993.
- Silver, P. G., S. L. Beck, T. C. Wallace, C. Meade, S. C. Myers, D. E. James, and R. Kuehnel, Rupture characteristics of the deep Bolivian earthquake of 9

- June 1994 and the mechanism of deep-focus earthquakes, *Science*, **268**, 69-73, 1995.
- Simmons, G., The velocity of compressional waves in various minerals at pressures to 10 kilobars, *J. Geophys. Res.*, **69**, 1117-1122, 1964.
- Skinner, B. J., Physical properties of end-members of the garnet group, *Am. Min.*, **41**, 428-436, 1956.
- Soga, N., Elastic constants of garnet under pressure and temperature, *J. Geophys. Res.*, **72**, 4227-4234, 1976.
- Spohn, T., and G. Schubert, Modes of mantle convection and the removal of heat from the earth's interior, *J. Geophys. Res.*, **87**, 4682-4696, 1982.
- Su, W., R.L. Woodward and A.M. Dziewonski, Degree 12 model of shear velocity heterogeneity in the mantle, *J. Geophys. Res.*, **99**, 6945-6980, 1994.
- Sumino, Y., and O. L. Anderson, *Handbook of Physical Properties of Rocks* , CRC Press, Boca Raton, FL, 1984.
- Sung, C., and R. G. Burns, Kinetics of high-pressure phase transformation: Implications to the evolution of the olivine-spinel transformation in the downgoing lithosphere and its consequences on the dynamics of the mantle, *Tectonophysics*, **31**, 1-32, 1976.
- Suzuki, I., and O.L. Anderson, Elasticity and thermal expansion of a natural garnet up to 1000 K, *J. Phys. Earth.*, **31**, 125-138, 1983.
- Turcotte, D. and G. Schubert, *Geodynamics - Applications of Continuum Physics to Geological Problems*, pp450, John Wiley & Sons, 1982.
- Takahashi, T., and L. Liu, Compression of ferromagnesian garnets and the effect of solid solution on the bulk modulus, *J. Geophys. Res.*, **75**, 5757-5766, 1970.

- Ulmer, P., V. Trommsdorf and E. Reusser, Experimental investigation into antigorite stability to 80 kbar, *Min. Mag.*, **58A**, 919-920, 1994
- Verma, R. K., Elasticity of some high density crystals, *J. Geophys. Res.*, **65**, 757-766, 1960.
- Watt, J. P., and L. Peselnick, Clarification of the Hashin-Shtrikman bounds on the effective elastic moduli of polycrystals with hexagonal, trigonal, and tetragonal symmetries, *J. Appl. Phys.*, **51**, 1525-1531, 1980.
- Weaver, J. S., T. Takahashi, and J. Bass, Isothermal compression of grossular garnets to 250 kbar and the effect of calcium on the modulus, *J. Geophys. Res.*, **81**, 1475-2482, 1976.
- Webb, S. L., The elasticity of the upper mantle orthosilicates olivine and garnet to 3 GPa, *Phys. Chem. Mineral*, **16**, 684-692, 1989.
- Webb, S., and I. Jackson, The pressure dependence of the elastic moduli of single-crystal orthopyroxene ($\text{Mg}_{0.8}\text{Fe}_{0.2}\text{SiO}_3$), *Eur. J. Mineral.*, **5**, 1111-1119, 1993.
- Weidner, D.J., H. Wang, and J. Ito, Elasticity of orthoenstatite, *Phys. Earth Planet. Int.*, **17**, 7-13, 1978.
- Weidner, D.J., Y. Wang, G. Chen, and J. Ando, Rheology measurements at high pressure and temperature (abstract), *EOS Trans. AGU*, Fall Meeting Suppl., **76**, f584, 1995.
- Wiens, D. A., J. J. McGuwere, and P. J. Shore, Evidence for transformational faulting from a deep double seismic zone in Tonga, *Nature*, **364**, 790-793, 1993.
- Wiggins, R.A. and D. V. Helmberger, Upper mantle structure of the Western United States, *J. Geophys. Res.*, **78**, 1870-1880, 1973.

- Wooster, W. A., Thermal conductivity in relation to crystal structure, *Z. Kristallogr.*, 138-149, 1936.
- Yan, Y. X., L.-T. Cheng, and K. A. Nelson, Impulsive stimulated scattering, in *Advances in Non-linear Spectroscopy*, edited by J. H. Clark & R. E. Hester, John Wiley Ltd., London, 1987
- Young, C., Dislocations in the deformation of olivine, *Amer. J. Sci.*, 267, 841-852, 1969.
- Zaug, J., E. H. Abramson, J. M. Brown, and L. J. Slutsky, Elastic constants, equation of state and thermal diffusivity at high pressure, in *High Pressure Research: Application to Earth and Planet Sciences*, edited by Y. Syono & M. Manghnani, American Geophysical Union, Washington D. C., 157-166, 1992
- Zaug, J., E. H. Abramson, J. M. Brown, and L. J. Slutsky, Sound velocities in olivine at Earth mantle pressures, *Science*, 260, 1487-1489, 1993.
- Zaug, J., L. J. Slutsky, and J. M. Brown, Equation of state and relaxation of methanol at high pressure and temperature, *J. Phys. Chem.*, 98, 6008, 1994.
- Zielhuis, A. and R.D. Hilst, Mantle structure beneath the eastern Australian region from partitioned waveform inversion. *Geophys. J. Int.*, 127, 1-16, 1996.
- Ziman, J. M., *Electrons and Phonons*, Oxford University Press, London, 1962.
- Zindler, A., and S. R. Hart, Chemical geodynamics, *Ann. Rev. Earth Planet. Sci.*, 14, 493-571, 1986.

Personal Vita

Personal information

Mu Chai was born in March 21, 1961 in Qingdao, Shandong,
People's Republic of China.

Father: Professor Xianghao Chai.

Mother: Professor Yuzhi Cui.

Wife: Yang Liu.

Daughter: Jessica Yubo Chai

Education

Ph.D., Geophysics, 1996, University of Washington, Seattle, Washington.

M.S., Physics, 1990, Bowling Green State University, Bowling Green, Ohio.

B.S., Optics, 1982, Shandong University, Jinan, Shandong, China.